

AD-A257 088



**SPIRIT I
FINAL FLIGHT REPORT**

Donald R. Smith
Anthony J. Ratkowski
Steven M. Adler-Golden

Michael W. Matthew
W. F. Grieder
E. N. Richards

15 May 1991

DTIC
ELECTE
SEP 02 1992
S A D

APPROVED FOR PUBLIC RELEASE; DISTRIBUTION UNLIMITED.

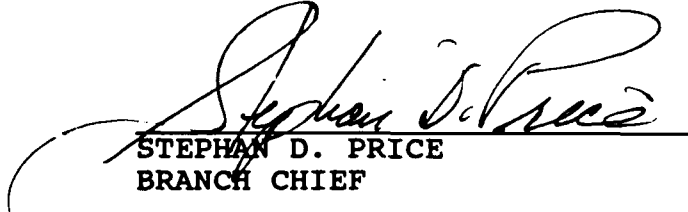


**PHILLIPS LABORATORY
DIRECTORATE OF GEOPHYSICS
AIR FORCE SYSTEMS COMMAND
HANSOM AIR FORCE BASE, MA 01731-5000**

92-24213



"This technical report has been reviewed and
is approved for publication"


STEPHAN D. PRICE
BRANCH CHIEF

FOR THE COMMANDER


R. EARL GOOD
DIVISION DIRECTOR

This report has been reviewed by the ESD Public Affairs Office (PA) and is releasable to the National Technical Information Service (NTIS).

Qualified requestors may obtain additional copies from the Defense Technical Information Center. All others should apply to the National Technical Information Service.

If your address has changed, or if you wish to be removed from the mailing list, or if the addressee is no longer employed by your organization, please notify GL/DAA, Hanscom AFB, MA 01731. This will assist us in maintaining a current mailing list.

Do not return copies of this report unless contractual obligations or notices on a specific document requires that it be returned.

REPORT DOCUMENTATION PAGE

Form Approved
OMB No. 0704-0188

Public reporting for the collection of information is estimated to average 1 hour per response, including the time for reviewing instructions, searching existing data sources, gathering and maintaining the data needed, and completing and reviewing the collection of information. Send comments regarding this burden estimate or any other aspect of this collection of information, including suggestions for reducing this burden, to Washington Headquarters Services, Directorate for Information Operations and Reports, 1215 Jefferson Davis Highway, Suite 1204, Arlington, VA 22202-4302, and to the Office of Management and Budget, Paperwork Reduction Project (0704-0188), Washington, DC 20503.

The Spectral Infrared Interferometric Telescope (SPIRIT 1) experiment, launched on April 8, 1986, from Poker Flat Research Range, Alaska, was a rocket-borne probe designed to measure long-wavelength infrared emissions from an IBC class III aurora in the limb-viewing geometry. The primary instrument was a cryogenically cooled, five-detector Michelson interferometer mated to a high-off-axis-rejection telescope. The spectra provide a comprehensive data base on molecular emission features in the nighttime sky in the 500- to 2000-cm⁻¹ (5- to 20- μ m) region. This report provides a detailed overview of the SPIRIT 1 flight and mission and the analysis of the flight data.

14. SUBJECT TERMS			15. NUMBER OF PAGES
Rocketborne measurements	Earthlimb radiance	Carbon dioxide	262
Atmospheric measurements	Auroral emissions	Nitric oxide	
Mesospheric measurements	Cryogenic interferometer	Ozone	
17. SECURITY CLASSIFICATION OF REPORT			18. SECURITY CLASSIFICATION OF THIS PAGE
Unclassified	Unclassified	Unclassified	20. LIMITATION OF ABSTRACT
			SAR

Accession For		
NTIS	CRA&I	<input checked="" type="checkbox"/>
DTIC	TAB	<input type="checkbox"/>
Unclassified		<input type="checkbox"/>
Justification		
By _____		
D. t. b. t. o. / _____		
Exhibitatory Classes		
D. t. b. t. o. / _____		
SAC/CL		

DTIC QUALITY INSPECTED 3

Contents

1. EXECUTIVE SUMMARY	1
2. INTRODUCTION	3
3. INSTRUMENTATION DESCRIPTION	4
3.1 Payload Sensors	4
3.2 Interferometer Description	6
4. ROCKET FLIGHT SUMMARY	9
4.1 Launch Description	9
4.2 Flight Description	9
5. INSTRUMENT AND ROCKET PERFORMANCE SUMMARY	11
5.1 Vehicle Performance Summary	11
5.2 Interferometer Performance Summary	12
5.3 Ancillary Sensors Performance Summary	12
5.4 Flight Anomalies	13
5.4.1 Image-Intensified Film Camera Door	13
5.4.2 NASA TRADAT and Uplink Command	13
5.4.3 Scan Anomaly	14
5.4.4 Hasselblad Film Camera	14
5.4.5 Interferometer Detector and Pre-Amplifier Non-Linearities	15
6. DATA SUMMARY	15
6.1 Telemetry and Tracking Summary	15
6.1.1 Telemetry Summary	15
6.1.2 Tracking Summary	16

6.2	IR Data Summary	17
6.2.1	IR Data Review	17
6.2.2	Anomalies Affecting IR Data	18
6.2.3	Harmonic Distortions Caused by Nonlinear Effects	19
6.3	Photometer Data Summary	20
6.4	Horizon Sensor Data Summary	22
6.5	TV Camera Operation and Data Summary	23
6.6	Film Camera Data Summary	24
6.7	Ground-Based Data Summary	25
7.	DATA REDUCTION	27
7.1	Pointing and Tangent Height Determination	27
7.1.1	Initial Tangent Height Determination	27
7.1.2	Final Tangent Height Determination	32
7.1.2.1	Method for Determining the Final Tangent Heights	33
7.1.2.2	Computational Details of Method	34
7.1.2.3	Discussion of Tangent Height Results	36
7.2	Interferometer Data Processing	36
7.3	Spectral Emission Estimates	39
8.	CALIBRATION OF INTERFEROMETER DATA	44
8.1	Introduction	44
8.2	Open-Filter Mode	44
8.2.1	Relative Wavelength Response	44
8.2.2	Absolute Responsivities	44
8.2.2.1	Method 1	44
8.2.2.2	Method 2	47
8.2.3	Open-Filter Calibration Summary	50
8.3	Responsivities With the Bandpass Filters	52
8.4	Calibration Summary	52
9.	DATA ANALYSIS SUMMARY	52
9.1	Introduction	52
9.2	Atmospheric Limb Radiation	53
9.2.1	Viewing Geometry	53
9.2.2	CO ₂ 15 μm	53
9.2.3	Ozone 9.6 μm	55
9.2.4	Ozone Hot Bands (10.8-12.5 μm)	55
9.2.5	Nitric Oxide (5.3 μm)	59
9.3	Anomalous Background Radiation	59
9.3.1	General Characteristics	59
9.3.2	Explanation of the SPIRIT 1 Anomalous Data	70
9.3.3	Contamination Discussion	75
9.3.4	Spectroscopic Properties of Silanes and Silicones	75
9.4	Identification of the Specific Compound Observed by SPIRIT 1	78
9.5	Sources of Silicones	79
9.5.1	General Discussion	79
9.5.2	Rocket Booster Contamination	80
9.5.3	Payload Contamination	80
9.5.4	Main Sensor Internal Contamination	83
9.6	Spectral Properties of ECP-2200 Black Paint	84
9.6.1	General Discussion	84
9.6.2	Measurement Technique	84
9.6.3	Sample Description and Preparation	87
9.6.4	Discussion of Results	88
9.7	Telescope Leakage Summary	101

REFERENCES	105
APPENDIX A: TABULATION OF INTERFEROMETER SCANS	109
APPENDIX B: TABULATION OF PAYLOAD TRAJECTORY AND HORIZON SENSOR TANGENT HEIGHTS	119
APPENDIX C: SAMPLE OF RAW INTERFEROGRAMS	137
APPENDIX D: SAMPLE OF TRANSFORMED SPECTRA	173
APPENDIX E: THE 9-12 μ m ATMOSPHERIC OZONE EMISSION OBSERVED IN THE SPIRIT 1 EXPERIMENT	209
APPENDIX F: UPPER ATMOSPHERIC INFRARED RADIANCE FROM CO ₂ AND NO OBSERVED DURING THE SPIRIT 1 ROCKET EXPERIMENT	219
APPENDIX G: IDENTIFICATION OF 4- TO 7-QUANTUM ν_3 BANDS IN THE ATMOSPHERIC RECOMBINATION SPECTRUM OF OZONE	233
APPENDIX H: PROGRAM PARTICIPANTS	247

Illustrations

1. Nominal SPIRIT 1 Mission.	5
2. SPIRIT 1 Detector Focal Plane Layout Illustrating Angular Subtense in Object Space.	7
3. SPIRIT 1 Onboard Photometer Filter Characteristics.	8
4. Comparison of Preplanned Scan Pattern and Actual Spatial Scan Pattern Flown by SPIRIT 1.	15
5. Best-Fit Payload Trajectory from NASA TRADAT Tracking Data.	17
6. Calibration Interferogram and Spectrum of 11-13 μ m Filter Region Showing Effect of Harmonic Distortions.	21
7. Simulation of Harmonic Distortions due to Nonlinear Effects.	22
8. Horizon Sensor Tangent Heights and 3914Å Photometer Data (Auroral Brightness) vs Time After Launch. (TAL)	23
9. Picture From the On-board TV Camera Showing the Location of the SPIRIT 1 Interferometer Focal Plane Relative to the Auroral Form Being Observed for a Time Late in the Flight.	24
10. Picture From the On-board TV Camera Showing the Burnt-Out Castor Second-Stage Booster Moments After Payload Separation	25
11. (a) Auroral Intensity as Measured by the Ground-based Meridian-Scanning Photometer at T + 16 sec. TAL. (b) Auroral Intensity as Measured by the Ground-based Oblique Scanning Photometer at T + 16 sec. TAL.	28
12. The Auroral Intensity as Seen From the Ground-based (a) Meridian-and (b) Oblique-Scanning Photometers at T + 6 min. 50 sec. TAL and the Ground-based All-sky Television Image for the Same Time.	29
13. Tangent-Height Geometry Illustrating the Need to use Earth Radius at the Tangent Point When Computing Tangent Height.	31

14. Examples of SPIRIT 1 Flight Interferograms for all Five Detectors.	38
15. Examples of Processed SPIRIT 1 Interferogram Data Showing a Raw Interferogram, a Processed Interferogram, a Low-resolution Spectrum, and a Mertz Phase-corrected Spectrum.	40
16. Examples of Apodizing Window Functions Showing the Window Characteristics Required for a One-sided Interferogram to Produce Scanning Functions Identical to Two-sided Apodizing Windows.	41
17a. Effects of Apodizing Windows on the Emission Spectrum in the 12 μm Window Region.	42
17b. The Scanning Function for the Kaiser-Bessel Apodization Window Used to Process the SPIRIT 1 Interferogram.	43
18. Relative Wavelength Response Curve for Detector No. 2.	45
19. $\text{CO}_2 \nu_2$ Limb Radiance Profile and Average of SPIRE Data.	48
20. The Ratio of Detector No. 2 to Detector No. 4 Observed $\text{CO}_2 (\nu_2)$ Radiances at 15 μm as a Function of the Mean Voltage (Flux) Level for Detector No. 2.	49
21. Detector No. 2 Responsivity at 685 cm^{-1} vs the Mean Voltage (Flux) Level.	51
22. Ozone 9.6 μm Altitude Profile from SPIRIT 1 (Points) and Average Profile from SPIRE Nighttime and Terminator Scans (Solid Line).	56
23. Altitude Profile of Ozone Hot Bands Below 95 km.	57
24. Ozone Hot Band Spectra from Filter No. 1 Scans.	58
25. NO Fundamental Altitude Profile from SPIRIT 1 (Points) and Average Profile from SPIRE (Solid Line).	60
26. Raw Interferograms for All Five (5) SPIRIT 1 Detectors for Scan 112.	61
27. The Spectrum of the Earthshine-like Anomalous Background (Scan 112 $\times 10^4$) Compared to a LOWTRAN Calculation of Upwelling Radiation for a 135° Zenith Angle Case.	62
28. Spectra of the Anomalous (Leakage) Background at two Different Background Levels.	63
29. Intensity of the 900 cm^{-1} Peak Feature of the Anomalous Background vs Time After Launch as Measured by Detector No. 1.	65
30. The SPIRIT 1 Anomalous Background for Different Detectors and Scans.	66
31. Occurrence of the 12 Brightest Anomalous Scans Compared to the Sensor Tangent Height.	67
32. Intensity of the 900 cm^{-1} Spectral Feature vs Payload Altitude.	68
33. Intensity of the 900 cm^{-1} Spectral Feature vs Sensor Tangent Height.	69
34. The Detector No. 2 Signal Level vs the Detector No. 1 Signal Level for the 900 cm^{-1} Spectral Feature.	71
35. Observed Inband Window Radiance vs Angle to the Earth's Horizon for Detector No. 2.	73
36. Anomalous Ratio Spectrum Obtained by Dividing the Anomalous Background Spectrum (Scan 134) by the Earthshine Spectrum (Scan 112).	74

37. Spectrum of Dow Corning 90-006-2 Silicone Sealant (Solid Curve) Compared With the SPIRIT 1 Anomalous Ratio Spectrum (Dotted Curve).	81
38. The Spectra of Silicone Pump Oil (DC-704) and Paint Resin (DC-808) Compared With the SPIRIT 1 Anomalous Spectrum.	85
39. A Comparison of the Reflection Spectrum of 3M ECP-2200 Black Paint With the SPIRIT 1 Anomalous Spectrum.	86
40. The Specular Reflection Spectra of 3M-ECP-2200 Paint (Sample 1).	90
41. The Diffuse Scatter Spectrum of 3M-ECP-2200 Paint (Sample 1) for 65° Angle of Incidence and 10° Collection Angle.	91
42. A Comparison of the Specular Reflection Spectra of One-and Two-Coat Samples of 3M-ECP-2200 Paint.	92
43. A Comparison of the Specular Reflection Spectra of a Single Coat of 3M-ECP-2200 Paint on a Polished (Upper Curve) and Roughened (Middle Curve) Surface.	93
44. The Specular Reflection Spectra of a Single Coat of 3M ECP-2200 Paint at 80° Angle of Incidence.	94
45. A Comparison of the Diffuse Scatter Spectra of a Single Coat Sample of 3M-ECP-2200 Paint for Two Different Angular Combinations.	96
46. A Comparison of the Diffuse Scatter Spectra of a Single Coat Sample of 3M-ECP-200 Paint for Two Different Angular Combinations.	97
47. A Comparison of the Diffuse Scatter Spectra of one (Upper Curve), two (Middle Curve) and Three (Lower Curve) Coat Samples of 3M-ECP-2200 Paint for a Typical Angular Combination (65°/10°).	98
48. A Comparison of the Diffuse Scatter Spectra of a Single Coat of 3M-ECP-2200 Paint on a Polished (Upper Curve), Roughened (Middle Curve) and Untreated. (Lower Curve) Surface for a (65°, 10°) Angular Combination.	99
49. Contributing Rays for the Specular Reflection (R) and Diffuse Scatter (S) Cases for Non-opaque Samples.	100
50. Anomalous Leakage Spectrum From SPIRIT 1 Rocketborne Sensor (Upper Curve), a MODTRAN Calculation of an Upwelling Earthshine Spectrum (Middle Curve) and a SPIRIT Anomalous Spectrum With the Source Function Removed (Lower Curve) Which was Obtained by Taking the Ratio of the two Upper Curves.	102
51. A Comparison of two SPIRIT 1 Ratio Spectra With a Typical Diffuse Scatter Spectrum for the 3M-ECP-2200 Paint.	103

Tables

1. SPIRIT 1 Interferometer Specifications.	6
2. SPIRIT 1 Mission Event Table.	11
3. Interferometer Sequence of Events.	12
4. Measurement Events and Highlights.	19
5. SPIRIT 1 Ground Sites and Instrumentation.	26
6. SPIRIT 1 Detector Responsivities.	46
7. Summary of SPIRIT 1 Spectral Scans.	54
8. SPIRIT 1 Telescope Leakage Ratio vs Detector Location.	70
9. Organo-Silicon Compounds.	77
10. SPIRIT 1 Anomalous "Absorption" Frequencies.	79
11. Paint Sample Descriptions.	87
12. Band Center Frequencies (cm ⁻¹).	89

Acknowledgements

The SPIRIT 1 experiment was a success as a result of the dedicated efforts of many scientists, engineers and technicians associated with numerous organizations. Special appreciation and acknowledgement is extended to Lt Col Thomas Walsh of the Defense Nuclear Agency (DNA) who was the DNA program manager of SPIRIT 1. He showed great patience during the difficult times and continually encouraged and supported the technical workers through all phases of the program. The authors also wish to acknowledge the participation of the following individuals and their organizations: Peter Dybwad, Ronald Huppi, Reed McKenna, and Charles Eastman of Stewart Radiance Laboratory for the engineering, development, and calibration of the interferometer, E. R. Huppi of the Phillips Laboratory Optical Environment Division (PL/GPO) for invaluable inputs to the interferometer design and the development of the processing software, H. Curtis, D. Kush, R. Wiley, R. Hull, and A. Messer of Space Data Corporation for the engineering and field support for all aspects of the rocket, payload, telemetry and launch of the payload, E. McKenna, M. Depero, and S. Hoskins of PL/SX for environmental testing of the payload and field support and mission control during the launch, C. Howlett of USU for designing, fabricating, and supporting most of the ancillary sensors, G. Allred and P. Mace of USU for manning the SPIRIT ground stations and especially to A. Steed, also of USU, for discerning an intensifying class II aurora that became a bona fide class III⁺ event, Lt. H. Baker of PL/SX for important engineering inputs and field support of the experiment, including the IR horizon sensor, N. Brown, P. Young (posthumously), C. Coe, and S. Bonham of PFRR for excellent range support during very trying times, D. Akerstrom of PL/GPO and H. Miranda of Miranda Laboratories for developing and implementing instrument alignment procedures, M. Maris and L. Bates of USU for implementing contamination control-techniques, P. Doyle of PL/GPO for logistics support, and Carol Foley, Susan Delay, E. R. Hegblom, and Brian Sullivan of Boston College for their efforts in the processing and analysis of the data.

SPIRIT 1 Final Flight Report

1. EXECUTIVE SUMMARY

The SPIRIT 1 experiment, launched on April 8, 1986, was a rocketborne probe designed to measure the long-wavelength infrared emission spectra from an IBC class III aurora in the limb-viewing geometry. The primary instrument was a cryogenically cooled, five-detector Michelson interferometer mated to a high-off-axis-rejection telescope. Approximately 140 spectral scans were recorded covering tangent heights of ~40-225 km and a spectral range of ~450-2500 cm^{-1} . Most of these scans have an apodized resolution of 8-11 cm^{-1} ; however, 17 scans were measured at ~1 cm^{-1} resolution. During most of the flight the instrument was pointed slightly away from the bright auroral arc; however, later in the flight direct views of the arc were obtained at tangent heights below ~108 km. The spectra provide a comprehensive data base on a number of molecular emission features in the nighttime sky, including $\text{CO}_2 \nu_2$ (15 μm), $\text{O}_3 \nu_3$ (9.6 μm), and $\text{NO} \Delta\nu = 1$ (5.3 μm).

This report provides a summary of the in-flight performance of the on-board and ground-based sensors, as well as other rocket instrumentation and systems. Several flight anomalies are described and explained.

Results of a preliminary analysis of the infrared data from the SPIRIT 1 cryogenic interferometer indicates that two sources of radiation were observed by the SPIRIT 1 IR sensor.

The first source is radiation due to atmospheric emissions from the earthlimb, and includes the well-known $\text{CO}_2 \nu_2$ (15 μm), $\text{O}_3 \nu_3$ (9.6 μm), and NO fundamental (5.3 μm) bands.

In general, the atmospheric earthlimb emission correlates well with previous observations such as SPIRE and the current ARC and SHARC models of the quiet nighttime atmosphere.

The second source of radiation is an anomalous background due to leakage of off-axis radiation from the lower atmosphere and earth into the sensor's field of view. This background is bright enough to dominate all of the LWIR window regions at tangent heights above ~100 km. At higher tangent heights, only the brightest atmospheric radiators can be seen above this background. Above ~190 km this background dominates in all bands throughout the LWIR. This anomalous behavior is caused by the scatter of off-axis radiation due to both internal effects and external contamination. The external contamination is consistent with the release of particles from the ACS used to orient the payload. The internal scattering problem has been identified as a large-angle baffle-scattering effect. The high-resolution spectrum of this background has been identified as that of a methyl-phenyl siloxane (silicone) compound and traced to a silicone resin in the black paint used to coat the internal surface of the telescope baffle.

Spectral limb radiance data for $\text{CO}_2 \nu_2$, $\text{O}_3 \nu_3$, and $\text{NO} \Delta\nu = 1$ 5.3 μm emissions obtained in the SPIRIT 1 rocket experiment are presented and discussed in Section 8. The data cover auroral intensities from several kR to over 200 kR as measured at 391.4 nm, and a ~65-190 km tangent height range at high latitudes (60-65°N). The primary observations are:

1. The $\text{CO}_2 \nu_2$ radiance agrees with previous experiments to within a factor of 2.
2. The $\text{O}_3 \nu_3$ radiance below 95 km also agrees with other previous nighttime measurements to within a factor of 2. Above 95 km tangent height the $\text{O}_3 \nu_3$ radiance measured by SPIRIT 1 is significantly lower than previous observations and the current earthlimb radiance model.¹
3. No auroral enhancements are apparent in either the $\text{CO}_2 \nu_2$ or $\text{O}_3 \nu_3$ bands. This result is in sharp contrast to the observations made during the HIRIS experiment² (flown in April 1976 from the same launch site) in which dramatic auroral enhancements were reported for both bands. (The results from SPIRIT 1 have led to a recent re-examination of the HIRIS data.³ This new analysis has resulted in an alternative interpretation of the HIRIS data which attributes the unusually high radiance values observed during the HIRIS

¹ Degges, T.C. and D'Agati, A.P. (1986) A user's guide to the AFGL/Visidyne high altitude infrared radiance mode computer program. Rep., VI-785. Visidyne Corp.

² Stair, A.T., Jr., Pritchard, J., Coleman, I., Bohne, C., Williamson, W., Rogers, J., and Rawlins, W.T. (1983) The rocket-borne cryogenic (10° K) high-resolution interferometer spectrometer flight-HIRIS: Atmospheric and auroral infrared emission spectra. *Appl. Opt.*, **22**:1056.

³ Smith, D.R., Phillips Laboratory, AFSC, Private Communication.

earthlimb scans to a combination of pointing errors, rapid tumbling, and off-axis leakage effects resulting from the absence of a high-off-axis-rejection telescope. This explanation brings the HIRIS results into close agreement with SPIRIT 1, and with other previous measurements as well).

4. SPIRIT 1 data in the 10-12.5 μm region represents a significant improvement over previous data. Spectral structure due to partially resolved bands has been assigned to ozone hot bands resulting from the three-body recombination mechanism; $\text{O}_2 + \text{O} + \text{M} = \text{O}_3 + \text{M}$. Recently published results from high-resolution (1 cm^{-1}) spectral measurements obtained by the CIRRIS 1A experiment from the Space Shuttle⁴ has established that the spectral structure in this region is entirely due to pure rotational transitions of OH (ν, N) where $\nu = 0, 1, 2$ and $N = 24-33$, and that only the underlying continuum can be attributed to ozone hot bands. The current atmospheric radiance model seriously under-predicts the radiance on the long-wavelength side (11-12.5 μm) of the 10-12.5 μm window. The fraction of energy in the ozone hot bands relative to the fundamental band (9.6 μm) is a factor of 2 lower than that measured by the SPIRE (non-auroral) experiment. (This may reflect a lower concentration of atomic oxygen relative to the atmosphere measured by SPIRE).
5. SPIRIT 1 measured significantly less radiance from nitric oxide (5.3 μm) than in previous high-latitude observations. (A factor of 3 to 7 less than SPIRE, for example).
6. Nitric oxide (NO) hot bands associated with the auroral $\text{N}^2 \text{D} + \text{O}_2$ mechanism are somewhat difficult to discern. It is estimated that they comprise at most 10 percent of the total 5.3 μm NO emission in SPIRIT 1 above 120 km, where the 391.4 nm intensity observed was below 40 kR. This estimate is within the range of previous auroral observations.

2. INTRODUCTION

The SPIRIT 1 experiment was a rocketborne atmospheric probe to measure the spectral characteristics of infrared emissions from a bright aurora in a limb-viewing geometry. The payload instrumentation included ancillary sensors to assist in the characterization of the auroral event. The prime instrument aboard the SPIRIT 1 payload was a cryogenically cooled.

⁴ Smith, D.R., Blumberg, W.A.M., Nadile, R.M., Lipson, S.J., Huppi, E.R., Wheeler, N.B., and Dodd, J.A. (1992) Observation of high- N hydroxyl pure rotation lines in atmospheric emission spectra by the CIRRIS 1A space shuttle experiment, *Geophys. Res. Lett.*, **19**, Number 6.

flex-pivot, Michelson interferometer mated to a high-stray-light-rejection telescope. Utah State University designed and developed most of the payload instruments. The booster system was developed by Space Data Corp., Tempe, AZ, who also integrated the payload. The program was managed and directed by the Phillips Laboratory Geophysics Directorate's Optical Environment Division (PL/GPO) for the Defense Nuclear Agency (DNA/RAAE) in support of Strategic Defense Initiative Organization (SDIO) measurement requirements and Air Force system needs. An illustration showing the basic experimental concept is presented in Figure 1.

Field operations associated with the launch of the SPIRIT 1 payload lasted from early December 1985 to April 1986. These activities culminated in the launch of the payload at 09:42:25 GMT on 8 April 1986. The payload was launched from the University of Alaska's Poker Flat Research Range at which all preflight activities involving final assembly and preflight checks were conducted.

3. INSTRUMENTATION DESCRIPTION

3.1 Payload Sensors

The on-board instrumentation consisted of six sensors. The primary sensor was a cryogenic telescopied Michelson interferometer cooled by supercritical helium. The interferometer was designed and fabricated by Utah State University - Stewart Radiance Laboratory (USU/SRL) in Bedford, MA, while the telescope was provided by System Sensor Group (SSG) in Waltham, MA. Utah State University - Space Dynamics Laboratory (USU/SDL) at Logan, Utah supplied a ruggedized RCA Low-Light-Level Television Camera in a pressurized container to collect visual data, a modified Nikon 35 mm camera with a Varo Image Intensifier for post-flight star field position data, and a telescopied photometer for real-time auroral intensity data collection. An IR Horizon Sensor that utilized a conical scanning device which sensed crossings of the 15 μ m atmospheric CO₂ layer at 40 km was used to derive real-time tangent heights of the scene being viewed. This sensor was furnished by Ithaco, Inc. of Ithaca, NY. The sixth sensor was a modified 70 mm Hasselblad film camera with a 200 frame film magazine and a 150 mm Sonnar lens intended to provide a post-flight visual record of auroral features. Each exposure was to be annotated with the day, hour, minute, second, tenths and hundredths of a second as supplied by an on-board time code generator. Epsilon Laboratories of Burlington, MA supplied the Hasselblad camera, the timecode generator, and a film annotation (day and time information) module for the USU/SDL 35 mm film camera. A summary of all the SPIRIT 1 program participants is given in Appendix H.

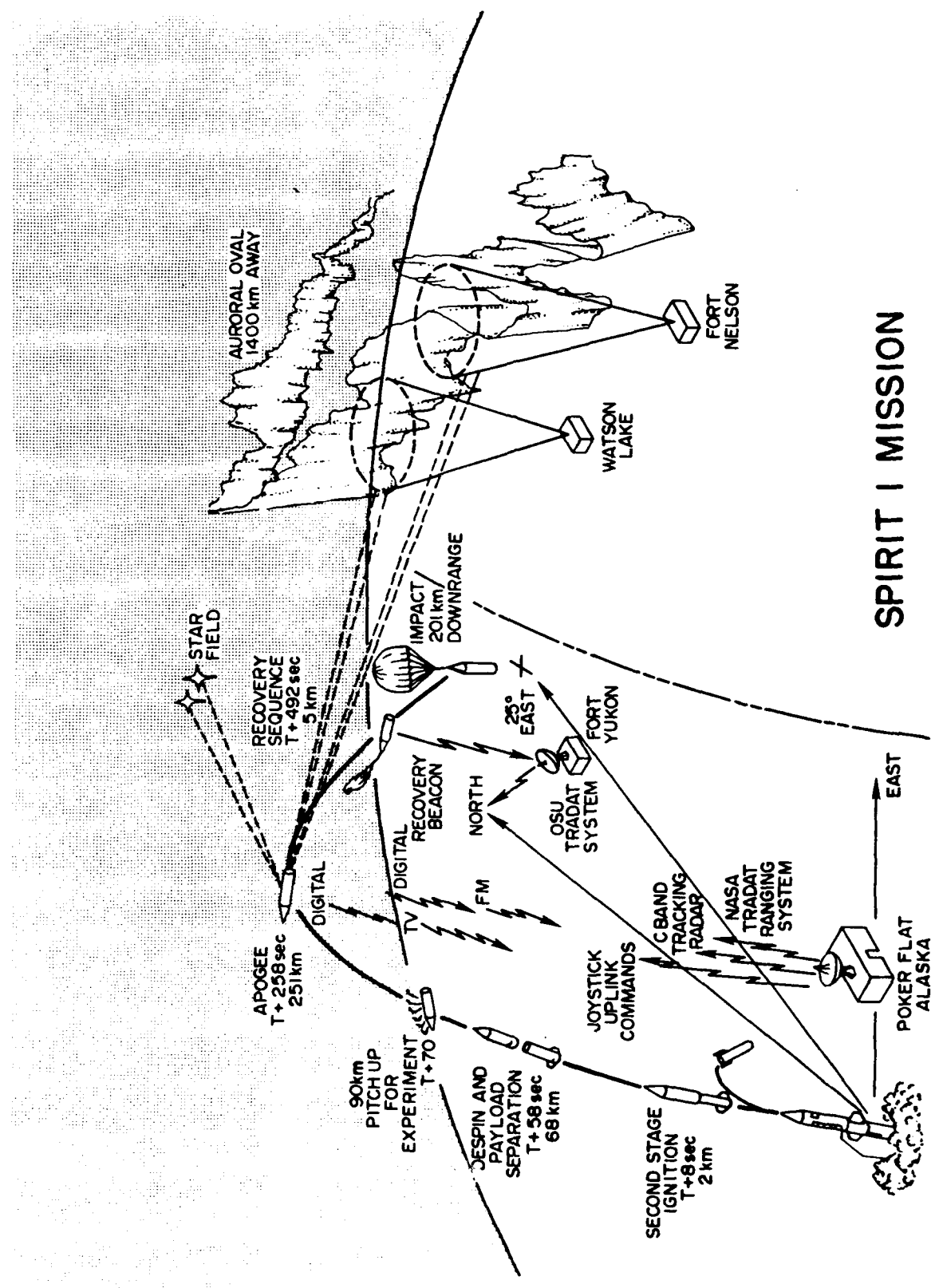


Figure 1. Nominal SPIRIT 1 Mission

3.2 Interferometer Description

The interferometer, designed and fabricated at Stewart Radiance Laboratory, is a Michelson flex-pivot design. The telescope was designed and fabricated by Systems Sensor Group (SSG), Waltham, MA. The instrument was cooled by liquid helium, which maintained the focal plane at 8° K and the telescope at approximately 20° K. Three optical filters were used at preprogrammed periods during the flight. They were designated Filter No. 0 (open filter, 2.5 to 24 μ m response), Filter No. 1 (bandpass filter, 10.2 to 12.8 μ m response) and Filter No. 2 (low-pass filter, 2.5 to 8.2 μ m response). Other pertinent interferometer specifications are given in Table 1.

The instrument was kept cooled and evacuated during transport from PL/GPO to Poker Flat and during all subsequent field operations prior to launch.

The focal plane contains an array of five Si:As LWIR detectors which were designed to have a combined dynamic range of 10^8 . The detectors are numbered 1 through 5 in order of decreasing size and sensitivity. Their arrangement on the focal plane is depicted in Figure 2, which is a projection of the array onto the angular field of view. Since the focal plane orientation with respect to the horizon is essentially as shown in the figure, detector No. 1 viewed the highest tangent altitude, detector No. 5 the lowest, and detectors Nos. 2 and 4 nominally viewed the same altitude.

Table 1. SPIRIT 1 Interferometer Specifications

Aperture Diameter (interferometer)	1.875 in.	
Aperture Diameter (telescope)	6 in.	
Detector type	Si:As, 5 elements	
Drive length		
short	approximately 0.1 cm in 1 sec	
long	approximately 1.0 cm in 10 sec	
Detector	Area (cm²)	NESR* (watts/cm²-sr-cm⁻¹)
Det No. 1	1.309×10^{-1}	1.8×10^{-12}
Det No. 2	5.226×10^{-2}	4.0×10^{-12}
Det No. 3	7.720×10^{-3}	1.0×10^{-11}
Det No. 4	4.065×10^{-3}	3.3×10^{-11}
Det No. 5	4.065×10^{-3}	0.8×10^{-11}

*Noise Equivalent Spectral Radiance (NESR) are average values estimated from measured flight data for the open filter taken at 80, 100, and 120 km tangent heights.

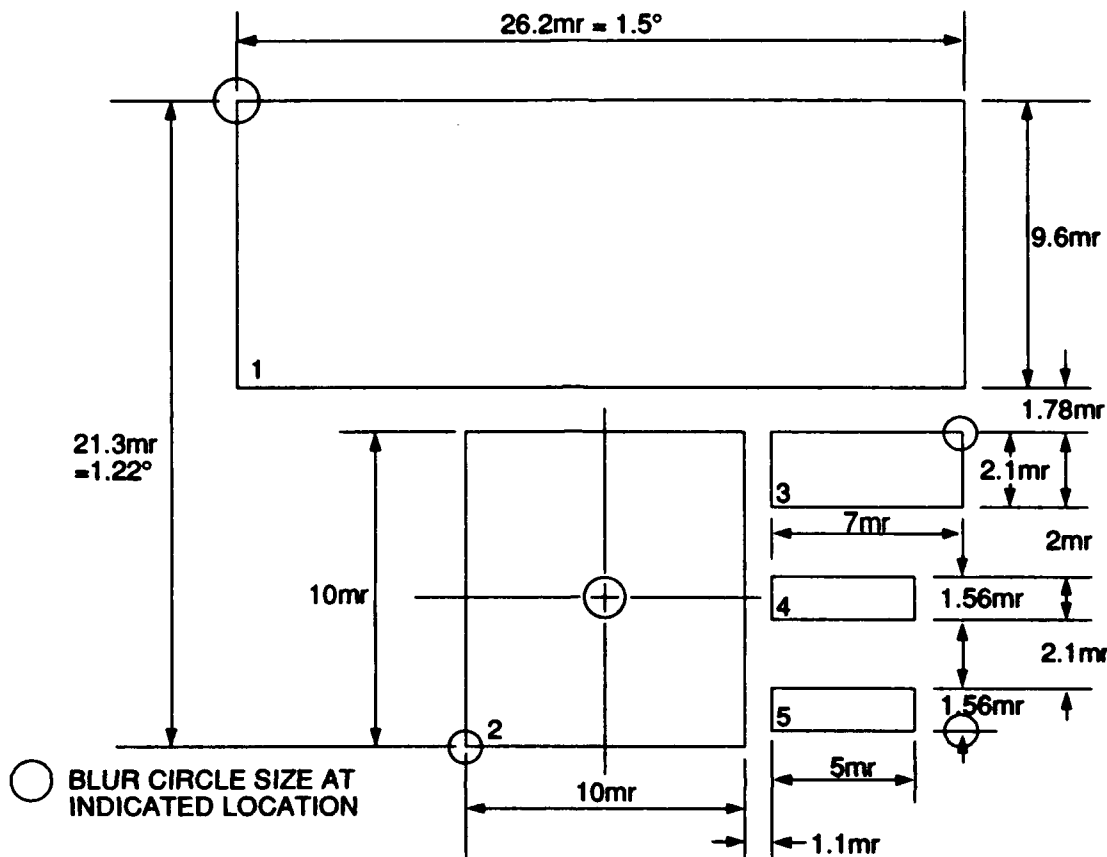


Figure 2. SPIRIT 1 Detector Focal Plane Layout Illustrating Angular Subtense in Object Space

A photometer (center wavelength 3909 \AA and FWHM 32 \AA) was co-aligned with interferometer detector No. 2 and had the same field of view. The spectral characteristics of the photometer filter are shown in Figure 3. The sensor contained an EMR 541 N detector and was capable of measuring brightness from 0.2 kR to 2 MR .

The SPIRIT 1 payload also contained several ancillary sensors. A television camera co-aligned with the main sensor's nominal field of view (FOV) provided real-time auroral images for ground-controlled payload pointing during flight. An infrared horizon sensor provided real-time line-of-sight (LOS) tangent heights. Two film cameras were also included on the payload: one with a FOV overlapping that of the television to provide high-spatial-resolution

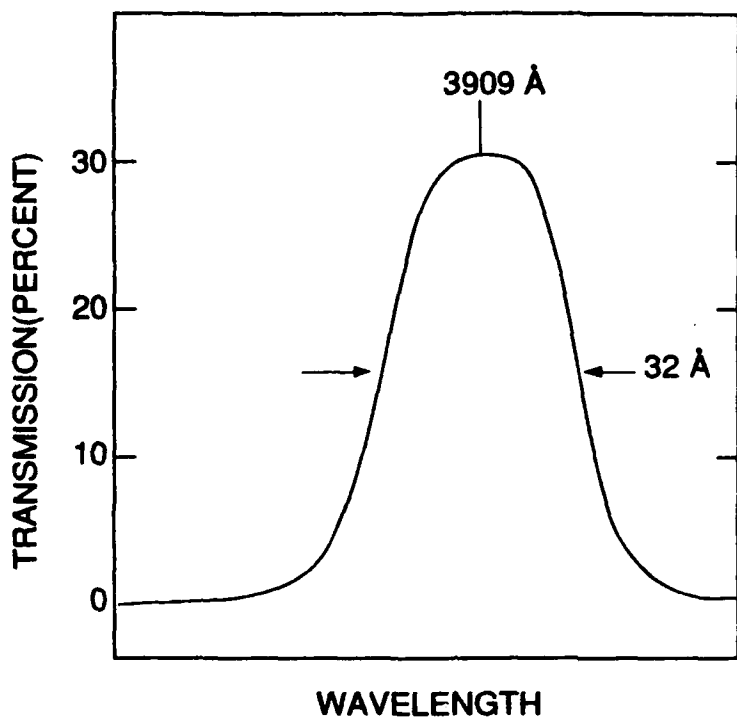


Figure 3. SPIRIT 1 Onboard Photometer Filter Characteristics

images for post-flight auroral documentation; the second camera, designated the celestial aspect sensor (CAS), provided post-flight star images for establishing LOS pointing angles. A gyro system and a three-axis magnetometer provided corroborative payload attitude information. With the exception of the two film cameras, data measured in flight was transmitted to ground receivers over two PCM and one FM - FM telemetry link. The television signal was transmitted over a separate video link. Film camera exposures were stored on-board the payload and processed after recovery of the film magazines. All optical ancillary sensors were nominally aligned with the interferometer FOV (detector No. 2) with the exception of the CAS which was offset from the nominal FOV by 45° in the payload pitch plane.

4. ROCKET FLIGHT SUMMARY

4.1 Launch Description

The SPIRIT 1 payload was launched on 8 April 1986 at 09:42:25 (UT). The auroral event that resulted in the decision to launch the payload exceeded the initial launch criterion for the payload by a significant margin, with a maximum photometer reading from Ft. Nelson on the order of 200 kR as measured at 5577 Å.

The window for launch on 8 April 1986 was limited to the period between 0615 and 0945 (UT) due to both evening and morning twilight intervention. Weather conditions at the Ft. Nelson site were optimal, with no cloud cover and excellent visibility. Peace River had some high thin haze that hid the dimmer stars, but bright stars were visible and auroral activity could be observed without significant attenuation. Watson Lake was overcast and observations from that site were severely hampered. During the early part of the 8 April window, auroral activity was typically quiet with very low intensity.

Shortly before 0900 (UT) auroral activity increased, with an arc structure appearing, and came close to meeting the launch criterion. The auroral arc proceeded into a breakup phase, but generally held north of the arc's original position. Diffuse aurora spread toward the zenith as observed at Ft. Nelson and Peace River. During this period the SPIRIT 1 payload was counted down to T-3 min, and was held at that point.

Subsequent to the above breakup activity, a second arc formed at a much higher elevation than the initial one. This form was first evident from the Peace River site and shortly thereafter from Ft. Nelson. When the second arc became noticeably structured it had achieved an elevation of approximately 45-50° as viewed from Ft. Nelson, and had brightened to the 15-20 kR level. Further brightening was observed progressing toward the Ft. Nelson site from the east at levels that appeared to significantly exceed the launch criterion, and project scientists made the decision to launch the SPIRIT 1 rocket. The auroral arc continued to brighten during final countdown, launch, and ascent of the vehicle and maintained a high intensity, gradually progressing southward throughout the flight.

4.2 Flight Description

The SPIRIT 1 vehicle was launched from a fixed-rail launcher on Pad 4 of the University of Alaska, Poker Flat Research Range, Fairbanks, Alaska. The vehicle was launched at an azimuth of 56.1° from true north and at an elevation of 86.4° (corrected for wind weighting). The payload reached 100 km at 82 seconds after first-stage ignition, attained a maximum altitude of 239.2 km (148.64 statute miles) 4.21 minutes after launch and spent 359 seconds collecting data.

Once the payload was in flight, scientific data and housekeeping data were collected on board the rocket and transmitted via four telemetry links to ground tracking and receiving antennas at Poker Flat and Fort Yukon, Alaska. After second-stage burnout, the vehicle was

despun and the motor was separated from the payload by the actuation of four explosive nuts between the interstage and the payload cylinder. The two masses were separated at 26.5 ft/sec. by a pressurized rubber bag.

To observe the aurora 1400 km away, the payload sensors (having small fields of view) were scanned vertically through the auroral oval. This was accomplished by the onboard MACS (Microprocessor Attitude Control System). The microprocessor processed position and rate data from the payload gyroscopes and actuated gaseous nitrogen thrusters to point the payload instruments at desired points in space. The MACS was designed to proceed through a preprogrammed scan pattern but was designed to be interrupted by uplink commands to allow the project scientist to override the preprogrammed scan with manual scans or to introduce offsets. The MACS performed well in proceeding through its preprogrammed scan pattern, except that during an azimuth scan towards the south an inadvertent roll caused the payload to view the "hard earth". Operation of the uplink command was not available for most of the mission even though many attempts were made to offset the programmed scan. None was successful until late in flight.

On 8 April 1986 at 11:00 AM local time, the SPIRIT 1 payload was spotted next to the Yukon River near Circle, Alaska from the air by a search team from the 25th TASS (Nelson AFB). During reentry the recovery parachutes deployed at approximately 2.5 km (8,200 ft) altitude, based upon trajectory data from the Oklahoma State University TRADAT system data at Fort Yukon, Alaska. OSU estimated the payload impact coordinates to be at 65° 59' north latitude and 144° 12' east longitude. The payload was recovered approximately one quarter of a mile away from these coordinates. On 10 April 1986, a CH-3 helicopter flew to the impact site and the payload was recovered and returned to PFRR. Table 2 shows the sequence of events from launch to impact.

Table 2. SPIRIT 1 Mission Event Table

EVENT	TIME AFTER LAUNCH (TAL)	ALTITUDE (KM)
Launch	0.0	0.0
Talos Burnout	5.7	1.2
Castor Ignition	8.0	1.9
Pitch/Roll Crossover	21.5	8.6
Max Q	24.0	10.6
Castor Burnout	48.0	47.4
ACS Purge	49.0	49.3
Camera Door Eject	5.0	1.0
Despin	54.0	58.6
Separator/Begin ACS Capture	58.0	66.0
Cover Open	66-73	87.0
Scan Start/Uplink Enable	70.0	87.0
Back-up Cover Open	88-100	104.0
Apogee	253.3	239.2
Cover Close	453-460	69.0
End Scan/Spin Up for Reent	457.0	51.0
Recov Beacon On/Recov Pos	457.0	22.5
Begin Recovery Sequence	580.0	2.5
Loss of Track	641.0	1.2

5. INSTRUMENT AND ROCKET PERFORMANCE SUMMARY

5.1 Vehicle Performance Summary

The SPIRIT 1 sensors were carried aloft on a ballistic trajectory by a two-stage, unguided, spin-stabilized, solid-propellant rocket vehicle to an altitude of 239.2 km. The trajectory was approximately 8.5 km lower than pre-flight predictions, primarily due to a 58 lb increase in payload weight over earlier estimates. The nominal launch parameters called for an azimuth of 50.0° and elevation of 84.0°. The actual launch parameters were modified to 56.1° and 86.4° to correct for the effects of wind. However, the actual payload impact point indicates a flight azimuth of 58.28°, an 8.28° shift from the 50.0° pre-launch estimate. This implies that a small tip-off of 0.44° must have occurred during launch, probably due to a wind gust.

5.2 Interferometer Performance Summary

The SPIRIT 1 interferometer operated normally up to the moment of launch. Normal operation was temporarily interrupted during initial ascent, as expected, but returned to normal shortly before second-stage burnout at T + 41 sec (time after launch, TAL). The interferometer then continued to operate normally throughout the remainder of the flight. The interferometer cover-open command occurred at T + 66 sec and the cover reached the fully open position at T + 73 sec at an altitude of 90 km. Payload ACS capture was not completed at this time, and the payload instruments were pointing down at the earth. The payload began a preplanned pitch-up maneuver at approximately T + 85 sec, and the first unsaturated interferograms were recorded at T + 94.98 sec. The payload was at an altitude of 125 km. From this point on, a total of 177 high-(1 cm⁻¹) and low- (8 cm⁻¹) resolution spectral scans were recorded prior to the cover-close command at T + 453 sec, for a total of 359 seconds of measurement time. A listing of the interferometer sequence of events is given in Table 3.

Table 3. Interferometer Sequence of Events

EVENT	TIME (TAL-SEC)
Normal Operation Returns	41
In-flight Calibrations	56-69
Filter No. 2 Inserted	56
Cover Open Command	66
Open Filter Inserted	70
Cover Fully Open	73
Filter No. 1 Inserted	270-271
Filter No. 2 Inserted	320-322
Open Filter Inserted	344-345
Filter No. 1 Inserted	425-426
Cover Close Command	453
Reflector Plate Inserted	453-455
In-flight Calibrations	455-480
Cover Fully Closed	460
Loss of Signal (LOS)	556

5.3 Ancillary Sensors Performance Summary

Based on the preliminary data obtained from the five ancillary sensors, it appears that all performed as designed, with the exception of the Hasselblad film camera. The anomalies of

the Hasselblad film camera are discussed in Section 5.4.4. A summary of the data obtained from the other four sensors is contained in Section 6 of this report.

5.4 Flight Anomalies

Five anomalies occurred during the SPIRIT 1 flight. Several of these anomalies were serious enough to degrade performance or cause a loss of mission data. Despite these anomalies, all mission success criteria were met. The anomalies are discussed below.

5.4.1 Image-Intensified Film Camera Door

The first anomaly was an indication that the cover for the IIFC opened prematurely. The programmed time for the cover opening was $T + 51.5$ sec. However, at $T + 5$ sec (end of Talos maximum thrust) the door monitor switch showed that the cover had opened. This was later confirmed when the door was found on the ground outside the blockhouse. A protective quartz window behind the cover prevented any physical damage to the instrument due to aerodynamic forces and/or debris. Post-flight reduction of data indicates that the relay to fire the pyro cover release mechanism did indeed close at $T + 51.5$ sec as planned. It is assumed that aerodynamic forces, in combination with venting of the air space behind the door, caused a failure in the door-retaining screw or the portion of the door around the retaining screw.

5.4.2 NASA TRADAT and Uplink Command

SPIRIT 1 was launched at 09:42:25 GMT with a good NASA trajectory data (TRADAT) signal being received. At 09:42:36 GMT telemetry was successfully switched to autotrack. At 09:43:51 GMT NASA TRADAT signal strength had become so weak that the TRADAT system was unable to discern the payload's signal. At 09:47:23 GMT the TRADAT signal strength was again strong enough for the TRADAT system to function. The slant range when the signal was lost was only 115.55 km. This seems to show that attenuation of the signal due to range was not the problem.

The SDC uplink command system had a problem similar to the NASA TRADAT system. At launch the signal strength was good, but it rapidly deteriorated, so that by 09:44:01 GMT the signal strength was below the level at which the onboard software would accept an uplink command. By 09:49:22 GMT the offset command was sent and the MACS began acting upon the commands it was receiving. Between 09:48:04 and 09:49:22 GMT the joystick was held in the yaw-left medium position. This was done without prior acknowledgement of the offset command. Once the offset command was acknowledged, the uplink command system worked correctly for the remainder of the flight.

An interesting point regarding the NASA TRADAT and SDC uplink command signals is that both were sent and received on the same set of antennas. It is known that antennas have lobes (areas of high signal strength) and nulls (areas of low signal strength). It may be possible

that the antenna pair that were used by the NASA TRADAT and the SDC uplink were positioned in such a manner that during part of the flight the signals were being transmitted through nulls. Further research is being conducted by SDC to explore this theory.

Another contributing factor to the SDC uplink problem was the matching of the signal strength software lock-out voltage and the RCC 103-2 receiver output voltage. SDC has flown many of these receivers on other programs (HAVE SLED II, and ELIAS, for example) and has used a software lock-out voltage of 1.25 V. This means that commands emerging from the output of the receiver with a signal strength indication of less than 1.26 V are ignored. Historically the RCC 103-2 receiver would produce a 1.25 V signal for an RF input level of -95 dBm. The receiver on SPIRIT 1 however, produced a 1.25 V signal for an RF input level of -75 dBm. This meant that the output signal of the SPIRIT 1 receiver was effectively locked-out for a 20 dBm stronger RF input than that for which the software was designed.

5.4.3 Scan Anomaly

The SPIRIT 1 programmed scan pattern shown in Figure 4 was nominally followed. An anomaly occurred during the large yaw maneuver occurring at T + 343 sec during flight. The payload appeared to roll and pitch during this maneuver, causing the instruments to view the "hard earth." Concluding the yaw maneuver at approximately T + 400 sec, the payload returned to the correct programmed point and continued to scan correctly until interrupted by uplink commands. The MACS responded to the uplink commands as designed.

The cause of this anomaly is believed to be cross-coupling of the platform gyro axes. Platform gyros are physically limited due to their construction. When large angular excursions are performed on more than one axis in certain combinations, cross-coupling will occur. Prior to the yaw maneuver, a pitch maneuver of -90° was executed. The combination of the pitch and then the yaw maneuver could have caused cross-coupling in the roll axis.

5.4.4 Hasselblad Film Camera

The Hasselblad film camera was programmed to begin recording with the first interferometer scan and to continue with one picture per scan. The film developed from the Hasselblad shows that the camera began taking exposures at T + 70 sec and took 8 exposures approximately 2.5 sec apart before ceasing operation. Post-flight inspection of the camera indicates that one of the Nicad batteries was swollen, indicating that some type of power problem had occurred. This agrees with telemetered data that show the +6 V monitor and the camera response monitor dropping below readable levels after 7 exposures. Epsilon will issue a more detailed report of the camera failure at a later date.

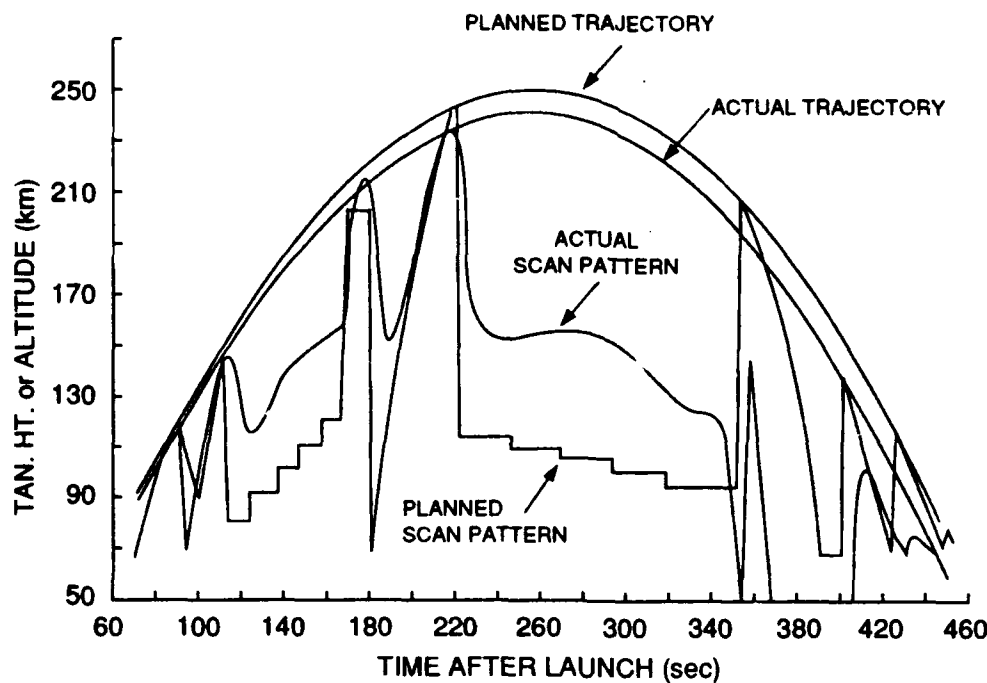


Figure 4. Comparison of Preplanned Scan Pattern and Actual Spatial Scan Pattern Flown by SPIRIT 1

5.4.5 Interferometer Detector and Pre-Amplifier Nonlinearities

Nonlinear effects in the interferometer detectors and pre-amplifiers caused harmonics to appear in the spectra. This problem appears to be an important factor only when the interferometer is being operated in the open filter mode. This anomaly will be described in more detail in Section 6.2.3.

6. DATA SUMMARY

6.1 Telemetry and Tracking Summary

6.1.1 Telemetry Summary

Data from the SPIRIT 1 sensors and payload systems were telemetered to the ground by four downlink transmitters for reception at both PFRR and Ft. Yukon. Primary interferometer data were carried on one of two PCM links at 16-bit accuracy (Link II) and are of excellent quality with very few dropouts. Back-up interferometer data were also carried on

the second PCM link (14-bit accuracy) and on a backup FM/FM link as well. These back-up data have been examined and also appear to be of excellent quality. The ancillary sensor data and miscellaneous payload housekeeping data were telemetered on the remainder of the second PCM link (Link IV) and exhibit few dropouts. Ranging, ACS (gyros and magnetometers) and some Horizon Sensor data, along with the remainder of the payload housekeeping data, were transmitted on the FM/FM link and are of equally good quality. The TV signal was transmitted over a separate video link (Link I) and good-quality pictures were received and recorded from payload separation, throughout the data-collection portion of the flight, and into the recovery phase. Two uplink receivers were used for ranging and uplink commands. A 547 MHz receiver was used for both NASA ranging and ACS uplink commands. A separate 550 MHz receiver was used for ranging from Ft. Yukon by Oklahoma State University. Anomalies with the uplink control were already discussed in Section 5.4.

6.1.2 Tracking Summary

NASA telemetry at Poker Flat began recording trajectory data (TRADAT) at launch and attained autotrack at 09:42:36 GMT, 11 sec following liftoff (T = 0 was at 09:42:25). Difficulties were encountered with the TRADAT signal at approximately 111 km altitude, 86 sec after launch. Signals were regained at T + 297 sec, 09:47:22 GMT, with an altitude of 229.2 km. NASA TRADAT lost signal towards the end of the flight at T + 557 sec, 09:51:38 GMT, at a payload altitude of 5.2 km. A discussion of the NASA TRADAT signal problem is discussed in Section 5.4 on Flight Anomalies.

OSU telemetry at Fort Yukon began gathering good TRADAT trajectory data at 09:42:54 GMT, T + 29 sec at an altitude of 16.4 km. OSU TRADAT had good signal throughout the flight until the payload signal was lost at T + 640 sec, 09:53:05 GMT, at a payload altitude of approximately 1 km.

The best least-squares trajectory fit derived from the OSU data is shown in Figure 5 and is also tabulated in Appendix B. A calculation of the shadow height is also shown and indicates that the payload remained in darkness throughout the entire flight. From these data, apogee occurred at T + 256 sec. at a payload altitude of 240.68 km.

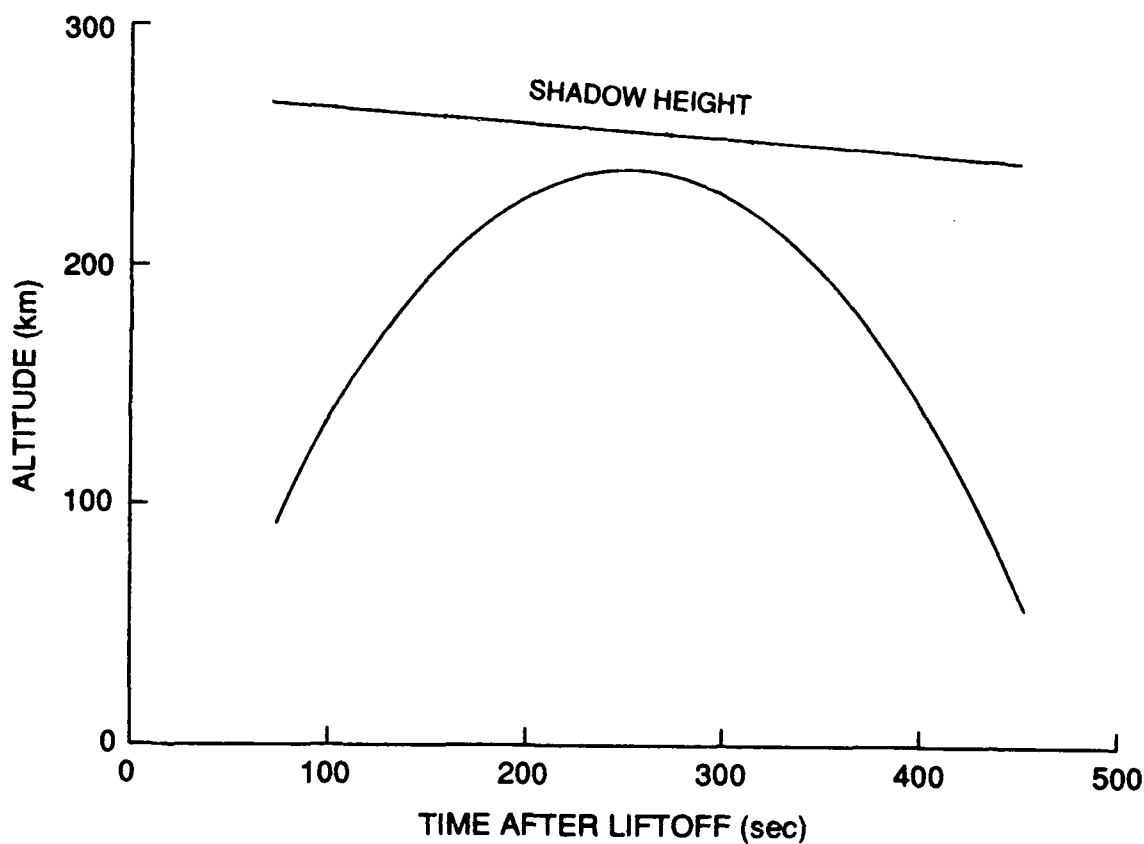


Figure 5. Best-Fit Payload Trajectory from NASA TRADAT Tracking Data

6.2 IR Data Summary

6.2.1 IR Data Review

The SPIRIT 1 interferometer began collecting atmospheric emission data on scan 78 at 94.98 sec TAL with the sensor at an altitude of 125 km. It continued to collect data throughout the flight, with the last data scan occurring at 452.79 sec TAL (scan 254). At 453 sec the cover began to close, thus ending the data-collecting period of the flight. Between these times 177 spectral scans were conducted (160 low-resolution scans and 17 high-resolution scans). Thirty-four of these scans occurred when the sensors were viewing the "hard earth" due to the scan anomaly, described in Section 5.4, that resulted in saturation of all five interferometer channels. For the remainder of the measurement time, two to five detectors were active during each interferometer scan, resulting in a total of 471 separate interferograms. The smaller detectors (numbers 4 and 5) become insensitive at higher tangent heights, whereas the larger detectors (numbers 1 and 2) become saturated at lower tangent heights. On the average, therefore, only about three detectors were active during a given scan.

Of the 143 good spectral scans, 69 occurred during the upleg and 74 occurred during the downleg portion of the flight. This data base covers a range of tangent heights from 28 to 234 km and auroral intensities from 1 to 210 kR (at 3914 Å). The maximum auroral intensity (210 kR) was recorded during scan No. 236 at 429.44 sec TAL. This scan was a low-resolution measurement with the 11 μ m bandpass filter in place (Filter No. 1) and produced four interferograms covering tangent heights from 73 to 80 km. The highest auroral intensity with the open filter was recorded during scan No. 223 at 412.48 sec TAL and measured 125 kR. Three detectors were active during this scan and covered tangent heights from 98-102 km.

A summary of the highlights of the IR data is given in Table 4, and a sample of the data is given in Appendix D.

6.2.2 Anomalies Affecting IR Data

Five flight/instrumentation problems impacted or degraded the IR data to some degree. The first was the lack of real-time uplink control during most of the flight, which prevented acquisition of the brightest part of the aurora and which also prevented offset of the pre-programmed scan pattern to correct for gyro error and drift. In general, the scan pattern was approximately 40 km (1.8° measured from apogee) too high. This error would have been corrected using the joystick offset mode had the uplink been active in the early part of the flight. As a result of this problem most of the data-collection time was spent looking slightly above and slightly to the south of the most intense aurora. This especially affected the high-resolution data scans, and resulted in all of the high-resolution data being collected at tangent heights between 120 and 200 km. We had planned to collect high-resolution data throughout the auroral altitude region from 75 to 125 km.

The second anomaly to affect the IR data was the ACS scan anomaly which caused the sensors to be pointed down at the earth and saturated all five interferometer channels for 39.2 sec (368.0-407.2 sec TAL) during the flight. This caused an 11 percent loss of data during an important part of the mission. Fortunately, the Microprocessor Attitude Control System (MACS) was able to return the payload to the correct pointing position, preventing a greater loss in mission data.

During a significant portion of the central part of the flight rather large fluctuations were observed on all detectors of the interferometer. The source of these fluctuations is not known at this time. However, it would appear that scattered earthshine from particles is a likely explanation.

In addition to the above fluctuations, smaller fluctuations in the interferometer signal have been observed that may correlate with releases from the ACS thrusters.

The last anomaly that affected the IR data was a harmonic distortion effect which resulted from non-linear interferometer detectors and/or preamplifiers. This effect will be discussed in detail in the next section.

Table 4. Measurement Events and Highlights

EVENT	TIME (SEC/TAL)	ALT (km)
Normal Operation Returned	41	
In-flight Calibrations	56-69	
Cover Open Command	66	80
Cover Fully Open	73	92
First Unsaturated Interferograms	95	125
Fluctuations Appear in IR Data	173-260	210-239
Fluctuations Re-appear in IR Data	343-363	203-185
Scan Anomaly Causes Sensors to Look at "Hard Earth"	367-405	181-135
Best Auroral Data	410-445	
Maximum Auroral Intensity (Open Filter)-126kR	412.5	
Uplink Control Becomes Active	420	
Maximum Auroral Intensity (Bandpass Filter)-210 kR	429.4	
Last Good Data Scan	452.8	
Cover Close Command	453	59
Reflector Plate	453	
Cover Fully Closed	460	46
In-flight Calibrations	464-480	
Los (PFRR)	456	

6.2.3 Harmonic Distortions Caused by Nonlinear Effects

Many of the SPIRIT 1 IR spectra recorded with the open filter in place exhibit second and third harmonics of the strong 15 μm CO_2 emission. The amplitude of the second harmonic is as much as 2-4 percent of the fundamental and the amplitude of the third harmonic is an order of magnitude less than the second. A large DC component is also present. In the typical atmospheric spectrum in the LWIR region, the 15 μm CO_2 emission (and sometimes also the 9.6 μm O_3 emission) is 2-3 orders of magnitude brighter than other emissions in the spectrum. Therefore, these artificial (distortion) bands are of comparable magnitude to a number of real atmospheric emissions of interest. No similar effect was observed in the spectra obtained with either of the two bandpass filters, both of which filtered out the 15 μm CO_2 band. In any event, harmonics of features inside the filter passband would fall outside of the passband and thus not cause a problem in interpretation.

Examination of the laboratory calibration data taken with the open filter failed to reveal the presence of distortions in the spectra; such effects are difficult to discern in this data due to the smooth, broad spectral shape of the "black body" calibration source. However, the presence of this effect can be seen in calibration data for the 11 μm bandpass filter: (filter

No. 1) these data provide a reasonable simulation of an atmospheric emission spectrum dominated by one strong feature. Figure 6 shows a filter No. 1 calibration interferogram, illustrating the asymmetric compression effect (squashed-down top) characteristic of this type of distortion. The spectrum resulting from this interferogram is also shown in Figure 6. The presence of second and third harmonics, plus a large zero-frequency component, confirm the existence of a non-linear process or system. Although these nonlinearities are believed to arise in the detectors and/or pre-amplifiers, considerably more calibration measurements will be required to determine their exact source and to characterize them quantitatively.

A nonlinear model that simulates the observed effect has been developed by Boston College (E. Richards, private communication) and is illustrated in Figure 7. Correction algorithms based on this and similar models have been developed, but only limited success has been achieved in applying them to the actual data.

6.3 Photometer Data Summary

The on-board photometer measured the background emission level at 3914 Å throughout the flight starting at payload separation and continuing through reentry. This sensor was coaligned with the central detector (No. 2) of the interferometer array and is therefore an accurate measure of the auroral level being viewed by detector No. 2 only. These values should be used only as an approximate measure of the auroral levels for the other four detectors, which point to different tangent heights and positions relative to detector No. 2. The data from the photometer is of excellent quality and does not appear to show any anomalies. The calibrated output from this sensor for the entire flight is shown in Figure 8. In addition, the time-averaged value of the photometer's output was calculated for each interferometer scan and these values are listed (together with the standard deviation) in Appendix A.

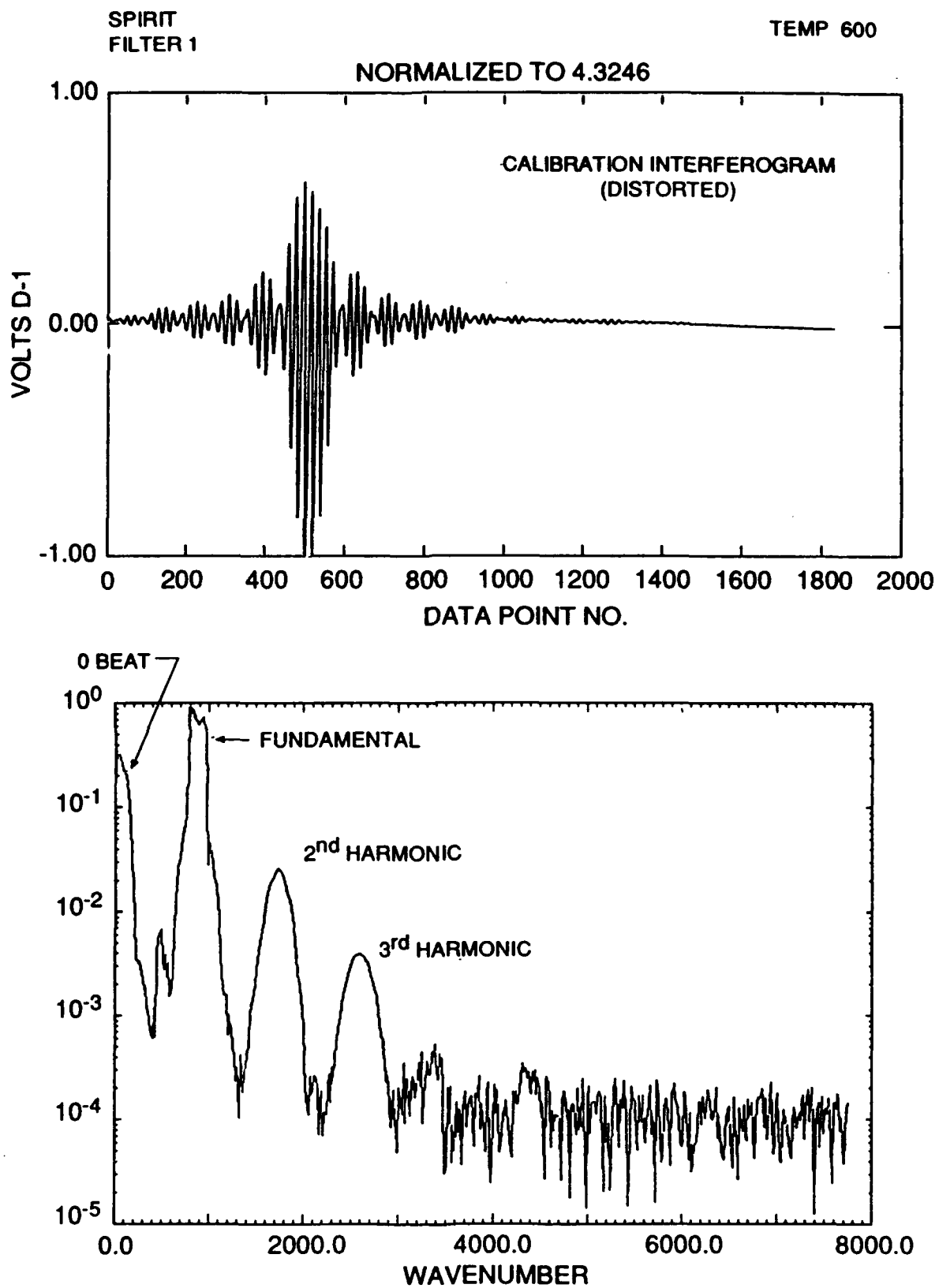


**Figure 6. Calibration Interferogram and Spectrum of 11 - 13 μ m
 Filter Region Showing Effect of Harmonic Distortions**

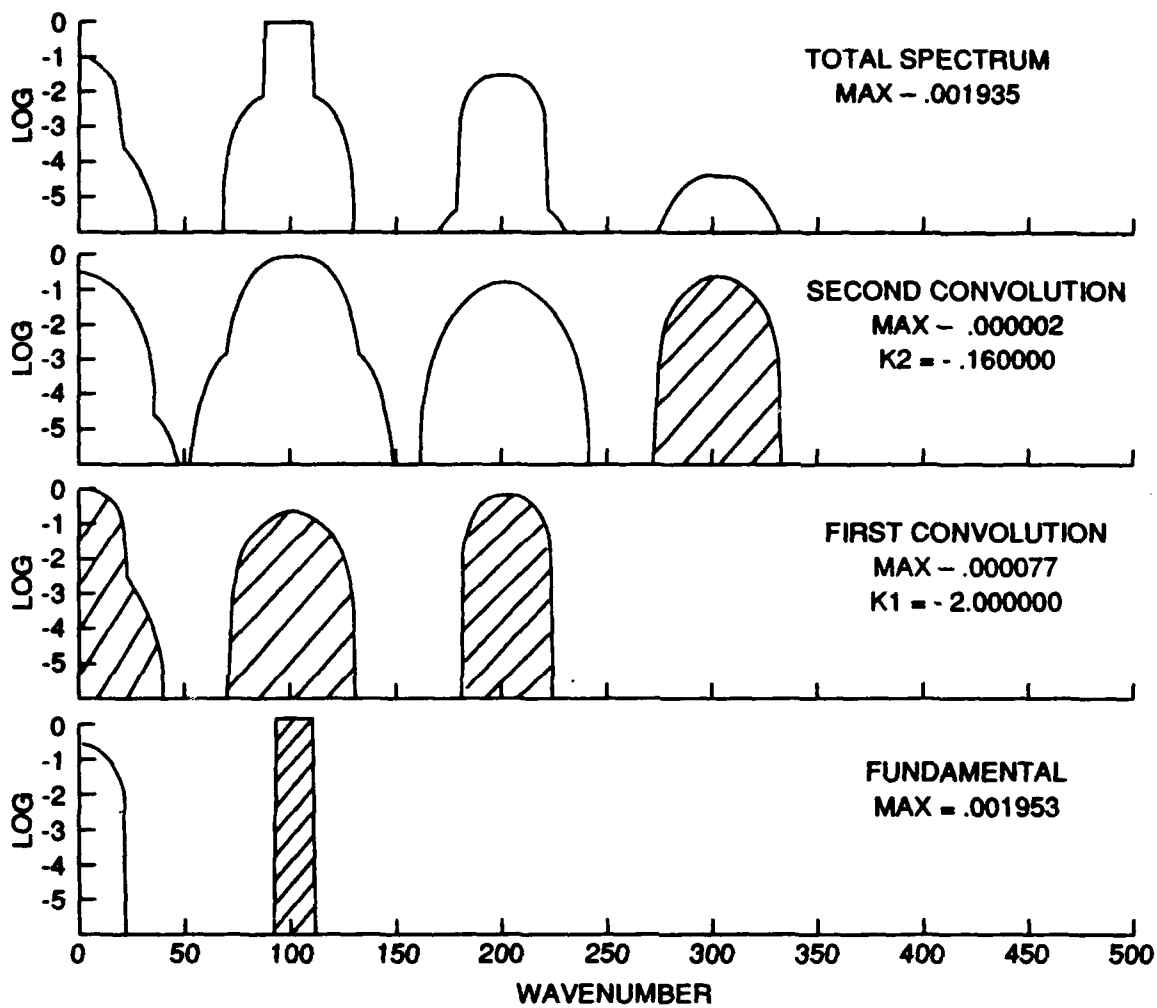


Figure 7. Simulation of Harmonic Distortions due to Nonlinear Effects

6.4 Horizon Sensor Data Summary

The on-board IR horizon sensor appears to have operated normally throughout the entire flight. All appropriate calibrations and offsets have been applied to the data and tangent heights have been calculated for each detector in the interferometer array. These values, along with the payload coordinates, are listed in Appendix B for every half second throughout the flight. The calculated tangent heights for the central detector (No. 2) are also shown plotted versus time for the entire flight in Figure 8. The average values of the tangent height for detector No. 2 were calculated for each interferometer scan and have also been included in the listing in Appendix A.

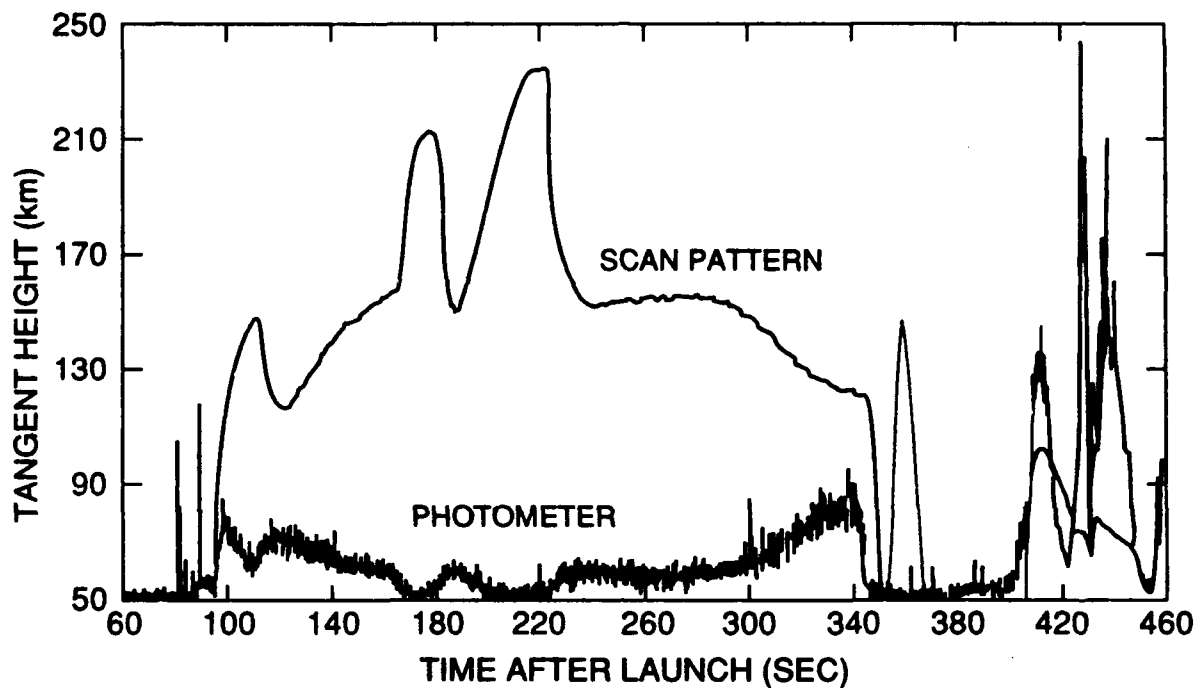


Figure 8. Horizon Sensor Tangent Heights and 3914 Å Photometer Data (Auroral Brightness) vs Time After Launch (TAL). These data correspond to interferometer Detector No. 2 only.

6.5 TV Camera Operation and Data Summary

The on-board low-light-level TV camera operated as expected throughout the flight. Good-quality pictures (Figure 9) were received and recorded at Poker Flat from the time of payload separation through initial reentry. Acceptable-quality pictures were also received at Ft. Yukon during the recovery phase after main parachute deployment occurred.

Good-quality pictures were obtained on the auroral form being observed throughout the flight. In addition, the TV camera provided documentation of the booster/payload separation. The video tape shows the hot second-stage booster being pushed away from the payload with an axial orientation and with a slow spin, indicating a clean separation with virtually no tip-off (Figure 10).

Due to the high quality of the TV data, numerous stars are visible throughout the flight, making it possible to obtain corroborative pointing information from the video tape. To facilitate its use for this purpose, a time code has been added to the video tape so that this data can be used to obtain corroborative pointing information, as well as auroral intensities for all five detectors. These analyses are now in progress.

6.6 Film Camera Data Summary

Of the two film cameras flown as a part of the SPIRIT 1 payload, only the intensified 35 mm camera (star camera) appears to have produced useful data. The problem with the Hasselblad camera has been discussed earlier.

The film from the star camera has been developed, copied, and reviewed. These data are of good quality with fiducial marks, time code, and stars clearly evident in each frame.

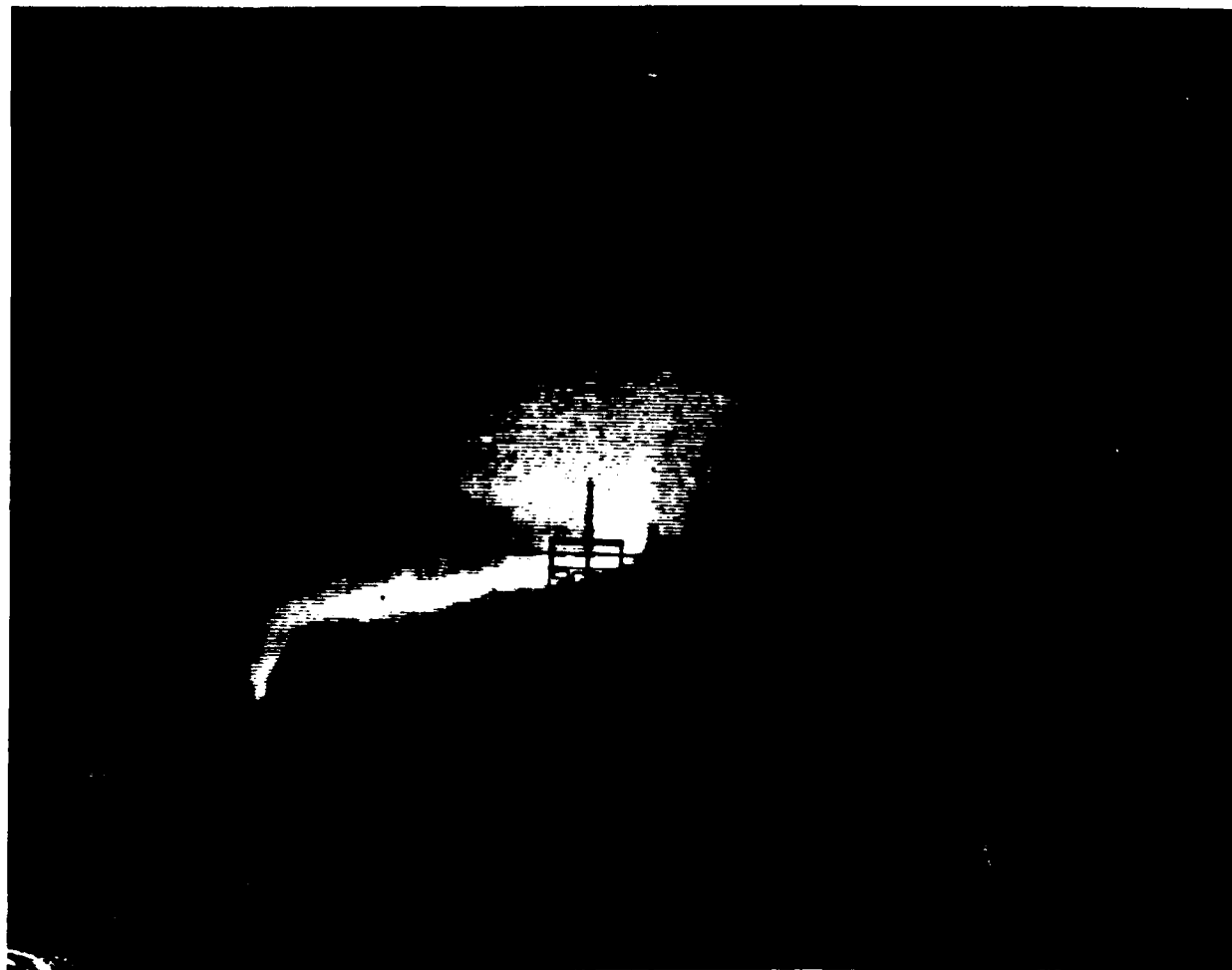


Figure 9. Picture From the On-board TV Camera Showing the Location of the SPIRIT Interferometer Focal Plane Relative to the Auroral Form Being Observed for a Time Late in the Flight

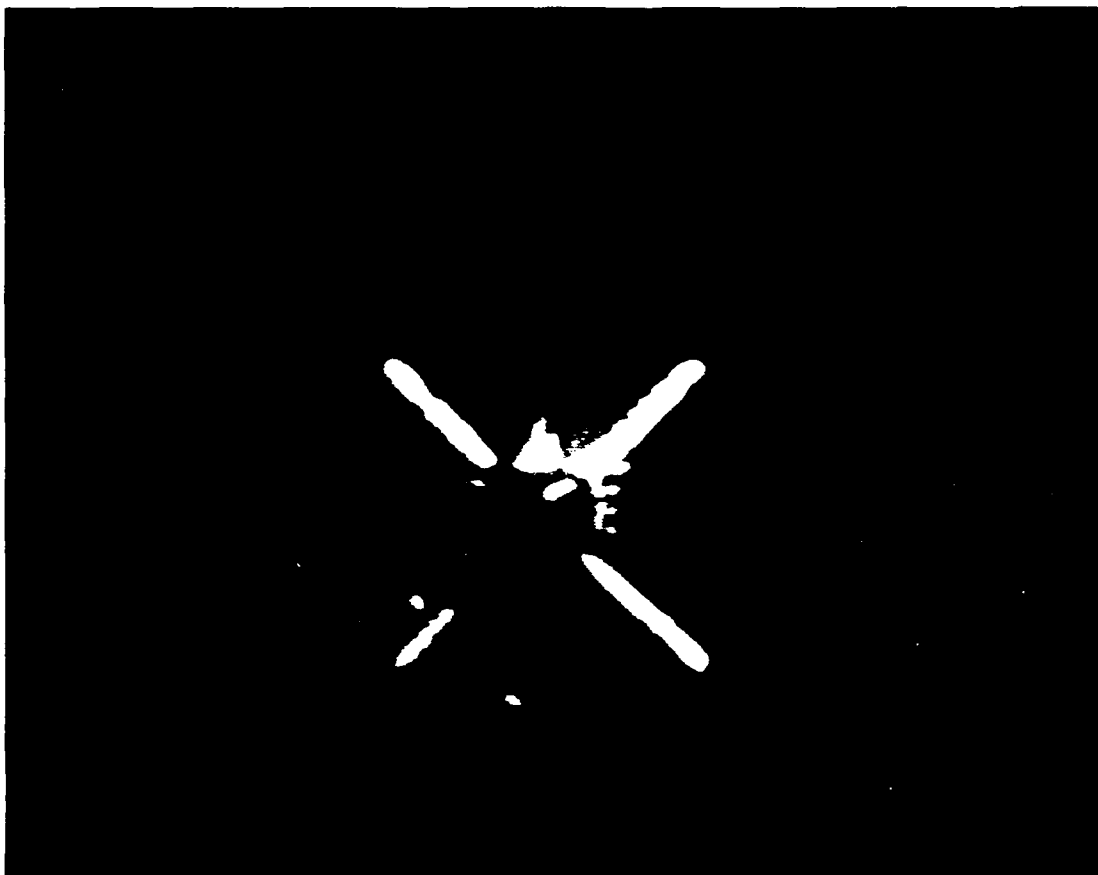


Figure 10. Picture From the On-board TV Camera Showing the Burnt-Out Castor Second-Stage Booster Moments After Payload Separation

6.7 Ground-Based Data Summary

Remote field sites associated with the launch of the vehicle were situated at Ft. Nelson, British Columbia; Peace River, Alberta; and Watson Lake, Yukon Territories. The primary purpose of these three Canadian sites was to provide observations for determining when optimum auroral conditions existed for launch of the SPIRIT 1 vehicle. During flight, the rocket instruments looked across Canada to view auroral forms in the earth limb. This placed the tangent point at Ft. Nelson, B.C. at apogee and at Watson Lake during upleg and downleg, hence, observations from these sites were desirable. The Watson Lake, Yukon Territories, and Peace River, Alberta sites were well situated to observe auroral activity both east and west of Ft. Nelson. They were used to provide a broader observational base to assist in determining when conditions were appropriate for launch, and also to provide an opportunity for forecasting for Ft. Nelson. Ft. Nelson and Watson Lake could independently provide the information necessary for evaluation and documentation of the launch of the payload if an appropriate auroral event occurred. Each of the ground stations communicated their

observations to the Project Scientist at the launch site via standard telephone links. Table 5 describes the instrumentation available at the sites. Typical data recorded from the Ft. Nelson ground site for two different times during the SPIRIT 1 flight are shown in Figures 11 and 12.

Table 5. SPIRIT 1 Ground Sites and Instrumentation

SITE	INSTRUMENTATION	MEASUREMENT/PURPOSE
Ft. Nelson, B.C.	All-sky LLLTV	Observe and record visible auroral forms-continuous recorded coverage.
	Meridian Scanning Photometers	Sky brightness at 5577Å and 3914Å along magnetic meridian-continuously recorded, scanned N to S, each 7 sec. (approx.).
	Scanning Photometers	Sky brightness at 5577Å, and 6300Å along oblique meridian formed by points at PFRR & Ft. Nelson (for example, rocket flight path). Scanned NW to SE, each 16 sec. (approx.)-continuously recorded.
	Magnetometers	Earth's magnetic field strength in X, Y, and Z axes-continuously recorded.
	Graphic aided zonal energy recorder (GAZER)	LLTV enhanced images of auroral forms. Images are filtered for, blue-3950Å peak, 120Å 1/2 BW, red-tube peak 6000-7000Å, tube cutoff approx. 6100Å, filter cutoff at 6100Å, green-5200Å peak, 80Å 1/2 BW, open-visual auroral forms B/R infers electron energy
	Visual observations	General visual auroral activity
	Two Telephones	Communications
Watson Lake, Yukon Territories	All-sky LLLTV	Observe and record visible auroral forms
	Meridian Scanning Photometers	Sky brightness at 3914Å, 5577Å, and 6300Å along magnetic meridian-continuously recorded, scanned N to S each 7 sec. (approx.)

Table 5. SPIRIT 1 Ground Sites and Instrumentation Cont'd.

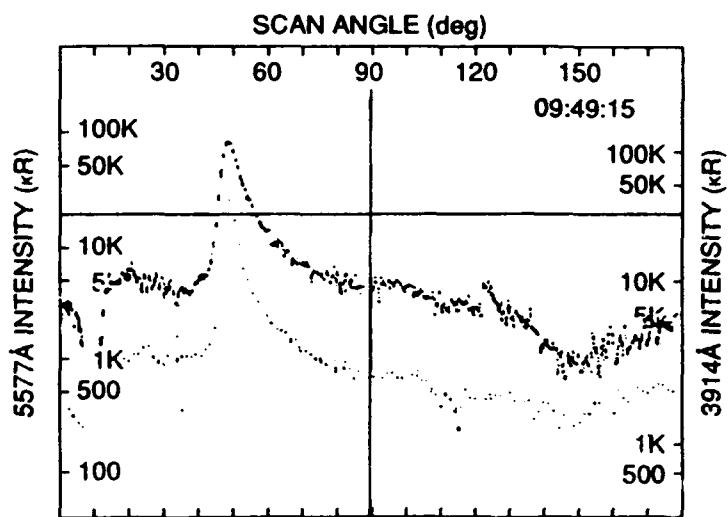
	Filter Cameras (2)	Operated during flight POS 1-records LLLTV POS 2&3-film cameras, 50 mm, F/0.95, B&W, 20° FOV, sequential 2, 4, 8 sec exp POS 4-film camera, 24 mm, F/1.4, 55° x 75° FOV, B&W POS 5-same as 4 with color POS 6-intensified film camera 9.8 mm, F/1.8, 104° FOV.
	Sheet Film Camera	Single Time Exposure
	Visual Observations	General Visual Auroral Activity
	Telephone	Communications
Peace River, Alberta	Photometer	Sky Brightness at 5577Å, hand-held and pointed
	Cordless Telephone	Communications

7. DATA REDUCTION

7.1 Pointing and Tangent Height Determination

7.1.1 Initial Tangent Height Determination

To reconstruct the spatial scan pattern traced by the SPIRIT 1 detectors, the payload aspect (altitude) was analyzed as a function of time after launch. Several sensors onboard the SPIRIT 1 payload provided data for aspect determination (Celestial Aspect Sensor, Horizon Sensor, TV, ACS/gyro, and magnetometers). Data from the IR horizon sensor was considered to be the primary pointing data and will be discussed first. The payload trajectory used in the post-flight computation of tangent heights (see Figure 5) was derived from analysis of the PFRR NASA TRADAT data by PL/GPD (during the flight the nominal payload trajectory was used for the real-time tangent height display).



Meridian scanning photometers at T+16 sec. The heavy (upper) trace is 5577 Å, the lighter (lower) trace is 3914 Å.

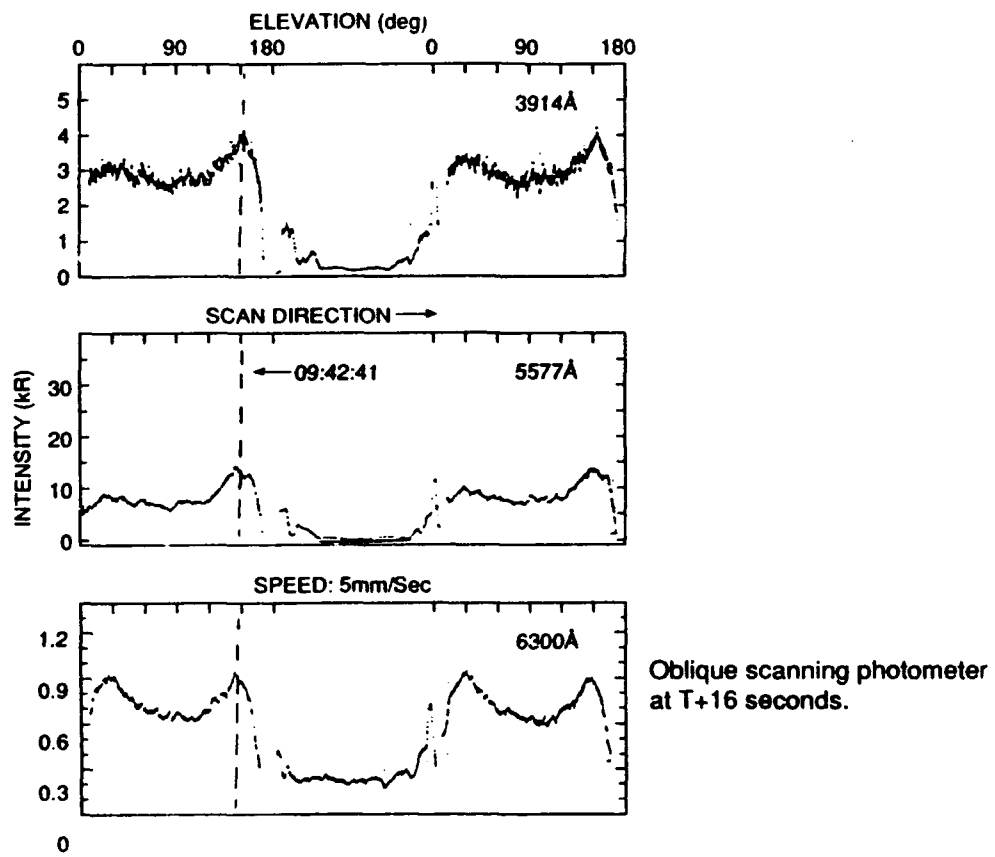
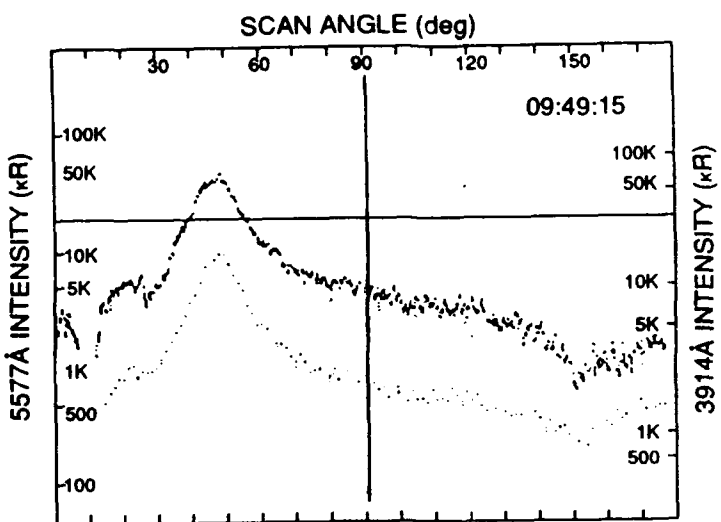


Figure 11. (a) Auroral Intensity as Measured by the Ground-based Meridian Scanning Photometer at T + 16 sec TAL. The heavy (upper) trace is for the 5577 Å channel, the lighter (lower) trace is for 3914 Å. (b) Auroral Intensity as Measured by the Ground-based Oblique Scanning Photometer at T + 16 sec TAL



Meridian scanning photometers at T+ 6 min 50 sec. The heavy (upper) trace is 5577 Å, the lighter (lower) trace is 3914 Å.

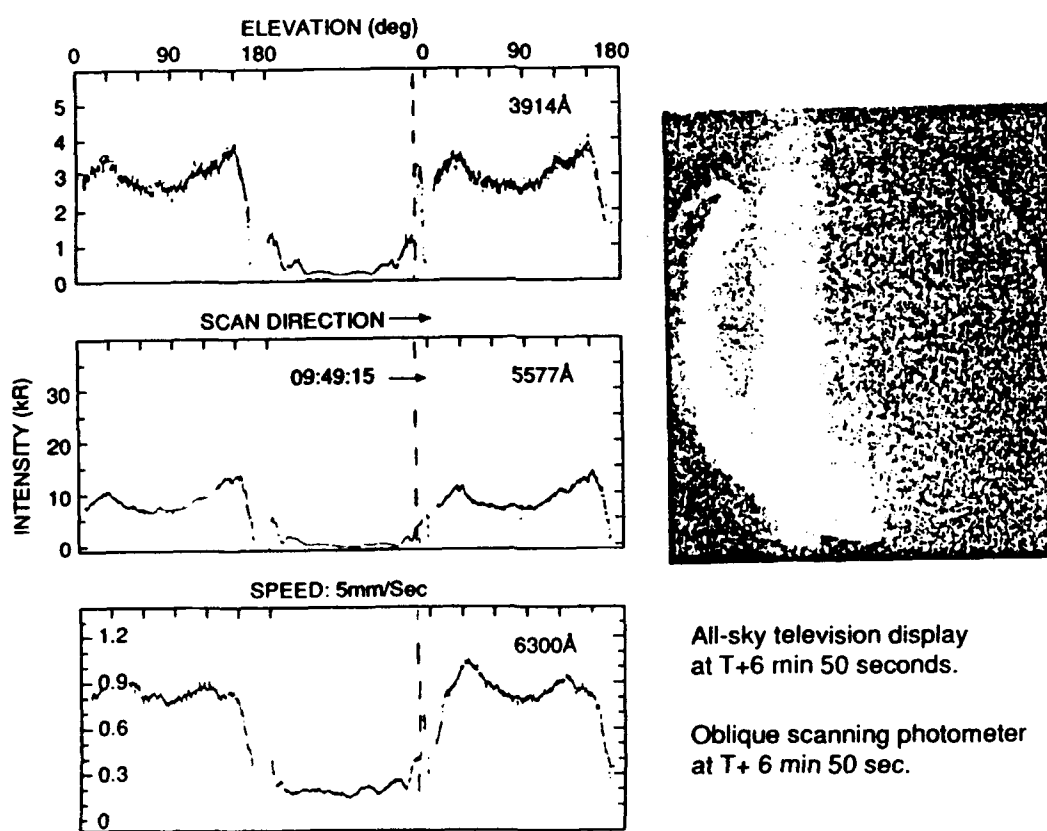


Figure 12. The Auroral Intensity as Seen From the Ground-based (a) Meridian- and (b) Oblique-Scanning Photometers at 1 + 6 min. 50 sec TAL and the Ground-based All-sky Television Image for the Same Time

The SPIRIT 1 horizon sensor was manufactured and calibrated by Ithaco, Inc., Ithaca, New York. The system operates by scanning a small field of view (FOV) in a 45-degree (half angle) cone about the SPIRIT 1 nominal line of sight (LOS). By sensing the peak of the atmosphere's 15 μm CO₂ emission layer (at about 40 km tangent height) the horizon sensor measures the angle between the LOS and the local nadir, which can be related to the tangent height viewed by the LOS. The LOS tangent height is given by (see Figure 13)

$$H_t = (R_p + h) \sin G_p - R_t \quad (1)$$

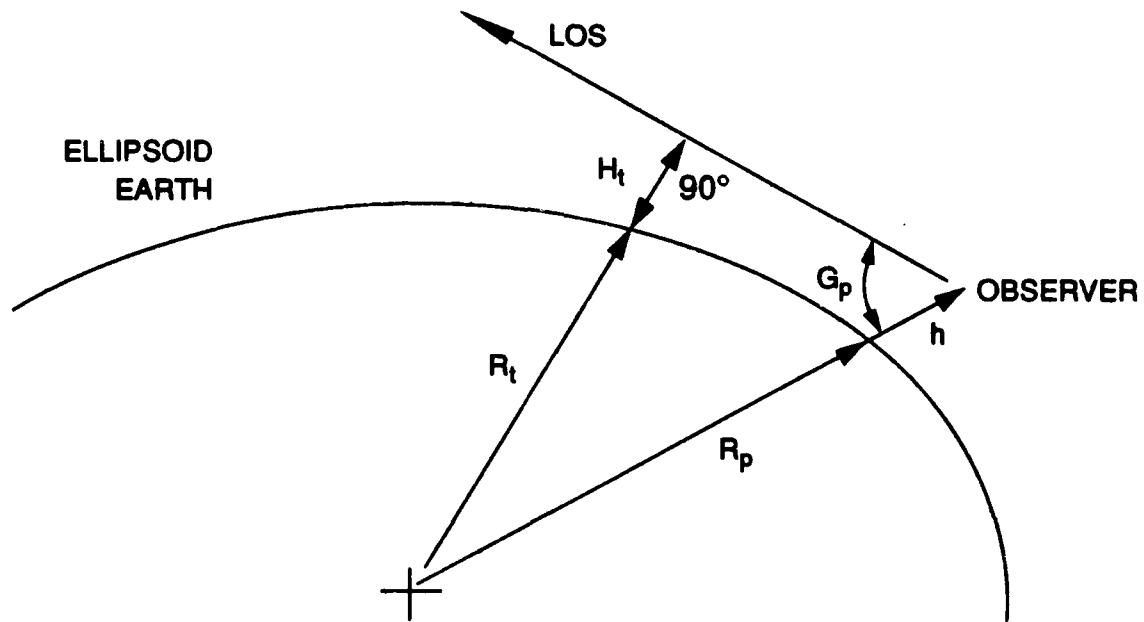
where

H_t = tangent height
 h = payload altitude
 R_p = earth radius at the payload location
 R_t = earth radius at the tangent point location
 G_p = angle between LOS and local nadir

The primary statistical errors in tangent height determination are due to the following uncertainties:

1. the altitude of the peak of the CO₂ layer (± 3 km).
2. measuring the angle traversed by the FOV between crossings of the CO₂ layer (± 1 mrad)
3. calibration uncertainties in converting horizon sensor output volts to degrees.

When combined, these uncertainties produce a tangent height uncertainty of approximately ± 4 km at 100 km tangent height for the SPIRIT 1 trajectory. There is an additional important source of tangent height uncertainty that is not statistical. This occurs when large detectors (which span large tangent heights in object space) view emissions whose intensities are exponentially dependent on tangent height. Even assuming constant responsivity across the detector, the centroid of the signal is displaced from the center of the detector. Thus, an incorrect interpretation of the source tangent height can result by assuming the signal originates from the center of the detector. An estimate of this apparent displacement in tangent height (Δh_c) is given by



LOS = LINE OF SIGHT

h = PAYLOAD ALTITUDE

H_t = TANGENT ALTITUDE (HEIGHT)

G_p = POINTING ANGLE

R_t = EARTH RADIUS AT TAN POINT

R_p = EARTH RADIUS AT PAYLOAD ALTITUDE

Figure 13. Tangent-Height Geometry Illustrating the Need to Use Earth Radius at the Tangent Point When Computing Tangent Height

$$\Delta h_c = H_s \cdot \frac{h_1}{2} + \frac{h_1}{1 - \exp(h_1/H_s)} \quad (2)$$

where

H_s = scale height of a particular emission species

h_1 = tangent height subtense of a specific detector.

The following example demonstrates this effect. Consider detector No. 2, which spans a tangent height range of 14 km when viewing a 100 km tangent height. For O_3 (scale height of 5 km) the tangent height displacement is about -2.9 km and for CO_2 (scale height of 15 km) the displacement is about -1.1 km. Thus, in a single spectral scan in which both of these species are present, there is a difference of approximately 1.8 km in their tangent height origins. Obviously this effect can only be corrected if the scale heights of all the measured emitters are known, which is not in general true. Consequently, no Δh_c corrections have been made to the results presented in this report.

The SPIRIT 1 tangent heights were derived from the horizon sensor data for 80 to 462 sec TAL. These data are plotted in Figure 4 along with the actual trajectory flown. In addition, the data are compared to the preplanned trajectory and scan pattern. The data show that the actual scan pattern was approximately 40 km higher than planned and also that the trajectory was about 7 km lower than planned. The sun terminator was computed for the flight time and is also shown in Figure 5. It shows that the payload was not sunlit at any time during the flight. The solar disk was well outside the sensor's FOV and auroras under observation were not sunlit.

7.1.2 Final Tangent Height Determination

The initial set of tangent heights for the five IR sensors in the SPIRIT 1 interferometer were derived by calibrating and drift-correcting the gyro data using data from the Ithaco horizon sensor (IHS) and the celestial aspect camera (CAS). These tangent heights are an important factor in subsequent IR data analyses that lead to atmospheric radiance profiles, and are a limiting factor in the accuracy of those profiles.

This method took advantage of the fast response time of the gyro (on the order of 0.1 sec) and the absolute accuracy of the IHS, which is referenced to the altitude of the upper edge of the CO_2 layer (at approximately 40 km) that triggers the IHS. Data from the IHS, which was aligned co-axially with detector No. 2 on the center of the interferometer axis, was used to provide an absolute tangent height reference for the gyro during periods of low payload motion.

The CAS data offers the greatest accuracy of all three attitude sensors due to the combination of fast time response (limited by the shutter speed) and the use of the star field. However, due to time and funding limitations, only a portion of the CAS data has been reduced. The CAS results available have been compared with the gyro-derived tangent heights, and reveal agreement to within an average of 2 km. This reasonable overall agreement indicated that the tangent height determination method had been largely successful. However, discrepancies as large as ~5 km did occasionally appear, and tangent height errors of similar sizes were also supported by results from our IR data analysis.

In an attempt to further reduce these discrepancies, a new set of tangent heights for the interferometer axis (detector No. 2) based on data from the IHS was derived. By applying the difference between the new results and the initial gyro-derived tangent heights as a correction, a set of new tangent heights for all five detectors was generated. The method for generating these final tangent heights is briefly described below. Comparisons with the gyro and CAS data are provided, and tabulations of tangent height versus time after launch (TAL) and scan and detector number are attached.

7.1.2.1 Method for Determining the Final Tangent Heights

The method involves correcting the IHS data for its slow time response (relative to the gyro) by using data from the gyro, and also correcting for the eccentricity of the earth, which was incompletely treated in the IHS data reduction. The time response correction is as follows. First, the gyro-derived tangent height $h(t)$ is used to synthesize a signal, $\theta(t)$, which represents the output of a hypothetical "fast" IHS, where $\theta(t)$ is the half-angle of the arc traced by the IHS between crossings of the CO_2 layer. Next, $\theta(t)$ is convolved with an instrument function that describes the time-averaging and delaying effects in the IHS. The mathematical details of the instrument function are described in the next section. This convolution operation results in a "slow" signal, $\theta_s(t)$, which represents the hypothetical output of a "real" IHS with the same view.

From this point on, either of two procedures may be followed to generate time-response-corrected tangent heights. In procedure 1, $\theta_s(t)$ is used to generate a "slow" tangent height $h_s(t)$. The difference between the original "fast" $h(t)$ from the gyro and the "slow" $h_s(t)$ is then applied as a correction to the tangent heights derived from the IHS. In procedure 2, the difference between $\theta(t)$ and $\theta_s(t)$ is taken, and is applied to the θ from the IHS. This results in a corrected θ that is used to generate the new tangent heights. We have found that these two procedures yield essentially the same results.

The earth eccentricity correction arises from the fact that the earth radius at the CO_2 layer crossing points may be different from the value at the payload location. This difference is computed at each of the two crossing points, averaged, and applied as a correction to the CO_2 layer height.

Other minor adjustments may also be applied to account for misalignment between the IHS and the CAS, and to account for a difference from the assumed value of the CO_2 layer altitude

of 39.6 km. However, excellent agreement was obtained with the CAS data without these adjustments.

7.1.2.2 Computational Details of Method

Mathematical and computational details of the method are given here. The IHS instrument function $I(t-t_0)$ with which $\theta(t)$ is convolved (that is, integrated over the variable t_0) represents the relative contribution of the value of θ at time t_0 prior to the actual time t of the displayed reading. It is itself the convolution of three functions.

$$I(t-t_0) = m * n * p \quad (3)$$

where m , n , and p represent the instrument functions associated with each of three stages in the data acquisition and processing. The first stage is the acquisition of θ within the measurement time interval of 0.5 sec between successive sweeps of the sensor. The associated function f is taken to be a boxcar ("square") function of width 0.5 sec, corresponding to an average over the sweep. The second stage is the lag between the current time and the end of the last sweep, during which time the last reading is displayed. Since this lag is uniformly distributed over the current sweep, g is identical to f . The third stage is the introduction of an electronics time constant of 0.3 sec which smooths the output. The associated function p is an exponential with an 0.3 sec $1/\theta$ time. The net convolution $I(t-t_0)$ has the appearance of a skewed Gaussian with a mean $t-t_0$ (delay time) of 0.8 sec.

Details of the conversion between tangent height H_t and angle θ are as follows. Let

$$H_t = y(\theta) \quad q = y^{-1}(H_t) \quad (4)$$

where $y(\theta)$ is found from Eqs. (1.1) and (2.2) in the Boston College draft report (SPIRIT 1 Report, Hor. Sens. 1, Sept. 30, 1986). In that report, θ is denoted as $Q_{tot}/2$, and y^{-1} is given by

$$\theta = \cos^{-1} [(r + H_t - z + d)/s] \quad (5)$$

where

a = instrument height

x = height of CO_2 layer

r = earth radius

$$c = \sqrt{(r + a)^2 - (r + x)^2}$$

$$s = \sqrt{(r + a)^2 - (r + H_t)^2}$$

$$z = \sqrt{(c - 2^{1/2}s)^2 + (r + x)^2}$$

$$d = (s^2 - (r + H_t - z)^2)/2(r + H_t)$$

A few remarks on the value of r are appropriate. Boston College used separate values of the earth radius at the tangent point and at the payload in converting between G_p (the angle to the nadir) and tangent height in Eq. (1.1). They used a single radius (the payload value) in the remainder of the calculation [Eq. (2.1)]. Since we have performed a "back-and-forth" calculation, starting from H_t and regenerating a new H_t , a single r value could be used throughout; the difference between the payload and tangent point r 's assumed by Boston College shows up in our calculation as slightly altered values of θ and G_p . The effect of a still different r at the CO_2 layer crossing points has not thus far been considered, and is included in the following treatment, which fully corrects for earth eccentricity effects.

Eq. (1.2) of the Boston College report was used to calculate the earth radius at the latitudes Z_p , Z_1 , and Z_2 corresponding to the payload and each of the two CO_2 layer crossing points, respectively. The payload latitude was taken as the average, 65.4° . Z_1 and Z_2 were computed using Eq. (1.3) of the Boston College report, which requires the azimuth angles of the CO_2 crossings relative to due north. These angles are displaced from the payload azimuth angle (which is known) by $+\delta$ and $-\delta$, where δ is approximately 45 deg. A more accurate value for δ is given by

$$d = \tan^{-1} [(r + H_t) \sin/(z - d)]. \quad (6)$$

As mentioned earlier, the eccentricity correction is an increment added to the CO_2 layer height equal to the difference between the earth radius Z_p and the average of the earth radius at Z_1 and Z_2 . The rationale for taking the average is that the half-angle θ output by the IHS is actually the average of the half-angles for each CO_2 layer crossing, and changes in θ are linear in small changes in r . The eccentricity correction is typically between 0.5 and 2 km, and is correlated with increasing payload height. This is due to the fact that the payload is pointed

southeast, so that more southern latitudes, hence a larger radius, is viewed with increasing payload height.

Computer implementation of the method used the following procedure. Input files consisted of (1) the IHS instrument function $I(t - t_0)$ computed for 50 time steps prior to t_0 , and (2) a listing of attitude angles, payload heights, and tangent heights from the gyro and the IHS for the duration of the flight, at approximately 8500 time steps (1 time step = 1/24 sec). Three output files were generated containing (1) the new tangent heights h_{corr} , along with the current (gyro) tangent heights h_{gyro} and the original (uncorrected) IHS tangent heights h_{ihs} ; (2) the differences $h_{ihs} - h_{gyro}$; and (3) the differences $h_{corr} - h_{gyro}$. A program option permits listing outputs every n (integer) time steps. Typically, n was set to 10, resulting in output files of 854 lines with time steps of 0.417 sec.

The h_{new} - versus - time output file was used to derive new tangent heights for each interferometer scan and detector, as follows. The Detector No. 2 tangent heights were derived by interpolation using the nominal TAL of the scan (based on the time of the critical peak of the interferogram). Then, the difference between the new and old values was taken and applied as a correction to the remaining four detectors.

7.1.2.3 Discussion of Tangent Height Results

The new tangent heights are superior to the previous, gyro-derived results in two important comparisons. First, the differences with the CAS data now average less than 1 km, and the largest differences are less than 2 km. The second comparison is an internal consistency check, in which spectral scans obtained during rapid pointing maneuvers (when the tangent heights are most uncertain) are grouped with other scans having virtually the same CO_2 and O_3 radiance levels, and thus essentially the same tangent heights. It is found that within each group of scans the new tangent heights are much closer to each other than are the previous tangent heights.

The IR data have been examined using the new tangent heights. The overall level of scatter is similar to what was found using the gyro-derived tangent heights. The CO_2 and NO profiles have been raised by 3-4 km, while the O_3 profile is essentially unchanged, despite substantial differences between old and new tangent heights in certain scans. Since we believe the new tangent heights are accurate to within 1-2 km, the scatter is probably due to real horizontal variations in the atmosphere - specifically, a lowering of the atmosphere with increasing distance from the payload.

7.2 Interferometer Data Processing

The output from the interferometer is an interferogram, or autocorrelation function, whose Fourier transform produces an estimate of the spectrum of the incident radiation. In the interferometer the incident beam of radiation is split into two optical paths, then recombined so as to cause a modulated interference pattern as one path length is varied. The

interferogram consists of the intensity record of the interference pattern sensed by a detector. The spectral resolution that may be obtained from an interferogram is inversely proportional to its length but is also dependent upon the data processing algorithms employed. At a point near the zero path difference a peak occurs due to constructive interference of all wavelengths. This is defined as the "critical peak" of the interferogram, and is the point of "zero lag" if the interferogram is considered to be an autocorrelation function.

The SPIRIT 1 interferometer design was such that interferograms were generated over the full path difference on only one side of the critical peak. The rationale for this design is that if the interferogram is perfectly symmetric, having no phase errors, only one side is needed to derive the spectrum and the other side is redundant information. Thus, by making the interferograms one-sided, one can maximize spectral resolution by taking full advantage of the available mirror drive length. However, since perfect symmetry of the sampled interferogram is rarely achieved, some samples were taken on the other side of the critical peak to provide information for phase correction of the interferogram. Some examples of actual SPIRIT 1 flight interferograms are shown in Figure 14.

Three significant anomalies were present in the SPIRIT 1 raw interferogram data. First, they show the presence of occasional spikes (possibly due to energetic particle effects on detectors) or telemetry dropouts and /or missing points due to buffer storage overload. Most of the spikes due to dropouts and buffer overload occur near the telemetry maximum voltage limit, and were detected by comparing successive data points to a running mean and using a standard deviation criterion. The points flagged by this process were replaced by the value of the previous data point. Other spikes (which were generally smaller and more random in amplitude) were treated by modeling six points around the spike and replacing the spike with a fitted value.

Second, the interferogram dc level was not always constant throughout a scan but, in many cases, exhibited low-frequency trends. These trends are thought to be due to changes in the viewed atmospheric IR emission caused by spatial drift of the LOS or due to radiation scattering from particles that drifted through the field of view. These anomalies were corrected in two ways. If the trend was due to particles, as indicated by short fluctuations in the DC level, the interferogram was high-pass-filtered to remove the trend. If the atmospheric emission changed, as indicated by a monotonic trend, the interferogram was low-pass-filtered and this result was used to window the interferogram in such a manner as to remove the trend. This processing produced interferograms that were eventually used to generate the spectra.

Third, the SPIRIT 1 interferograms exhibit symptoms of nonlinear system response. This is apparent in the central portion of the interferograms shown in Figure 14 in which the interferogram signal appears to be flattened on top. It is speculated that this effect is due to compression and subsequent expansion of the dynamic range (companding) and/or dielectric relaxation processes.

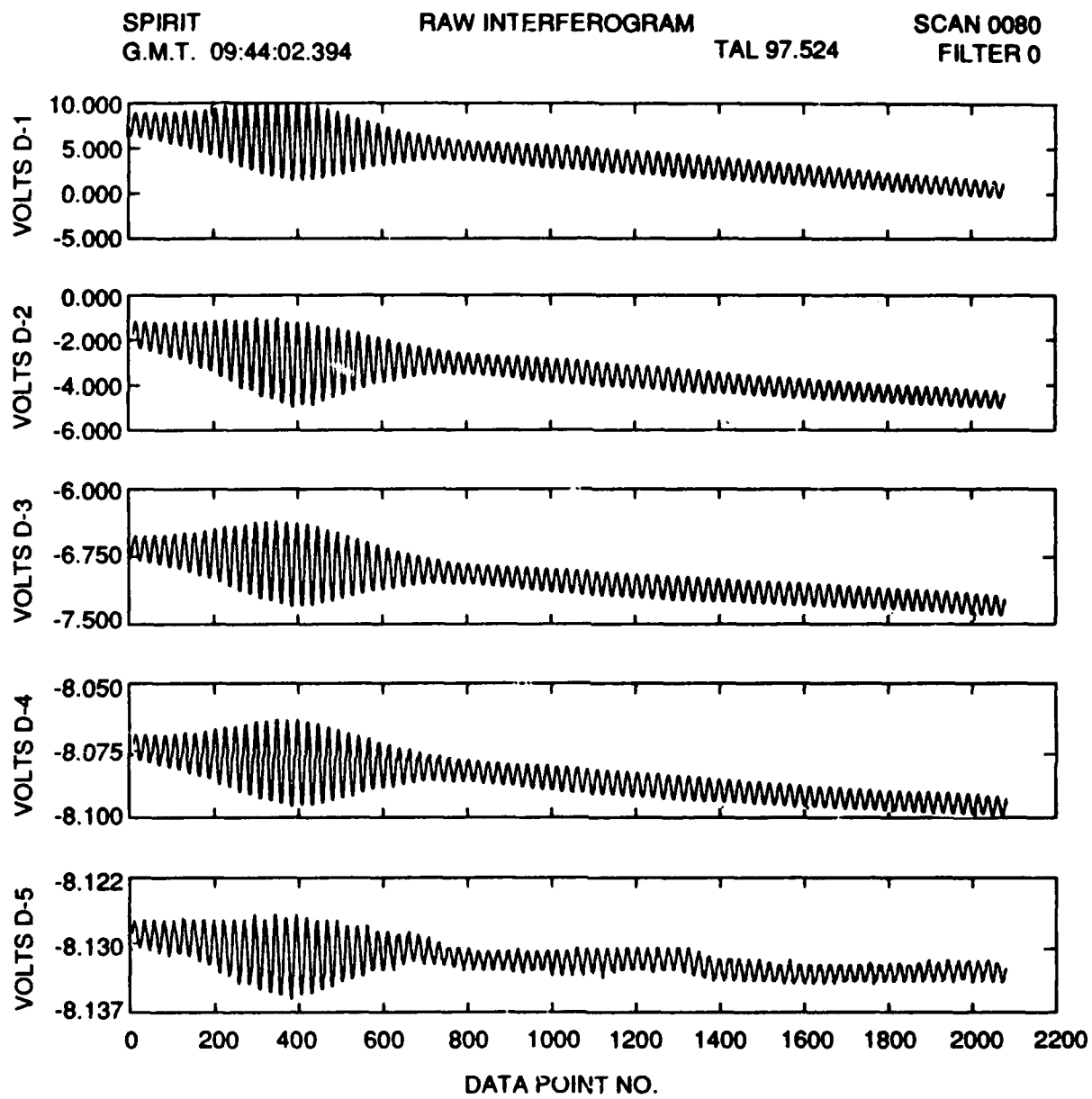


Figure 14. Examples of SPIRIT 1 Flight Interferograms for all Five Detectors

The companding nonlinearity results from electronic preamplifier nonlinear input/output characteristics and effectively convolves the spectrum with itself one or more times producing harmonics of the true spectrum. Companding nonlinearities increase with increasing total incident photon flux. The dielectric relaxation process is dependent upon detector bias level and causes the frequency response of the interferometer to be nonlinear. The net effect of these processes is to produce ghost spectra at short wavelengths. Examples of ghost spectra in

the SPIRIT 1 data are shown in Figure 15. As yet no practical method has been found to correct the spectra for nonlinear anomalies.

7.3 Spectral Emission Estimates

There are two important considerations in estimating the spectra from the processed single-sided interferograms described above. These are selection of apodization windows and the method of correcting for phase errors in the spectra.

The choice of apodization windows depends on the spectral features one wishes to analyze. In Fourier analysis of interferometer data, it is common to consider the Fourier transform of the windowed interferogram to be identical to the Fourier transform of the apodizing window (called the scanning function) convolved with the transform of the interferogram.^{5,6} In general, scanning functions that yield high spectral resolution in the central lobe exhibit higher sidelobes that can result in undesirable out-of-band leakage. Scanning functions that have suppressed sidelobes exhibit poorer spectral resolution. This is illustrated in Figure 16 in which the high-resolution triangular window is compared to the suppressed-sidelobe window of the Kaiser-Bessel (K-B) function.⁷ If one wishes to analyze the spectral structure of high-level signals for which side-lobe leakage is not important, then the best choice would be the triangular window. However, if one desires to analyze the low-level radiance floor of the 12 μm window band (Figure 17a) it would be desirable to use the K-B window to suppress leakage from adjacent intense portions of the spectra. Figure 17a shows the effect of each of these windows when applied to model interferograms derived from model spectra.¹

The Mertz phase correction method has been employed to generate the SPIRIT 1 spectra.⁸ In this method it is assumed that the phase of the spectrum is slowly varying and can be estimated by the phase derived from the portion of the interferogram around the central peak (low resolution phase). The Mertz phase-corrected spectrum $S(\sigma)$ is related to the interferogram by:

$$S(\sigma) = |I(\sigma)| \cos [(\psi(\sigma) - \phi(\sigma))] \quad (7)$$

⁵ Saki, H., Vanasse, G.A., and Forman, M.L. (1968) Spectral recovery in Fourier spectroscopy. *J. Opt. Soc. Am.*, **58**:54

⁶ Forman, M.L., Steel, W.H., and Vanasse, G.A. (1966) Correction of asymmetric interferograms obtained in Fourier spectroscopy. *J. Opt. Soc. Am.*, **56**:59.

⁷ Harris, F.J. (1978) On the use of windows for harmonic analysis with the discrete Fourier transform. *Proc. IEEE*, **66**, No. 1.

⁸ Mertz, L. (1967) Auxiliary computation for Fourier spectroscopy. *Infrared Physics*, **7**:17.

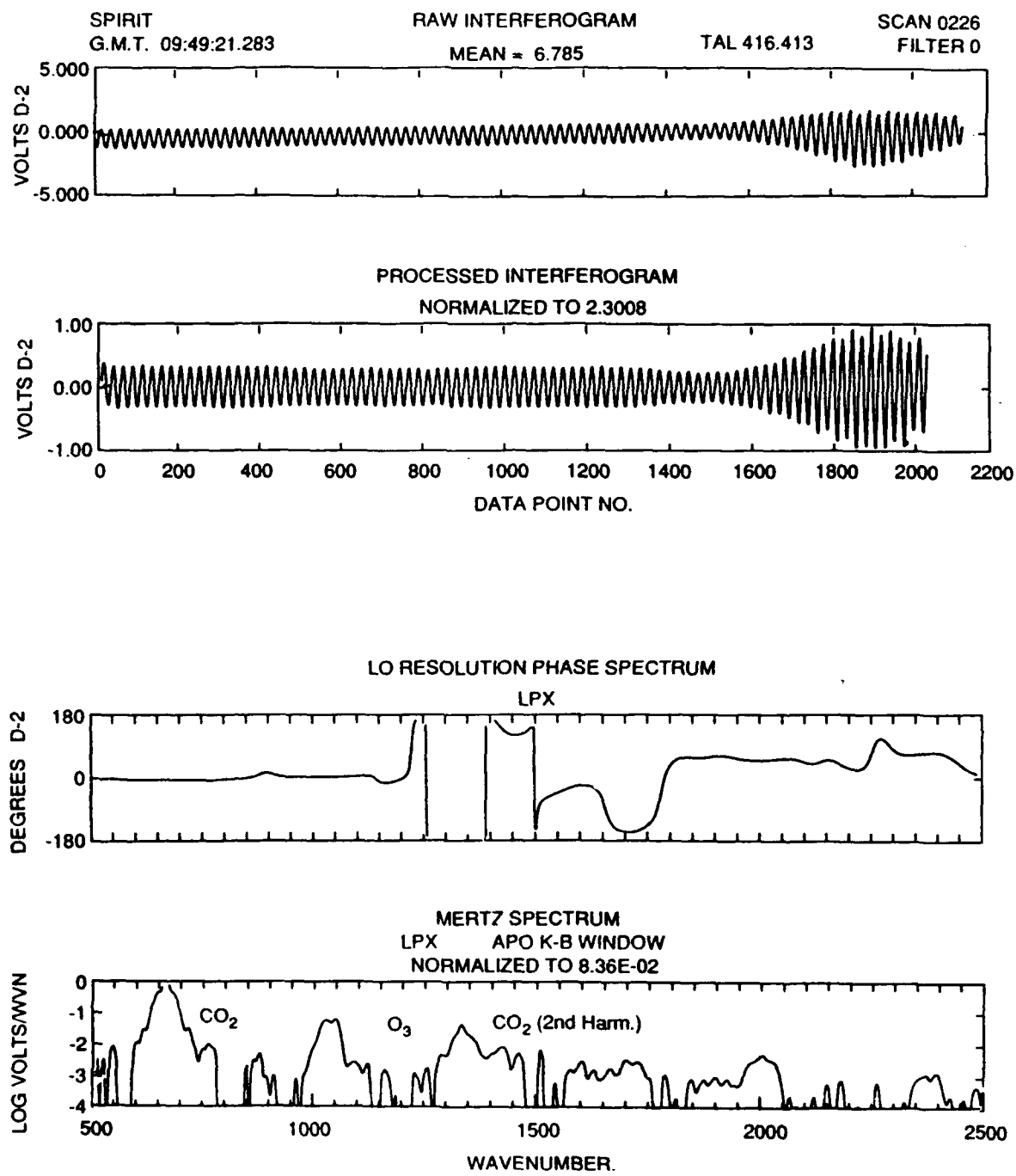
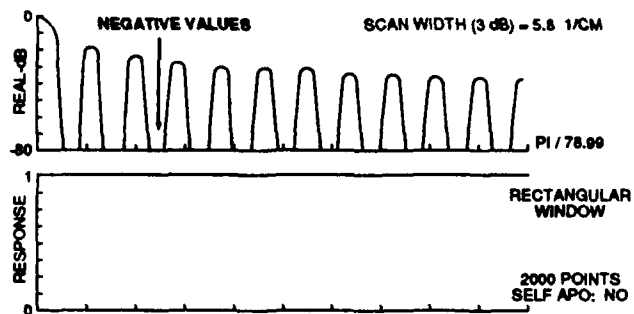


Figure 15. Examples of Processed SPIRIT 1 Interferogram Data Showing a Raw Interferogram, Processed Interferogram, a Low-resolution Spectrum, and a Mertz Phase-corrected Spectrum

where

$|I(\sigma)|$ = amplitude of the transform of the apodized one-sided interferogram
 $\psi(\sigma)$ = phase of apodized one-sided interferogram, and
 $\Phi(\sigma)$ = low-resolution phase .

DOUBLE-SIDED INTERFEROGRAM



SINGLE-SIDED INTERFEROGRAM

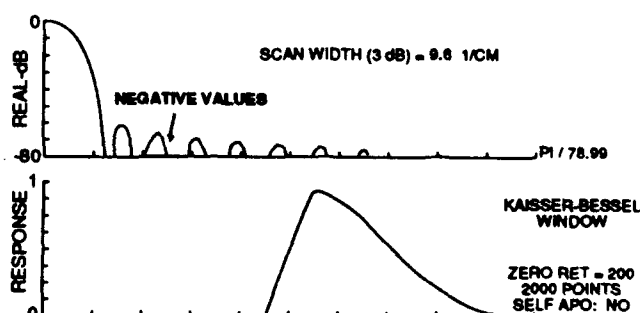
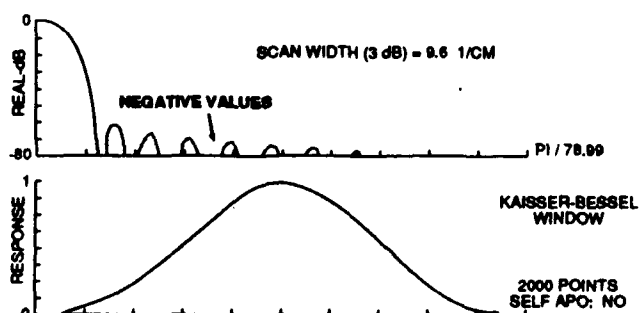
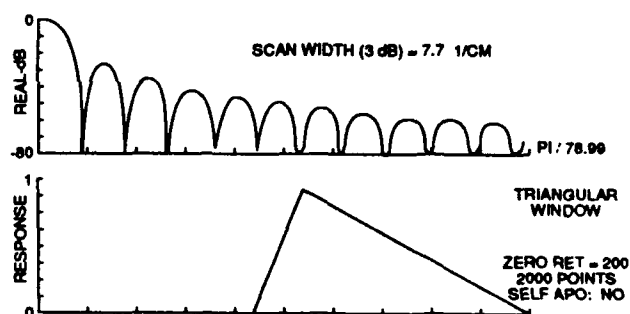
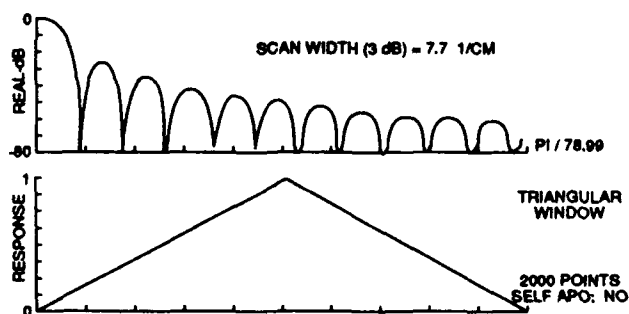
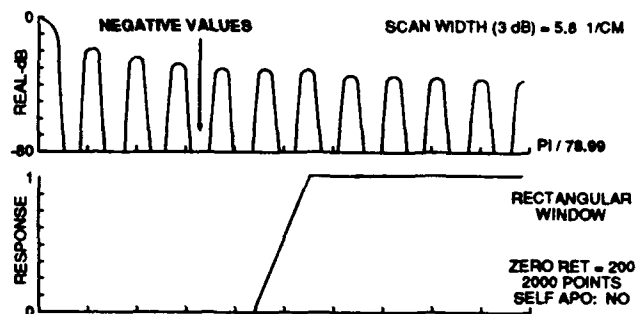


Figure 16. Examples of Apodizing Window Functions Showing the Window Characteristics Required for a One-sided Interferogram to Produce Scanning Functions Identical to Two-sided Apodizing Windows

STANDARD ATMOSPHERE CONDITION 1
NIGHT LIMB SPECTRAL RADIANCE 100 KM TAN HT
RES= 1CM⁻¹

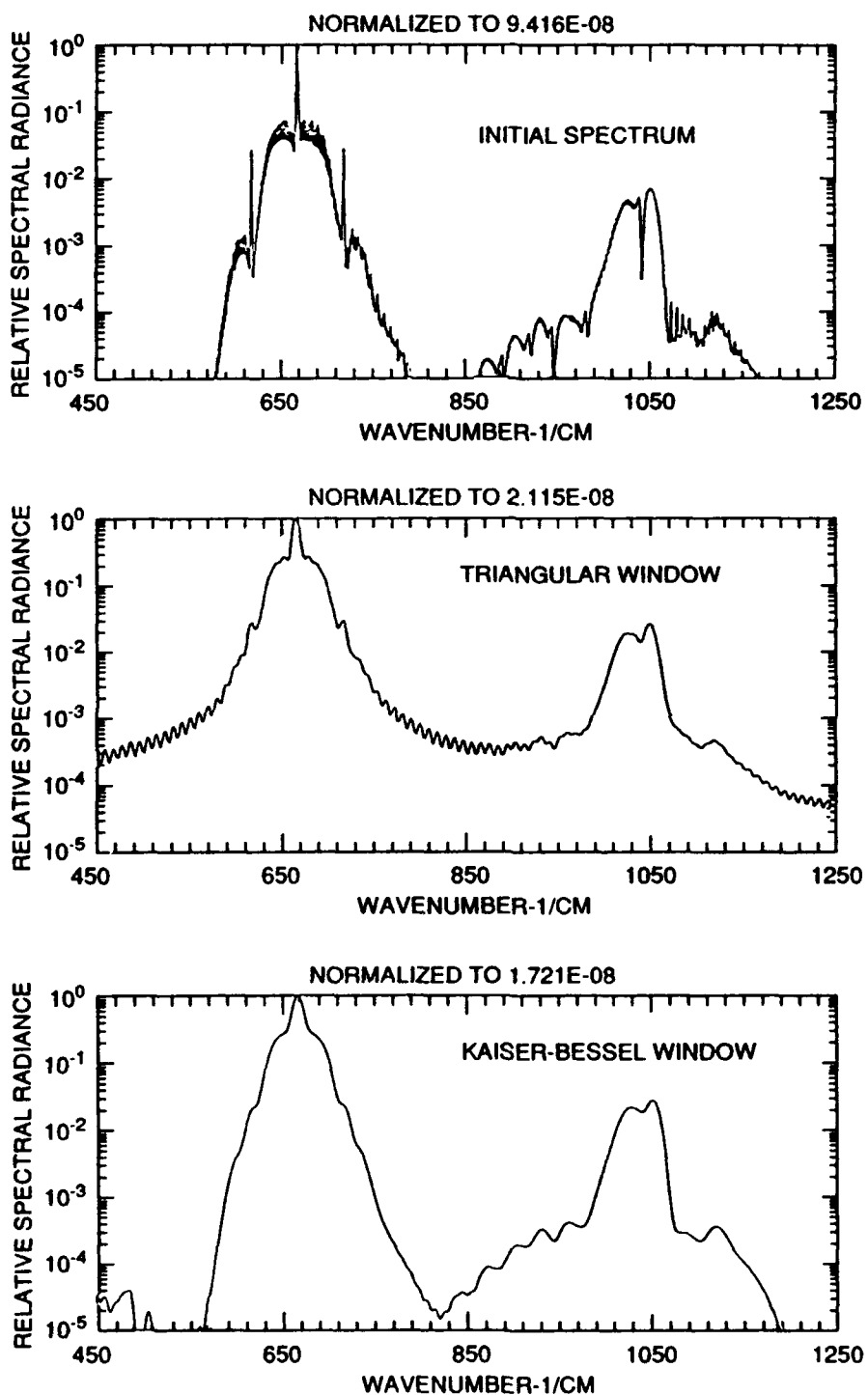


Figure 17a. Effects of Apodizing Windows on the Emission Spectrum in the 12 μm Window Region

An example of the raw interferogram, processed interferogram, low-resolution phase, and Mertz-corrected spectra for SPIRIT 1 data is shown in Figure 15. It should be noted that when the spectral signal is high the low-resolution phase is flat and near zero. However, in the vicinity of the ghost spectra the phase tends toward 180° . This is characteristic of the companding nonlinearity anomaly.

To suppress the effects of sidelobes and to assure the spectral purity of the data in the window regions, the SPIRIT 1 interferograms were processed with the K-B window; for applications in which high resolution is most important the interferograms could be reprocessed using an alternate window function that maximizes spectral resolution at the expense of sidelobe contamination, such as a triangular window. The scanning function corresponding to the Kaiser-Bessel window used to process the SPIRIT 1 interferograms is shown in Figure 17b.

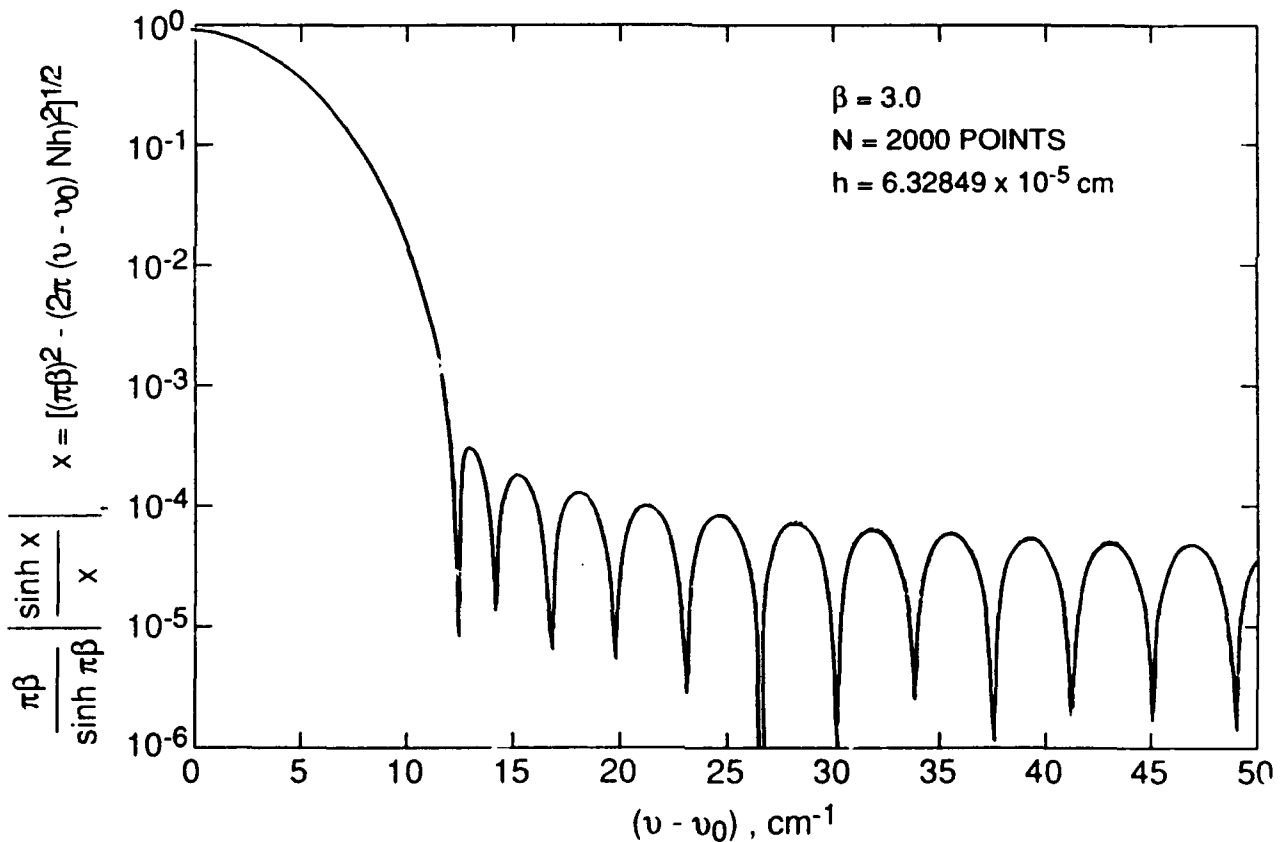


Figure 17b. The Scanning Function for the Kaiser-Bessel Apodization Window Used to Process the SPIRIT 1 Interferogram

8. CALIBRATION OF INTERFEROMETER DATA

8.1 Introduction

The raw spectra in volts/cm⁻¹ that are derived from the processed interferograms must be corrected for wavelength response using the relative curves for each detector, and then scaled using the absolute responsivities, R, (in V W⁻¹ cm²/sr) for each detector.

8.2 Open-Filter Mode

8.2.1 Relative Wavelength Response

The relative wavelength response curves were obtained from analysis of post-flight calibration spectra measured by P. Dybwad at Stewart Radiance Laboratory.⁹

A typical wavelength response curve obtained in the post-flight calibration is shown in Figure 18. The response rolloff towards high frequency leads to increased noise in the calibrated spectra, although not in the raw spectra, which are expressed in volts/cm⁻¹. All five detectors have very similar response curves, except that the larger detectors show somewhat more high frequency rolloff as the result of a slight wavefront curvature in the interferometer.

8.2.2 Absolute Responsivities

Absolute responsivities have been assigned to each detector based on Method 1 below. An alternative method, Method 2, yields a different set of responsivities and is also described.

Because most of the calibration data were obtained at flux levels much higher than were observed in the atmospheric measurements, and because the data have scatter as well as potential systematic error, judgement is required to derive responsivities applicable to the flight data. The two methods are as follows:

8.2.2.1 Method 1

First, the responses of the five detectors relative to each other were determined by comparing the 15 μ m CO₂ signals from different detectors viewing the same tangent height. The relative responses turn out to be in the ratios 15: 2.0: 1.0: 0.029: 0.007 for detector Nos. 1 through 5, respectively. Essentially the same ratios were found using other nearby wavelengths, including the 9.6 μ m ozone band and filter No. 1 (window region) data. This is

⁹ Dybwad, P., and Huppl, R.J.(1987) SPIRIT 1 postflight calibration report, Rep. SRL-87-2 Utah State University/Stewart Radiance Lab., Bedford, MA, and Dybwad, J.P., Huppl, R.J., McKenna, R.E., Saletnik, D.P., Thomas, B.J., and Griffiths, V. (1987) Report on a rocket-borne, telescopied Fourier transform spectrometer operating at 10° K, Proc. SPIE Int. Soc. Opt. Eng., 787, 114.

consistent with calibration data indicating that all of the detectors have similar relative response curves.

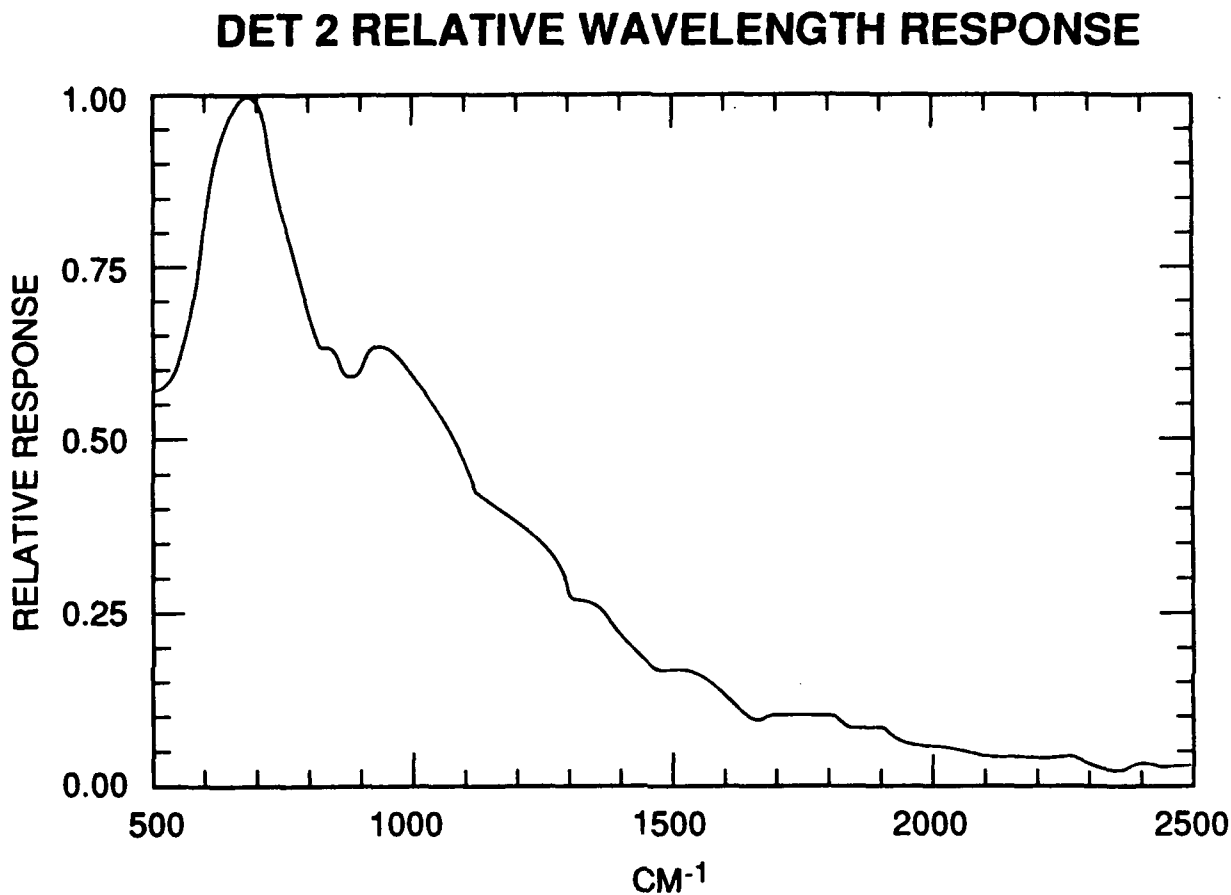


Figure 18. Relative Wavelength Response Curve for Detector No. 2

Next, an absolute responsivity of 2.7×10^6 was chosen for detector No. 3 (all responsivities will be reported in units of $V W^{-1} cm^2 sr$ at $685 cm^{-1}$). This value provided the best overall agreement to the post-flight calibration data. Scaling the above relative responses with this absolute value leads to responsivities of 4.0×10^7 for detector No. 1, 5.3×10^6 for detector No. 2, 7.8×10^4 for detector No. 4, and 1.9×10^4 for detector No. 5, as listed in Table 6. These values are nearly identical to ones determined⁹ entirely from the post-flight calibration data, which are available for detector Nos. 2, 3, and 4 only (2.8×10^6 for detector No. 3, 7.6×10^4 for detector No. 4, and 5.0×10^6 for detector No. 2 at around 5 V mean DC output voltage). The latter values have been adopted in the preliminary data reduction. As mentioned earlier, these

calibration data were obtained using flux levels that are typically much higher than were observed in the atmospheric measurements.

Table 6. SPIRIT 1 Detector Responsivities
($V W^{-1} cm^2 sr$ at $685 cm^{-1}$)

<u>Detector No.</u>	<u>Method 1</u>	<u>Method 2</u>
1	4.0×10^7	2.4×10^7
2	5.3×10^6	$3.2 \times 10^6, V \leq 0.27$ $1.05 \times 10^6 \ln(80V), V > 0.27$
3	2.7×10^6	1.6×10^6
4	7.8×10^4	4.6×10^4
5	1.9×10^4	1.1×10^4

Figure 19 shows the altitude profile of the CO_2 $15 \mu m$ band radiance using the derived responsivities. All of the detectors yield essentially the same profile with the exception of detector No. 2, which gives increased radiance below ~ 105 km; the difference is approximately a factor of 2 in the 90-100 km range. This behavior is consistent with dielectric relaxation of the detector, a non-linear effect that increases its responsivity at high flux levels. This effect is shown in greater detail in Figure 20, which plots the ratio of apparent $15 \mu m$ radiances derived from detector Nos. 2 and 4, which viewed essentially the same tangent height. The mean (DC) voltage output from detector No. 2, which is plotted along the x axis, is a measure of the flux. The solid line is from a fit to post-flight calibration data, as discussed in Subsection 8.2.2.2.

The similarity of the CO_2 $15 \mu m$ profiles from the other detectors suggests, but does not prove, that they are all behaving linearly (that is, have constant responsivity) over their operating ranges. In Subsections 8.2.2.2 and 8.2.3 further evidence is presented that supports linearity in detector Nos. 3 and 4, and, by implication, in detector Nos. 1 and 5 as well. We therefore feel fairly confident that the shapes of the profiles of CO_2 and other emitters derived from detectors other than detector No. 2 are accurate.

8.2.2.2 Method 2

In this alternative method, detector No. 2 is corrected for dielectric relaxation using low-flux data, and this corrected responsivity serves as a reference for determining the responsivities of the other detectors. This approach is based on the observation that the full set of detector No. 2 calibration data shows a flux dependence similar to that seen in the atmospheric data. This is illustrated in Figure 21, which plots the measured responsivity at 685 cm^{-1} as a function of the detector's DC voltage output. (The data shown were derived from the cold-collimator scans at a number of wavelengths, with or without filters, which were normalized to 685 cm^{-1} by correcting for wavelength response and filter transmission). The oblique line between 0.27 and 10 V is an approximate fit to the data, and is given by

$$\text{Det 2 Responsivity} = 1.05 \times 10^6 \ln(80V). \quad (8)$$

where V is the DC voltage.

Next, we assume that detector No. 4 has constant responsivity, then Eq. (8) should be proportional to the (Det 2)/(Det 4) radiance ratios in Figure 20, which are derived from flight data. Normalizing Eq. (8) to a ratio of 2.0 at 6 VDC yields

$$(\text{Det 2})/(\text{Det 4}) \text{ ratio} = 0.33 \ln(80V). \quad (9)$$

Eq. (9) has been plotted in Figure 20 as the oblique line, and is seen to fit the flight data quite well over this flux range.

It is unphysical to extrapolate Eqs. (8) and (9) to lower fluxes, since Eq. (9) does not give the correct asymptotic ratio of unity. Put another way, the responsivity of detector No. 2 cannot decline indefinitely with decreasing flux, but instead must level off to a constant value. The simplest solution is to redefine the detector No. 2 responsivity as a constant below 0.27 V, the flux level at which Eq. (9) equals 1.0. The constant responsivity value turns out to be 3.2×10^6 , shown as the vertical line segment in Figure 21.

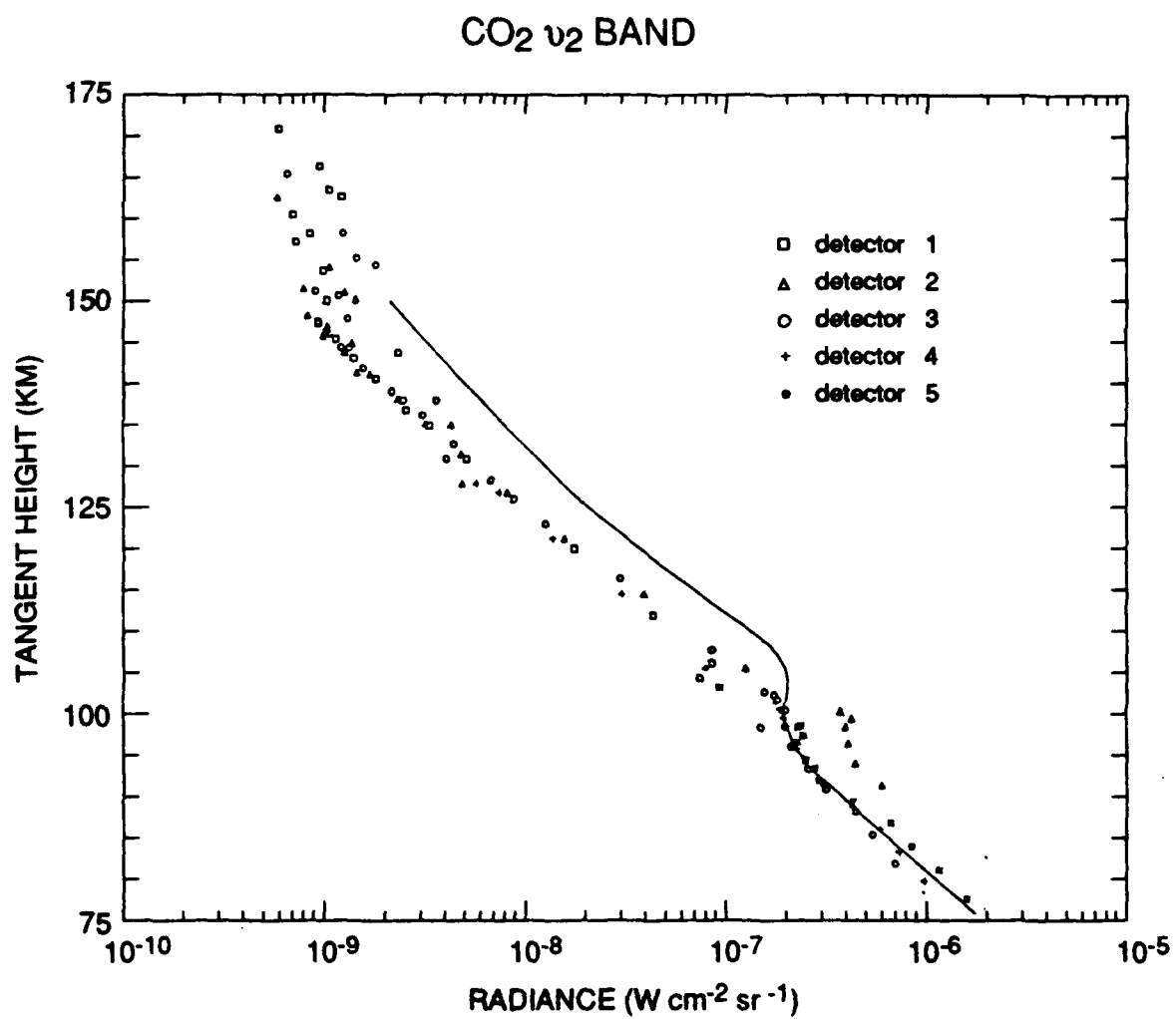


Figure 19. CO₂ ν_2 Limb Radiance Profile, and Average of SPIRE Data

DET 2/ DET 4 RADIANCE RATIO

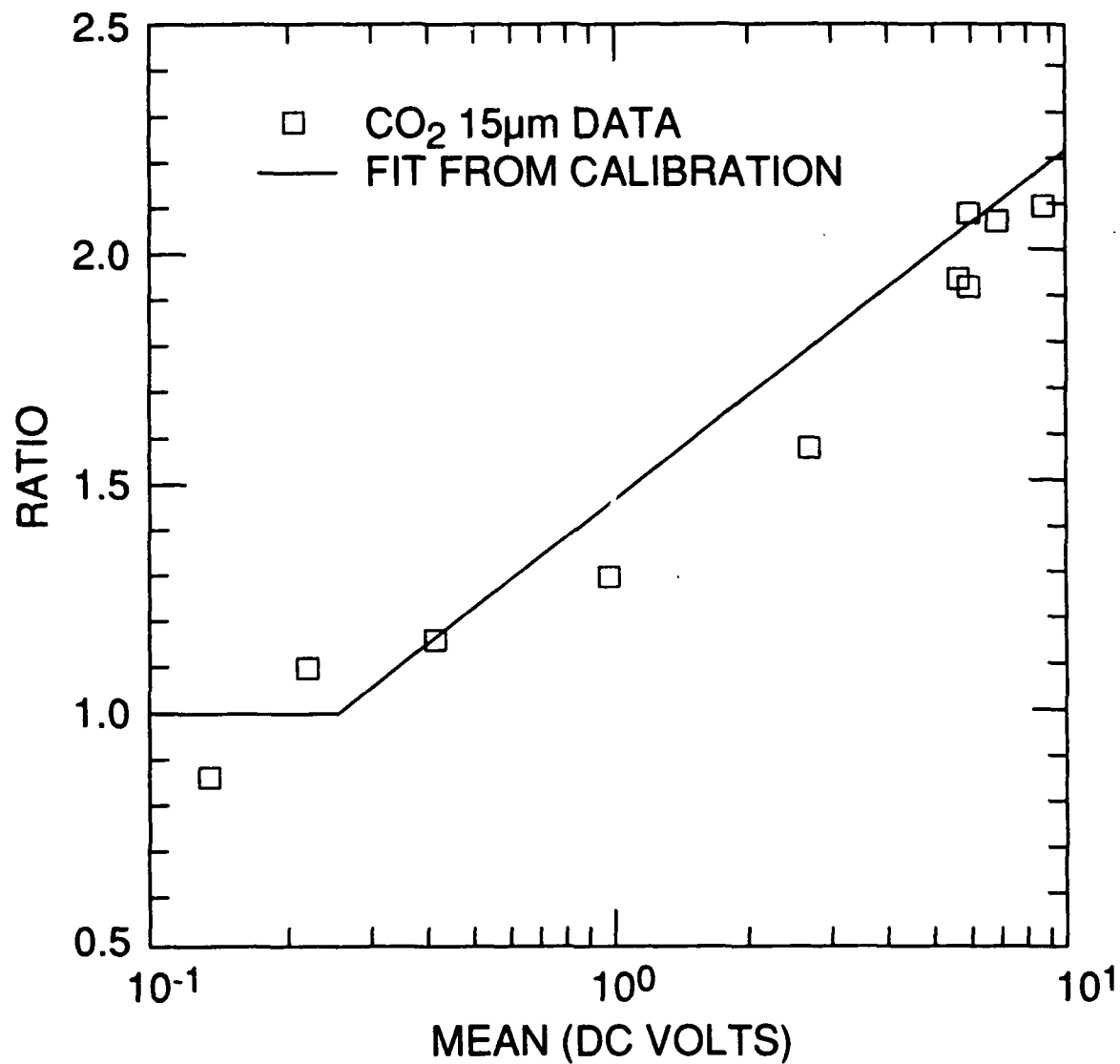


Figure 20. The Ratio of Detector No. 2 to Detector No. 4 Observed CO_2 (ν_2) Radiances at $15 \mu\text{m}$ as a Function of the Mean Voltage (Flux) Level for Detector No. 2

The new detector No. 2 responsivity function given by Eq. (8) above 0.27 V and 3.2×10^6 below 0.27 V leads to virtually identical altitude profile shapes in all 5 detectors. However, the responsivities given in Subsection 8.2.2.1 for the other detectors lead to a factor of 1.7 difference in absolute radiance between detector No. 2 and the others. To make the radiance consistent among all five detectors, the Subsection 8.2.2.1 responsivities for detector Nos. 1, 3, 4 and 5 would need to be divided by 1.7. This results in the responsivities given in the second column of Table 6.

In conclusion, Method 2 has not completely eliminated inconsistencies, but instead has replaced one inconsistency (the anomalous detector No. 2 profile shape) with another (an inconsistency between the calibration and the flight data on the relative responses of the detectors). The latter inconsistency may be more palatable because, except for detector No. 2, the calibration was done at high fluxes.

8.2.3 Open-Filter Calibration Summary

To summarize the two calibration choices, Method 1 accepts the detector Nos. 3 and 4 responsivities derived from the post-flight calibration, and regards the anomalously high atmospheric radiance levels seen in detector No. 2 below ~105 km as erroneous. In this case, the CO₂ radiance profile is correctly depicted in Figure 19 for detector Nos. 1, 3, 4 and 5. The alternative, Method 2, uses the detector No. 2 responsivity given by Eq. (8) above 0.27 V, which fits the laboratory and flight data over a wide flux range, and divides the Method 1 responsivities for the other detectors by 1.7. Using Method 2 results in derived atmospheric radiance levels which are a factor of 1.7 higher than with Method 1.

At the present time we cannot recommend one method over the other, although we note in the next section that the higher radiances resulting from Method 2 are in closer agreement with SPIRE data. In this report we have employed Method 1, understanding that it may underestimate the true radiances.

DET 2 RESPONSIVITY AT 685 CM⁻¹

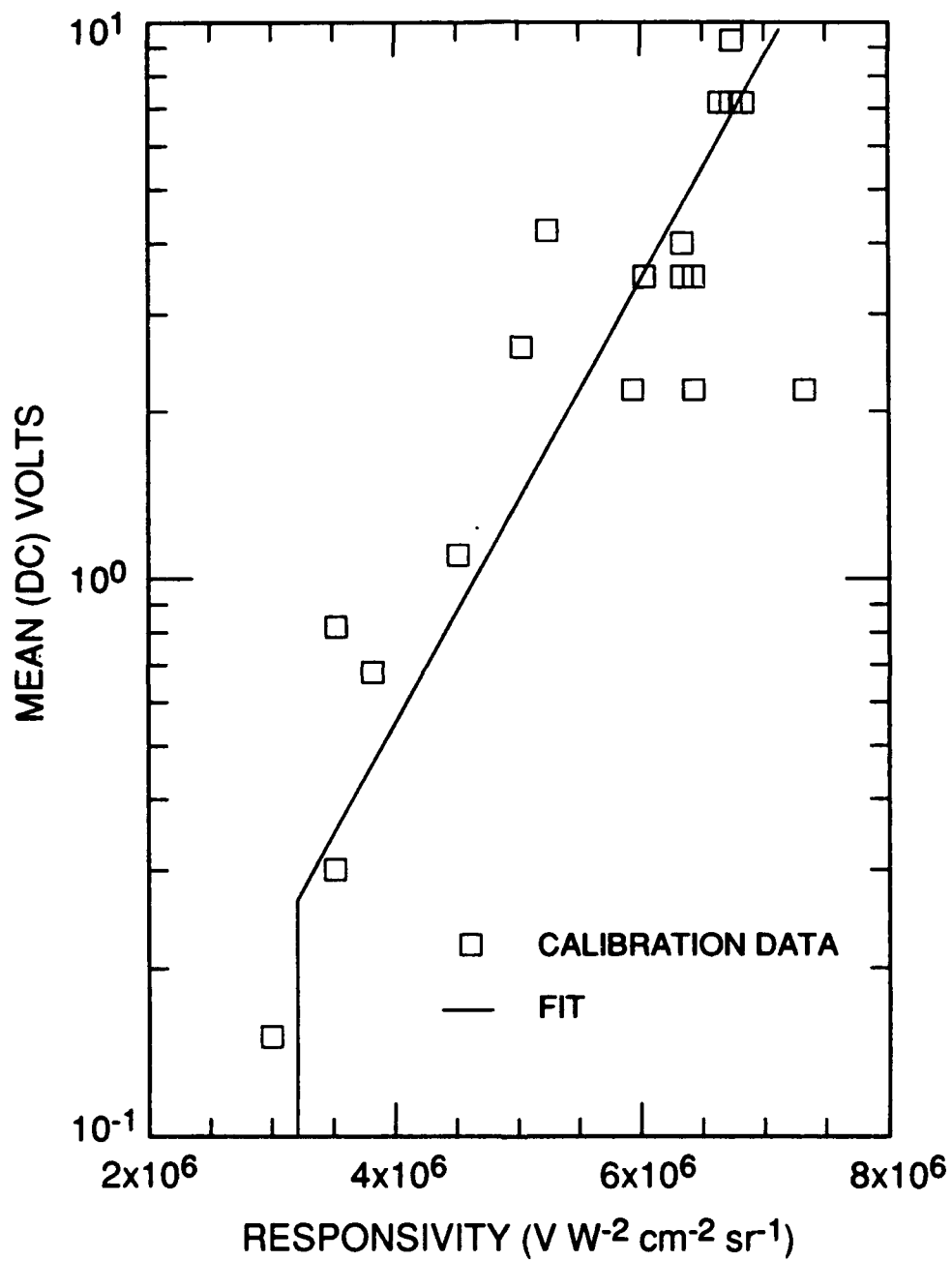


Figure 21. Detector No. 2 Responsivity at 685 cm⁻¹ vs the Mean Voltage (Flux) Level

The factor of ~2 uncertainty in the absolute calibration is important to bear in mind when comparing SPIRIT 1 data with other observations. However, we believe that there is considerably less uncertainty in the relative altitude profiles, that is, their shapes and the relative intensity relationships among different species.

8.3 Responsivities With The Bandpass Filters

In this report we have assumed constant transmission factors of 0.75 for both bandpass filters, which are consistent with the post-flight calibration and are close to the average in-band transmissions from curves supplied by the manufacturer (Dydwad, 1988). The use of a constant transmission factor is adequate for computing the integrated band radiances in the window (10.8 - 12.0 μm) and NO (5.0 - 5.7 μm) regions that these filters cover, since the transmission curves are reasonably flat. However, for highly accurate band shapes the exact transmission curves will be included in future data analyses.

8.4 Calibration Summary

The factor of ~2 calibration uncertainty arises from inconsistencies between the laboratory post-flight calibration and the flight data. These inconsistencies could be due to systematic error, or they could be related to the differences in conditions of the laboratory and flight measurements. These include differences in the intensity and spectral distribution of the radiation sources, which may affect the detectors in ways that have not been completely characterized.

9. DATA ANALYSIS SUMMARY

9.1 Introduction

Two sources of radiation are observed in the SPIRIT 1 data. The first is due to the atmospheric limb, and includes the well-known $\text{CO}_2 \nu_2$ (15 μm), $\text{O}_3 \nu_3$ (9.6 μm), and NO fundamental (5.3 μm) bands. As anticipated, the atmospheric limb emission correlates well with previous observations (such as SPIRE).^{10,11} The second source of radiation is out-of-field-

¹⁰ Nadile, R.M., Stair, A.T., Jr., Wheeler, N.B., Frodsham, D.G., Wyatt, C.L., Baker, D.J., Grieder, W.F. (1978) SPIRE-spectral infrared rocket experiment (preliminary results), AFGL-TR-78-0107, Air Force Geophysics Laboratory, ADA058504.

¹¹ Stair, A.T., Jr., Sharma, R.D., Nadile, R.M., Baker, D.J., and Grieder, W.F. (1985) Observations of limb radiance with a cryogenic spectral infrared rocket experiment, *J. Geophys. Res.*, **90**:9763.

of-view energy (also referred to as "contamination" or "anomalous" or "scattered" background radiation). The spectrum of this background at times resembled earthshine, but more often it had a different shape, resembling the absorption spectrum of siloxane (silicone) compounds. The atmospheric limb radiation and the anomalous background radiation are discussed in detail in Sections 9.2 and 9.3, respectively.

A brief listing of the usable scans is provided in Table 7. The usable open filter data consist essentially of the upleg scans 78-149 (many of which are heavily contaminated with background), plus low-altitude, downleg scans 219-232. The filter No. 1 (window region) data consist of a number of heavily contaminated scans from the middle of the flight, plus uncontaminated scans between 70 and 80 km near the end of the flight. The filter No. 2 (NO band) data consist of only five scans, but good NO data are also available with the open filter.

In generating the atmospheric limb profiles shown in the following section, all scans were visually inspected, and only those which were largely free of background contamination or noise were included. Subsequently, several scans that appeared to have unreliable tangent height assignment were dropped; they had occurred during rapid tangent height changes.

9.2 Atmospheric Limb Radiation

9.2.1 Viewing Geometry

Through most of the flight, the sensor altitude was sufficiently above the tangent height that virtually the full limb was viewed for all emitters. The main exceptions are around scans 86-90 on the upleg and after scan 238 on the downleg, when the view was between full limb and half limb. Fortunately, in these cases the observed radiation (CO₂ and NO on the upleg, ozone hot bands on the downleg) is optically thin, so geometric factors that normalize the radiance to a full limb view are easily generated. We note that SPIRE, to which the SPIRIT 1 data are compared below, had a full limb view at all times.

9.2.2 CO₂ 15 μm

The 15 μm CO₂ (ν_2) altitude profile is shown in Figure 19. Agreement with SPIRE daytime and terminator data (solid line) is within approximately a factor of 2 at all altitudes. Viewing geometry corrections are not included, but they would affect only a small portion of the data (around 130-150 km), leading to slightly higher radiances. The data below ~105 km are mainly from the end of the flight, when the strong auroral arc was viewed. Better agreement with SPIRE above ~105 km (but worse below this altitude) would be obtained if the Method 2 responsivities (leading to 1.7 times more radiation) were adopted.

Table 7. Summary of SPIRIT 1 Spectral Scans

<u>Description</u>	<u>Time after launch (sec)</u>	<u>Scan Nos.</u>	<u>Comments</u>
Pre-launch calibration	-11.7 - -1.5	1-9	Blackbody source
In-flight calibration (NO filter)	57.0-68.4	48-57	Blackbody source
Open filter data	95.0-268.7	78-149	Tangent hts to 235 km
Window filter data	271.5-318.6	151-163	Background contaminated
NO filter data	322.5-343.5	166-170	NO 5.3 μ m band
Open filter data	344.4-348.3 364.1-366.7 407.2-424.2	171-174 186-188 219-232	Background contaminated Rapid tangent ht variation Tangent hts below 107 km
Window filter data	426.9-446.3	234-249	Ozone hot bands
In-flight calibration (thin film heater)	456.9	257	Blackbody source; alignment test

Above ~150 km, background radiation and noise contribute noticeably to the data. However, the peak radiance at 670 cm^{-1} is less sensitive to these uncertainties than is the integrated band radiance and could be used to extend the CO_2 profile to altitudes as high as ~200 km.

The single SPIRE nighttime scan, Spatial Scan 8, is somewhat higher than the daytime and terminator data. This is contrary to predictions of atmospheric models and also leads to poorer agreement with SPIRIT 1. The possibility of an instrumental or data reduction artifact

affecting SPIRE Scan 8 should be considered. For a more detailed analysis of the SPIRE 1 CO₂ (v₂) data see Appendix F.¹²

9.2.3 Ozone 9.6 μm

The ozone 9.6 μm (v₃) altitude profile is shown in Figure 22 for selected data in the 80-140 km region that show minimal background contamination. Above ~105 km the radiation in this bandpass is all or nearly all due to contamination effects. At lower altitudes the data agree very well with SPIRE nighttime and terminator data (solid line) in terms of both shape and absolute radiance level.¹³ Since the profile is extremely sensitive to altitude above ~90 km, the good agreement confirms the consistency etc. between SPIRE 1 and SPIRE absolute radiances. A more extensive discussion of ozone (v₃) emission observed by SPIRE 1 can be found in Appendix E.¹⁴

9.2.4 Ozone Hot Bands (10.8-12.5 μm)

This wavelength range covers the "window" region in which ozone hot bands emit. The altitude profile is shown Figure 23 for all scans of good quality that do not require a viewing geometry correction.

These data combine open filter scans from detector 3 above 80 km with filter No. 1 scans from detector Nos. 1, 2 and 3 at and below 80 km. (Unfortunately, between 80 and 95 km, detector No. 3 was virtually the only one yielding useful data in this bandpass: detector No. 1 was saturated, detector No. 2 was mostly saturated, and detector Nos. 4 and 5 had poor signal-to-noise.) In the open filter scans, detector No. 3 was exposed to intense flux from CO₂ that was blocked by filter No. 1. The observation that the low-(filter No. 1) and high-flux (open filter) data from detector No. 3 join smoothly at 80 km supports the argument that, except for detector No. 2, the detectors are operating reasonably linearly.

Data from SPIRE in this bandpass unfortunately are not correctly represented in the compendium tables. From inspection of the raw scans we find that the SPIRE radiance has an altitude profile very similar to that shown in Figure 23, but its absolute intensity is some 3 times larger (2 times larger using the Method 2 responsivities).

The source of radiation in this "window" region is chemiluminescence from ozone hot bands produced via $\text{O} + \text{O}_2 + (\text{N}_2, \text{O}_2)$ recombination and partially quenched by N₂ and O₂. Since O₂ and N₂ should show very little variability, and the influence of temperature variability on the recombination and quenching rates should be small, we conclude that the

¹² Adler-Golden, S.M., Smith, D.R., and Matthew, M.W. (1991) Atmospheric infrared radiance from CO₂ and NO observed during the SPIRE 1 rocket experiment, *J. Geophys. Res.*, **96**:11319.

¹³ Green, B.D., Rawlins, W.T., and Nadile, R.M. (1986) Diurnal variability of vibrationally excited mesospheric ozone as observed during the SPIRE mission, *J. Geophys. Res.*, **91**:311.

¹⁴ Adler-Golden, S.M., Matthew, M.W., Smith, D.R., and Ratkowski, A.J. (1990) 9-12 μm atmospheric ozone emission observed in the SPIRE 1 experiment, *J. Geophys. Res.*, **95**:15243.

lower radiance in SPIRIT 1 may reflect lower atomic oxygen concentration in this altitude range (70-90 km). Unfortunately we can only speculate on this possibility.

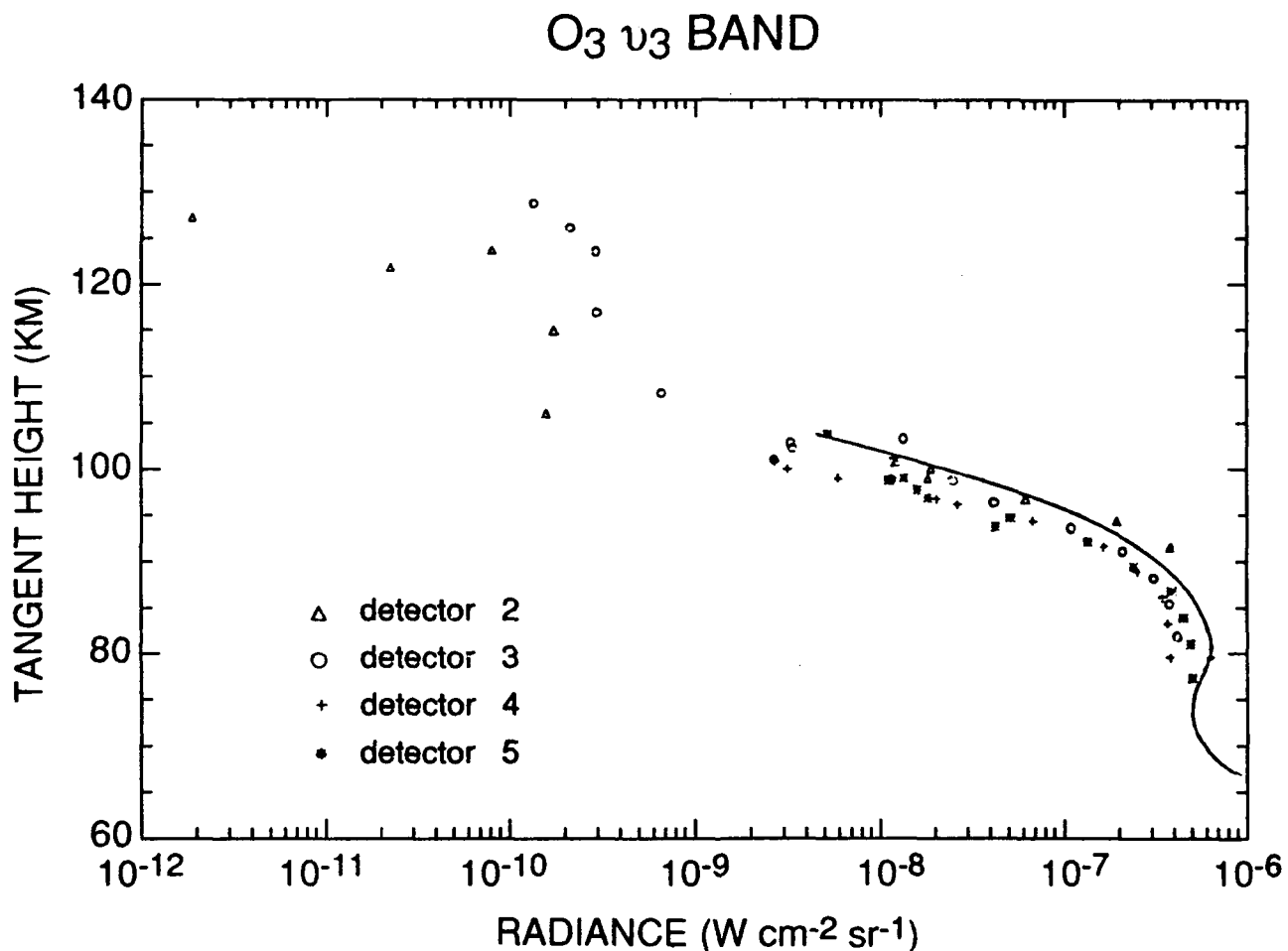


Figure 22. Ozone 9.6 μ m Altitude Profile from SPIRIT 1 (Points) and Average Profile from SPIRE Nighttime and Terminator Scans (Solid Line)

SPIRIT 10.8-12 μ OZONE

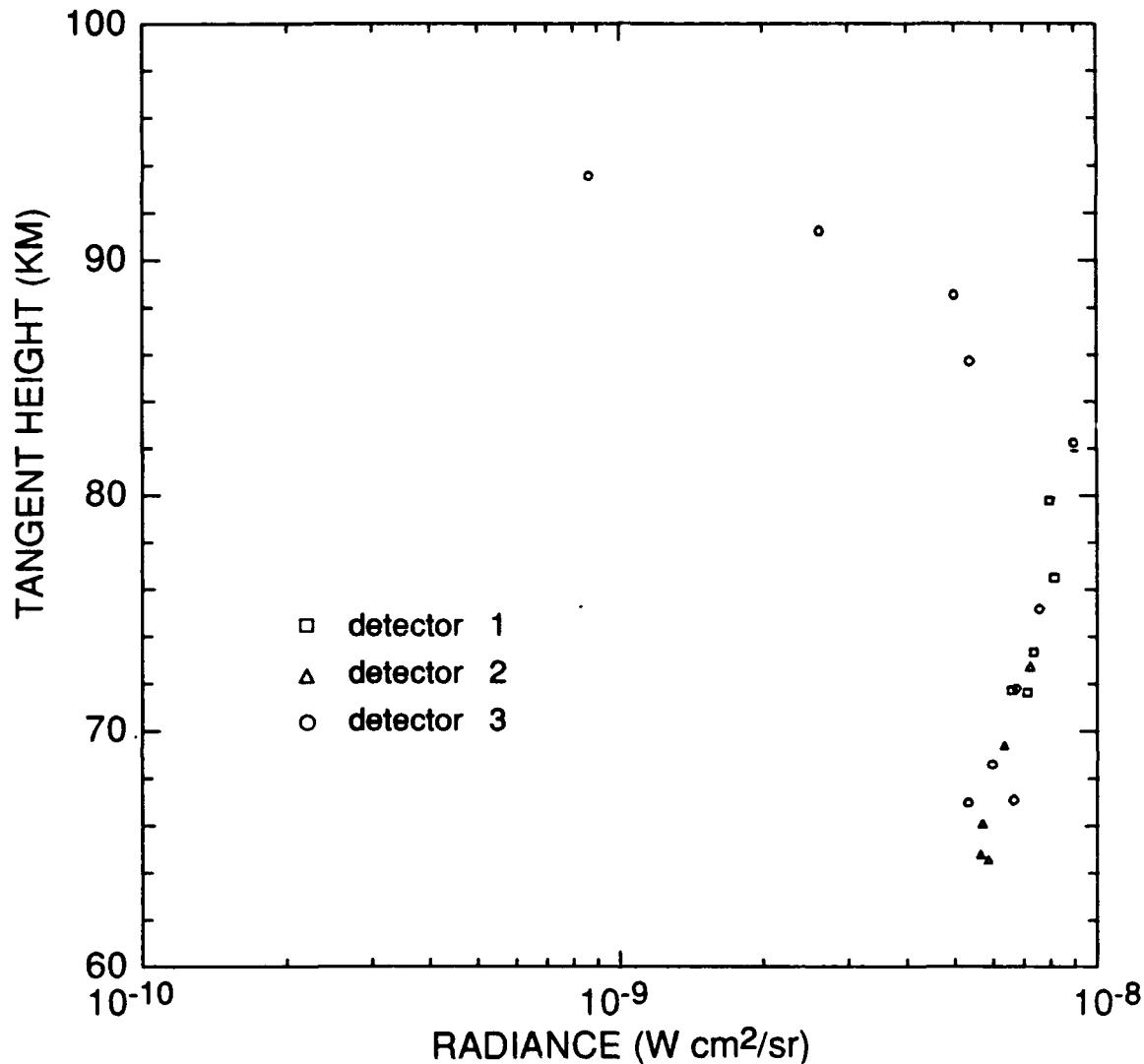


Figure 23. Altitude Profile of Ozone Hot Bands Below 95 km

In contrast to the bulk of the SPIRIT 1 data, the ozone hot-band data were acquired at the end of the flight when the instrument was finally pointed at the bright auroral arc. The decrease in intensity compared with SPIRE might be a bona fide auroral effect, but one should not draw this conclusion without carefully considering other possible causes.

The SPIRIT 1 data on ozone hot bands in the 70-90 km range represent a vast improvement over SPIRE in terms of spectral resolution. As shown in Figure 24, structure due to partially resolved bands is visible. Even better resolution has been obtained by processing the interferograms with a triangular and rectangular apodization windows instead of the Kaiser-

Bessel window. A detailed analysis of the SPIRIT 1 data in the ozone hot band region (10.4-12.2 μm) is presented in Appendix G.¹⁵

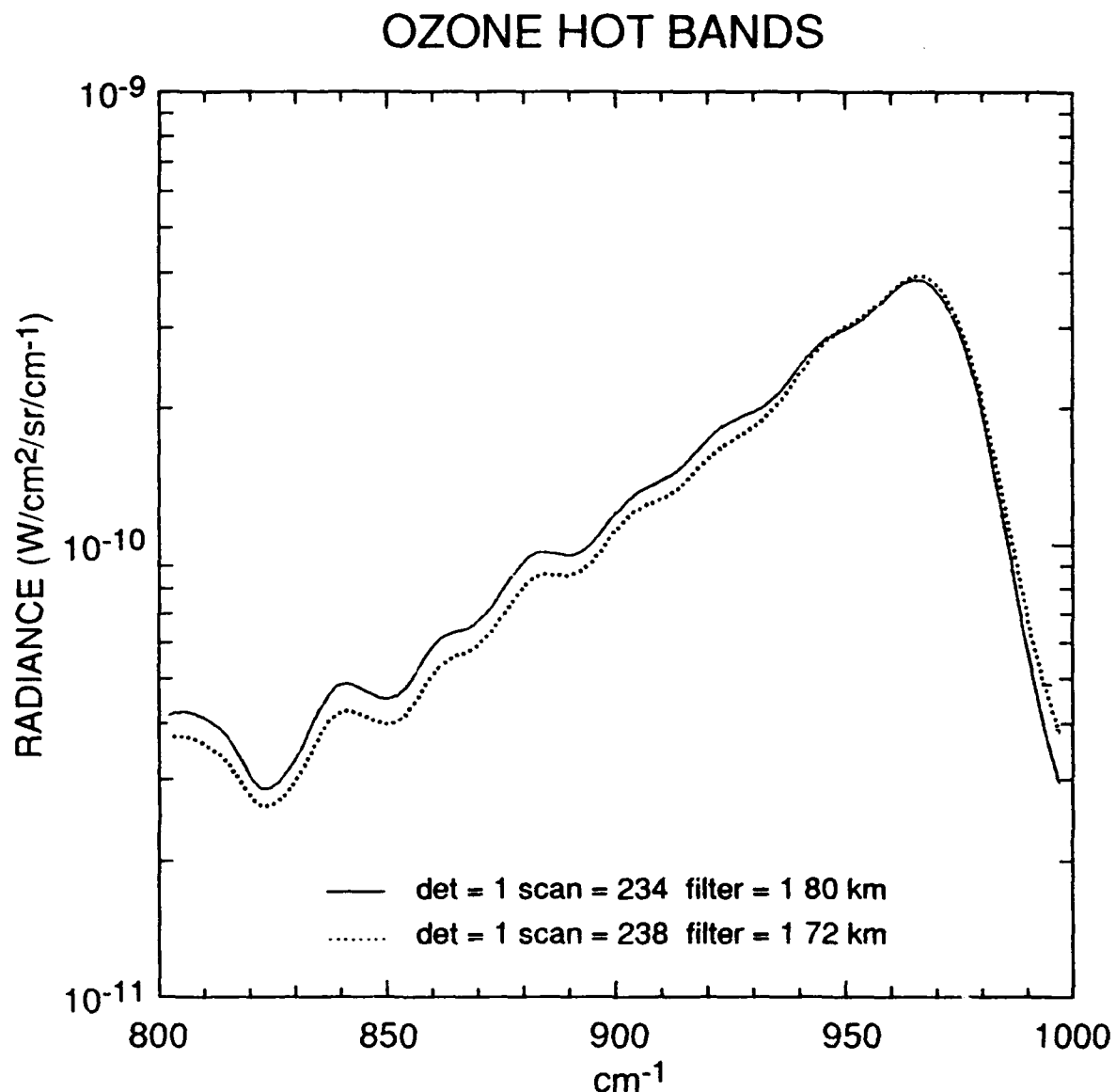


Figure 24. Ozone Hot Band Spectra from Filter No. 1 Scans.
Note filter cutoff above $\sim 970 \text{ cm}^{-1}$

¹⁵ Adler-Golden, S.M., and Smith, D.R. (1990) Identification of 4- to 7-quantum v_3 bands in the atmospheric recombination spectrum of ozone. *Planet. Space Sci.* **38**:1121.

9.2.5 Nitric Oxide (5.3 μm)

The nitric oxide (NO) altitude profile is shown in Figure 25. The data have much more scatter than the CO₂ or ozone data. Part of this scatter reflects consistent differences between the detectors, indicating that the relative calibrations of the detectors in this wavelength range are not quite correct. Detector noise may be another source of scatter. However, even after taking into account scatter and absolute calibration uncertainty, it is clear that there is significantly less NO emission (by around a factor of 3 to 7) than was measured during the SPIRE flight, for which the average results above 125 km are approximated by the solid line in Figure 25.

Recently, UV measurements of NO levels in the low-latitude thermosphere have been reported from the Solar Mesosphere Explorer satellite.¹⁶ A factor of ~7 decline in NO was found from January 1982 to April 1985, which they ascribed to the decline in solar activity over that period. If a similar effect occurs at high latitudes as well, this could explain the difference between the SPIRE (Oct. 1977) and SPIRIT 1 (Apr. 1986) NO data.

9.3 Anomalous Background Radiation

9.3.1 General Characteristics

As mentioned previously, the spectra of the anomalous backgrounds exhibit, at different times, two distinctly different appearances. In the brightest of these spectra, the interferograms are found to have large-amplitude, low-frequency fluctuations, as though the sensor viewed objects moving across or through the field of view. An example is shown in Figure 26. As is illustrated by this example, these fluctuations are usually nearly identical in all detectors. The spectra of these scans exhibit the characteristics of "pure" earthshine such as Scan 112, detector 2, shown in Figure 27, but occur in only a relatively few scans. A LOWTRAN calculation¹⁷ of upwelling emission from the earth agrees extremely well with this scan. Since the sensor was pointed at a tangent height of 154 km at the time, and the radiation is quite bright (10^{-4} as bright as the earth), it cannot be due to an ordinary off-axis-rejection problem, but suggests the presence of a substantial quantity of reflective, spectrally flat material in the field of view.

¹⁶ Barth, C.A., Tobiska, W.K., Siskind, D.E., and Cleary, D.D. (1988) Solar-terrestrial coupling: Low-latitude thermospheric nitric oxide, *Geophys. Res. Lett.*, **15**:92.

¹⁷ Knetzys, F.X., Shettle, E.P., Gallery, W.O., Chetwynd, J.H., Jr., Abreu, L.W., Selby, J.E.A., Clough, S.A., Fenn, R.W. (1983) Atmospheric transmittance/radiance: computer code LOWTRAN 6, AFGL-TR-83-0187, Hanscom AFB, MA, ADA137786.

NO 5.3 μ BAND

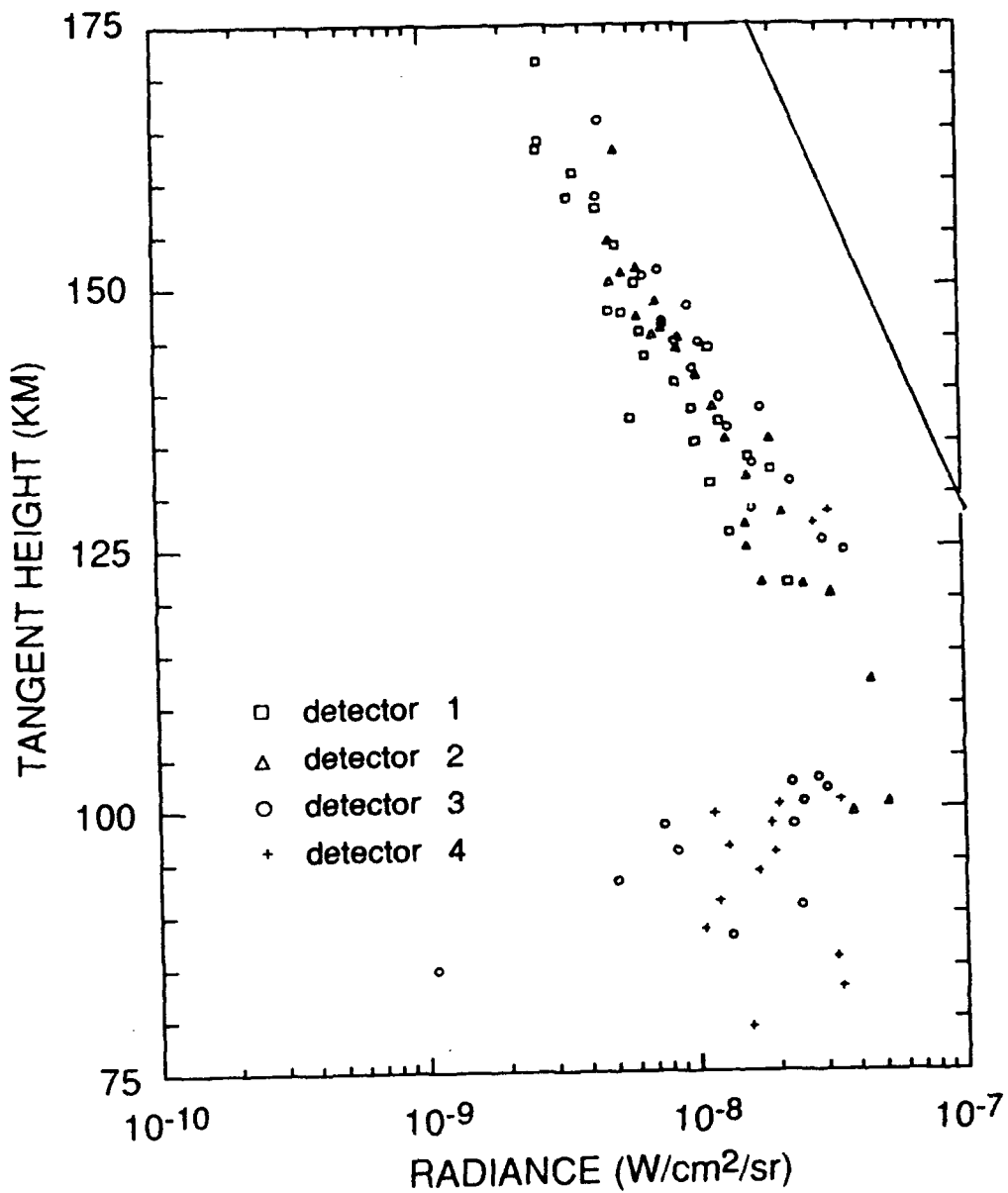


Figure 25. NO Fundamental Altitude Profile from SPIRIT 1 (Points) and Average Profile from SPIRE (Solid Line)

A lower-level anomalous background is seen continuously throughout the flight, and is shown in the lower curve in Figure 28. Comparison with Figure 27 shows that this spectrum is very different from an earthshine spectrum. Note, in particular, the strong peak near 900 cm^{-1} and the strong feature at 1265 cm^{-1} which appears to be an absorption band. To produce this

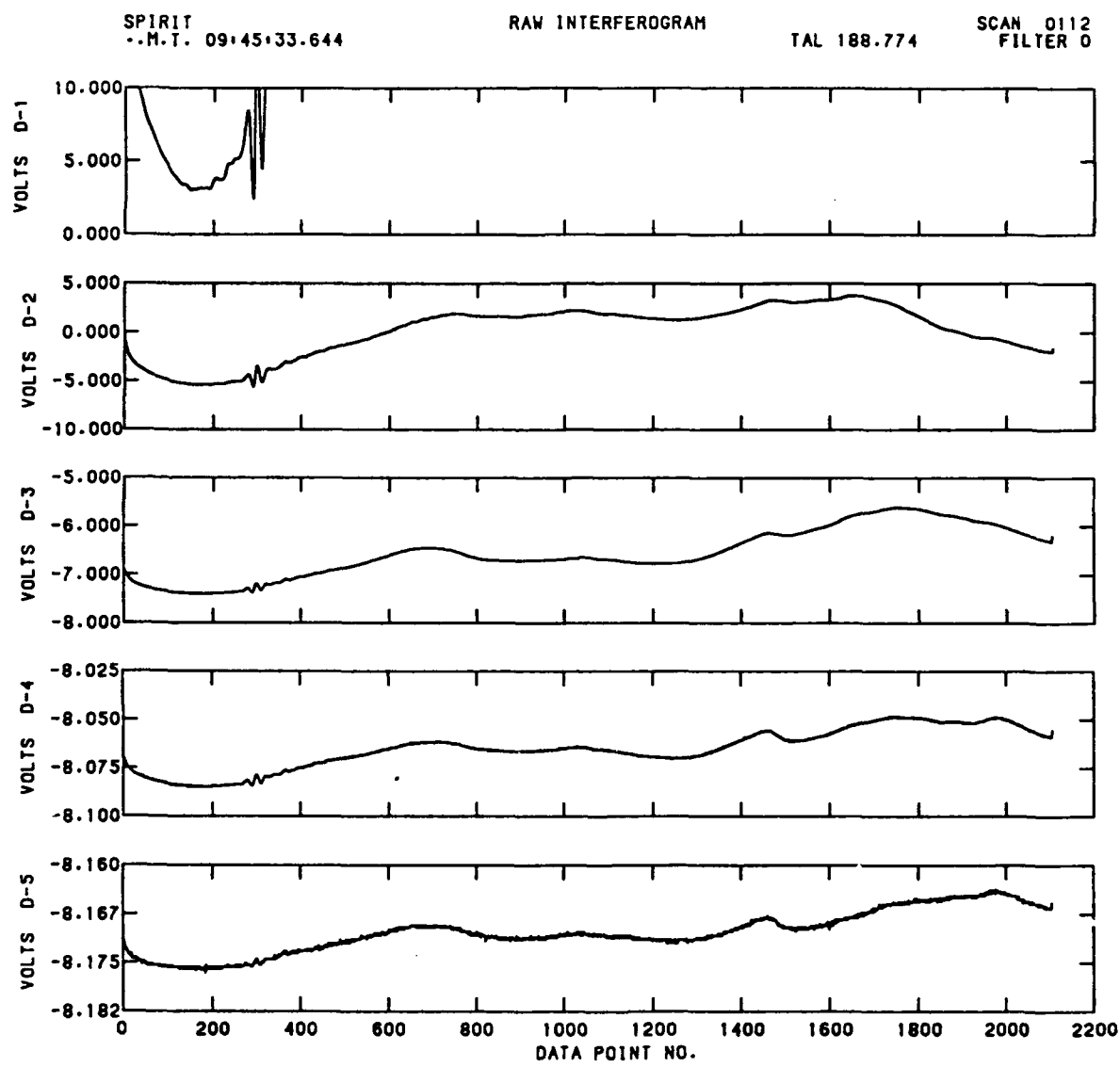


Figure 26. Raw Interferograms for all Five (5) SPIRIT 1 Detectors for Scan 112

EARTHSHINE SPECTRUM

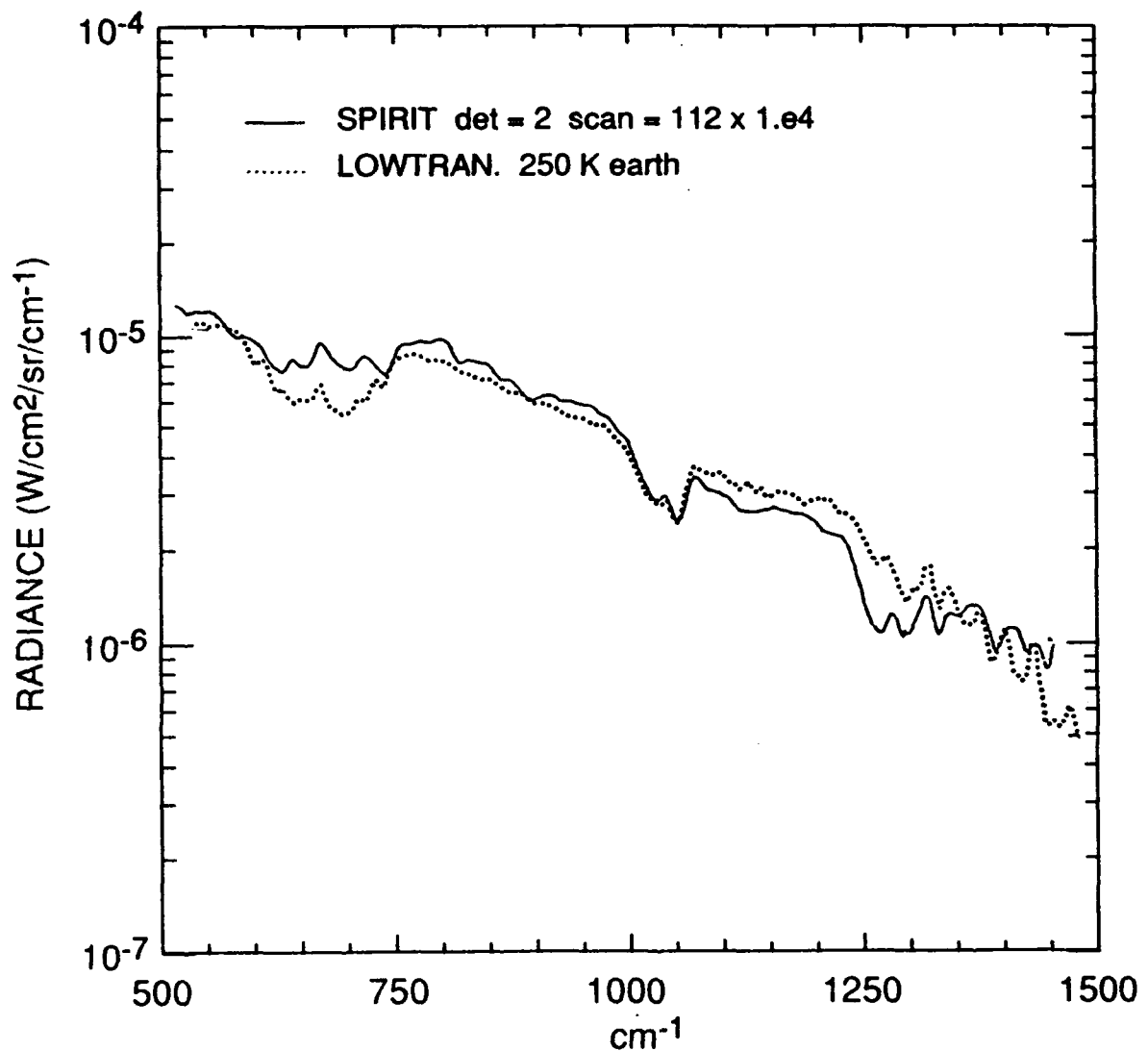


Figure 27. The Spectrum of the Earthshine-like Anomalous Background (Scan 112×10^4) Compared to a LOWTRAN Calculation of Upwelling Radiation for a 135° Zenith Angle Case

SPIRIT ANOMALOUS BACKGROUND

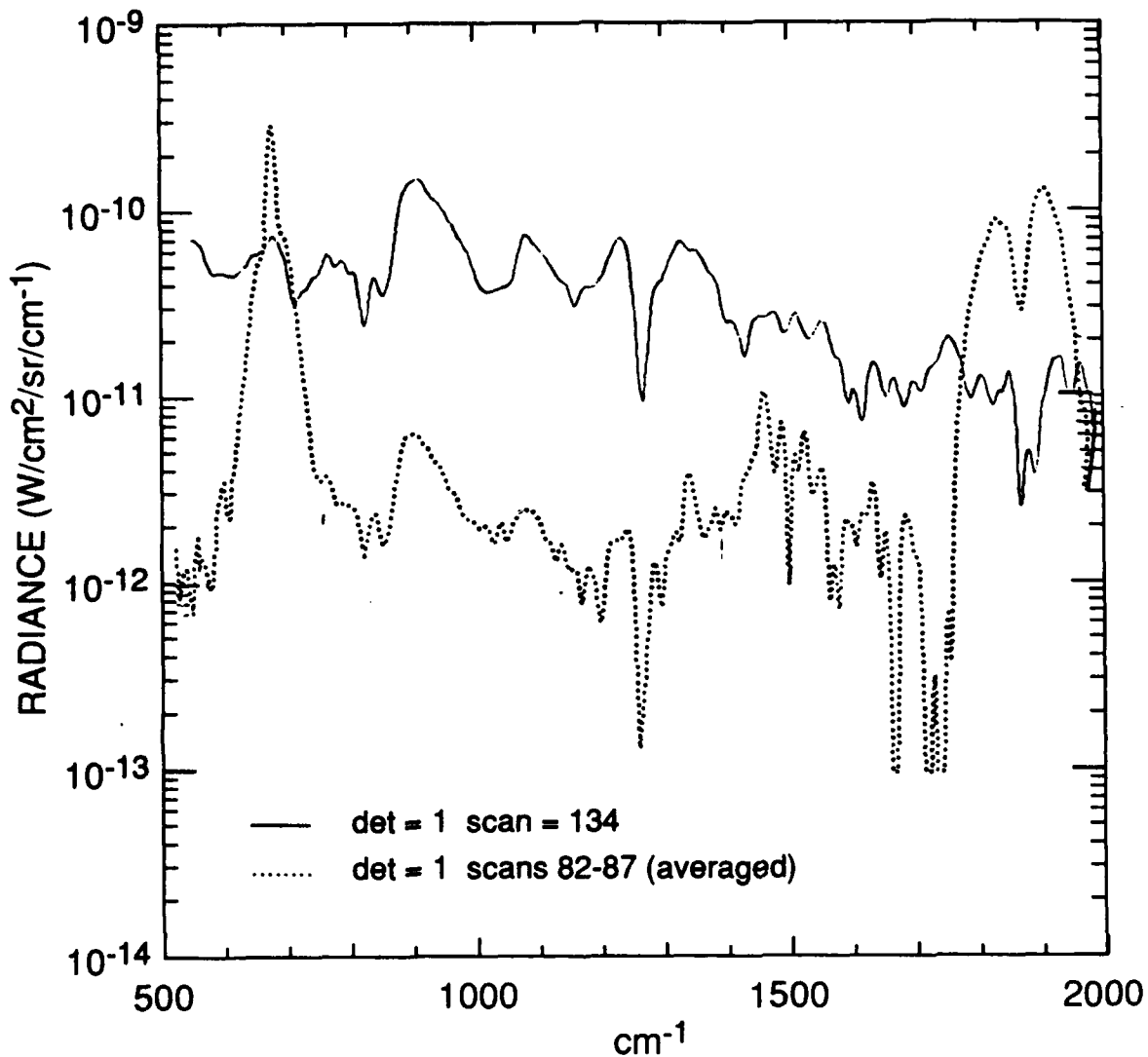


Figure 28. Spectra of the Anomalous (Leakage) Background at two Different Background Levels

curve, several consecutive detector No. 1 scans covering tangent heights of 121-141 km were co-added to improve the signal-to-noise ratio in the window regions in which the anomalous background can be seen. Atmospheric emission features from CO_2 , NO , and H_2O (ν_2) are superimposed on top of the anomalous background.

This background radiance is most evident in the data from detector No. 1 in which it appears approximately three times brighter than in the data from any other detector. It is also only observable in scans with tangent heights above ~100 km, where radiation from ozone and other species is no longer dominant. As mentioned above, this background is observed to have a different intensity in each detector with the level decreasing in the following order: detector No. 1 > detector No. 3 > detector No. 2. In general, this background is too weak to be seen in detector Nos. 4 and 5, which are the two smallest and least sensitive detectors.

Several times during the flight this background became brighter by an order of magnitude or more as can be seen from Figure 29 in which the intensity of the most prominent feature of this background (at 900 cm^{-1}) is plotted as a function of time after launch (TAL). The characteristic spectrum of this brighter background is shown in the upper curve in Figure 28 and again by the three curves in Figure 30. The times at which these bright spectra suddenly appeared are generally coincident with abrupt changes in payload attitude, when a maximum frequency of ACS thruster firings occurred. This is illustrated in Figure 31 which shows the occurrence of the brightest anomalous scans relative to the payload motion (as reflected by the sensor tangent height).

The first cluster of strong scans occurs at approximately 125 sec, near a tangent height minimum after the first down-scan ACS maneuver. The next cluster of strong scans starts at the beginning of the second down-scan maneuver, and the third occurs at the minimum between the second down-scan and the next up-scan maneuver. We note that since these data represent the upleg portion of the flight, a plot of intensity versus payload altitude displays essentially the same clustering features (see Figure 32).

The clustering of the strong background scans and their apparent correlation with payload maneuvers suggests a dependence on the frequency of ACS thruster firings. When the 900 cm^{-1} anomalous signal is plotted versus tangent height, as is shown for detector No. 1 in Figure 33, an often-observed profile emerges for the weaker anomalous data, in contrast to the brighter scans, which appear to be essentially independent of tangent height. The predominant characteristic of this weaker background is a nearly flat tangent height profile above 100 km that exhibits a slight decrease in radiance with increasing tangent height. This result is in excellent agreement with several other rocketborne LWIR earthlimb measurements.¹⁸ In this earlier report it was shown that those profiles can be modelled as off-axis leakage radiance from the earth and the lower atmosphere due to insufficient off-axis rejection (OAR) performance of the sensor's telescope system.

¹⁸ Smith, D.R. (August 17-19, 1988) Evidence for off-axis leakage radiance in high-altitude IR rocketborne measurements, *Stray Light and Contamination in Optical Systems, Proc. of the SPIE Conference, San Diego, CA*, 30:967.

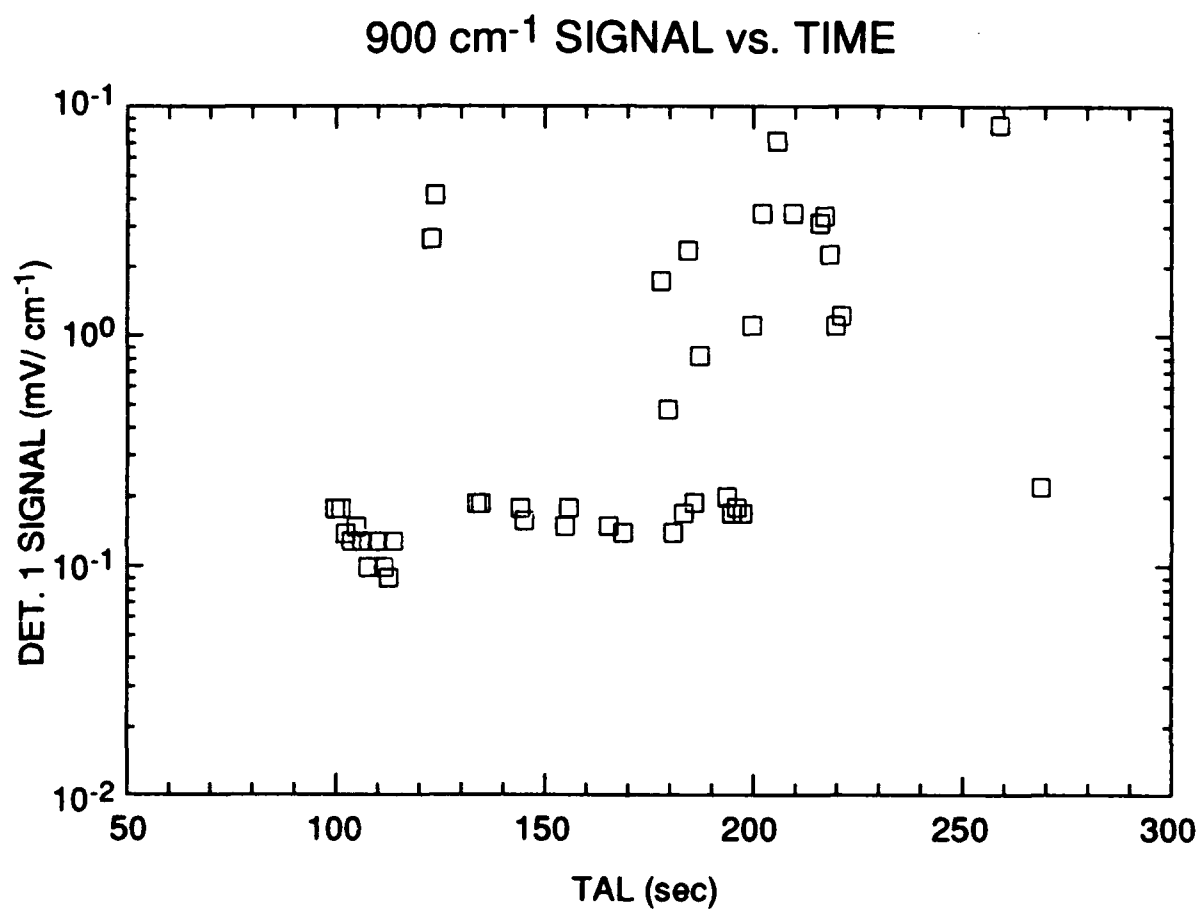


Figure 29. Intensity of the 900 cm⁻¹ Peak Feature of the Anomalous Background Versus Time After Launch as Measured by Detector No. 1

SPIRIT ANOMALOUS BACKGROUND

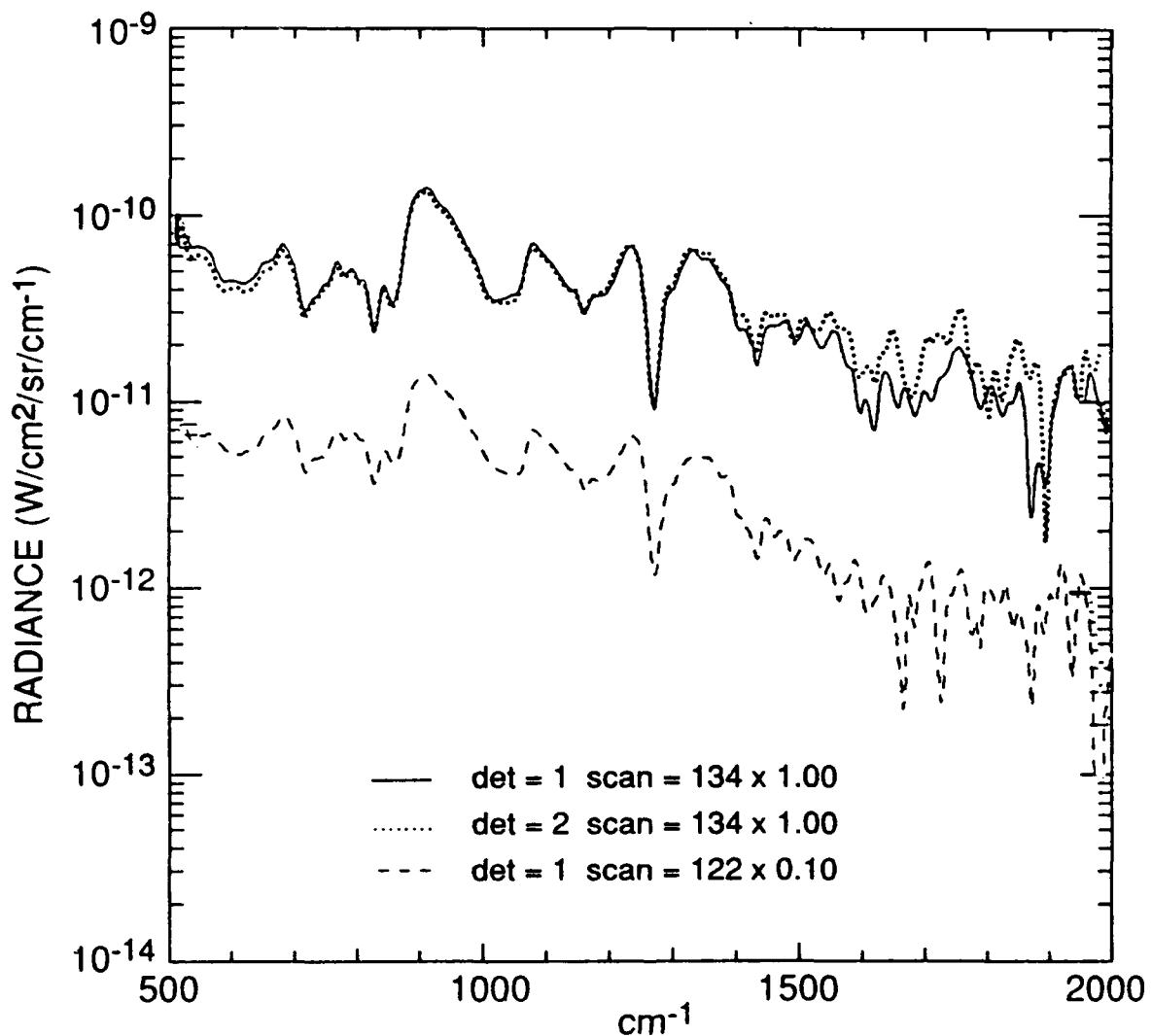


Figure 30. The SPIRIT Anomalous Background for Different Detectors and Scans

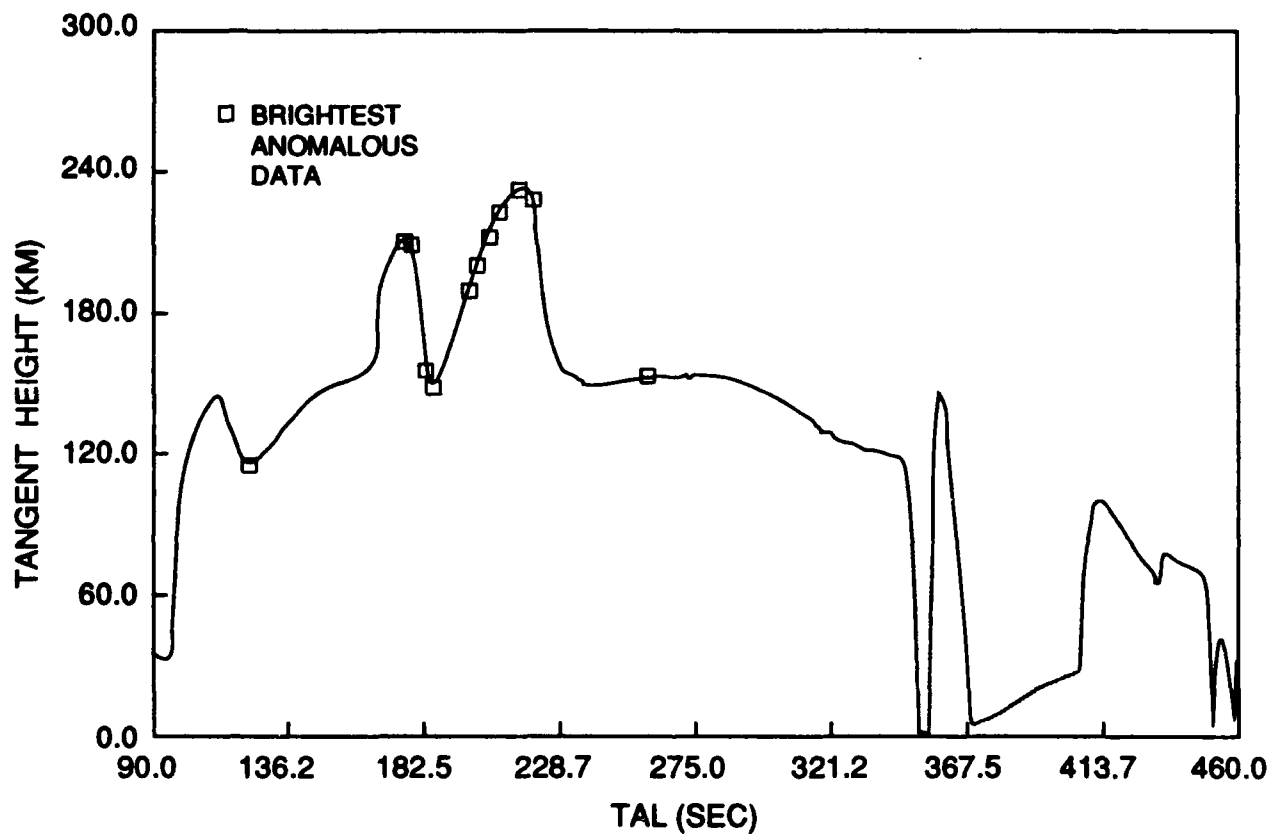
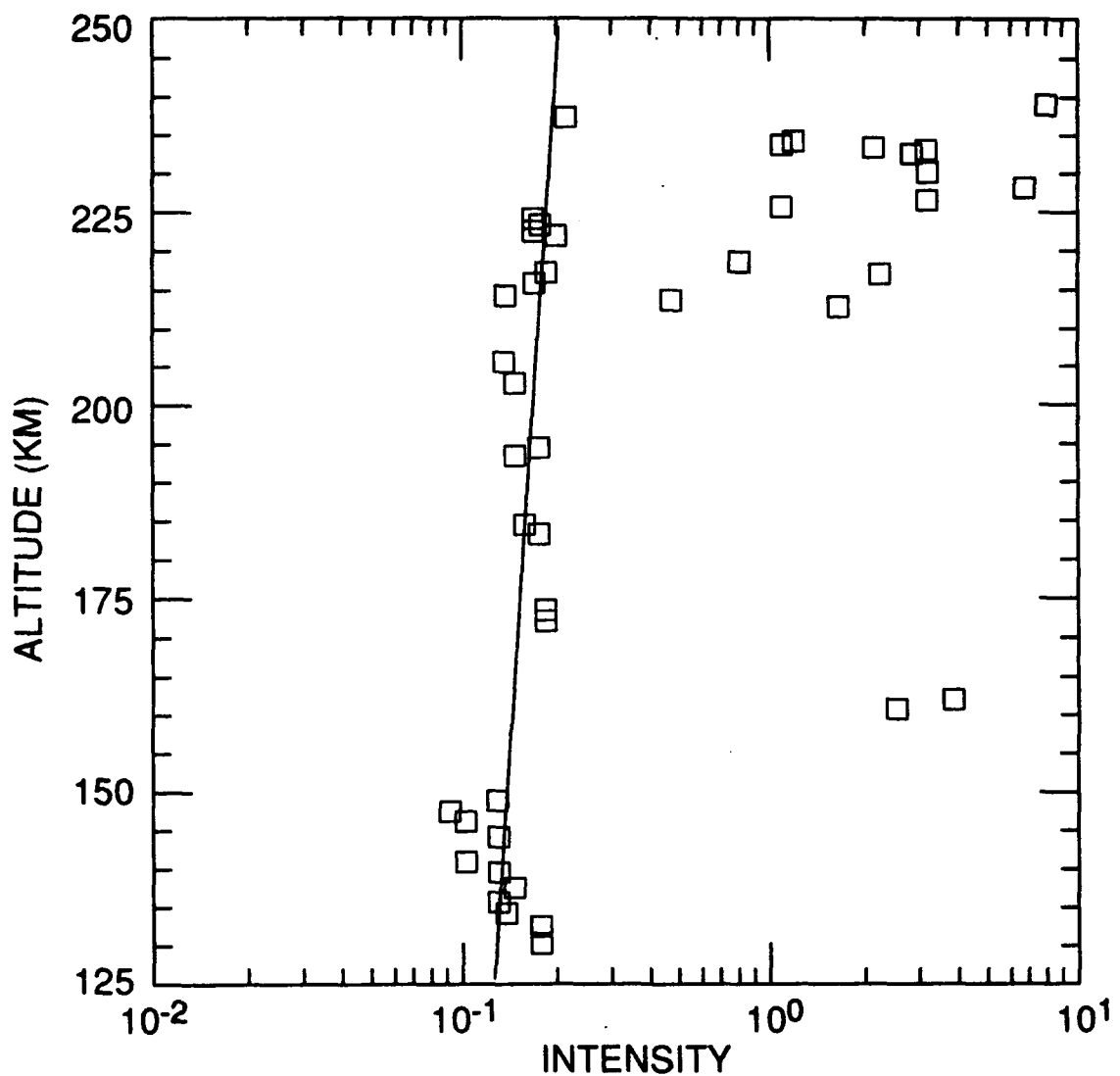


Figure 31. Occurrence of the 12 Brightest Anomalous Scans Compared to the Sensor Tangent Height

900 CM⁻¹ INTENSITY vs PAYLOAD ALTITUDE



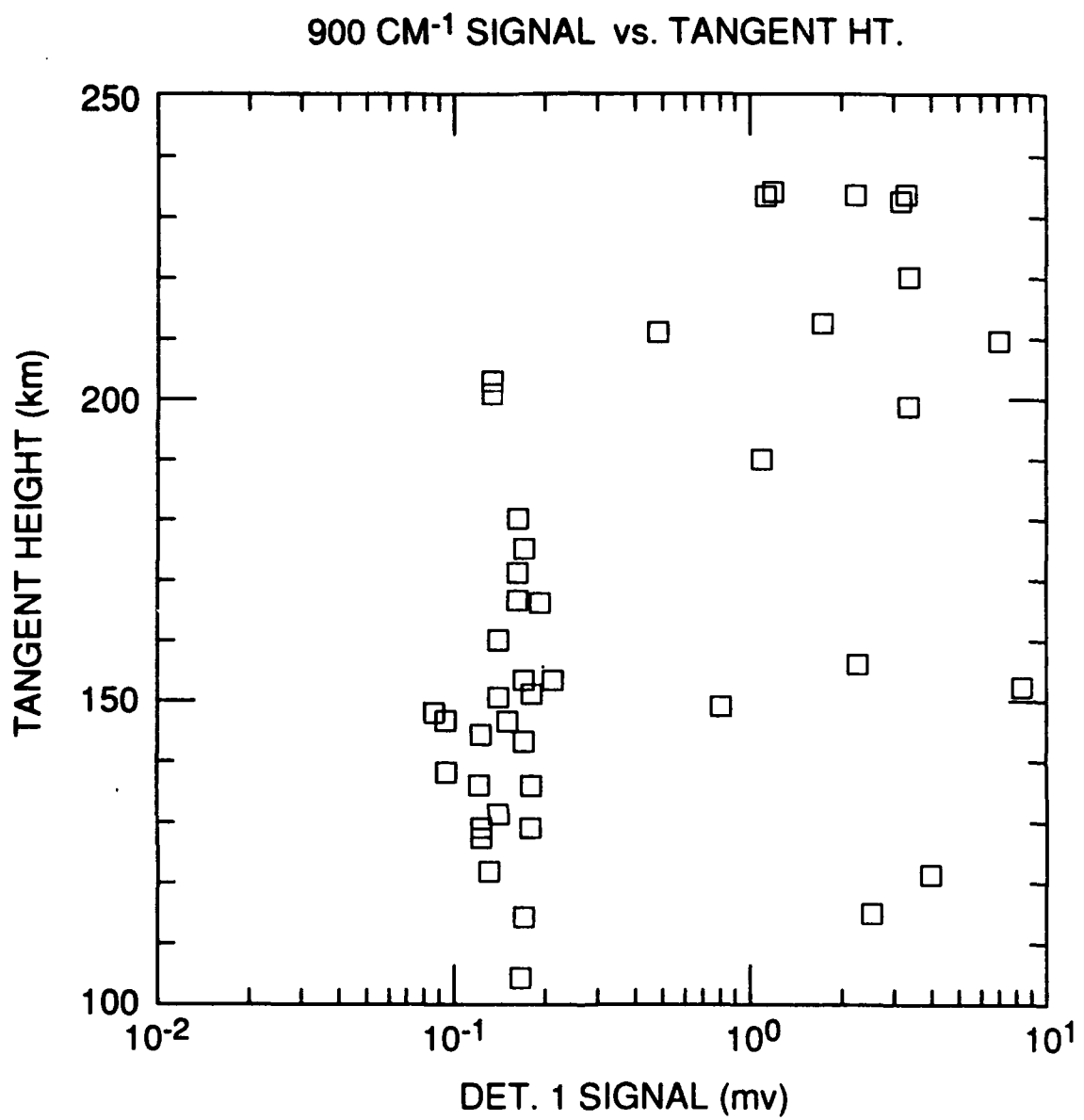


Figure 33. Intensity of the 900 cm⁻¹ Spectral Feature vs Sensor Tangent Height

It has been stated previously that the brighter anomalous background is observed equally by all detectors while the weaker (baseline) background is observed preferentially in detector No. 1 and to a lesser degree in detector Nos. 3 and 2, in that order. This effect is illustrated in Figure 34 in which the signal at 900 cm^{-1} observed by detector No. 1 is plotted against the signal at 900 cm^{-1} observed by detector No. 2. The brighter scans exhibit a 7:1 ratio of detector output voltages, whereas the weaker ones give a 25:1 ratio. Since the ratio of the detector responsivities is 7:1, this indicates that the brighter (baseline) background is seen equally by both detectors. Data from the other detectors indicates that the entire focal plane is illuminated uniformly when the sensor is viewing this brighter anomalous background.

The measured ratios of the baseline anomalous background at 900 cm^{-1} for detector Nos. 1 and 3 relative to detector No. 2 are shown in Table 8. The ratios of the off-axis angle measured from the center of the focal plane (optical axis) to the edge and corner of these same detectors are also shown for comparison. This data suggests a possible correlation of this background with the angular displacement of a particular detector from the optical center of the focal plane.

Table 8. SPIRIT 1 Telescope Leakage Ratio vs Detector Location

	DET No. 1	DET No. 3	DET No. 2
MEASURED LEAKAGE BACKGROUND RATIO DETX/DET2	3.0 - 3.6	2.0 - 2.4	1.0
RATIO OF OFF-AXIS ANGLE @ DETECTOR EDGE	3.3	2.6	1.0
RATIO OF OFF-AXIS ANGLE @ DETECTOR CORNER	3.0	2.0	1.0

9.3.2 Explanation of the SPIRIT 1 Anomalous Data

The anomalous backgrounds observed during the SPIRIT 1 experiment clearly cannot be explained by a single effect or mechanism. However, it is clear that the source of the radiation for each of these various backgrounds is identical: upwelling radiation from the earth and the lower atmosphere modified by the transmission of the atmosphere (that is, earthshine). Yet to be determined is the exact mechanism (or combination of mechanisms) by which this radiation reaches the detectors. It is also relatively certain that the brightest anomalous scans (that is, those which exhibit a spectrum characteristic of "pure earthshine") are caused by earthshine scattered from small particles in the sensor's FOV. It seems likely that these

particles are originating from, or are somehow being dislodged by, the operation of the payload attitude control system (based on the evidence of Figure 31).

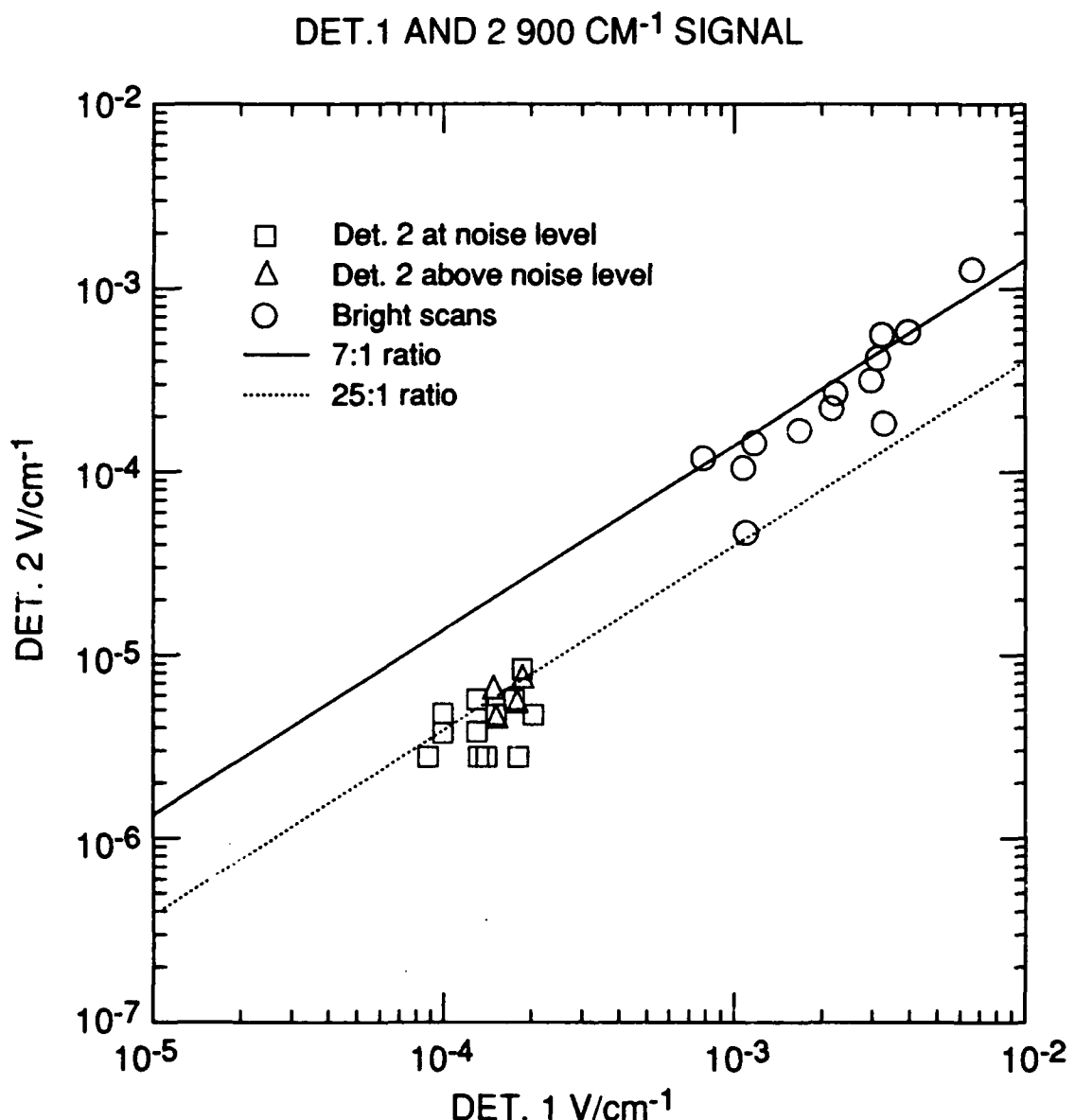


Figure 34. The Detector No. 2 Signal Level Versus the Detector No. 1 Signal Level for the 900 cm⁻¹ Spectral Feature.

Equally as clear is that the (baseline) anomalous background is due to a classic telescope off-axis leakage problem caused by insufficient rejection of out-of-field energy by the sensor's telescope. This background was essentially constant throughout the flight and fits all of the

spatial characteristics associated with this effect. This conclusion follows by plotting only those scans in which the baseline anomalous background is dominant against the angle between the sensor's FOV and the earth's horizon, as is shown in Figure 35. The spectral characteristics of the baseline anomalous background, however, are not immediately identifiable as earthshine radiation, although the spectrum is predominantly that of a blackbody with a temperature of ~280 K. The spectral features in this background appear to be primarily "absorption-type" structure but the bands cannot be ascribed to any known atmospheric species. It seemed possible that this structure was the result of scattering from some contaminant deposited on the optical surfaces of the telescope rather than a pure absorption spectrum. Although it is possible that this scattering (or absorption) was occurring in the near field of the sensor, we think it is far more likely that this "coloring" of the spectrum is due to an internal scattering problem.

Assuming that the source of illumination is earthshine, the "scattering" spectrum associated with the anomalous background may be obtained by taking the ratio of the anomalous spectrum to the earthshine spectrum (as shown in Scan 112, detector No. 2). The result is shown in Figure 36. Note the strong narrow bands at approximately 821, 1265, and 1426 cm^{-1} and slightly weaker and broader features at 575, 705, 1000, and 1157 cm^{-1} . It was first conjectured that these features were associated with one or more contaminant species. This conclusion would not be surprising since evidence of contamination has been seen in many earlier rocketborne experiments.¹⁹ We noted that a number of these programs, including ICECAP,^{20,21} HAVE-SLED, and EBC,²² among others, had observed three strong features at nearly the same spectral locations as the three strongest bands measured by SPIRIT 1. The average measured frequencies and estimated uncertainties were 813 ± 10 , 1250 ± 15 , and $1450 \pm 20\text{ cm}^{-1}$ respectively. However, these strong features had been observed in emission, rather than absorption, and a very strong feature observed at $1083 \pm 8\text{ cm}^{-1}$ was either absent or significantly altered in the SPIRIT 1 data. This series of four bands has been identified as being characteristic of silicone compounds,¹⁹ although the source of this contamination was never located. In the two ICECAP experiments these four anomalous emissions, and other weaker bands, were seen to decrease continuously throughout the flight after an initial increase, apparently consistent with a payload outgassing effect. We speculated that the reduced amount of scattered earthshine associated with the vertical geometry of these other experiments and a higher temperature of the "contaminant" might explain the dominance of

¹⁹ Smith, D.R., and Ratkowski, A.J. (1986) Contamination in rocket-borne IR measurements, *Proc. of the 13th Annual Meeting on Upper-Atmospheric Studies by Optical Methods*, Report 86-28, Univ. of Oslo.

²⁰ Rogers, J.W., Stair, A.T., Jr., Wheeler, N.B., Wyatt, C.L., and Baker, D.J. (1976) AFCRL-TR-76-0274, Environmental Research Paper No. 583, AFGL, Hanscom AFB, MA, ADA038239

²¹ Rogers, J.W., Stair, A.T., Jr., Wheeler, N.B., Wyatt, C.L., and Baker, D.J. (1977) AFCRL-TR-77-0113, Environmental Research Paper No. 597, AFGL, Hanscom AFB, MA, ADA045466.

²² Ulwick, J.C., Baker, K.D., Stair, A.T., Jr., Frings, W., Hennig, R., Grossman, K.U., and Hegblom, E.R. (1985) Rocket-borne measurements of atmospheric infrared fluxes, *J. Atmos. Terr. Phys.*, 47:123.

self-emission in these earlier cases over the scattered upwelling radiation observed in our data.

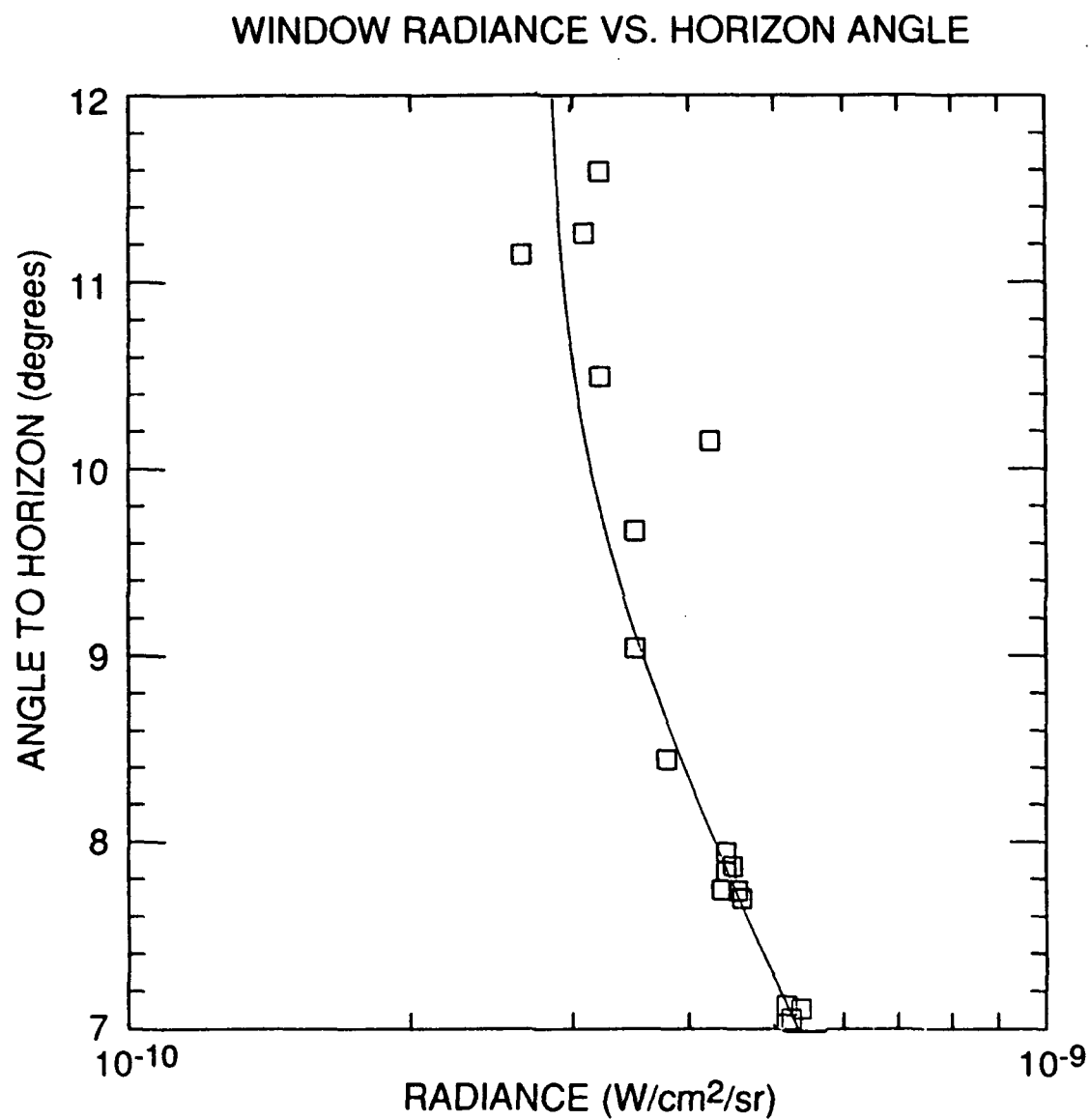


Figure 35. Observed Inband Window Radiance vs Angle to the Earth's Horizon for Detector No. 2. $\Delta\lambda = 10.2\text{-}12.0\text{ }\mu\text{m}$

ANOMALOUS SCATTERING SPECTRUM

1.5x scan 134/scan 112 det 2

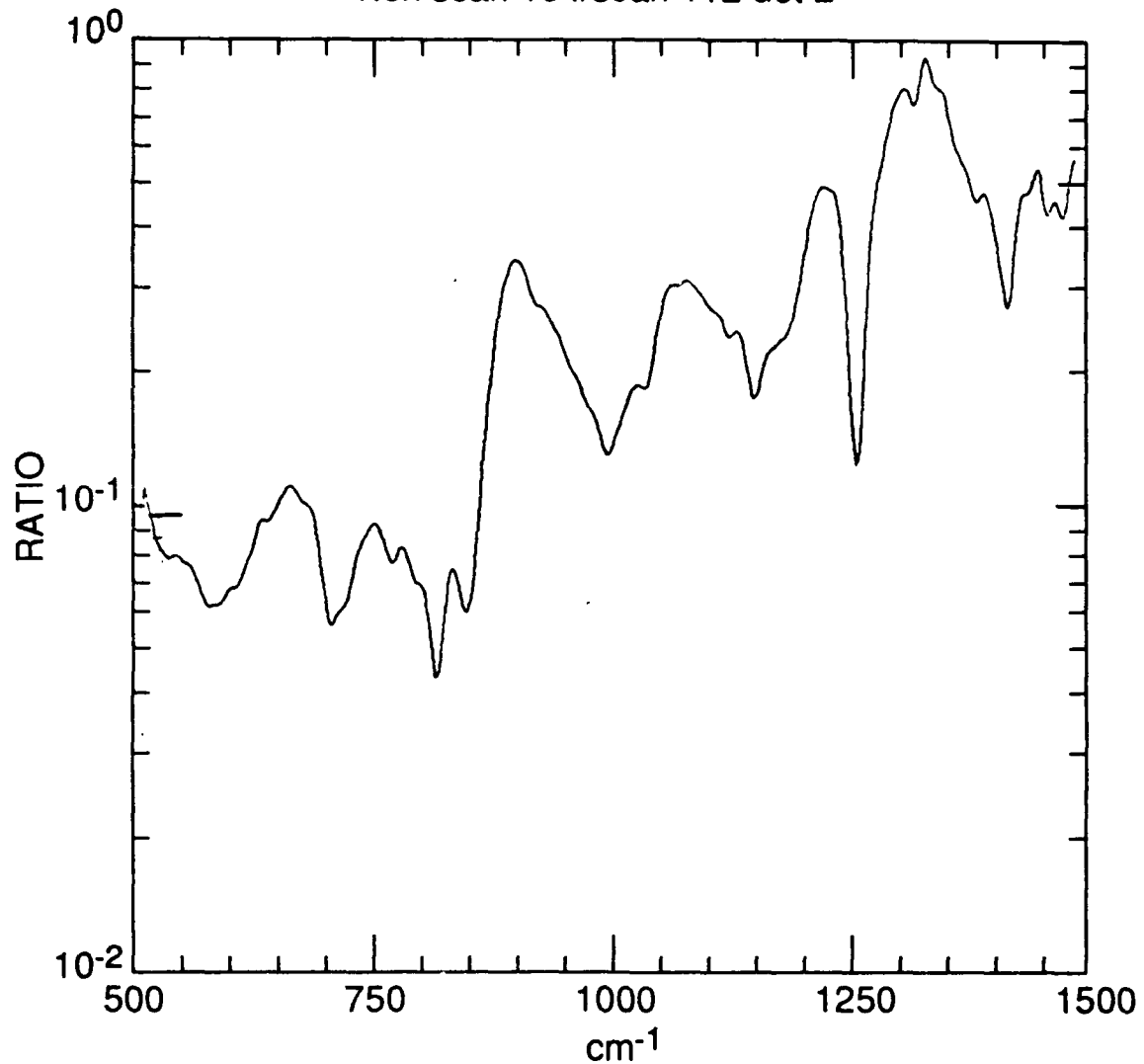


Figure 36. Anomalous Ratio Spectrum Obtained by Dividing the Anomalous Background Spectrum (Scan 134) by the Earth-shine Spectrum (Scan 112)

It was also noted that the two strongest anomalous bands in the SPIRIT 1 flight data also appear as weak absorption features in the SPIRIT 1 post-flight calibration data. (Nearly identical features have also been observed in the pre-flight calibration data of the very similar companion sensor to be employed in the CIRRIS IA experiment; E. Ray Huppi, private communication.) The average measured frequencies of these anomalous calibration features are 816 ± 10 and $1258 \pm 10 \text{ cm}^{-1}$. Another similar calibration feature at 871 cm^{-1} is either missing or shifted to 845 cm^{-1} in the SPIRIT 1 flight data. The presence of these three features

in the SPIRIT 1 calibration data, in conjunction with the fact that the baseline anomalous in-flight background was constant throughout the entire flight strongly suggested that the problem was internal to the SPIRIT 1 sensor. However, it is important to remember here that only off-axis radiation was "colored" by this effect in the case of the in-flight data.

9.3.3 Contamination Discussion

During testing of the CIRRIS IA sensor a visible film was observed on the primary mirror. The mirror was subsequently cleaned with a cleaning solution (a mixture of ethyl alcohol and acetone), and this solution, along with a clean control sample of the same solution, was sent to a testing laboratory for analysis using gas chromatography/mass spectrometry. The analysis indicated the presence of 0.1 percent to 0.5 percent by volume of a contaminating substance, while the control sample showed no contamination. A computerized library search yielded two possible matches for the contaminant:

- 1) 2(methoxyamino) - 3 - methyl butanoic acid and
- 2) tetramethyl silane, $(CH_3)_4Si$.

The infrared absorption spectrum of tetramethyl silane shows strong bands at 696, 869, 1254, and 1430 cm^{-1} , with the two strongest vibration bands from this molecule being those at 869 and 1254 cm^{-1} .²³ These features are in excellent agreement with the anomalous calibration features observed in the calibration data at 871 and 1258 cm^{-1} respectively.

Based on the discussion above, silanes and silicones were determined to be the most likely candidates to explain the anomalous spectra observed in the SPIRIT 1 flight data at the higher tangent heights, and in the SPIRIT 1 and CIRRIS IA calibration data.

9.3.4 Spectroscopic Properties of Silanes and Silicones

Silicones are compounds which have the general formula $(R-SiO-R')_n$ and are more correctly called polysiloxanes. The most commonly used silicones are the polydimethylsiloxanes and the polymethylphenylsiloxanes. The former is the main constituent in silicone rubbers; the latter is often found in resins used as auxiliaries in the paint industry. Silicone greases and sealants are usually polydimethylsiloxanes whereas silicone oils are generally either polydimethyl- or polymethylphenyl siloxane. Silicone vacuum pump oil is a polymethylphenylsiloxane.

The infrared spectra of polysiloxanes and similar silicon compounds have been extensively studied and are well characterized.²⁴ In general, the spectra of silanes and

²³ Simon, J. and McMahon, H.O. (1952) Infrared spectra of some alkyl silanes and siloxanes in gaseous, liquid, and solid phases, *J. Chem. Phys.*, **20**:905.

²⁴ Smith, A.L. (1974) *Analysis of Silicones*, John Wiley and Sons, Inc., New York, p. 247.

siloxanes are relatively simple and the various alkoxy silanes and siloxanes can easily be distinguished from one another. Frequencies which have been suggested as being characteristic of specific groupings linked to silicon are listed in Table 9.²⁵ Normally, vibration bands involving chemical groups with silicon are relatively strong (about five times as strong as those of similar groups with carbon). The strong absorption band near $7.9\text{ }\mu\text{m}$ ($1261 \pm 4\text{ cm}^{-1}$) occurring in all compounds with Si-CH_3 groups is assigned by various authors to either the CH_3 - rocking vibration or the symmetric deformation mode of the methyl groups, with the latter being the more widely accepted assignment. In either case, the specificity of this nearly invariant band in silicones is not in question, and it provides almost certain evidence for the existence of the methyl group. The number of such groups attached to the silicon can then be determined from the positions of the Si-C bands and the methyl rocking modes. Vibrations involving the stretching of the Si-C link occur in the $900\text{-}700\text{ cm}^{-1}$ region, but are considerably influenced by the nature of the substituent groupings. Therefore, to quote from Reference 25, the "... only consistent bands likely to be associated with this linkage are those which arise from invariant groupings such as Si-CH_3 , Si-phenyl , etc.....(while the)... rocking vibrations of these groups may also be expected to give rise to characteristic absorptions at higher frequencies...A band near 800 cm^{-1} can always be expected when two methyl groups are attached to a silicon atom, and its absence can be used to show the absence of this grouping. On the other hand, the presence of this band could also be associated with only a single methyl substitution...In compounds containing the grouping $\text{Si}(\text{CH}_3)\text{R}_1\text{R}_2\text{R}_3$, Richards and Thompson²⁶ found that a band usually occurred near 800 cm^{-1} , but that it varied in position with the nature of the R groups more than in the compounds in which more than one methyl group is present." This band appears in the range of $814\text{-}802\text{ cm}^{-1}$ in the cyclic polymers, but is practically invariant at 800 cm^{-1} in the open-chain materials. A second band near 700 cm^{-1} ($14.3\text{ }\mu\text{m}$) which occurs in both the open-chain and cyclic materials is also believed to be associated with the $-\text{Si}(\text{CH}_3)_2-$ groupings. Bands at 841 cm^{-1} and 755 cm^{-1} have been associated with vibrations involving the $\text{Si}(\text{CH}_3)_3$ end-groups of the open-chain polymer and are considered to be sufficiently characteristic for the identification of this grouping.

A strong band at 1429 cm^{-1} ($7.0\text{ }\mu\text{m}$) is regarded as being characteristic of the silicon-phenyl link. A second band near 1124 cm^{-1} is also associated with the Si-phenyl band, but is described as being less constant in frequency and, thus, less useful for identification purposes.

The siloxane bond is characterized by a broad absorption band in the $9\text{-}10\text{ }\mu\text{m}$ region. Only in low-molecular-weight siloxanes with a small number of siloxane units is this absorption fairly sharp. The Si-O absorption appears as a very strong band in the range $1090\text{-}1020\text{ cm}^{-1}$ for both open-chain and cyclic compounds, with the open-chain compounds showing a slight preference for the lower end of the range. For the most part, these absorptions are essentially independent of the nature of the substituent groups. However, a clear-cut distinction does exist between the trimeric and tetrameric forms of the cyclic silicon polymers, with the Si-O band occurring between 1020 and 1010 cm^{-1} in cyclic trimers and

²⁵ Bellamy, L.J. (1958) *The Infrared Spectra of Complex Molecules*, John Wiley and Sons, Inc., New York, p. 334.

²⁶ Richards, and Thompson (1949) *J. Chem. Soc.*, 124.

between 1090 and 1080 cm^{-1} in the cyclic tetramers. In addition to the Si-O stretching vibration, a second absorption is expected in the 500-300 cm^{-1} region arising from the valance bending of the Si-O link. The far-infrared spectra of poly (dimethylsiloxane) and poly (methylphenylsiloxane) both show "very strong" bands at 475 cm^{-1} , which are assigned to the Si-O-Si bending mode.

Table 9. Organo-Silicon Compounds

Frequencies of Silicon-Containing Groups (cm^{-1})		
$\text{Si}(\text{CH}_3)_3$	1260, 1250.	near 840 and 755, 715-680, 660-435.
$\text{Si}(\text{CH}_3)_2$	$1258 \pm 5.$	near 850 and 800.
$\text{Si}(\text{CH}_3)$	$1258 \pm 5.$	near 765.
$\text{Si}(\text{CH}_2)$	1250-1200.	760-670.
SiC_6H_5	1125, 1100.	
Si-O-C	1110-1080.	
Si-O-Si	Cyclic	Trimmers 1020-1010. Tetramers 1090-1080. Larger Rings 1080-1050.
	Open Chain	1093-1076, 1055-1020.
SiH	Overall	2280-2050.
	SiH_3	Alkyl 2153-2142 Aryl 2157-2152.
	SiH_2	Dialkyl 2138-2117. Diaryl 2147-2130.
	SiH	Trialkyl 2105-2095. Triaryl 2132-2112.
SiF	100-830.	
Si-Cl	Usually one band between 600-550, overall 650-370.	

9.4 Identification of the Specific Compound Observed by SPIRIT 1

The identification of the specific species "coloring" the SPIRIT 1 anomalous flight data from the infrared spectra alone was complicated by a number of issues resulting from a lack of knowledge concerning the physical properties and/or state of the material. Most important was specific knowledge of the phase and temperature of the material and whether scattering or absorption was the dominant effect (the former being a convolution of the particle size and the real index of refraction as well as the absorption coefficient). The precise position of an absorption band is affected by changes of phase or of crystal form, as well as by changes in the molecular geometry or the nature of the substituent groups. For example, when going from the liquid to the crystalline solid the increased intermolecular forces cause relatively small shifts in frequency to occur. More importantly, however, the increased order of the crystal will often cause some bands to disappear from the spectrum while in some instances additional bands may appear. In general, the effects of molecular association lead to lower stretching frequencies and higher deformation frequencies with the overall shifts being small in either case.

In the SPIRIT 1 sensor all internal surfaces were cryogenically cooled to temperatures in the range of $\sim 10\text{-}30^\circ\text{K}$. At these temperatures most internal contaminants are expected to be solids cryodeposited on the cold surfaces inside the sensor. Unfortunately, measurements of the infrared absorption spectra of most complex molecules and polymers have been made primarily on liquid films at room temperature. The effects of large temperature differences can be expected to have a considerable influence on the absorption pattern, especially where polymorphic crystalline forms are anticipated.

Despite the above-mentioned concerns a positive identification of the specific species responsible for the anomalous features in the SPIRIT data was made on the basis of the comparison in Table 10. This table compares the observed "absorption" band centers from the SPIRIT 1 anomalous background spectrum with those for two typical methylphenyl siloxane (silicones) in the $\sim 500\text{-}2000\text{ cm}^{-1}$ spectral region. In all, 17 relatively strong "absorption" bands can be discerned in the SPIRIT 1 anomalous background spectra between $470\text{-}2000\text{ cm}^{-1}$ ($5\text{-}21\text{ }\mu\text{m}$). The frequencies of these observed bands are in excellent agreement with the corresponding bands in the absorption spectra of the two polymethylphenyl silicone compounds listed in Table 10. Based on this comparison it was determined that a methylphenyl siloxane compound was responsible for the series of sharp features observed in the SPIRIT 1 background data.

Table 10. SPIRIT 1 Anomalous "Absorption" Frequencies

SPIRIT 1 $\sigma(\text{cm}^{-1}) \pm 5 \text{ cm}^{-1}$	TENTATIVE ASSIGNMENT	SILICONE OILS (METHYL-PHENYL SILOXANE)	
		DOW 704 $\sigma(\text{cm}^{-1})$	METHYL-PHENYL DIMETHYLOXYSILANE $\sigma(\text{cm}^{-1}) \pm 5 \text{ cm}^{-1}$
470	Si-O-Si Bending		
575	Si-C stretch (sym)	570 \pm 10	
705	Si-C stretch (asym)	700 \pm 5	705
-		733	743
-		-	779
821		797 \pm 10	810
845	Si-C stretch	847 \pm 5	842
1000	Si-C ₆ H ₅	1000 \pm 5	1002
1045	Si-O-Si	1020 \pm 5	1033
		1060 \pm 25	1090
1130	Si-C ₆ H ₅	1120 \pm 10	1128
1157	Si-O-c	1158 \pm 5	1195
1265	Si-CH ₃	1265 \pm 5	1265
1426	Si-C ₆ H ₅	1430 \pm 5	1434
1473	-		1463
1488 \pm 10		1488	
1596 \pm 10	C ₆ H ₅ -	1593	1593
1816 \pm 10	C ₆ H ₅ -	1825	
1880 \pm 10	C ₆ H ₅ -	1890	
1950 \pm 10	C ₆ H ₅ -	1960	

9.5 Sources of Silicones

9.5.1 General Discussion

The identification of methyl-phenyl siloxane as the "contaminant" species in SPIRIT 1 led to a search for possible sources of this compound within the SPIRIT 1 experimental hardware. Although special care had been taken to exclude silicones from the SPIRIT 1 payload, several sources were still uncovered. These sources are discussed in detail below.

9.5.2 Rocket Booster Contamination

An inquiry at Morton Thiokol, the manufacturer of the Castor second-stage booster, revealed that silicone rubber was applied extensively to the interior of the engine nozzle. The compounds used were Dow Corning 90-006-2 Aerospace Sealant and/or General Electric RTV 88.

A tube of the Dow Corning sealant was obtained from the manufacturer, and cured samples of various thicknesses were prepared. IR transmission spectra of the samples were measured at Eastern Analytical Laboratories (N. Billerica, MA). The spectrum from a 240 μm thick sheet was used to estimate the thicknesses of thinner samples using Beer's law. The infrared spectrum from approximately 15 μm thick sample is shown in Figure 37 where it is compared to a SPIRIT 1 anomalous spectrum. The main component of this sealant is polydimethylsiloxane and this was confirmed by its spectrum which is in excellent agreement with various similar preparations published in the literature, such as the spectrum of silicone grease found on p. 142 of Reference 27. Based on this evidence the silicone sealant used in the Castor booster was ruled out as a possible source of the SPIRIT 1 anomalous data.

9.5.3 Payload Contamination

Considerable attention was paid to the issues of contamination control during the design and fabrication of the SPIRIT 1 payload. Several payload systems were specifically designed or modified to help minimize contamination.

The skin of the payload was nickel-plated aluminum. The nickel plating was added to give the payload a smooth, non-porous surface, to reduce surface offgassing of atmospheric gases during the flight. The skins were then polished to a surface smoothness of better than 2 microns (rms), producing a surface with a mirror finish. The polishing produced a surface which was nominally very smooth and exceptionally easy to clean.

The payload was vented during ascent, but was sealed while collecting IR data. The payload vent system (PVS) was an area of concern with regard to both cleanliness and reliability. The payload was vented through a manifold into four symmetrically placed vent holes on the skin of the payload. The vent holes are connected to the manifold with a semi-flexible plastic tubing. This was a double-wall tubing, with an inert inner lining, and an outer sleeve of flexible plastic. This assured that the interior of the tubing would not outgas during flight. The system valves were modified to assure that they would be open during ascent, and would close before measurements began. The system was designed to evacuate the interior of the payload to less than 0.5 psia in less than 40 seconds.

To protect the clean payload on the launch pad, a "cleanshell" was designed and constructed. This was a double-walled cylindrical ABS plastic shell which enclosed the payload. The shell kept the exterior surface of the payload clean and dry, and also provided thermal insulation for the payload during the Alaskan winter. Heated air was blown through

²⁷ Hummel, D.O. (1966) *Infrared Spectra of Polymers in the Medium and Long Wavelength Regions*, Interscience Publishers, New York, p. 70.

SILICONE SEALANT SPECTRUM

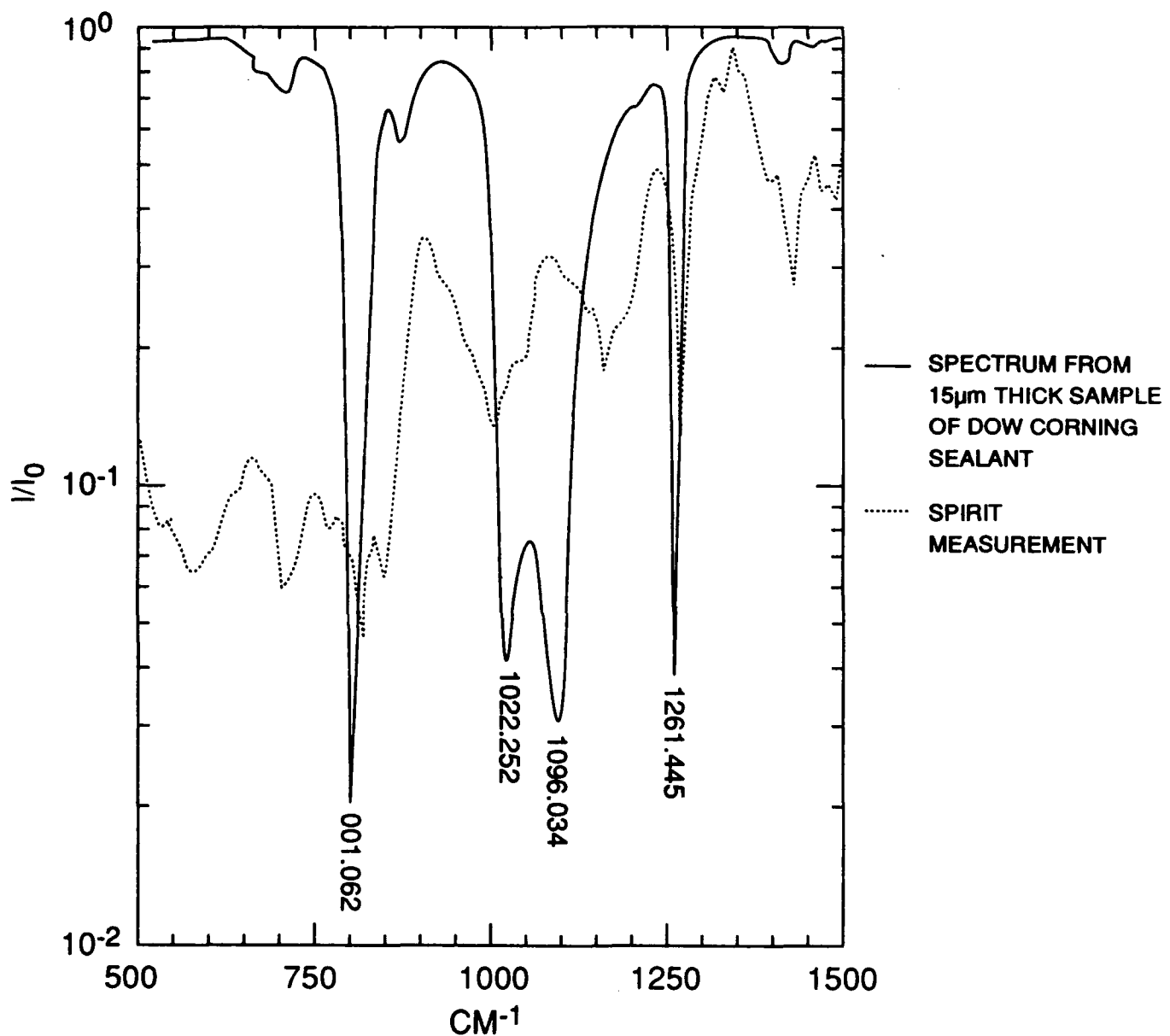


Figure 37. Spectrum of Dow Corning 90-006-2 Silicone Sealant (Solid Curve) Compared With the SPIRIT 1 Anomalous Ratio Spectrum (Dotted Curve).

the space between the inner and outer walls of the shell, to warm the payload without contaminating the payload skin. Dry nitrogen gas was flushed through the interior of the payload, and between the skin of the payload and the internal surface of the cleanshell. This was intended to degas the payload while on the launcher, and to reduce the contaminant levels prior to launch. The cleanshell was constructed in two semi-cylindrical halves.

Approximately one minute before launch, the two halves of the shell were pulled away from the payload. This allowed for an unencumbered launch, with a minimum exposure time to the environment around the pad. The final cleaning of the payload and the cleanshell, as well as the mounting of the cleanshell to the payload, were all performed in a clean room under class 100 conditions.

The ACS system received special attention as a possible source of contamination. Attention was focused on three main areas of concern:

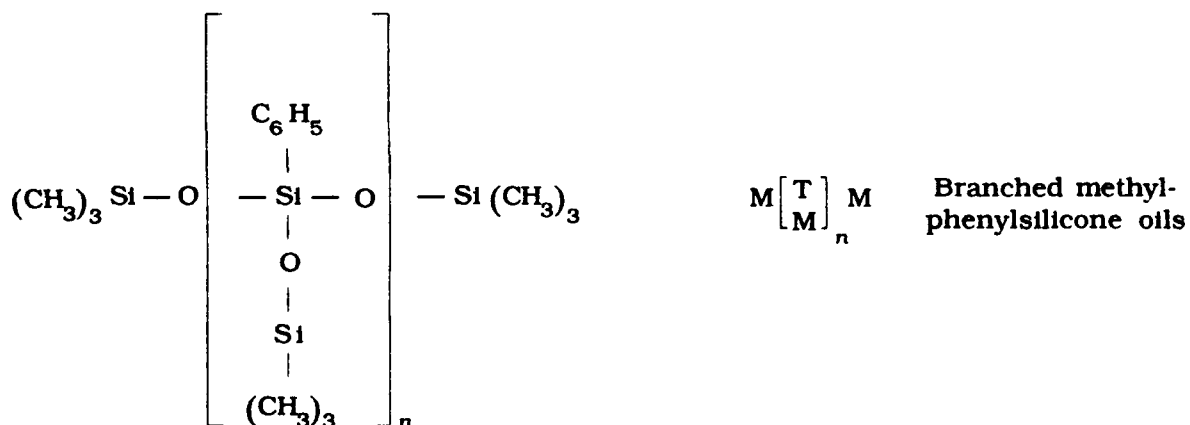
- 1) the quality of the gas supplied by the manufacturer,
- 2) the outgassing levels of the materials which contacted the gas, and
- 3) the methods used to clean the ACS hardware.

High-priority, research-grade nitrogen was used as the ACS gas. The ACS system was filled using 10-micron particulate filters to eliminate particle contamination in the gas. Most of the ACS hardware was made of stainless steel. The system was cleaned at the component level using ethyl alcohol and freon to eliminate particulate and chemical contamination. All parts were then subjected to a vacuum bakeout (8 hours at 125°F., 0.02 psia) to eliminate solvent residue prior to final ACS assembly. The system was reassembled under clean conditions and all outlets were capped with inert plugs to prevent recontamination of the system. From ACS reassembly until payload integration in Alaska, the system contained only pure nitrogen under pressure. The internal parts of regulators and bypass valves that were not compatible with the solvent cleaning procedures described above were still baked out along with the other system hardware. Finally, the ACS was purged during the rocket's ascent, prior to the start of the infrared measurements.

The only source of silicones in the payload section (excluding the sensor, which will be discussed in the next section) have been traced to the internal seals of several pressure regulators and bypass valves used in the ACS system that were lubricated with Dow Corning silicone grease. This grease is in all probability a polydimethyl-siloxane compound and thus is not the source of the silicone spectrum observed in the SPIRIT I flight data.

9.5.4 Main Sensor Internal Contamination

Special care was taken to exclude silicones from the SPIRIT 1 interferometer sensor. Evacuation of the sensor was accomplished using a turbo-molecular pump which was backed up by a roughing pump containing only hydrocarbon-based oil. O-ring seals were lubricated using only non-silicone-based grease and all internal (to the sensor) motor bearings were run without any lubrication. It is conceivable, however, that silicone contamination of the main sensor occurred during engineering testing or calibration. The instrument was evacuated and maintained at cryogenic temperatures for many months while conducting these activities. During this period the sensor was mated to calibration equipment and a helium leak detector, either of which may have become contaminated with silicone oil from diffusion pumps used to evacuate this equipment. Silicone diffusion pump oils are branched low-molecular-weight polymethylphenyl-siloxanes.^{28,29} The particular oil used in the diffusion pumps incorporated into the equipment mated to the SPIRIT 1 was Dow Corning 704, the spectrum of which is shown in Figure 38. As has been stated previously, this spectrum gives a close match to the SPIRIT 1 anomalous spectrum (see Figure 36). The constitution of branched methyl-phenylsilicone oils is shown below:



After considerably more effort, a second source of silicones internal to the SPIRIT 1 sensor was located. It has been determined that the flat, black, high-emissivity coating (3M Brand ECP-2200), used to paint the interior parts of the SPIRIT 1 telescope baffle contained 5-10 percent of a silicone resin. This resin has been identified as Dow Corning 808 which is a methylphenylsilicone. A sample of this paint resin was obtained from the manufacturer and its absorption spectrum was measured and compared to the SPIRIT anomalous spectrum (see Figure 38). This produced a more satisfactory match to the flight data than did the

²⁸ Noll, W. (1968) *Chemistry and Technology of Silicones*, Academic Press, New York, p. 409 & 670.

²⁹ Meals, R.N., and Lewis, F.M. (1959) *Silicones*, Reinhold Publ., p. 88.

comparison with the DC-704 pump oil spectrum. This paint is widely accepted as being a low-outgassing coating which significantly exceeds NASA's outgassing specifications when properly cured according to the manufacturer's recommendations. This coating was applied to the SPIRIT 1 telescope and was cured following the manufacturer's specifications (4 hours at 400°F). It seemed conceivable, however, that when exposed to a hard vacuum over an extended period of time (many months), as was the case in the SPIRIT 1 experiment, that enough material might have condensed on the colder surfaces of the telescope to have caused the effects observed in the data. The close match of the two spectra and the proximity of these painted surfaces to the telescope's primary mirror made the baffle coating the prime candidate to explain the anomalous features in the SPIRIT 1 data.

Next, a sample of the black paint was obtained from the manufacturer (3M) and the reflection spectrum was measured over the 500-2000 cm^{-1} spectral range. A comparison of this reflection data to the SPIRIT flight data produced even better agreement than had the comparison to the paint resin (see Figure 39). This convinced us that the black paint was responsible for producing the anomalous spectral features in the SPIRIT 1 data. However, the reflection spectrum of the paint showed a close resemblance to the absorption spectrum of the DC-808 resin and did not look much like the expected reflection spectrum. It appeared evident that the paint was not sufficiently opaque over much of the 500-2000 cm^{-1} spectral region.

9.6 Spectral Properties of ECP-2200 Black Paint

9.6.1 General Discussion

To better understand the implications of the initial reflection measurements on the ECP-2200 paint, we began a study to measure the high-resolution properties of this coating over the full wavelength region of interest for SPIRIT 1 data analysis.³⁰

9.6.2 Measurement Technique

A Bio-Rad (Digilab) Model FTS-40 Fourier Transform Interferometer at the University of Rhode Island was fitted with a Foxboro specular reflection attachment to measure both the specular and diffuse reflectance of the selected paint samples. The reflection attachment was modified various times to accommodate the wide range of incident and output angles required by this investigation.

³⁰ Brown, C.W., and Smith, D.R. (1990) High-resolution spectral reflection measurements on selected optical-black coatings in the 5-20 μm region, *SPIE Proc., Stray Radiation in Optical Systems*, 1331:210.

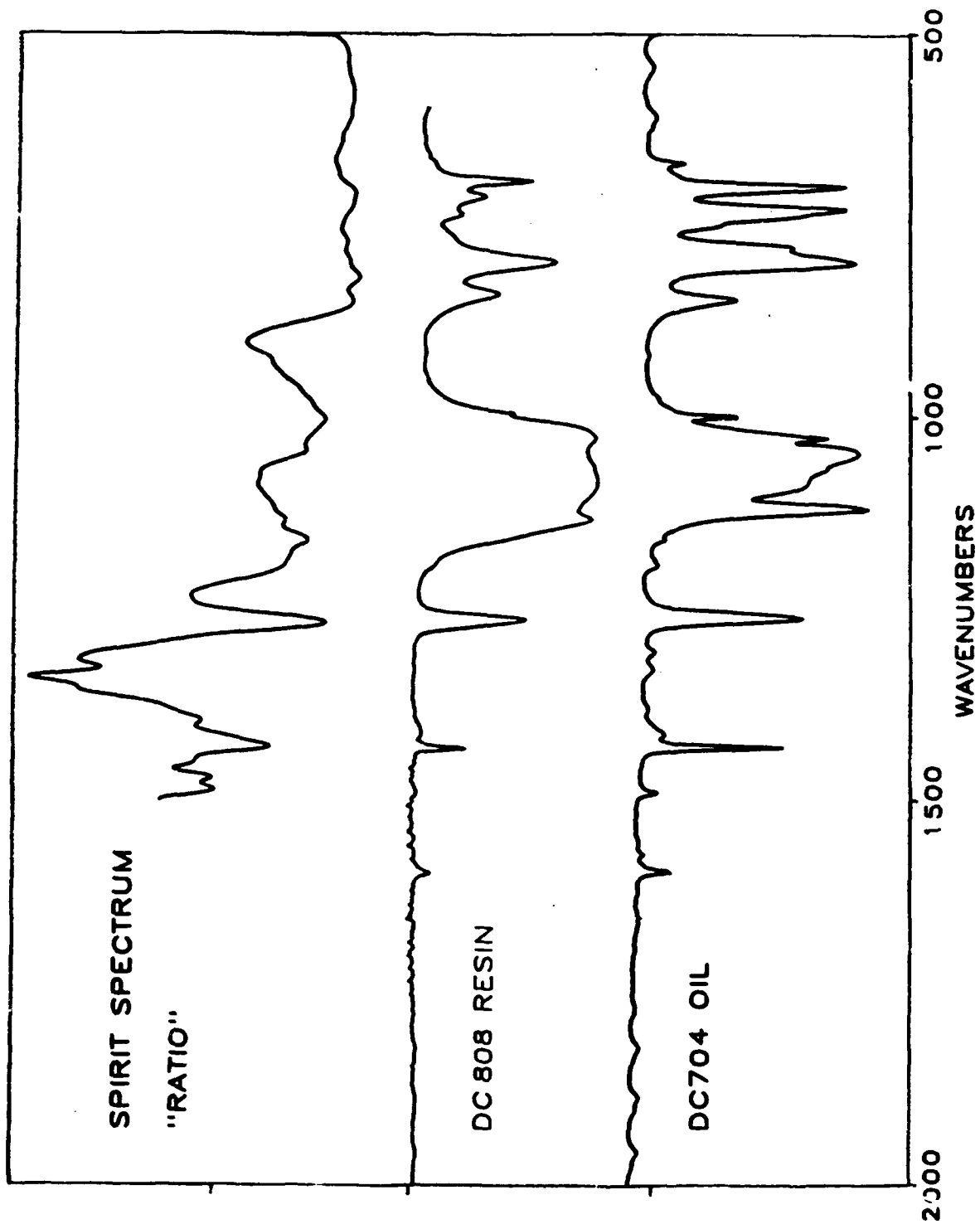


Figure 33. The Spectra of Silicone Pump Oil (DC-704) and Paint Resin (DC-808) Compared With the SPIRIT 1 Anomalous Spectrum

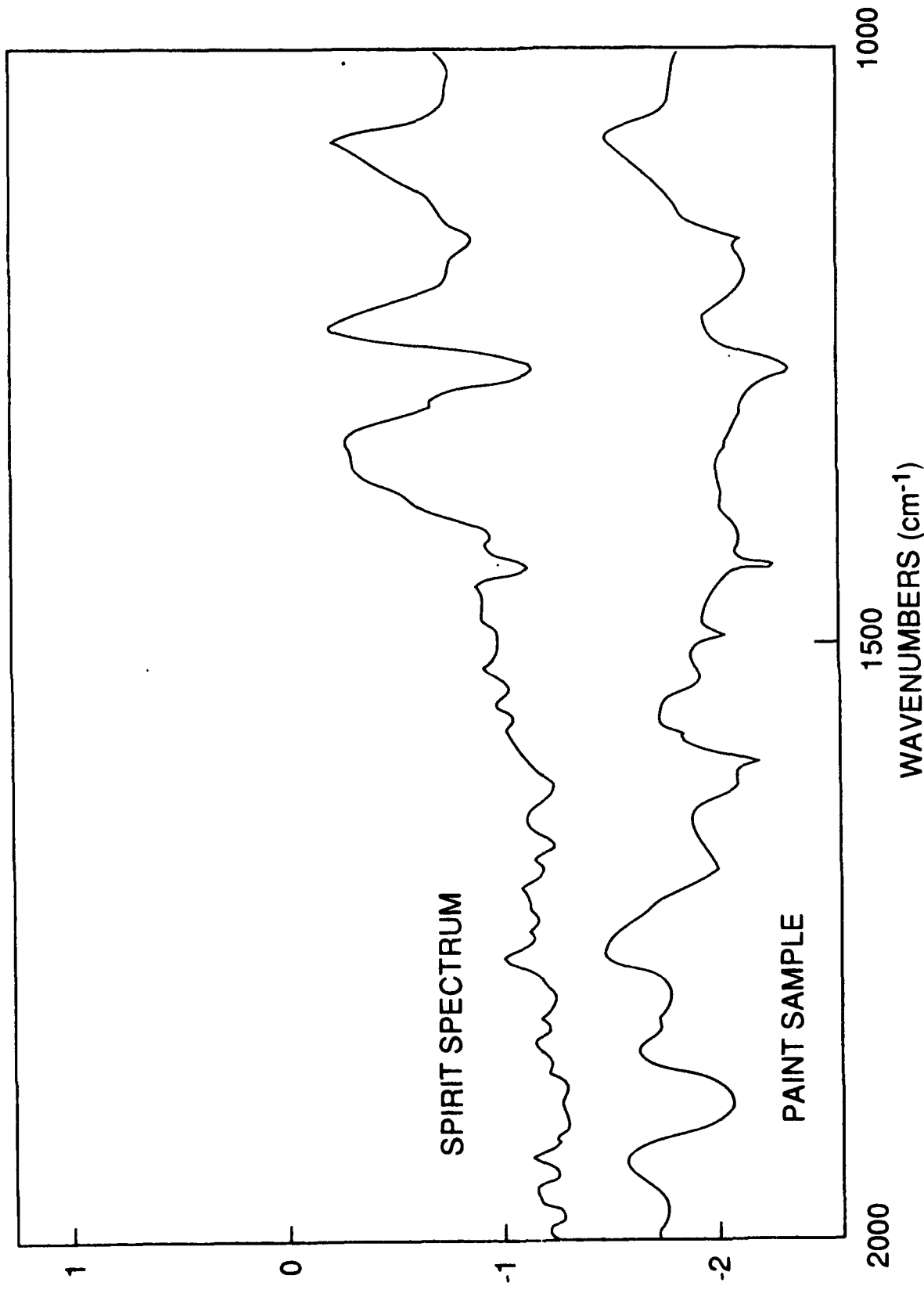


Figure 39. A Comparison of the Reflection Spectrum of 3M ECP-2200 Black Paint With the SPIRIT 1 Anomalous Spectrum

Individual spectra were 1 sec scans that covered the spectral range from 4400 - 500 cm^{-1} (2.3 - 20 μm) at a nominal resolution of 4 cm^{-1} . All spectra shown are the result of co-adding a minimum of 64 spectral scans for the specular reflection cases and at least 256 scans for the diffuse scatter data. Specular reflection measurements were made for incident angles of 10, 55, 65 and 80°. Diffuse scatter was measured for incident angles of 15°, 25, 55, 65 and 80° and with collection angles of 10, 65 and 80°. However, not all combinations of angles were measured for all samples.

9.6.3 Sample Description and Preparation

Five samples of 3M ECP-2200 black paint were prepared for us by SSG Inc., Waltham, MA. These five samples are described in Table 11. ECP-2200 paint was considered to be a flat black coating that diffusely scattered the majority of the radiation not absorbed in the material. All samples were prepared on 60-61 aluminum and were approximately 1 x 1 x 0.122 in. Prior to painting, the plates were cleaned with acetone and alcohol. The surface of sample No. 4 was polished to increase the back surface specular reflection while sample No. 5 was roughened with 320 grit paper until it looked coarse to the eye. The other samples were left untouched. No primer coat was used for these samples as none is required. Next the paint was mixed thoroughly and sprayed on. A second coat was applied to sample No. 2 after the first coat had dried overnight (overnight cures were approximately 16 hours). This process was repeated for the third coat which was applied to sample No. 3. The thickness of each coat was estimated to be 0.0010 in.

Table 11. Paint Sample Descriptions

Sample No. 1	-	Single coat of 3M ECP-2200 as applied to Spirit 1
Sample No. 2	-	Two coats of 3M ECP-2200
Sample No. 3	-	Three coats of 3M ECP-2200
Sample No. 4	-	Single coat of ECP-2200 on polished surface
Sample No. 5	-	Single coat of ECP-2200 on roughened surface

9.6.4 Discussion of Results

The results of both the specular reflection and diffuse scatter measurements for the 3M paint samples were somewhat surprising. The spectra of the specular reflectance for incident angles of 10 and 55° exhibit a considerable amount of absorption structure, looking much more like transmission or absorption spectra than reflection spectra. These spectra for a single coat sample (No. 1) are shown in Figure 40. The spectra of the diffuse scatter from these samples are all quite similar to the 10° specular case shown in Figure 40, although smaller by approximately an order of magnitude. These spectra exhibit the same series of absorption features present in the 10° specular reflection data. A typical diffuse scatter spectrum for a single coat 3M sample is shown in Figure 41. Note the close similarity of this spectrum to that shown in figure 40. Nearly all of the absorption bands present in these spectra can be correlated with absorption bands exhibited by the silicone binder (Dow-Corning 808) which is a primary ingredient of the ECP-2200 paint. The absorption spectrum of this silicone resin was shown in Figure 39. The presence of these absorption features in the reflection spectra of the 3M samples is a clear indication that these data are dominated by back surface rather than front surface effects. Only a small fraction of the energy incident on these samples was reflected or scattered at the front surface, the remainder being transmitted into the sample. At small angles of incidence for single coat samples a large fraction of this transmitted radiation remains unabsorbed and is specularly reflected from the aluminum substrate with relatively high efficiency. Upon returning to the front surface most of this radiation is transmitted to re-enforce the specular beam with a small fraction (small compared to the specular component but large compared to the front surface scatter) being forward scattered to increase the diffuse component. The fraction of the energy in the back surface reflected beam relative to the front surface component is strongly dependent on wavelength, with some wavelengths (near strong absorption bands) being heavily attenuated while others suffer much less (1/20) absorption. The ratio of the back surface to front surface contributions is greatest for the thinnest samples and the smallest angles of incidence, where the optical path lengths are at a minimum. Clearly, the magnitude of the back surface component can be affected by the thickness of the paint as well as by the condition of the aluminum substrate. Increasing the thickness by applying multiple coats will increase the absorption in the material and thereby reduce the back surface component. This effect is illustrated in Figure 42 where the specular reflection at 10° incidence for single coat (sample No. 1) and double coat (sample No. 2) samples are compared. The lower curve in this figure shows the ratio of the upper two curves, indicating a reduction of approximately a factor of 2. A comparable reduction or increase in reflection can also be achieved by alteration of the surface condition of the substrate prior to painting. This effect is shown in Figure 43 where the specular reflection at 10° angle of incidence is compared for sample Nos. 4 (polished substrate) and 5 (roughened substrate). As expected, polishing the substrate significantly increased the back surface specular reflection and thus the total specular reflection as well. Roughening the substrate surface, on the other hand, significantly reduced the total specular reflection by increasing the amount of transmitted energy scattered at the back surface, thereby reducing the back surface specular component. The lower curve in

Figure 43 gives the ratio of these two samples which shows a difference factor of between 3 and 4. As can be seen from Figure 40 this transparency or back-surface reflection effect is considerably reduced at 55° angle of incidence and, as shown in Figure 44, is totally absent for an incident angle of 80°.

Table 12. Band Center Frequencies (cm^{-1})
 $\pm 5\text{cm}^{-1}$

SPIRIT 1 OBSERVED	DC-808 PAINT RESIN ABSORPTION	3M ECP-2200 REFLECTION
W 1960 \pm 10	-	M 1967
M 1890 \pm 10	-	S 1880
M 1795 \pm 10	-	M 1796
-	-	M 1684
-	-	UR 1614
M 1595 \pm 10	W 1596	S 1595
-	-	W 1522
W 1490 \pm 10	-	W 1489
S 1430	M 1434	S 1431
S 1265	S 1263	S 1266
UR 1192	-	S 1186
S 1157	-	S 1157
UR 1130	S 1136	UR 1129
-	S 1088	-
S 1045	S 1032	W 1044
W 1000	W 1000	-
S 850	M 845	S 854
S 819	S 805	S 818
-	W 741	-
S 726	W 719	M 726
S 703	S 699	S 704
M 572	N.D.	S 565
S 522	N.D.	S 534

S = Strong, M = Medium, W = Weak, UR = Unresolved

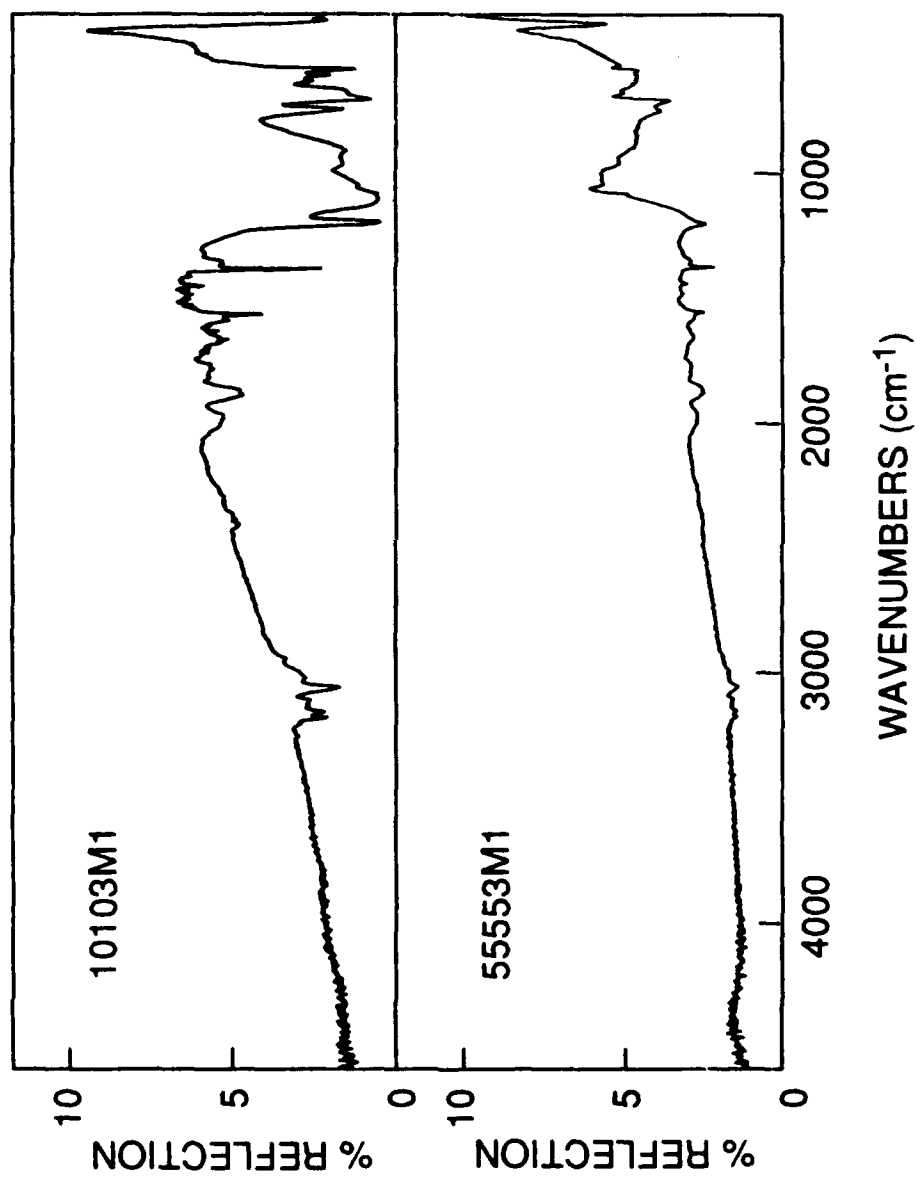


Figure 40. The Specular Reflection Spectra of 3M-ECP-2200 Paint (Sample 1)

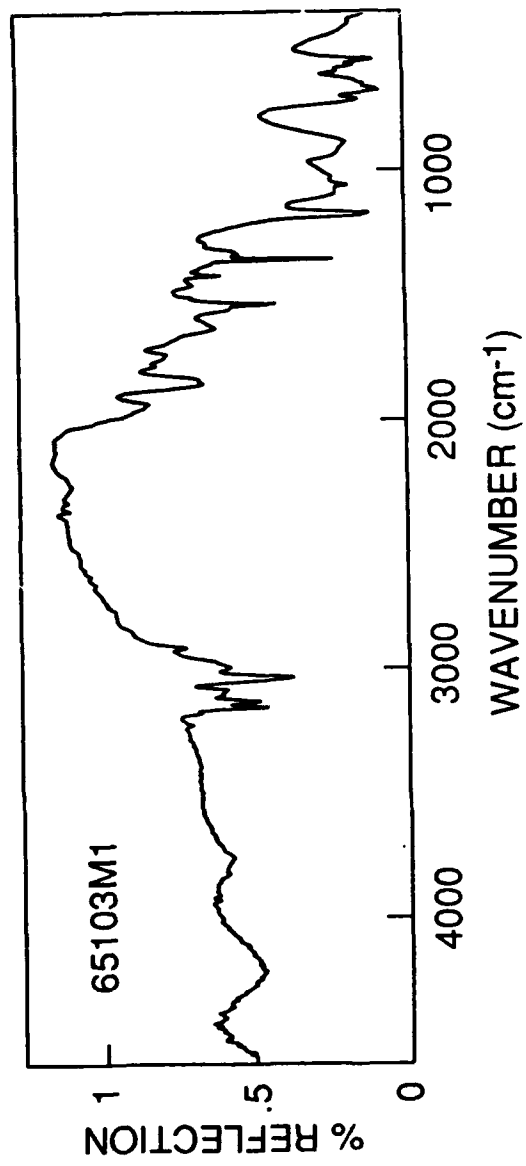


Figure 41. The Diffuse Scatter Spectrum of 3M-ECP-2200 Paint (Sample 1) for 65° Angle of Incidence and 10° Collection Angle

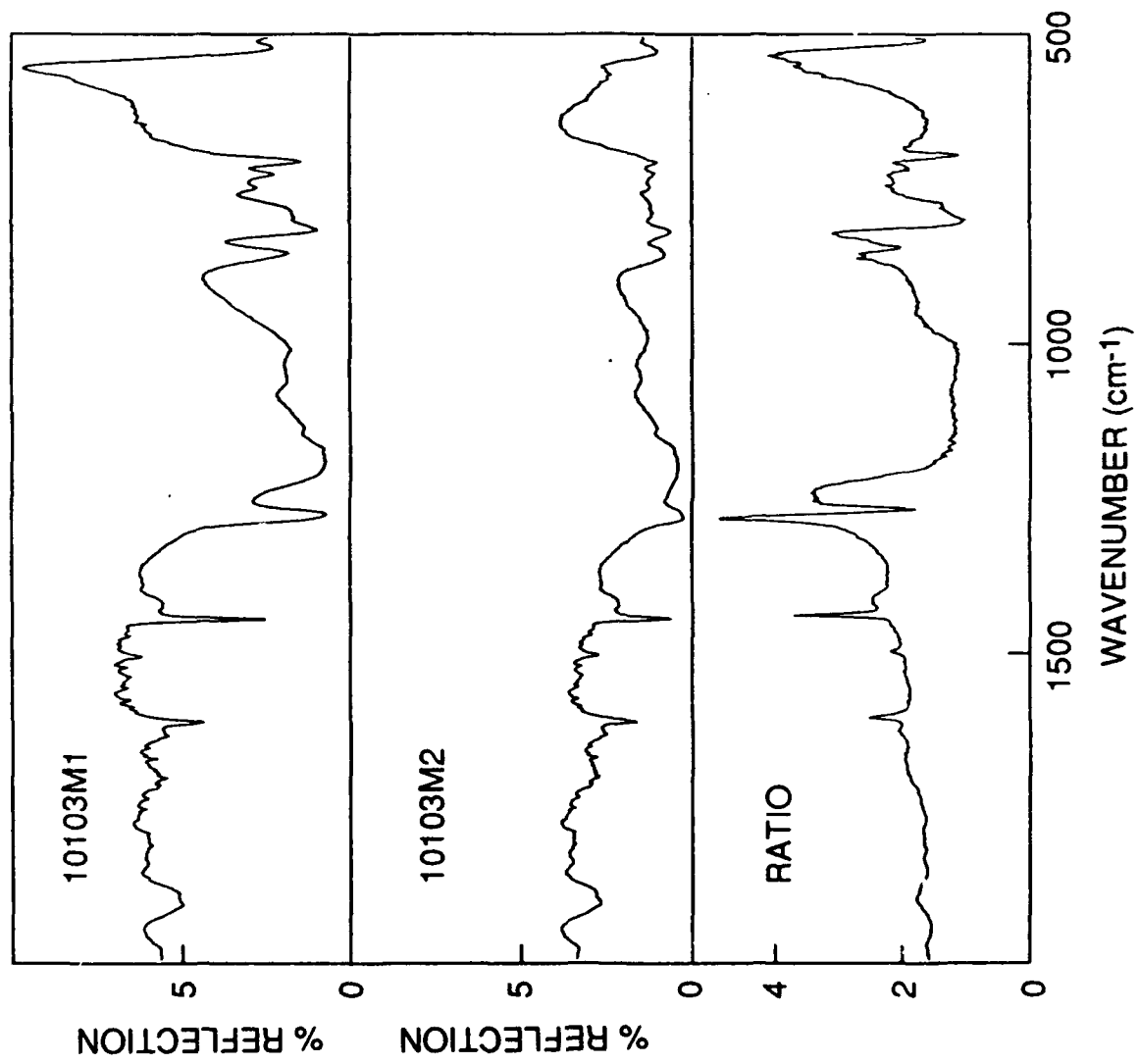


Figure 42. A Comparison of the Specular Reflection Spectra of One and Two-Coat Samples of 3M-ECP-2200 Paint

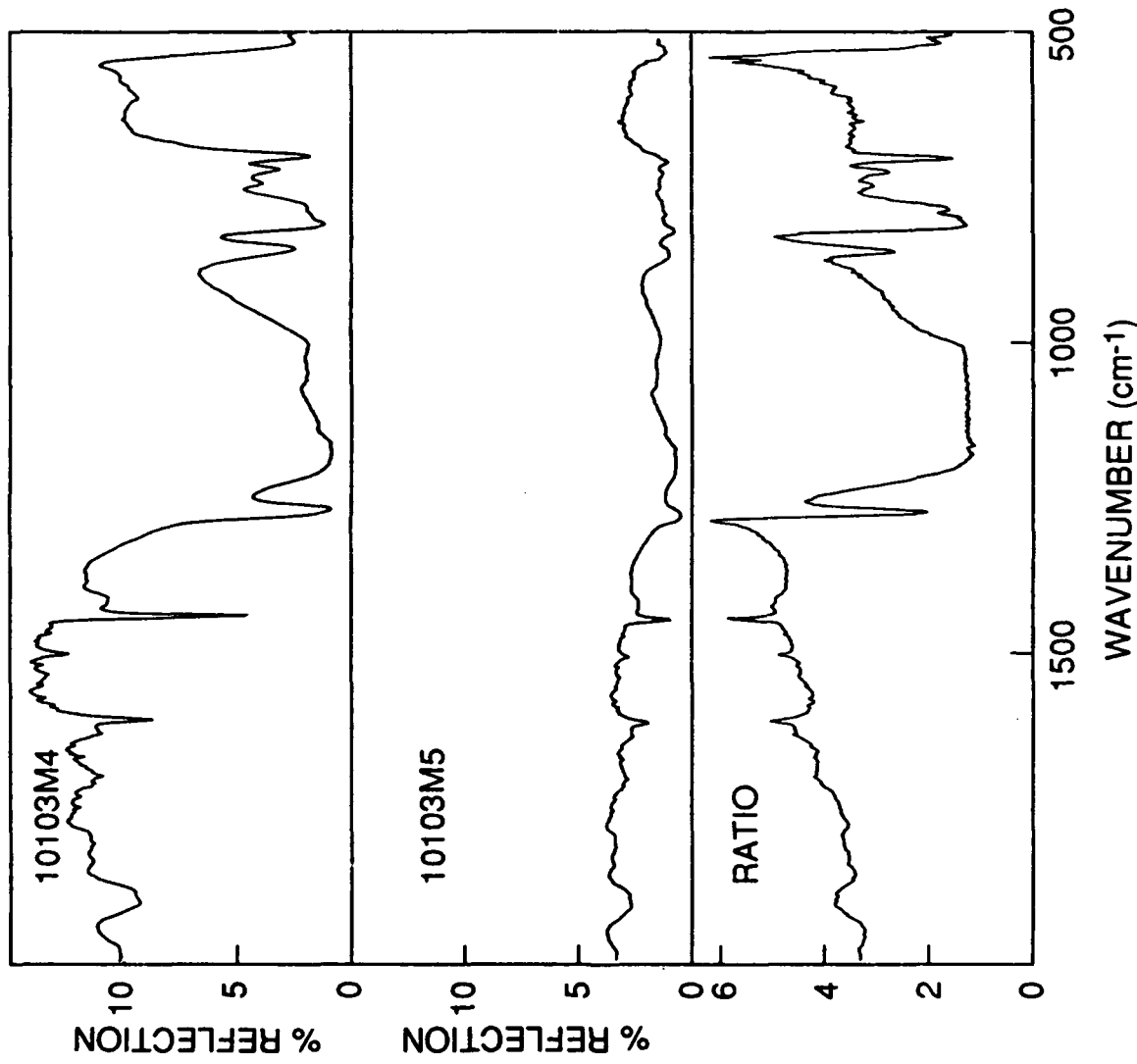


Figure 43. A Comparison of the Specular Reflection Spectra of a Single Coat of 3M-ECP-2200 Paint on a Polished (Upper Curve) and Roughened (Middle Curve) Surface

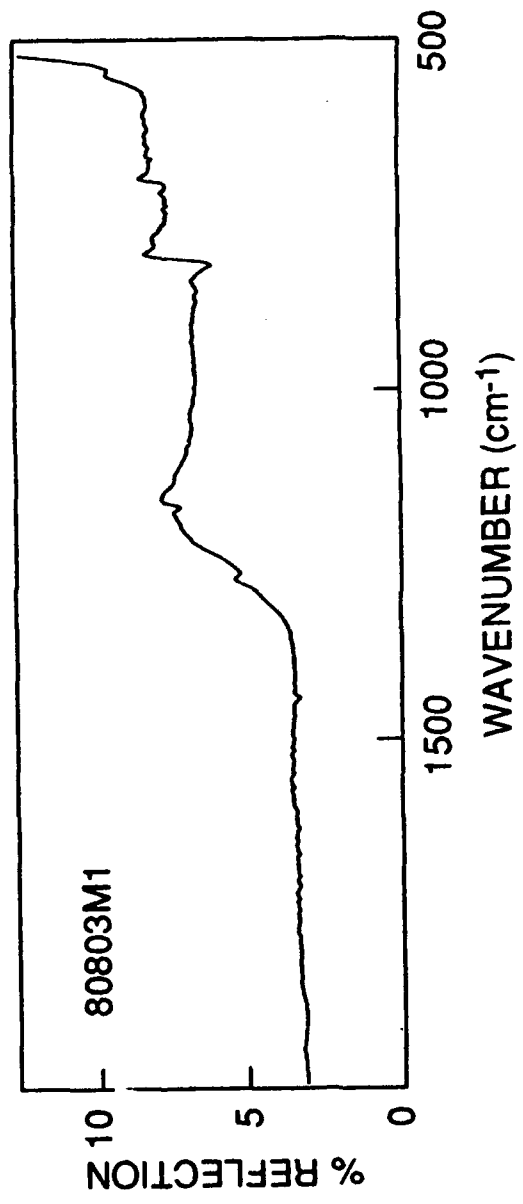


Figure 44. The Specular Reflection Spectra of a Single Coat of 3M-ECP-2200 Paint at 80° Angle of Incidence

The results of the diffuse reflection measurements on the 3M samples are much more difficult to interpret than those for specular reflection. As mentioned earlier, these data are also dominated by absorption rather than front-surface reflection effects. The diffuse reflection spectra from 2000 - 500 cm^{-1} for a number of different combinations of incident and collection angles are shown in Figures 45 and 46 for sample No. 1. These spectra are all similar in overall shape and exhibit a strong wavelength dependence due to the absorption properties of the paint. As previously noted these spectra also resemble the specular case for 10° incidence (Figure 40) with an attenuation factor of only about 5 - 8. In common with the specular reflection data, the diffuse reflection also varies by more than an order of magnitude with wavelength, reaching a maximum of 1.6 percent at 4.7 μm (2135 cm^{-1}) and minima of around 0.05 percent at several wavelengths beyond 12 μm . In general the diffuse reflection was 10 - 50 percent lower for small incident / large collection angle combinations as compared to large incident / small collection angle combinations, with the larger differences occurring in the shorter wavelength regions. As expected, the thicker samples (multiple coats) exhibited lower diffuse reflection owing to the increased absorption of the dominant back-surface-reflected rays. A comparison of the diffuse reflection for one-, two-, and three-coat samples is shown in Figure 47 for the (65°, 10°) combination. Also as expected, polishing the back surface prior to painting (sample No. 4) resulted in a significant decrease (25 - 50 percent) in the diffuse reflection, because appreciably more of the energy leaving the back surface was directed into the specular direction. On average, slightly larger decreases were observed for large incident/small collection angle combinations than for the reverse cases. The diffuse reflection of sample No. 4 is compared with that of sample Nos. 1 and 5 for a typical angular combination in Figure 48. Unexpectedly, the diffuse reflection for sample No. 5 (roughened back surface) also shows a decrease (10 - 30 percent) relative to sample No. 1 though not as large as that for sample No. 4. At present we do not have an adequate explanation for this result.

Whereas the specular reflection results can be explained in simple terms of front- and back-surface reflected components, the diffuse-scatter data appears to be more complicated. As illustrated in Figure 49 there are at least three front-surface-scattered components and one back-surface-scattered component (S3) that can contribute to the total scatter observed in any given direction. A fraction of the incident energy (I) is reflectively scattered from the front surface (S1) but some is also scattered into the sample where it can then reflect off of the back surface (S4). Another part of the incident beam (I) is transmitted into the sample and specularly reflected at the back surface. A fraction of this reflected radiation is then scattered upon exiting the front surface (S2). All of these scattered components, with the exception of the front-surface reflective scatter, are affected by the paint thickness (that is, the number of coats) and by the surface condition of the sample substrate. It is difficult to estimate the relative magnitudes of these various components for the different thicknesses and back surface conditions, in part because the back-surface-reflected and-scattered components are oppositely affected by changes in surface condition. Further complicating matters is the possibility of contributions from radiation scattered inside the sample, especially at the interfaces between the separate coats of the multi-layer samples.

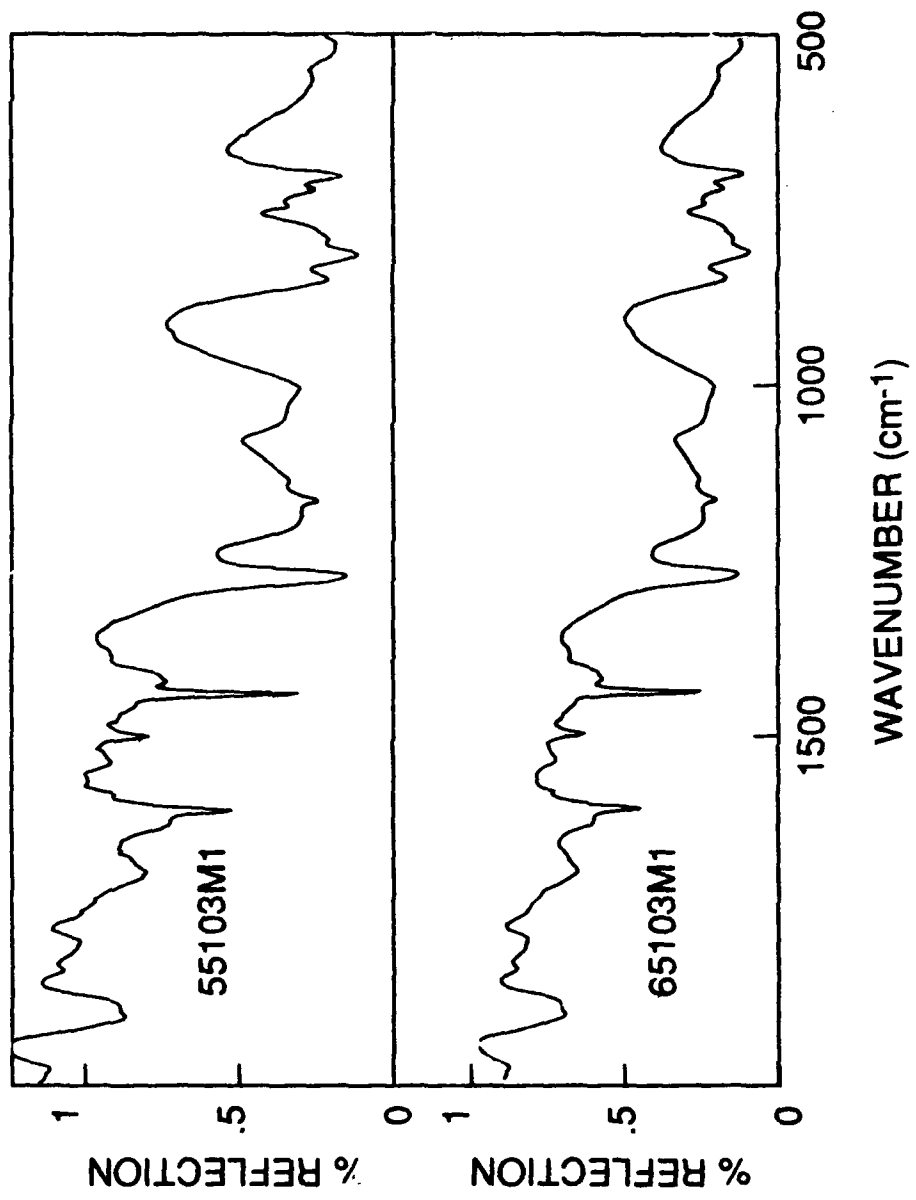


Figure 45. A Comparison of the Diffuse Scatter Spectra of a Single Coat Sample of 3M-ECP-2200 Paint for Two Different Angular Combinations

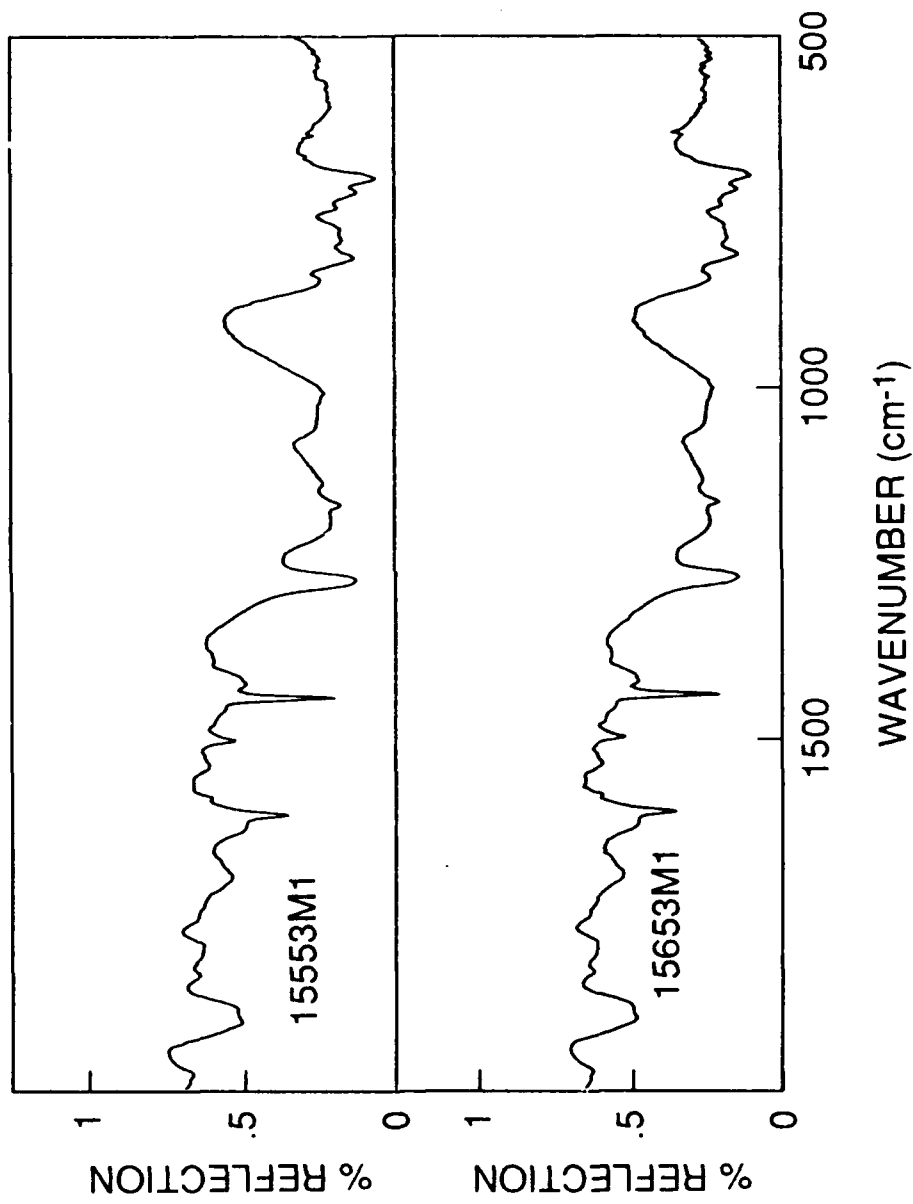


Figure 46. A Comparison of the Diffuse Scatter Spectra of a Single Coat of 3M-ECP-200 Paint for Two Different Angular Combinations

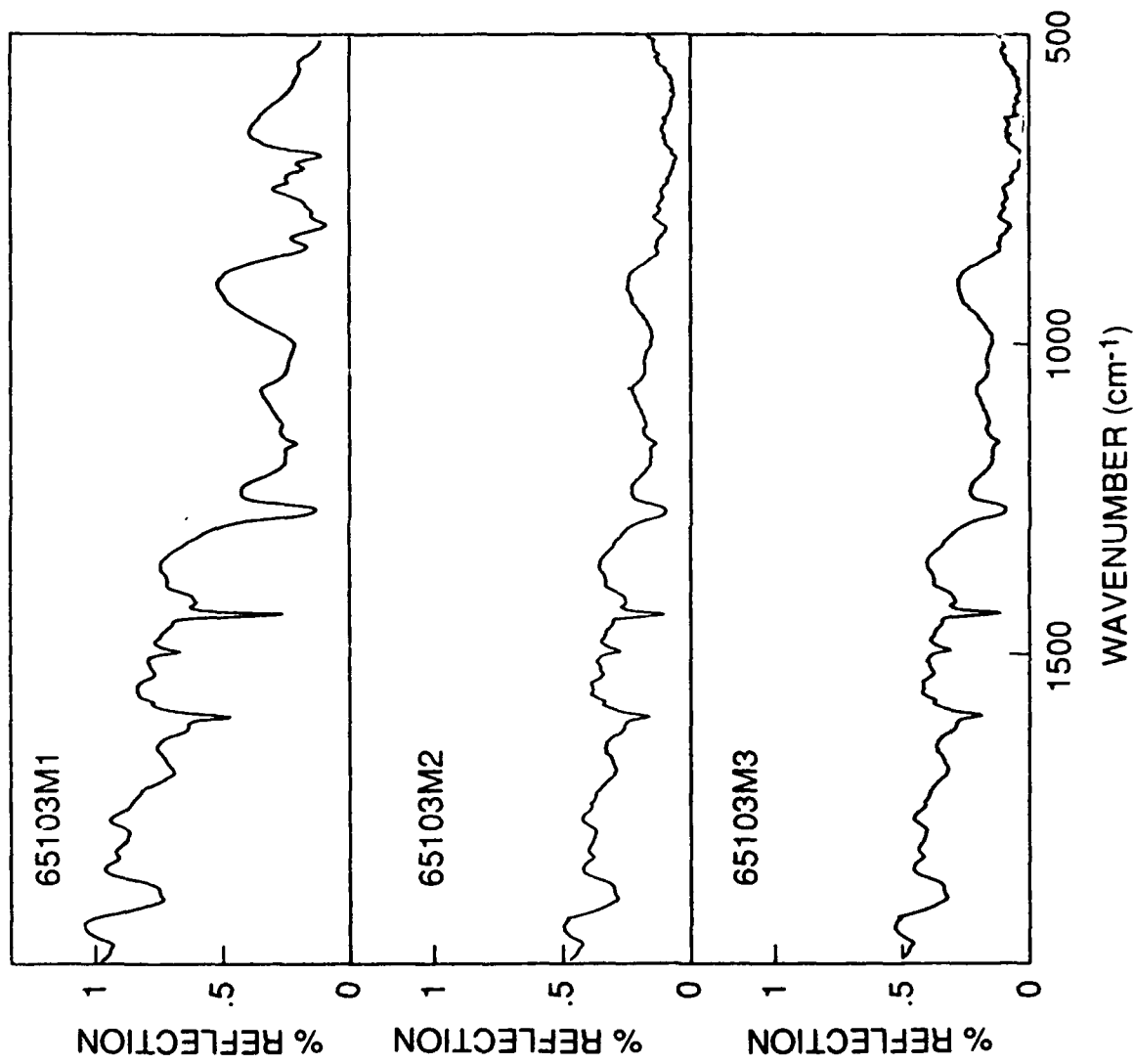


Figure 47. A Comparison of the Diffuse Scatter Spectra of one (Upper Curve), two (Middle Curve) and Three (Lower Curve) Coat Samples of 3M-ECP-2200 Paint for a Typical Angular Combination (65°/10°)

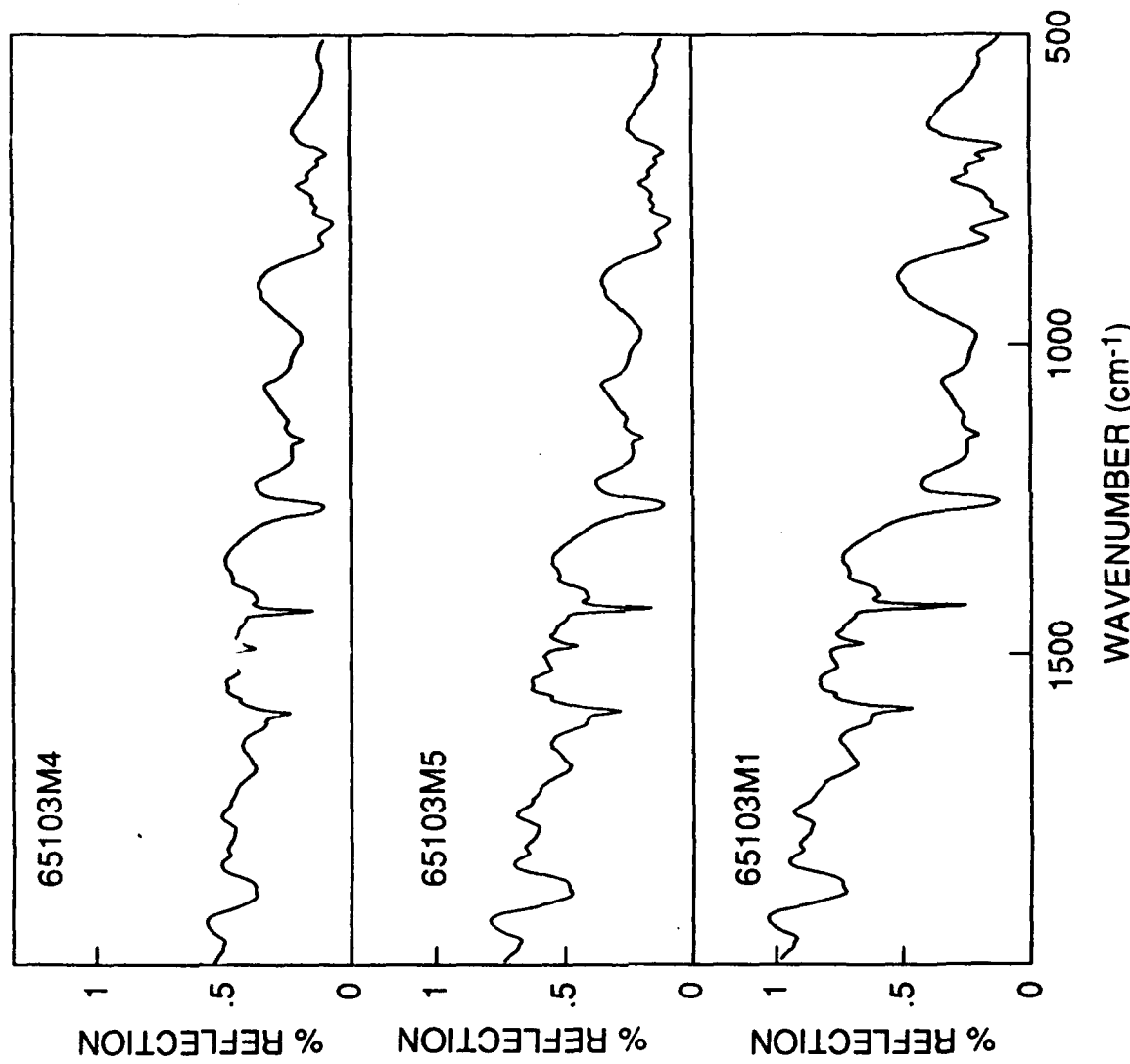


Figure 48. A Comparison of the Diffuse Scatter Spectra of a Single Coat of 3M-ECP-2200 Paint on a Polished (Upper Curve), Roughened (Middle Curve) and Untreated (Lower Curve) Surface for a (65°, 10°) Angular Combination

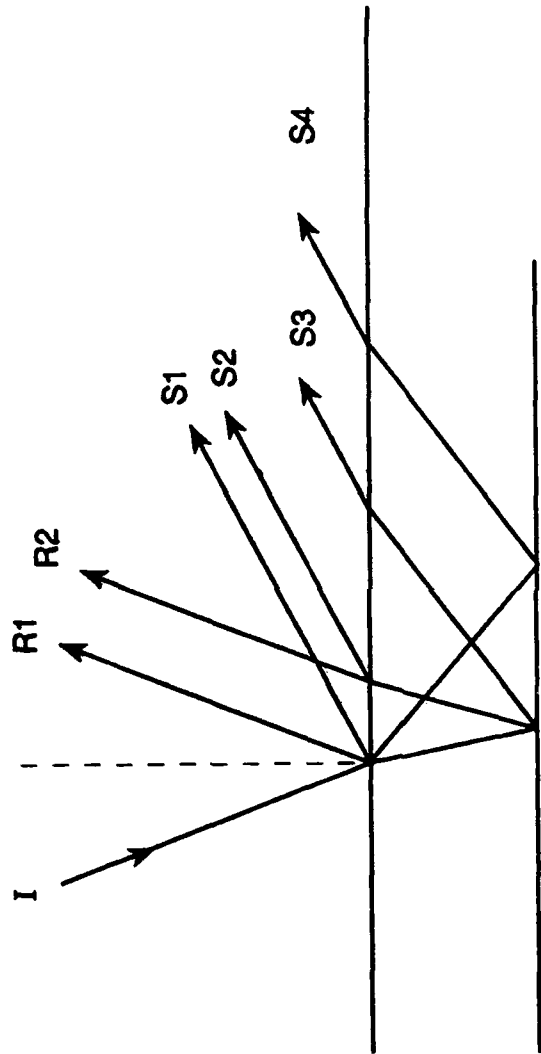


Figure 49. Contributing Rays for the Specular Reflection (R) and Diffuse Scatter (S) Cases for Non-opaque Samples

9.7 Telescope Leakage Summary

The leakage background observed by the SPIRIT 1 sensor exhibited a large number of spectral features (absorption bands) causing the stray light background to vary by more than an order of magnitude with wavelength. The leakage also varied with detector location, with off-axis detectors observing 2.5 to 3.5 times more leakage than the central (on-axis) detector. Despite these effects the nominal baseline leakage observed for the primary detector was less than 10^{-10} W/cm² sr μ m or about a factor of 10 lower than previous earthlimb sensors. The minimum leakage radiance was approximately 7×10^{-12} W/cm² sr μ m and occurred in the center of a strong but narrow absorption band at 1265 cm⁻¹. In addition, sporadically during the flight the mean stray light level increased by an order of magnitude or more, the apparent result of occasional particles transiting the telescope baffle. However, this had no apparent effect on the spectral shape of the leakage spectrum. A high resolution (1 cm⁻¹) spectrum of one such case (scan 147) is shown in the upper curve of Figure 50. Due to the increased signal level of this scan the spectrum exhibits excellent S/N ratio over most of the 1700 - 500 cm⁻¹ spectral range. This spectrum is characteristic of nearly all of the off-axis leakage dominated cases measured by the SPIRIT 1 sensor. It shows a large peak (maximum) near 900 cm⁻¹ and a sharp minimum at 1265 cm⁻¹ among numerous other features. To determine the source of this anomalous background this spectrum was divided by a calculated reference spectrum in an attempt to remove the source function from the data. The reference spectrum was calculated using the MODTRAN atmospheric code for sub-arctic winter conditions with an earth temperature of 250 K and a zenith angle of 135°. The result of this calculation is shown in the middle curve of Figure 50. This spectrum simulates the energy upwelling from the earth and lower atmosphere usually, referred to as "earthshine", which is the primary source of off-axis leakage. The lower curve in Figure 50 is the ratio of SPIRIT scan 147 to this earthshine spectrum and represents a reasonable estimate of a SPIRIT leakage spectrum with the source function removed. The original and ratio spectra were both cut off at around 1700 cm⁻¹ due to poor S/N in the higher wavenumber region. To improve the S/N in the 2000 - 1500 cm⁻¹ region a number of SPIRIT scans were co-added. The resulting spectrum was then smoothed using a 25 point filter and finally divided by the source spectrum. The resulting ratio spectrum is shown as the middle curve in Figure 51 where it is compared to the scan 147 ratio spectrum, which was also shown in Figure 50. The lower curve in Figure 51 shows a typical diffuse scatter spectrum for the 3M ECP-2200 black paint. The similarity of these three spectra is unmistakable. This comparison is convincing evidence that SPIRIT 1 off-axis leakage was dominated by baffle rather than mirror scatter. This result was unexpected based on both pre- and post-flight stray light analyses of the SPIRIT 1 telescope system, which predicted primary-mirror-scatter-limited performance.

It has been shown that the prominent spectral features in the anomalous stray light spectrum observed by the SPIRIT 1 earthlimb sensor are the result of radiation scattered from the SPIRIT telescope baffle, which was painted with a single coat of 3M-ECP-2200 black paint. The precise mechanism by which this scattered radiation reaches the detectors is not yet fully understood and is the subject of a continuing investigation.

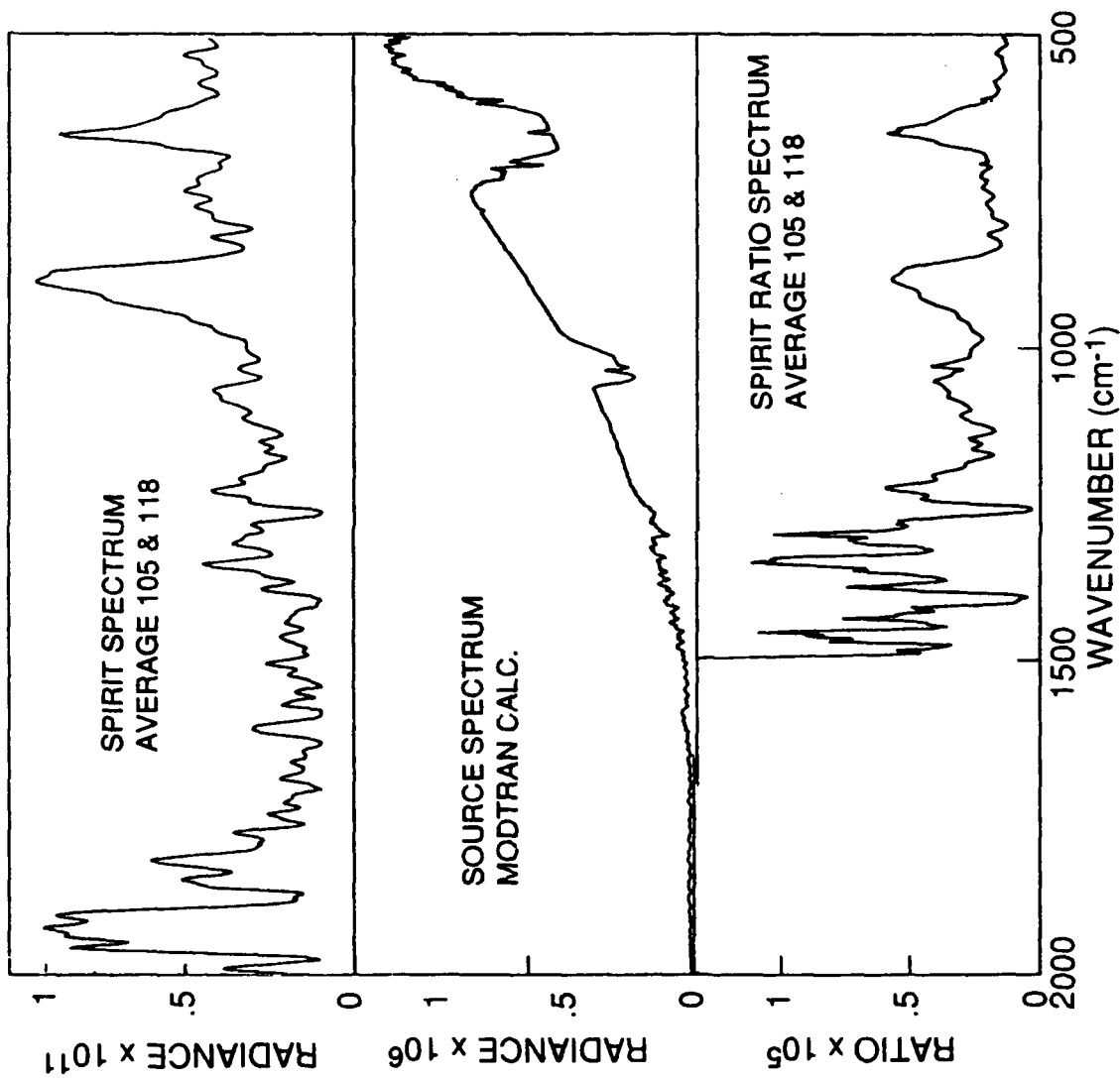


Figure 50. Anomalous Leakage Spectrum From SPIRIT 1 Rocketborne Sensor (Upper Curve), a MODTRAN Calculation of an Upwelling Earthshine Spectrum (Middle Curve) and a SPIRIT Anomalous Spectrum With the Source Function Removed (Lower Curve) Which was Obtained by Taking the Ratio of the two Upper Curves

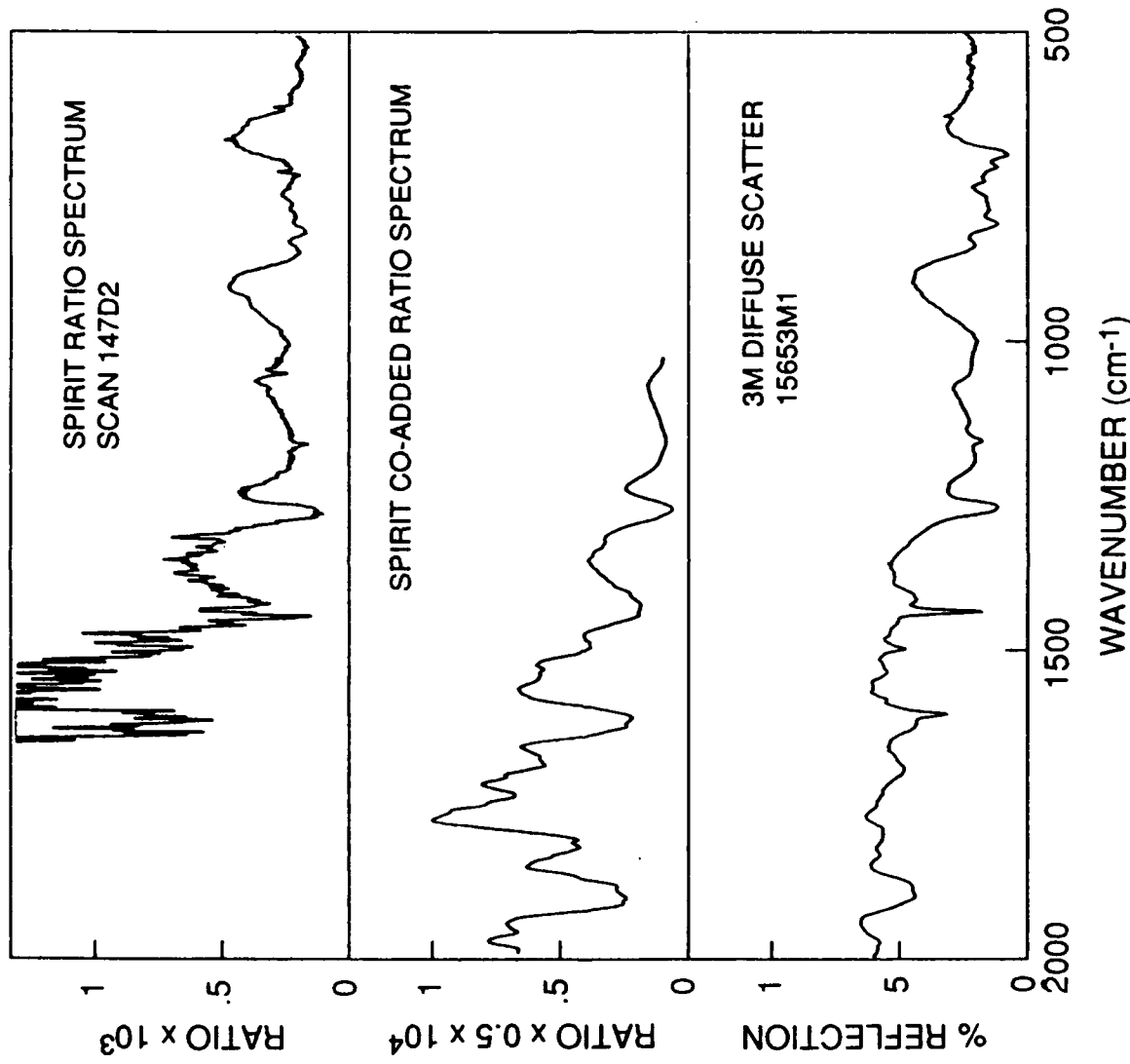


Figure 51. A Comparison of two SPIRIT 1 Ratio Spectra With a Typical Diffuse Scatter Spectrum for the 3M-ECP-2200 Paint

References

1. Degges, T.C. and D'Agati, A.P. (1986) A user's guide to the AFGL/Visidyne high altitude infrared radiance mode computer program, *Rep.*, VI-785, Visidyne Corp.
2. Stair, A.T., Jr., Pritchard, J., Coleman, I., Bohne, C., Williamson, W., Rogers, J., and Rawlins, W.T. (1983) The rocket-borne cryogenic (10° K) high-resolution interferometer spectrometer flight-HIRIS: Atmospheric and auroral infrared emission spectra, *Appl. Opt.*, **22**:1056.
3. Smith, D.R., Phillips Laboratory, AFSC, Private Communication.
4. Smith, D.R., Blumberg, W.A.M., Nadile, R.M., Lipson, S.J., Huppi, E.R., Wheeler, N.B., and Dodd, J.A. (1992) Observation of high-N hydroxyl pure rotation lines in atmospheric emission spectra by the CIRRIS 1A space shuttle experiment, *Geophys. Res. Lett.*, **19**, Number 6.
5. Saki, H., Vanasse, G.A., and Forman, M.L. (1968) Spectral recovery in Fourier spectroscopy, *J. Opt. Soc. Am.*, **58**:54
6. Forman, M.L., Steel, W.H., and Vanasse, G.A. (1966) Correction of asymmetric interferograms obtained in Fourier spectroscopy, *J. Opt. Soc. Am.*, **56**:59.
7. Harris, F.J. (1978) On the use of windows for harmonic analysis with the discrete Fourier transform, *Proc. IEEE*, **66**, No. 1.
8. Mertz, L. (1967) Auxiliary computation for Fourier spectroscopy, *Infrared Physics*, **7**:17.
9. Dybwad, P., and Huppi, R.J. (1987) SPIRIT 1 postflight calibration report, *Rep. SRL-87-2* Utah State University/Stewart Radiance Lab., Bedford, MA, and Dybwad, J.P., Huppi, R.J., McKenna, R.E., Saletnik, D.P., Thomas, B.J., and Griffiths, V. (1987) Report on a rocket-borne, telescoped Fourier transform spectrometer operating at 10 K, *Proc. SPIE Int. Soc. Opt. Eng.*, **787**, 114.

10. Nadile, R.M., Stair, A.T., Jr., Wheeler, N.B., Frodsham, D.G., Wyatt, C.L., Baker, D.J., Grieder, W.F. (1978) SPIRE-spectral infrared rocket experiment (preliminary results). *AFGL-TR-78-0107*, Air Force Geophysics Laboratory, ADA058504.
11. Stair, A.T., Jr., Sharma, R.D., Nadile, R.M., Baker, D.J., and Grieder, W.F. (1985) Observations of limb radiance with cryogenic spectral infrared rocket experiment. *J. Geophys. Res.*, **90**:9763.
12. Adler-Golden, S.M., Smith, D.R., and Matthew, M.W. (1991) Atmospheric infrared radiance from CO₂ and NO observed during the SPIRIT 1 rocket experiment. *J. Geophys. Res.*, **96**:11319.
13. Green, B.D., Rawlins, W.T., and Nadile, R.M. (1986) Diurnal variability of vibrationally excited mesospheric ozone as observed during the SPIRE mission. *J. Geophys. Res.*, **91**:311.
14. Adler-Golden, S.M., Matthew, M.W., Smith, D.R., and Ratkowski, A.J. (1990) 9-12 μm atmospheric ozone emission observed in the SPIRIT 1 experiment. *J. Geophys. Res.*, **95**:15243.
15. Adler-Golden, S.M., and Smith, D.R. (1990) Identification of 4- to 7-quantum v_3 bands in the atmospheric recombination spectrum of ozone. *Planet. Space Sci.*, **38**:1121.
16. Barth, C.A., Tobiska, W.K., Siskind, D.E., and Cleary, D.D. (1988) Solar-terrestrial coupling: Low-latitude thermospheric nitric oxide. *Geophys. Res. Lett.*, **15**:92.
17. Kneizys, F.X., Shettle, E.P., Gallery, W.O., Chetwynd, J.H., Jr., Abreu, L.W., Selby, J.E.A., Clough, S.A., Fenn, R.W. (1983) Atmospheric transmittance/radiance: computer code LOWTRAN 6. *AFGL-TR-83-0187*, Hanscom AFB, MA, ADA137786.
18. Smith, D.R. (August 17-19, 1988) Evidence for off-axis leakage radiance in high-altitude IR rocketborne measurements, stray light and contamination in optical systems. *Proc. of the SPIE Conference, San Diego, CA*, **30**:967.
19. Smith, D.R., and Ratkowski, A.J. (1986) Contamination in rocket-borne IR measurements. *Proc. of the 13th Annual Meeting on Upper-Atmospheric Studies by Optical Methods*, Report 86-28, Univ. of Oslo.
20. Rogers, J.W., Stair, A.T., Jr., Wheeler, N.B., Wyatt, C.L., and Baker, D.J. (1976) *AFCRL-TR-76-0274*, Environmental Research Paper No. 583, AFGL, Hanscom AFB, MA, ADA038239.
21. Rogers, J.W., Stair, A.T., Jr., Wheeler, N.B., Wyatt, C.L., and Baker, D.J. (1977) *AFCRL-TR-77-0113*, Environmental Research Paper No. 597, AFGL, Hanscom AFB, MA, ADA045466.
22. Ulwick, J.C., Baker, K.D., Stair, A.T., Jr., Frings, W., Hennig, R., Grossman, K.U., and Hegblom, E.R. (1985) Rocket-borne measurements of atmospheric infrared fluxes. *J. Atmos. Terr. Phys.*, **47**:123.
23. Simon, J. and McMahon, H.O. (1952) Infrared spectra of some alkyl silanes and siloxanes in gaseous, liquid, and solid phases. *J. Chem. Phys.*, **20**:905.
24. Smith, A.L. (1974) *Analysis of Silicones*, John Wiley and Sons, Inc., New York, p. 247.
25. Bellamy, L.J. (1958) *The Infrared Spectra of Complex Molecules*, John Wiley and Sons, Inc., New York, p. 334.
26. Richards, and Thompson (1949) *J. Chem. Soc.*, 124.
27. Hummel, D.O. (1966) *Infrared Spectra of Polymers in the Medium and Long Wavelength Regions*, Interscience Publishers, New York, p. 70.
28. Noll, W. (1968) *Chemistry and Technology of Silicones*, Academic Press, New York, p. 409 & 670.

29. Meals, R.N., and Lewis, F.M. (1959) *Silicones*, Reinhold Publ., p. 88.
30. Brown, C.W., and Smith, D.R. (1990) High-resolution spectral reflection measurements on selected optical-black coatings in the 5-20 μm region, *SPIE Proc., Stray Radiation in Optical Systems*, 1331:210.

Appendix A

Tabulation of Interferometer Scans

PROJECT SPIRIT

INTERFEROMETER SCAN PARAMETERS

86/07/16. 14.32.26.

F I L T Y P E R	E R T E R E R	GMT START TIME	TAL (SEC)	DATA POINTS	MSEC LENGTH	HORIZON SENSOR			TANGENT HEIGHT (KM)		
						AUORAL BRIGHTNESS	3914 A PHOTOMETER	TAN	TAN	TAN	S. DEV.
SCAN	0001	09:42:13.192	-11.678	2070	1045	0	.00	.00	.00	.00	.00
	0002	09:42:14.452	-10.408	2072	1044						
	0003	09:42:15.732	-9.38	2074	1044						
	0004	09:42:16.991	-7.879	2073	1045						
	0005	09:42:18.261	-6.609	2112	1065						
	0006	09:42:18.551	-5.319	2059	1034						
	0007	09:42:20.811	-4.059	2056	1034						
	0008	09:42:22.070	-2.000	2060	1035						
	0009	09:42:23.330	-1.540	2060	1034						
	0010	09:42:24.589	-1.281	678	379						
	0011	09:42:25.293	5.43	2204	1116						
	0012	09:42:26.635	6.765	2043	1157						
	0013	09:42:23.017	8.147	200	1132						
	0014	09:42:13.375	8.605	1099	482						
	0015	09:42:14.072	9.202	1941	798						
	0016	09:42:15.096	10.226	2394	921						
	0017	09:42:16.243	11.373	2290	931						
	0018	09:42:17.400	12.530	2257	880						
	0019	09:42:18.506	13.636	2020	798						
	0020	09:42:19.530	14.660	1912	778						
	0021	09:42:20.533	15.663	2095	820						
	0022	09:42:21.578	16.703	1363	532						
	0023	09:42:22.336	17.466	1553	716						
	0024	09:42:23.278	18.408	943	430						
	0025	09:42:23.943	19.073	1267	512						
	0026	09:42:24.691	19.821	817	327						
	0027	09:42:24.274	20.404	1246	461						
	0028	09:42:24.981	21.111	585	266						
	0029	09:42:24.503	21.633	838	349						
	0030	09:42:24.7107	22.237	455	216						
	0031	09:42:14.579	22.709	629	276						
	0032	09:42:14.621	23.251	569	236						
	0033	09:42:14.633	23.763	663	256						
	0034	09:42:14.930	24.470	027	010						
	0035	09:42:14.468	24.598	1955	881						
	0036	09:42:14.564	24.694	2303	1024						
	0037	09:42:10.813	42.943	2189	1034						
	0038	09:43:09.073	44.203	2157	1065						
	0039	09:43:10.363	45.493	2358	1055						
	0040	09:43:11.633	46.763	2086	1044						
	0041	09:43:12.903	48.033	2316	1116						
	0042	09:43:14.244	49.374	1957	893						
	0043	09:43:15.463	50.593	2213	1136						
	0044	09:43:16.825	51.963	1978	1003						
	0045	09:43:18.053	53.183	2205	1086						
	0046	09:43:19.364	54.494	2047	1106						
	0047	09:43:21.053	55.825	2355	943						
	0048	09:43:23.153	56.863	2251	1054						
	0049	09:43:24.290	56.283	2171	911						
	0050		59.420	2055	983						

PROJECT SPINRIT

INTERFEROMETER SCAN PARAMETERS

FILTER	TIME	GMT	START TIME	TAL (SEC)	DATA POINTS	MSEC LENGTH	AURORAL BRIGHTNESS			TAN AVE	S. DEV.	HORIZON SENSOR TANGENT HEIGHT (KM) OPTICAL AXIS
							3914 A PHOTOMETER AVE	3914 A PHOTOMETER S. DEV.	KR			
T > P & E	0051	09:43:25.496	60.620	2114	115.7	2.6	1.42	.0	.00			
	0052	09:43:26.870	62.000	2115	111.7	2.9	3.69	.0	.00			
	0053	09:43:28.212	63.342	2062	103.4	2.8	1.40	.0	.00			
	0054	09:43:29.471	64.601	2089	104.5	3.1	1.63	.0	.00			
	0055	09:43:30.741	65.971	2079	106.5	2.6	1.21	.0	.00			
	0056	09:43:32.021	67.151	2080	106.5	3.1	1.94	.0	.00			
	0057	09:43:33.311	68.441	2081	105.5	3.6	1.53	.0	.00			
	0058	09:43:34.591	69.721	2232	107.6	2.6	1.32	.0	.00			
	0059	09:43:35.892	71.022	2068	103.4	2.9	2.15	.0	.00			
	0060	09:43:37.152	72.882	1974	102.4	2.6	1.38	.0	.00			
	0061	09:43:38.391	73.521	2026	99.3	2.6	1.23	.0	.00			
	0062	09:43:39.609	74.739	2065	102.4	2.9	1.38	.0	.00			
	0063	09:43:40.858	75.988	2083	102.5	2.6	1.23	.0	.00			
	0064	09:43:42.108	77.238	2102	105.5	2.5	1.27	.0	.00			
	0065	09:43:43.378	78.008	2060	103.4	3.0	1.62	.0	.00			
	0066	09:43:44.637	79.767	2098	103.4	2.7	1.25	.0	.00			
	0067	09:43:45.897	81.027	2002	100.3	2.7	1.58	.0	.00			
	0068	09:43:47.125	82.255	2076	105.5	3.4	3.68	.0	.00			
	0069	09:43:48.395	83.625	2122	107.6	3.8	1.63	.0	.00			
	0070	09:43:49.696	84.826	2017	102.4	3.0	1.33	.0	.00			
	0071	09:43:50.945	85.075	2100	105.5	3.0	1.35	.0	.00			
	0072	09:43:52.235	87.365	2062	104.5	3.3	1.77	.0	.00			
	0073	09:43:53.505	88.635	2057	104.5	4.7	1.62	.0	.00			
	0074	09:43:54.775	89.905	2066	104.4	5.7	1.61	.0	.00			
	0075	09:43:56.045	91.175	2043	103.4	7.0	1.81	.0	.00			
	0076	09:43:57.304	92.434	2082	105.5	9.2	2.33	.0	.00			
	0077	09:43:58.564	93.714	2081	104.5	7.6	2.68	.0	.00			
	0078	09:43:59.854	94.984	2089	104.5	7.0	2.02	.0	.00			
	0079	09:44:01.124	96.254	2084	105.5	10.8	2.87	.0	.00			
	0080	09:44:02.394	97.524	2077	105.4	24.2	6.35	.0	.00			
	0081	09:44:03.674	98.804	2052	103.4	39.7	4.68	.0	.00			
	0082	09:44:04.933	100.053	2077	104.5	39.8	4.65	.0	.00			
	0083	09:44:06.203	101.333	2098	105.5	35.5	4.95	.0	.00			
	0084	09:44:07.483	102.613	2167	109.6	31.7	4.44	.0	.00			
	0085	09:44:08.804	103.334	2080	105.5	28.2	3.63	.0	.00			
	0086	09:44:10.074	105.204	2065	104.4	24.9	3.59	.0	.00			
	0087	09:44:11.344	106.414	2068	104.4	22.3	3.46	.0	.00			
	0088	09:44:12.613	107.443	2059	103.5	19.8	3.44	.0	.00			
	0089	09:44:13.873	109.003	2091	105.5	17.4	2.88	.0	.00			
	0090	09:44:15.153	110.263	2063	104.4	16.6	3.03	.0	.00			
	0091	09:44:16.413	111.543	1679	84.9	18.5	3.09	.0	.00			
	0092	09:44:17.477	112.807	1653	87.7	30.4	5.32	.0	.00			
	0093	09:44:17.001	122.311	1655	80.9	30.9	3.31	.0	.00			
	0094	09:44:18.015	129.145	1654	87.6	30.1	4.18	.0	.00			
	0095	09:44:19.528	132.658	1594	78.6	26.5	3.19	.0	.00			
	0096	09:44:18.521	122.651	1653	87.6	22.6	3.92	.0	.00			
	0097	09:44:19.034	143.164	1731	84.0	19.6	3.03	.0	.00			
	0098	09:44:19.089	144.219	1656	80.7	17.4	3.20	.0	.00			
	0099	09:44:19.623	153.753	1667	78.6	15.2	2.69	.0	.00			
	0100	09:44:19.595	154.725	1662	8838	14.4	1.51	.0	.00			

PROJECT SPirit

INTERFEROMETER SCAN PARAMETERS	DATA POINTS (EC)	WAVELENGTH (NM)	EXPOSURE TIME (SEC)
	290	5984	3041
	679	16658	8668
	264	2102	1075
	565	2064	1044
	824	2067	1055
	094	2100	1065
	384	2075	1045
	654	2074	1045
	924	2072	1044
	194	2083	1054
	474	2130	1075
	774	2108	1065
	064	2056	1035
	324	1980	1004
	553	2146	1075
	853	2080	1045
	123	2061	1034
	383	2051	1034
	642	2051	1034
	902	2062	1044
	1172	2055	1034
	431	2074	1045
	701	2073	1044
	971	2059	1044
	230	2040	1034
	490	2046	1034
	739	2046	1034
	999	2012	1013
	238	2057	1044
	497	2080	1055
	777	2072	1045
	047	2017	1024
	288	2081	1055
	566	2075	1045
	836	2191	1106
	167	2071	1045
	437	204	1014
	676	2084	1055
	956	2103	1065
	236	2057	1044
	506	16534	8798
	029	16554	8807
	563	2274	1116
	804	2070	1055
	1174	2072	1055
	454	2087	1055
	734	16332	8694
	155	16603	8837
	719	2245	1106

AURORAL BRIGHTNESS 3914 Å PHOTOMETER AVE KR	S.DEV. KR	HORIZON SENSOR					
		TANGENT HEIGHT (KM)	OPTICAL AXIS	TAN AVE	TAN S.DEV.	TAN AVE	TAN S.DEV.
9.9	3.19	160.6	4.61	160.6	4.61	160.6	4.61
31.0	2.00	202.3	9.28	202.3	9.28	202.3	9.28
22.4	1.17	212.2	2.20	212.2	2.20	212.2	2.20
3.2	1.40	211.0	1.14	211.0	1.14	211.0	1.14
5.6	2.20	200.5	4.04	200.5	4.04	200.5	4.04
8.3	2.25	182.8	4.25	182.8	4.25	182.8	4.25
11.5	2.52	167.6	3.37	167.6	3.37	167.6	3.37
13.8	2.40	156.6	2.21	156.6	2.21	156.6	2.21
14.5	2.70	151.7	.77	151.7	.77	151.7	.77
14.8	2.71	149.2	.28	149.2	.28	149.2	.28
13.9	2.78	150.2	.51	150.2	.51	150.2	.51
12.6	2.52	153.4	.94	153.4	.94	153.4	.94
11.4	2.63	157.2	.99	157.2	.99	157.2	.99
9.9	2.70	161.7	1.07	161.7	1.07	161.7	1.07
8.7	2.08	166.3	1.33	166.3	1.33	166.3	1.33
7.6	2.26	170.9	1.02	170.9	1.02	170.9	1.02
6.7	2.18	175.4	1.11	175.4	1.11	175.4	1.11
6.1	2.20	180.2	1.07	180.2	1.07	180.2	1.07
5.5	2.61	185.3	1.09	185.3	1.09	185.3	1.09
4.7	1.85	189.9	1.10	189.9	1.10	189.9	1.10
4.3	1.76	194.6	1.09	194.6	1.09	194.6	1.09
3.9	1.62	198.9	.87	198.9	.87	198.9	.87
3.6	1.48	202.9	1.01	202.9	1.01	202.9	1.01
3.4	1.51	206.5	.95	206.5	.95	206.5	.95
3.1	1.71	210.3	.86	210.3	.86	210.3	.86
2.8	1.59	214.0	.96	214.0	.96	214.0	.96
2.7	1.66	217.4	.77	217.4	.77	217.4	.77
2.6	5.32	220.7	.88	220.7	.88	220.7	.88
2.1	1.02	223.9	.78	223.9	.78	223.9	.78
2.3	2.50	227.0	.60	227.0	.60	227.0	.60
2.2	1.36	229.4	.50	229.4	.50	229.4	.50
1.7	1.26	231.3	.36	231.3	.36	231.3	.36
1.6	1.26	232.6	.23	232.6	.23	232.6	.23
1.4	1.91	233.2	.07	233.2	.07	233.2	.07
2.1	1.13	233.1	.08	233.1	.08	233.1	.08
1.7	1.24	233.4	.36	233.4	.36	233.4	.36
2.4	2.51	233.7	.70	233.7	.70	233.7	.70
3.4	1.26	224.8	3.55	224.8	3.55	224.8	3.55
4.6	1.26	208.4	3.89	208.4	3.89	208.4	3.89
6.0	1.77	193.7	3.28	193.7	3.28	193.7	3.28
10.7	2.91	163.6	8.87	163.6	8.87	163.6	8.87
13.5	2.69	151.0	1.21	151.0	1.21	151.0	1.21
12.8	2.43	150.9	.30	150.9	.30	150.9	.30
12.7	2.38	151.2	.31	151.2	.31	151.2	.31
12.7	2.68	151.1	.26	151.1	.26	151.1	.26
13.0	2.53	152.3	.41	152.3	.41	152.3	.41
13.0	3.11	153.8	.26	153.8	.26	153.8	.26
12.6	2.56	153.9	.42	153.9	.42	153.9	.42

PROJECT SPIRIT

INTERFEROMETER SCAN PARAMETERS

F I L L T Y P E R	E R	G M T S T A R T T I M E	T A L (S E C)	D A T A P O I N T S	M S E C L E N G T H	HORIZON SENSOR TANGENT HEIGHT (KM)			
						A U R O R A L B R I G H T S 3 9 1 4 A P H O T O M E R A V E K R	S D E V .	T A N A V E K R	S D E V .
0151	5	09:46:56.405	271.535	2071	1045	12.7	2.53	154.3	.45
0152	5	09:46:57.675	272.805	2082	1055	12.6	2.42	154.9	.37
0153	5	09:46:58.955	274.085	708	358	13.0	2.48	153.9	.20
0154	5	09:46:59.498	274.658	16804	8847	13.2	2.61	154.2	.35
0155	1	09:47:09.072	284.202	16627	6848	14.5	2.73	152.7	.85
0156	1	09:47:18.647	293.777	2288	1126	15.9	2.74	150.8	.18
0157	1	09:47:19.999	295.129	2081	1054	16.6	2.69	149.5	.14
0158	5	09:47:21.279	296.409	2070	1044	16.8	2.91	149.1	.40
0159	5	09:47:22.548	297.678	2084	1055	17.6	2.87	148.5	.47
0160	5	09:47:23.828	298.958	505	246	17.6	3.08	148.2	.27
0161	5	09:47:24.289	299.419	16723	6909	19.9	3.79	144.6	1.92
0162	5	09:47:33.925	309.055	16598	8838	28.4	4.80	137.1	2.12
0163	5	09:47:43.490	309.620	2261	1095	33.5	4.44	131.6	.69
0164	5	09:47:44.811	319.941	2587	1064	35.2	4.14	131.3	.40
0165	5	09:47:46.091	321.221	2485	1064	35.7	3.67	130.3	.46
0166	5	09:47:47.381	322.511	2149	1075	36.6	4.34	129.1	.37
0167	5	09:47:48.681	323.811	274	174	37.6	4.33	128.9	.05
0168	5	09:47:49.070	324.200	16883	8991	42.6	5.84	125.2	1.07
0169	5	09:47:58.788	319.918	16588	8827	46.6	4.82	121.6	.63
0170	2	09:48:08.342	343.472	1481	727	46.8	5.45	120.2	.04
0171	5	09:48:09.254	344.384	2173	1106	33.2	8.06	120.3	.18
0172	5	09:48:10.585	345.715	2152	1085	15.9	3.88	118.5	.52
0173	5	09:48:11.895	347.026	2153	1095	7.9	2.22	115.7	1.27
0174	5	09:48:13.217	348.347	2157	1095	5.4	1.89	106.3	3.69
0175	5	09:48:14.527	349.657	2158	1096	4.0	1.62	86.3	7.16
0176	5	09:48:15.848	350.978	2159	1096	3.7	1.44	49.4	1.95
0177	5	09:48:17.169	352.299	2153	1096	4.2	1.76	7.1	3.82
0178	5	09:48:18.490	353.620	2157	1096	3.5	1.47	0.0	0.00
0179	5	09:48:19.811	354.941	2153	1096	2.7	2.04	10.9	6.6
0180	5	09:48:21.122	356.252	2108	1065	2.2	1.69	84.9	20.76
0181	5	09:48:22.412	357.542	2103	1096	1.9	1.18	135.7	5.81
0182	5	09:48:23.733	358.863	2118	1065	2.0	1.27	146.5	.76
0183	5	09:48:25.024	360.154	2184	1106	2.4	1.17	144.7	1.56
0184	5	09:48:26.355	361.485	2109	1065	2.4	1.72	134.3	3.56
0185	5	09:48:27.645	362.775	2358	1086	2.5	2.38	119.2	3.69
0186	5	09:48:28.956	364.086	2154	1096	2.4	1.13	101.3	4.69
0187	5	09:48:30.267	365.397	2156	1095	2.8	1.24	83.7	4.54
0188	5	09:48:31.588	366.718	2159	1095	2.7	1.16	61.9	5.51
0189	5	09:48:32.909	368.039	2156	1095	3.1	4.43	39.2	5.21
0190	5	09:48:34.230	369.360	2154	1095	3.8	5.2	17.3	5.72
0191	5	09:48:35.540	370.670	2146	1096	3.8	5.7	2.01	9.5
0192	5	09:48:36.861	371.991	2152	1086	4.3	2.31	5.0	.32
0193	5	09:48:38.172	373.302	2145	1095	4.3	1.57	6.0	.21
0194	5	09:48:39.483	374.613	2152	1095	4.9	1.64	6.8	.33
0195	5	09:48:40.793	375.923	2159	1096	5.1	1.90	7.7	.24
0196	5	09:48:42.114	377.244	2154	1086	5.2	1.53	8.6	.31
0197	5	09:48:43.425	378.555	2148	1086	5.7	2.01	9.5	.20
0198	5	09:48:44.736	379.866	2146	1095	5.7	1.51	10.2	.34
0199	5	09:48:46.047	381.177	2150	1085	6.1	1.86	11.2	.31
0200	5	09:48:47.357	382.487	2145	1086	6.7	2.05	12.2	.23

F I L T E R	T Y P E	G M T	S T A R T	T A L (S E C)	D A T A P O I N T S	M S E C L E N G T	HORIZON SENSOR		
							TAN OPTICAL AXIS AVE	TAN TAN AVE	TAN S.DEV.
0201	S	09:48:48.668	383.798	2149	1086	6.6	1.86	13.0	.31
0202	S	09:48:49.979	385.109	2148	1085	7.2	1.86	14.0	.24
0203	S	09:48:51.279	386.409	2146	1086	7.2	1.79	14.9	.30
0204	S	09:48:52.590	387.720	2158	1086	7.4	2.29	15.8	.23
0205	S	09:48:53.801	389.031	2150	1085	7.5	2.24	16.6	.26
0206	S	09:48:55.212	390.342	2153	1085	7.5	2.47	17.6	.31
0207	S	09:48:56.522	391.652	2151	1086	7.1	2.10	18.6	.25
0208	S	09:48:57.833	392.963	2147	1085	6.9	2.04	19.5	.27
0209	S	09:48:59.134	394.264	2146	1085	7.0	1.89	20.5	.23
0210	S	09:49:00.434	395.564	2150	1086	7.0	1.96	21.3	.30
0211	S	09:49:01.745	396.875	2152	1075	7.2	2.02	22.2	.37
0212	S	09:49:03.035	398.185	2145	1075	6.6	2.05	23.2	.24
0213	S	09:49:04.336	399.466	2151	1065	6.1	2.37	24.1	.22
0214	S	09:49:05.626	400.756	2144	1065	8.3	2.35	24.5	.21
0215	S	09:49:06.916	402.046	2151	1075	10.5	2.36	25.4	.27
0216	S	09:49:08.217	403.347	2147	1075	15.0	3.13	26.4	.27
0217	S	09:49:09.517	404.647	2152	1075	27.2	4.64	27.3	.24
0218	S	09:49:10.818	405.948	2151	1085	32.7	4.84	28.5	.04
0219	S	09:49:12.118	407.248	2152	1085	40.9	4.98	55.5	.62
0220	S	09:49:13.429	408.559	2153	1085	56.5	9.08	79.1	.03
0221	S	09:49:14.740	409.870	2151	1075	92.6	10.95	92.2	.01
0222	S	09:49:16.040	411.170	2152	1085	118.8	8.07	98.2	.93
0223	S	09:49:17.351	412.481	2153	1085	125.9	7.44	100.9	.21
0224	S	09:49:18.662	413.792	2154	1085	120.1	8.25	101.0	.36
0225	S	09:49:19.972	415.102	2155	1086	103.8	9.11	99.1	.28
0226	S	09:49:21.283	416.413	2142	075	62.7	8.44	97.5	.65
0227	S	09:49:22.584	417.714	2139	075	60.3	6.71	94.7	.67
0228	S	09:49:23.884	418.014	2141	1075	43.2	5.37	92.3	.76
0229	S	09:49:25.185	420.315	2145	075	32.3	4.41	89.6	.81
0230	S	09:49:26.495	421.625	2146	1086	24.3	4.47	86.5	.70
0231	S	09:49:27.796	422.926	2147	1085	23.0	3.80	83.5	.82
0232	S	09:49:29.106	424.236	2152	036	28.0	3.53	80.7	.67
0233	S	09:49:30.407	425.537	2212	036	37.5	6.78	78.0	.59
0234	S	09:49:31.708	426.838	2145	1075	42.6	4.70	76.0	.64
0235	S	09:49:33.039	428.169	2083	075	89.0	64.49	73.6	.37
0236	S	09:49:34.308	429.438	2130	075	20.8	10.68	72.4	.55
0237	S	09:49:35.609	430.739	2134	1075	93.6	60.72	69.7	.62
0238	S	09:49:36.909	432.039	2137	1076	48.3	23.81	67.0	.68
0239	S	09:49:38.210	433.340	2136	1075	100.4	6.78	71.3	.45
0240	S	09:49:39.510	434.640	2113	1063	94.9	7.00	78.0	.35
0241	S	09:49:40.791	435.921	2131	1075	149.4	26.37	76.6	.20
0242	S	09:49:42.091	437.221	2137	1075	141.3	7.53	76.1	.28
0243	S	09:49:43.392	438.522	2133	1075	149.4	9.97	75.2	.12
0244	S	09:49:44.692	439.822	2146	1085	148.4	7.84	74.1	.29
0245	S	09:49:45.993	441.123	2139	1085	143.0	9.38	72.7	.25
0246	S	09:49:47.293	442.423	2136	1085	116.6	9.73	71.8	.25
0247	S	09:49:48.593	443.723	2135	1076	87.0	8.21	70.9	.18
0248	S	09:49:49.894	445.024	2123	1075	87.0	6.79	70.1	.18
0249	S	09:49:51.194	446.314	2131	1075	75.2	7.92	69.1	.95
0250	S	09:49:52.485	447.615	2117	1065	65.7	2.86	67.5	.70

PROJECT SPIRIT

PARAMETERS

F I L L T E R	T Y P E	R	G M T	S T A R T	T I M E	T A L (S E C)	D A T A P O I N T S	M S E C H	L E N G T H	S T I '	A V E	K R	T A N	A V E	K R	T A N	A V E	K R
										STI'	AVE	KR	STI'	AVE	KR	STI'	AVE	KR
0251	S	1	09:49:53.775	448.905	2116	1065	36.2	7.14	57.3	5.90								
0252	S	1	09:49:55.065	450.195	2148	1076	20.1	3.48	18.5	10.79								
0253	S	1	09:49:56.366	451.496	2208	1075	13.0	2.74										
0254	M	1	09:49:57.656	452.786	3306	1086	10.9	2.60	39.5	.24								
0255	S	3	09:49:59.172	454.302	2701	1106	9.2	2.98	40.3	.10								
0256	S	3	09:50:00.503	455.633	2583	1024	12.5	4.40		.0								
0257	S	3	09:50:01.742	456.872	2138	1116	44.3	15.58		.0								
0258	M	3	09:50:03.083	458.23	2935	1157	49.6	15.63	21.0	7.87								
0259	S	3	09:50:04.466	459.596	2315	911	37.7	7.36	32.5									
0260	S	3	09:50:05.602	460.332	2223	1147	29.7	4.95	42.5	.18								
0261	S	3	09:50:06.975	462.105	3401	1085	44.8	40.9										
0262	S	3	09:50:08.285	463.445	2311	1044	32.1	15.87	.0	.00								
0263	S	3	09:50:09.514	464.644	1794	1065	28.7	12.50		.00								
0264	S	3	09:50:10.804	465.934	1482	1065	73.2	53.09		.0								
0265	S	3	09:50:12.095	467.225	1429	1147	6.0	2.63		.0								
0266	S	3	09:50:13.467	468.597	1174	1096	42.3	43.44		.00								
0267	S	3	09:50:14.768	469.918	1102	932	21.4	24.16		.00								
0268	S	2	09:50:15.945	471.015	1201	1106	13.9	13.74		.00								
0269	S	2	09:50:17.276	472.056	1163	1209	22.3	24.85		.00								
0270	S	2	09:50:18.710	473.840	1601	1167	13.6	11.52		.00								
0271	S	2	09:50:20.102	475.232	1601	1106	27.3	29.51		.00								
0272	S	2	09:50:21.434	476.564	1128	942	19.1	27.59		.00								
0273	S	2	09:50:22.601	477.731	1690	1178	13.1	10.82		.00								
0274	S	2	09:50:24.004	479.134	1490	1044	18.1	14.21		.00								
0275	S	2	09:50:25.274	480.404	1802	1024	10.24	14.5		.00								
0276	S	2	09:50:26.523	481.653	2028	1127	8.5	3.28		.00								
0277	S	2	09:50:27.865	482.955	2097	993	18.5	21.33		.00								
0278	S	2	09:50:29.073	484.203	2107	1137	19.3	22.64		.00								
0279	S	2	09:50:30.425	485.555	1930	1013	14.9	20.06		.00								
0280	S	2	09:50:31.664	486.794	2025	1003	15.7	13.53		.00								
0281	S	2	09:50:32.882	488.012	2204	1198	19.3	15.04		.00								
0282	S	2	09:50:34.306	489.436	1836	952	24.6	18.29		.00								
0283	S	2	09:50:35.483	490.613	1579	994	14.8	12.92		.00								
0284	S	2	09:50:36.692	491.822	1663	1249	9.6	9.18		.00								
0285	S	2	09:50:38.166	493.296	1116	973	11.3	8.85		.00								
0286	S	2	09:50:39.364	494.494	1510	1055	16.2	17.13		.00								
0287	S	2	09:50:40.634	495.764	1579	1147	20.3	15.12		.00								
0288	S	2	09:50:41.996	497.126	1209	983	14.6	14.37		.00								
0289	S	2	09:50:43.194	498.324	1435	1096	12.0	13.38		.00								
0290	S	2	09:50:44.515	499.645	1904	1137	7.7	5.55		.00								
0291	S	2	09:50:45.877	501.007	1498	932	7.3	5.51		.00								
0292	S	2	09:50:47.034	502.164	1968	1290	12.8	12.71		.00								
0293	S	2	09:50:48.550	503.680	1673	1106	12.9	12.98		.00								
0294	S	2	09:50:49.881	505.011	1239	860	9.3	5.96		.00								
0295	S	2	09:50:50.966	506.096	1968	1117	6.7	6.74		.00								
0296	S	2	09:50:52.298	507.128	1575	1226	8.8	9.02		.00								
0297	S	2	09:50:53.752	508.882	1555	788	9.9	9.36		.00								
0298	S	2	09:50:55.765	509.995	1781	1096	7.1	4.65		.00								
0299	S	2	09:50:56.087	511.217	2086	1249	7.9	7.20		.00								
0300	S	2	09:50:57.561	512.691	1596	1055	9.1	8.48		.00								

HORIZON SENSOR		TANGENT HEIGHT (MM)		OPTICAL AXIS		TAN		TAN		S. DEV.	
AURORAL BRIGHTNESS		3914 A PHOTOMETER									
AVE											
KR											
DATA	WSEC	LENGTH									
POINTS											
0301	09:15:08.841	513.971	1659	952	7.8	7.43	0	.00	.00	.00	.00
0302	09:15:00.019	515.149	1828	1218	6.7	4.56	0	.00	.00	.00	.00
0303	09:15:10.148	516.563	1484	1126	8.3	5.60	0	.00	.00	.00	.00
0304	09:15:12.814	517.944	1543	1076	10.4	9.71	0	.00	.00	.00	.00
0305	09:15:04.115	519.245	1547	1024	8.1	6.58	0	.00	.00	.00	.00
0306	09:15:05.364	520.494	2026	1096	7.1	4.92	0	.00	.00	.00	.00
0307	09:15:06.685	521.815	1832	1116	5.9	2.17	0	.00	.00	.00	.00
0308	09:15:08.027	523.157	1743	1136	5.7	2.15	0	.00	.00	.00	.00
0309	09:15:09.388	524.518	1299	922	0	0.00	0	.00	.00	.00	.00
0310	09:15:10.525	525.655	1466	1024	0	0.00	0	.00	.00	.00	.00
0311	09:15:11.785	526.915	2113	1269	0	0.00	0	.00	.00	.00	.00
0312	09:15:13.280	528.410	2199	1198	0	0.00	0	.00	.00	.00	.00
0313	09:15:14.703	529.833	1685	1075	0	0.00	0	.00	.00	.00	.00
0314	09:15:16.004	531.134	2051	860	0	0.00	0	.00	.00	.00	.00
0315	09:15:17.089	532.219	2127	1239	0	0.00	0	.00	.00	.00	.00
0316	09:15:18.553	533.683	1867	840	0	0.00	0	.00	.00	.00	.00
0317	09:15:19.618	534.748	2076	1270	0	0.00	0	.00	.00	.00	.00
0318	09:15:21.113	536.243	2041	994	0	0.00	0	.00	.00	.00	.00
0319	09:15:22.332	537.462	1790	1055	0	0.00	0	.00	.00	.00	.00
0320	09:15:23.602	538.732	1559	1167	0	0.00	0	.00	.00	.00	.00
0321	09:15:24.995	540.125	2032	1064	0	0.00	0	.00	.00	.00	.00
0322	09:15:26.275	541.405	1450	1054	0	0.00	0	.00	.00	.00	.00
0323	09:15:27.555	542.685	2152	952	0	0.00	0	.00	.00	.00	.00
0324	09:15:28.722	543.852	1417	1178	0	0.00	0	.00	.00	.00	.00
0325	09:15:30.125	545.255	1966	1147	0	0.00	0	.00	.00	.00	.00
0326	09:15:31.497	546.627	1695	1055	0	0.00	0	.00	.00	.00	.00
0327	09:15:32.777	547.907	1617	1096	0	0.00	0	.00	.00	.00	.00
0328	09:15:34.098	549.228	2091	932	0	0.00	0	.00	.00	.00	.00
0329	09:15:35.255	550.385	2212	1014	0	0.00	0	.00	.00	.00	.00
0330	09:15:36.494	551.624	2220	1065	0	0.00	0	.00	.00	.00	.00
0331	09:15:37.785	552.915	1695	1136	0	0.00	0	.00	.00	.00	.00
0332	09:15:39.157	554.287	1454	1116	0	0.00	0	.00	.00	.00	.00
0333	09:15:40.498	555.628	1454	1137	0	0.00	0	.00	.00	.00	.00
0334	09:15:41.676	556.806	008	008	0	0.00	0	.00	.00	.00	.00

Appendix B

Tabulation of Payload Trajectory and Horizon Sensor Tangent Heights

Explanation of Listed Parameters

TIME	= Time after launch - seconds
ALT	= Payload altitude - kilometers
LAT.	= Payload geographic latitude - degrees
LONG.	= Payload geographic longitude - degrees
HEADING	= Payload heading relative to true north - degrees
GP	= Angle between nadir and optical centerline (LOS) - deg
QROT	= LOS omicron - degrees
LAT.	= Detector #2 tangent point latitude - degrees
LONG.	= Detector #2 tangent point longitude - degrees
TANHT-1	= Tangent height for detector #1 - kilometers
TANHT-2	= Tangent height for detector #2 - kilometers
TANHT-3	= Tangent height for detector #3 - kilometers
TANHT-4	= Tangent height for detector #4 - kilometers
TANHT-5	= Tangent height for detector #5 - kilometers

PROJECT SPIRIT ROCKET POSITION AND HORIZON SENSOR PARAMETERS

86/09/22. 10.47.46.

PAGE 1

PAYLOAD COORDINATES				POINTING				TANG. POINT COORD.			
TIME	ALT.	LAT.	LONG.	HEADING	GP	ROT	LONG.	ALT.	LAT.	LONG.	TANGT-1 : TANGT-2
80.500	104.174	65.100	147.066	56.475	100.273	-12.230	67.809	122.071	0.000	1.308	TANGT-5
81.000	104.971	65.101	147.062	56.478	125.203	-11.737	0.000	0.000	0.000	0.000	5.684
81.500	105.765	65.102	147.058	56.481	125.259	-12.224	0.000	0.000	0.000	0.000	0.000
82.000	106.557	65.103	147.054	56.484	125.208	-12.185	0.000	0.000	0.000	0.000	0.000
82.500	107.347	65.104	147.051	56.487	125.160	-12.140	0.000	0.000	0.000	0.000	0.000
83.000	108.134	65.105	147.047	56.490	125.129	-12.096	0.000	0.000	0.000	0.000	0.000
83.500	108.919	65.106	147.043	56.493	124.956	-11.691	0.000	0.000	0.000	0.000	0.000
84.000	109.701	65.107	147.040	56.496	125.032	-12.139	0.000	0.000	0.000	0.000	0.000
84.500	110.481	65.108	147.036	56.499	124.985	-12.094	0.000	0.000	0.000	0.000	0.000
85.000	111.258	65.109	147.032	56.502	124.938	-12.094	0.000	0.000	0.000	0.000	0.000
85.500	112.033	65.110	147.028	56.505	124.891	-12.094	0.000	0.000	0.000	0.000	0.000
86.000	112.806	65.111	147.025	56.508	124.730	-11.557	0.000	0.000	0.000	0.000	0.000
86.500	113.576	65.112	147.021	56.512	124.799	-12.094	0.000	0.000	0.000	0.000	0.000
87.000	114.344	65.113	147.017	56.515	124.762	-12.094	0.000	0.000	0.000	0.000	0.000
87.500	115.110	65.114	147.014	56.518	124.717	-12.094	0.000	0.000	0.000	0.000	0.000
88.000	115.872	65.115	147.010	56.522	124.672	-12.094	0.000	0.000	0.000	0.000	0.000
88.500	116.633	65.116	147.006	56.525	124.620	-11.550	0.000	0.000	0.000	0.000	0.000
89.000	117.391	65.117	147.003	56.528	124.584	-12.093	0.000	0.000	0.000	0.000	0.000
89.500	118.147	65.118	146.999	56.532	122.459	-7.415	0.000	0.000	0.000	0.000	0.000
90.000	118.906	65.119	146.995	56.535	91.119	-10.19	65.608	143.581	115.925	117.805	117.297
90.500	119.651	65.120	146.991	56.539	0.000	8.115	0.000	0.000	0.000	0.000	118.216
91.000	120.400	65.121	146.988	56.542	0.000	1.655	0.000	0.000	0.000	0.000	0.000
91.500	121.146	65.122	146.984	56.546	0.000	-2.294	0.000	0.000	0.000	0.000	0.000
92.000	121.880	65.123	146.980	56.549	0.000	-2.211	0.000	0.000	0.000	0.000	0.000
92.500	122.631	65.124	146.977	56.553	0.000	-0.029	0.000	0.000	0.000	0.000	0.000
93.000	123.370	65.125	146.973	56.556	0.000	-0.020	0.000	0.000	0.000	0.000	0.000
93.500	124.107	65.126	146.969	56.560	0.000	-0.069	0.000	0.000	0.000	0.000	0.000
94.000	124.841	65.127	146.965	56.564	0.930	-0.082	0.000	0.000	0.000	0.000	0.000
94.500	125.573	65.128	146.962	56.567	78.318	-0.009	0.000	0.000	0.000	0.000	0.000
95.000	126.302	65.129	146.958	56.571	79.545	-0.084	59.043	128.638	30.384	16.111	21.233
95.500	127.029	65.131	146.954	56.575	80.084	-0.129	59.411	129.406	41.308	28.350	32.641
96.000	127.754	65.132	146.951	56.579	80.960	-0.206	59.998	130.691	57.369	45.576	41.567
96.500	128.476	65.133	146.947	56.582	81.754	-0.277	60.519	131.896	70.709	59.976	56.397
97.000	129.196	65.134	146.943	56.586	82.464	-0.315	60.976	133.007	91.663	71.144	70.879
97.500	129.913	65.135	146.940	56.590	83.034	-0.329	61.336	133.921	69.880	83.878	78.716
98.000	130.628	65.136	146.936	56.594	83.624	-0.301	61.702	134.808	97.674	92.207	86.587
98.500	131.341	65.137	146.932	56.598	84.110	-0.302	61.998	135.701	103.701	98.675	93.476
99.000	132.051	65.138	146.929	56.602	84.555	-0.320	62.266	136.461	108.475	104.254	104.569
99.500	132.759	65.139	146.925	56.606	84.958	-0.315	62.504	137.160	113.285	109.030	106.847
100.000	133.465	65.140	146.921	56.610	85.217	-0.392	62.655	137.612	116.197	110.108	107.941
100.500	134.168	65.141	146.917	56.614	85.557	-0.363	62.852	138.217	119.602	113.970	111.952
101.000	134.869	65.142	146.914	56.618	85.872	-0.368	63.032	138.702	122.598	117.390	115.509
101.500	135.567	65.143	146.910	56.622	86.120	-0.392	63.172	139.232	124.967	121.771	120.694
102.000	136.263	65.144	146.906	56.626	86.308	-0.402	63.322	139.724	122.820	124.380	121.164
102.500	136.957	65.145	146.903	56.630	86.585	-0.459	63.431	140.087	129.159	124.912	123.341
103.000	137.648	65.146	146.899	56.634	86.868	-0.440	63.586	140.617	131.350	127.486	126.039
103.500	138.337	65.147	146.895	56.638	87.060	-0.483	63.690	140.977	132.961	130.623	129.356
104.000	139.024	65.148	146.892	56.642	87.226	-0.493	63.779	141.291	134.389	131.008	129.717
104.500	139.708	65.149	146.888	56.647	87.372	-0.483	63.857	141.568	135.678	132.493	131.266
105.000	140.390	65.150	146.884	56.651	87.457	-0.555	63.903	141.728	136.693	133.673	132.403

PAYLOAD COORDINATES				POINTING				POINT COORD.				
TIME	ALT.	LAT.	LONG.	HEADING	GP	QROT	LAT.	LONG.	GP	QROT	LAT.	LONG.
105.500	141.069	65.151	146.881	56.655	87.690	.560	64.026	142.177	138.211	135.456	135.456	134.367
106.000	141.746	65.152	146.877	56.659	87.806	.608	64.087	142.399	138.265	136.667	136.667	135.629
106.500	142.421	65.153	146.873	56.664	87.922	.569	64.147	142.623	140.292	137.850	138.740	136.862
107.000	143.083	65.154	146.870	56.668	88.033	.521	64.205	142.839	141.275	138.983	139.825	138.983
107.500	143.733	65.155	146.866	56.672	88.143	.512	64.262	143.054	142.231	140.089	140.882	139.198
108.000	144.431	65.156	146.862	56.677	88.250	.459	64.317	143.263	143.152	141.154	141.901	140.311
108.500	145.096	65.157	146.859	56.681	88.367	.406	64.377	143.493	144.068	142.228	142.924	141.435
109.000	145.759	65.158	146.855	56.685	88.499	.357	64.444	143.754	144.981	143.320	143.958	142.586
109.500	146.420	65.159	146.851	56.690	88.657	.296	64.523	144.068	145.895	144.447	145.016	143.781
110.000	147.078	65.160	146.847	56.694	88.758	.263	64.574	144.270	146.690	145.904	145.379	144.758
110.500	147.734	65.161	146.844	56.699	88.876	.239	64.632	144.506	147.479	146.328	146.802	145.759
111.000	148.387	65.162	146.840	56.703	88.968	.167	64.678	144.690	148.218	147.192	147.624	146.662
111.500	149.039	65.163	146.836	56.708	88.850	.166	64.622	144.445	148.757	147.570	148.055	147.989
112.000	149.687	65.164	146.833	56.712	88.732	.052	64.565	144.202	149.266	147.919	148.456	147.919
112.500	150.333	65.165	146.829	56.717	88.345	.052	64.437	143.418	149.258	148.387	148.93	147.584
113.000	150.977	65.166	146.825	56.721	87.973	.092	64.187	142.676	149.994	146.620	147.489	146.654
113.500	151.619	65.167	146.822	56.726	87.485	.130	63.935	141.716	148.022	144.068	144.984	143.805
114.000	152.259	65.168	146.818	56.730	86.903	.159	63.627	140.597	146.120	142.295	143.633	142.295
114.500	152.896	65.169	146.814	56.735	86.397	.212	63.352	140.642	143.995	141.483	141.044	139.483
115.000	153.530	65.170	146.811	56.740	85.950	.255	63.104	140.815	141.771	136.656	138.411	136.656
115.500	154.163	65.171	146.807	56.744	85.519	.274	62.861	138.029	139.263	133.563	135.508	133.563
116.000	154.793	65.172	146.803	56.749	85.190	.312	62.672	137.437	137.249	133.104	133.182	128.919
116.500	155.420	65.173	146.800	56.753	84.964	.351	62.541	137.033	135.930	129.478	131.666	129.478
117.000	156.045	65.174	146.796	56.758	84.696	.370	62.385	136.561	134.124	127.310	129.615	127.827
117.500	156.668	65.175	146.792	56.763	84.408	.375	62.215	136.058	131.968	124.764	125.372	122.236
118.000	157.289	65.176	146.789	56.768	84.187	.413	62.084	135.675	130.347	122.844	125.844	120.220
118.500	157.907	65.177	146.785	56.773	84.054	.427	61.904	135.444	129.565	121.881	124.468	121.881
119.000	158.523	65.178	146.781	56.777	83.874	.466	61.897	135.137	128.239	120.312	122.977	120.312
119.500	159.137	65.179	146.780	56.782	83.762	.447	61.829	134.944	127.607	122.242	119.528	116.718
120.000	159.748	65.180	146.774	56.787	83.630	.504	61.749	134.718	126.771	118.456	118.456	124.908
120.500	160.357	65.181	146.770	56.792	83.560	.504	61.707	134.597	126.511	118.158	118.158	115.259
121.000	160.964	65.182	146.767	56.797	83.448	.529	61.640	134.409	125.810	120.158	117.306	114.358
121.500	161.568	65.183	146.763	56.801	83.306	.528	61.553	134.169	124.705	116.008	116.922	116.922
122.000	162.170	65.184	146.759	56.806	83.185	.557	61.479	133.966	123.822	114.961	117.928	114.961
122.500	162.769	65.185	146.756	56.811	83.204	.600	61.491	133.993	124.653	115.816	115.816	112.761
123.000	163.366	65.186	146.752	56.816	83.147	.529	61.411	133.774	123.612	114.597	114.597	111.484
123.500	163.961	65.187	146.730	56.846	83.082	.657	61.417	133.785	124.319	115.316	115.316	112.929
124.000	164.554	65.188	146.749	56.821	83.162	.638	61.424	133.796	125.026	116.035	116.035	113.577
124.500	165.144	65.189	146.745	56.831	83.095	.681	61.428	133.799	125.667	116.681	116.681	113.577
125.000	165.732	65.190	146.737	56.836	83.069	.719	61.412	133.752	125.921	116.898	116.898	113.783
125.500	166.318	65.191	146.734	56.841	83.200	.715	61.462	133.875	127.474	118.556	118.556	115.474
126.000	166.901	65.192	146.720	56.871	83.233	.705	61.472	133.896	128.246	119.327	119.347	116.272
126.500	167.492	65.193	146.727	56.885	83.162	.696	61.473	133.892	128.824	119.924	122.904	119.924
127.000	168.080	65.194	146.723	56.856	83.199	.748	61.497	133.948	129.853	121.003	123.967	121.003
127.500	168.637	65.195	146.719	56.861	83.174	.772	61.482	133.903	130.115	121.230	124.205	121.230
128.000	169.211	65.196	146.716	56.866	83.200	.791	61.500	133.943	131.016	122.166	122.166	119.107
128.500	169.782	65.197	146.712	56.871	83.233	.772	61.521	133.992	131.983	123.176	123.176	120.130
129.000	170.351	65.198	146.708	56.877	83.270	.787	61.545	134.049	133.005	124.248	124.248	121.218
129.500	170.918	65.199	146.705	56.882	83.261	.791	61.541	134.031	133.463	127.631	127.631	121.659
130.000	171.483	65.200	146.701	56.887	83.253	.820	61.536	134.013	133.920	125.138	126.080	122.100

PAYLOAD COORDINATES

TIME	ALT.	LAT.	LONG.	HEADING	GP	QROT	LAT.	LONG.	POINT COORD.
130.500	172.045	65.201	146.697	56.892	83.275	-.830	61.551	134.046	TANHT-5
131.000	172.605	65.202	146.694	56.897	83.304	-.835	61.570	133.655	TANHT-4
131.500	173.163	65.203	146.690	56.902	83.311	-.831	61.575	134.088	TANHT-3
132.000	173.718	65.204	146.686	56.907	83.256	-.816	61.543	134.006	TANHT-2
132.500	174.271	65.205	146.683	56.912	83.264	-.854	61.596	136.012	TANHT-1
133.000	174.822	65.206	146.679	56.918	83.340	-.906	61.596	136.304	TANHT-0
133.500	175.371	65.207	146.675	56.923	83.281	-.836	61.561	136.031	TANHT-1
134.000	175.917	65.208	146.672	56.928	83.347	-.858	61.602	134.135	TANHT-0
134.500	176.460	65.209	146.668	56.933	83.397	-.836	61.634	134.214	TANHT-1
135.000	177.002	65.210	146.664	56.939	83.396	-.836	61.635	134.208	TANHT-0
135.500	177.541	65.211	146.661	56.944	83.483	-.858	61.689	134.348	TANHT-1
136.000	178.078	65.212	146.657	56.949	83.492	-.868	61.696	134.359	TANHT-0
136.500	178.612	65.213	146.654	56.954	83.511	-.906	61.712	134.397	TANHT-1
137.000	179.145	65.214	146.650	56.960	83.511	-.897	61.710	134.384	TANHT-0
137.500	179.674	65.215	146.646	56.965	83.542	-.868	61.730	134.431	TANHT-1
138.000	180.202	65.216	146.643	56.971	83.532	-.906	61.724	134.410	TANHT-0
138.500	180.727	65.217	146.639	56.976	83.547	-.887	61.735	134.431	TANHT-1
139.000	181.250	65.218	146.635	56.981	83.496	-.887	61.704	134.342	TANHT-0
139.500	181.771	65.219	146.632	56.987	83.511	-.863	61.744	134.442	TANHT-1
140.000	182.289	65.220	146.628	56.992	83.559	-.883	61.767	134.499	TANHT-0
140.500	182.805	65.221	146.624	56.997	83.627	-.897	61.788	134.548	TANHT-1
141.000	183.319	65.222	146.621	57.003	83.612	-.869	61.780	134.520	TANHT-0
141.500	183.830	65.223	146.617	57.008	83.608	-.906	61.778	134.509	TANHT-1
142.000	184.339	65.224	146.613	57.014	83.594	-.887	61.771	134.482	TANHT-0
142.500	184.846	65.225	146.610	57.019	83.529	-.777	61.731	134.368	TANHT-1
143.000	185.351	65.226	146.606	57.025	83.536	-.734	61.736	134.376	TANHT-0
143.500	185.853	65.227	146.603	57.030	83.600	-.792	61.777	134.479	TANHT-1
144.000	186.353	65.228	146.599	57.036	83.519	-.777	61.728	134.340	TANHT-0
144.500	186.850	65.229	146.595	57.041	83.542	-.825	61.743	134.374	TANHT-1
145.000	187.346	65.230	146.592	57.046	83.529	-.825	61.736	134.349	TANHT-0
145.500	187.839	65.231	146.588	57.052	83.542	-.772	61.745	134.366	TANHT-1
146.000	188.329	65.232	146.584	57.058	83.524	-.792	61.735	134.333	TANHT-0
146.500	188.818	65.233	146.581	57.063	83.512	-.825	61.729	134.309	TANHT-1
147.000	189.304	65.234	146.577	57.068	83.515	-.772	61.732	134.309	TANHT-0
147.500	189.787	65.235	146.573	57.074	83.451	-.753	61.693	134.199	TANHT-1
148.000	190.269	65.236	146.570	57.080	83.466	-.734	61.703	134.219	TANHT-0
148.500	190.748	65.237	146.566	57.085	83.480	-.748	61.720	134.238	TANHT-1
149.000	191.225	65.238	146.563	57.091	83.494	-.715	61.722	134.258	TANHT-0
149.500	191.699	65.239	146.559	57.096	83.456	-.710	61.671	134.191	TANHT-1
150.000	192.172	65.240	146.555	57.102	83.440	-.667	61.691	134.052	TANHT-0
150.500	192.642	65.241	146.552	57.108	83.413	-.676	61.676	134.096	TANHT-1
151.000	193.109	65.242	146.548	57.113	83.408	-.676	61.673	134.099	TANHT-0
151.500	193.575	65.243	146.544	57.119	83.444	-.638	61.696	134.154	TANHT-1
152.000	194.038	65.244	146.541	57.124	83.402	-.633	61.671	134.081	TANHT-0
152.500	194.499	65.245	146.537	57.130	83.387	-.619	61.663	134.052	TANHT-1
153.000	194.957	65.246	146.534	57.136	83.365	-.599	61.650	134.012	TANHT-0
153.500	195.413	65.247	146.530	57.141	83.299	-.518	61.611	133.899	TANHT-1
154.000	195.867	65.248	146.526	57.147	83.351	-.556	61.644	133.982	TANHT-0
154.500	196.319	65.249	146.523	57.153	83.377	-.517	61.660	133.019	TANHT-1
155.000	196.766	65.250	146.519	57.158	83.348	-.523	61.644	133.967	TANHT-0

PAYLOAD COORDINATES			POINTING			TANG. POINT COORD.		
TIME	ALT.	LAT.	LONG.	HEADING	GP	QROT	LAT.	LONG.
155.500	197.215	65.251	148.515	57.164	83.364	-4.460	61.655	133.991
156.000	197.680	65.252	146.512	57.170	83.334	-4.437	61.637	133.937
156.500	198.102	65.253	146.508	57.175	83.316	-4.427	61.639	133.935
157.000	198.542	65.254	146.505	57.181	83.302	-4.427	61.638	133.925
157.500	198.980	65.255	146.501	57.187	83.308	-3.365	61.624	133.881
158.000	199.416	65.256	146.497	57.192	83.389	-3.322	61.613	133.846
158.500	199.849	65.257	146.494	57.198	83.239	-3.331	61.583	133.760
159.000	200.280	65.258	146.490	57.204	83.216	-3.331	61.569	133.717
162.000	202.818	65.260	146.486	57.210	83.249	-2.255	61.591	133.768
162.500	203.233	65.265	146.483	57.215	83.272	-1.197	61.606	133.802
163.000	203.646	65.266	146.481	57.221	83.243	-1.159	61.589	133.751
163.500	204.056	65.267	146.476	57.227	83.216	-1.159	61.592	133.710
164.000	204.464	65.268	146.472	57.233	83.223	-1.159	61.579	133.710
164.500	204.870	65.268	146.468	57.238	83.216	-1.159	61.575	133.694
165.000	205.273	65.269	146.447	57.219	83.244	-0.996	61.578	133.695
165.500	205.675	65.270	146.443	57.244	83.170	-0.987	61.553	133.590
166.000	206.074	65.271	146.439	57.265	83.299	-0.939	61.634	133.798
166.500	206.470	65.272	146.436	57.290	83.173	-0.005	61.551	133.611
167.000	206.865	65.273	146.432	57.282	83.090	-0.033	61.500	133.471
167.500	207.257	65.274	146.450	57.267	83.151	-0.019	61.539	133.567
168.000	207.647	65.269	146.447	57.273	83.150	-0.095	61.540	133.561
168.500	208.034	65.275	146.443	57.279	83.170	-0.187	61.553	133.590
169.000	208.419	65.277	146.418	57.320	86.036	-0.325	63.258	138.551
169.500	208.802	65.278	146.414	57.325	86.054	-0.277	63.562	139.565
170.000	209.183	65.279	146.410	57.331	87.012	-2.533	63.796	140.374
170.500	209.562	65.280	146.407	57.337	87.360	-2.393	63.982	141.038
171.000	209.938	65.281	146.403	57.343	87.716	-2.056	64.169	141.728
171.500	210.312	65.282	146.399	57.349	87.986	-1.866	64.309	142.357
172.000	210.683	65.283	146.396	57.355	88.156	-1.722	64.396	142.591
172.500	211.052	65.284	146.392	57.361	88.321	-1.468	64.481	142.918
173.000	211.419	65.285	146.389	57.366	88.395	-1.622	64.569	143.265
173.500	211.784	65.286	146.385	57.372	88.615	-1.333	64.629	143.504
174.000	212.147	65.287	146.381	57.378	88.736	-0.084	64.689	143.745
174.500	212.507	65.288	146.378	57.384	88.835	-0.090	64.739	143.945
175.000	212.865	65.289	146.374	57.390	88.876	-1.056	64.760	144.025
175.500	213.220	65.290	146.371	57.396	88.912	-0.095	64.778	144.095
176.000	213.574	65.291	146.367	57.402	88.933	-0.085	64.790	144.135
176.500	213.925	65.292	146.363	57.407	88.946	-0.085	64.798	144.162
177.000	214.274	65.293	146.360	57.413	88.992	-1.04	64.772	144.044
177.500	214.620	65.294	146.356	57.419	88.964	-0.052	64.807	144.186
178.000	214.964	65.295	146.352	57.425	88.970	-0.052	64.812	144.197
178.500	215.306	65.296	146.349	57.431	88.766	-0.031	64.713	143.773
179.000	215.646	65.297	146.345	57.437	88.414	-0.058	64.540	143.057
179.500	215.983	65.298	146.342	57.443	87.718	-1.121	64.187	141.669
180.000	216.316	65.298	146.338	57.449	86.868	-1.121	63.737	140.022

PROJECT SPIRIT ROCKET POSITION AND HORIZON SENSOR PARAMETERS

86/09/22. 10.47.46.

PAGE 5

PAYLOAD COORDINATES		POINTING		TANG. POINT COORD.	
TIME	ALT.	LAT.	LONG.	HEADING	GP
TIME	ALT.	LAT.	LONG.	QROT	LONG.
180.800	216.651	65.299	146.334	57.555	85.971
181.000	216.982	65.300	146.331	57.461	85.984
181.500	217.310	65.301	146.327	57.467	85.984
182.000	217.636	65.302	146.324	57.472	85.984
182.500	217.960	65.303	146.320	57.478	83.364
183.000	218.281	65.304	146.316	57.484	82.934
183.500	218.601	65.305	146.313	57.490	82.539
184.000	218.917	65.306	146.309	57.496	82.289
184.500	219.232	65.307	146.305	57.502	82.055
185.000	219.544	65.308	146.302	57.508	81.858
185.500	219.855	65.309	146.298	57.514	81.658
186.000	220.162	65.310	146.295	57.520	81.689
186.500	220.468	65.311	146.291	57.526	81.679
187.000	220.771	65.312	146.287	57.532	81.648
187.500	221.072	65.313	146.284	57.538	81.648
188.000	221.371	65.314	146.280	57.544	81.674
188.500	221.667	65.315	146.277	57.550	81.719
189.000	221.962	65.316	146.273	57.555	81.784
189.500	222.253	65.317	146.269	57.561	81.873
190.000	222.543	65.318	146.266	57.567	81.981
190.500	222.830	65.319	146.262	57.573	82.000
191.000	223.116	65.320	146.258	57.579	82.094
191.500	223.398	65.321	146.255	57.585	82.194
192.000	223.679	65.322	146.251	57.591	82.304
192.500	223.957	65.322	146.248	57.597	82.319
193.000	224.233	65.323	146.244	57.603	82.499
193.500	224.507	65.324	146.240	57.609	82.615
194.000	224.778	65.325	146.237	57.615	82.715
194.500	225.047	65.326	146.233	57.621	82.800
195.000	225.314	65.327	146.220	57.627	82.853
195.500	225.579	65.328	146.226	57.633	83.016
196.000	225.841	65.329	146.222	57.639	83.132
196.500	226.101	65.330	146.219	57.645	83.258
197.000	226.359	65.331	146.215	57.651	83.368
197.500	226.615	65.332	146.211	57.657	83.454
198.000	226.868	65.333	146.208	57.663	83.658
198.500	227.119	65.334	146.204	57.668	83.784
199.000	227.368	65.335	146.201	57.675	83.910
199.500	227.614	65.336	146.197	57.680	84.047
200.000	227.858	65.337	146.193	57.686	84.102
200.500	228.100	65.338	146.190	57.692	84.296
201.000	228.240	65.339	146.186	57.698	84.441
201.500	228.577	65.340	146.183	57.704	84.594
202.000	228.813	65.341	146.179	57.710	84.710
202.500	229.045	65.342	146.175	57.716	84.770
203.000	229.276	65.343	146.172	57.722	84.973
203.500	229.504	65.344	146.168	57.728	85.119
204.000	229.730	65.344	146.165	57.734	85.215
204.500	229.954	65.345	146.161	57.740	85.342
205.000	230.175	65.346	146.157	57.746	85.442

PAYLOAD COORDINATES				POINTING				TANG. POINT COORD.			
TIME	ALT.	LAT.	LONG.	HEADING	GP	QROT	LAT.	LONG.	TANG. 1	TANG. 2	TANG. 3
205.500	230.395	65.347	146.154	57.752	85.639	1.044	63.103	137.541	216.252	210.652	212.565
206.000	230.612	65.348	146.150	57.758	85.776	1.005	63.182	137.786	211.482	212.069	213.922
206.500	230.826	65.349	146.146	57.764	85.927	.982	63.268	138.059	218.776	213.579	215.356
207.000	231.039	65.350	146.143	57.770	86.094	1.010	63.363	138.362	220.119	215.141	216.503
207.500	231.249	65.351	146.139	57.776	86.248	1.006	63.450	138.645	221.332	216.565	216.565
208.000	231.457	65.352	146.136	57.782	86.402	.953	63.536	138.927	222.487	217.930	219.506
208.500	231.662	65.353	146.132	57.788	86.553	.972	63.620	139.579	223.579	220.738	219.229
209.000	231.866	65.354	146.128	57.793	86.693	.77	63.698	139.468	224.564	220.406	221.853
209.500	232.067	65.355	146.125	57.799	86.885	.953	63.803	139.829	225.770	221.875	223.237
210.000	232.265	65.356	146.121	57.805	87.084	.935	63.911	140.543	226.930	224.582	223.308
210.500	232.462	65.357	146.118	57.811	87.261	.901	64.006	140.543	227.917	224.537	224.537
211.000	232.656	65.358	146.114	57.817	87.467	.895	64.115	140.939	228.951	225.854	226.958
211.500	232.848	65.359	146.110	57.823	87.697	.895	64.236	141.385	229.979	227.197	226.097
212.000	233.038	65.360	146.107	57.829	87.886	.890	64.335	141.754	230.776	228.253	227.237
212.500	233.225	65.361	146.103	57.835	88.081	.854	64.436	142.138	231.514	228.258	228.329
213.000	233.410	65.362	146.099	57.841	88.339	.819	64.567	142.652	232.312	230.410	229.596
213.500	233.593	65.363	146.096	57.847	88.533	.829	64.650	143.040	232.866	231.230	230.501
214.000	233.774	65.363	146.092	57.853	88.684	.874	64.740	143.343	233.283	232.855	232.419
214.500	233.952	65.364	146.089	57.859	88.943	.766	64.868	143.871	233.760	232.688	233.137
215.000	234.128	65.365	146.085	57.865	89.164	.763	64.975	144.323	234.083	233.314	232.865
215.500	234.302	65.366	146.081	57.871	89.421	.799	65.099	144.857	234.305	233.889	233.555
216.000	234.474	65.367	146.078	57.877	89.647	.799	65.205	145.328	234.408	234.302	234.439
216.500	234.643	65.368	146.074	57.882	89.816	.855	65.284	145.681	234.459	234.646	234.585
217.000	234.810	65.369	146.070	57.888	90.097	.799	65.413	146.863	234.913	234.813	234.779
217.500	234.975	65.370	146.067	57.894	90.321	.799	65.514	145.378	234.903	234.912	234.978
218.000	235.137	65.371	146.063	57.900	90.544	.790	65.614	144.888	233.782	234.908	234.646
218.500	235.297	65.372	146.060	57.906	90.753	.780	65.705	144.429	233.822	234.467	235.080
219.000	235.455	65.373	146.056	57.912	90.870	.741	65.756	144.906	233.231	234.804	234.804
219.500	235.611	65.374	146.052	57.918	90.904	.626	65.772	144.090	233.283	234.903	234.481
220.000	235.764	65.375	146.049	57.924	90.588	.608	65.636	145.681	234.779	234.305	235.750
220.500	235.915	65.376	146.045	57.930	90.987	.569	65.370	146.017	235.553	235.914	235.899
221.000	236.064	65.377	146.042	57.936	90.188	.517	64.998	144.330	236.030	235.294	235.634
221.500	236.211	65.378	146.038	57.942	88.202	.546	64.514	142.313	234.803	232.713	231.837
222.000	236.355	65.379	146.034	57.948	87.280	.478	64.037	140.492	231.888	228.532	227.247
222.500	237.173	65.384	146.013	57.983	83.341	.498	63.516	138.654	226.995	222.317	223.933
223.000	237.301	65.385	146.009	57.989	82.903	.673	61.498	132.672	194.934	225.210	235.491
223.500	237.428	65.386	146.005	57.995	82.611	.637	61.315	132.194	191.153	215.631	213.557
224.000	237.551	65.387	146.002	57.996	83.838	.659	62.672	135.966	201.913	209.210	208.842
224.500	237.673	65.388	146.000	57.972	84.276	.572	62.339	134.984	210.577	203.106	200.490
225.000	237.792	65.389	146.016	57.977	83.760	.608	62.027	134.100	205.123	196.947	194.102
225.500	237.909	65.390	145.991	58.019	81.814	.709	60.807	130.915	180.123	169.293	168.555
226.000	238.024	65.391	145.987	58.025	81.632	.742	60.689	130.628	177.423	165.589	162.367
226.500	238.137	65.392	145.984	58.031	81.492	.766	60.598	130.407	175.324	164.056	162.056
227.000	238.247	65.393	145.980	58.037	81.403	.790	60.541	130.267	174.020	162.632	162.750
227.500	238.355	65.394	145.994	58.013	81.981	.704	60.914	131.101	182.526	171.924	168.296
228.000	238.471	65.395	145.991	58.019	81.814	.627	61.771	133.396	191.584	189.714	185.589
228.500	238.589	65.396	145.997	58.025	81.632	.673	61.498	132.672	194.934	186.409	184.409
229.000	238.706	65.397	145.994	58.001	82.332	.676	61.138	131.744	187.396	177.272	173.799
229.500	238.823	65.398	145.998	58.007	82.143	.709	61.018	131.440	187.795	174.414	170.857
230.000	238.940	65.399	145.994	58.013	81.981	.608	61.027	134.100	196.947	194.102	192.247

PAYLOAD COORDINATES		POINTING		TANG. POINT COORD.		TANHT-1		TANHT-2		TANHT-3		TANHT-4		TANHT-5		
TIME	ALT.	LAT.	LONG.	HEADING	GP	QROT	LAT.	LONG.	GP	QROT	LAT.	LONG.	GP	QROT	LAT.	LONG.
230.500	238.460	65.395	145.973	58.048	81.236	.895	60.433	130.003	171.519	159.903	63.762	155.948	81.236	.895	60.433	130.003
231.000	238.564	65.396	145.969	58.054	81.158	.900	60.329	129.750	169.051	158.614	62.756	154.624	81.158	.900	60.329	129.750
231.500	238.665	65.397	145.965	58.060	81.075	.657	60.309	129.700	168.634	156.757	61.146	157.216	81.075	.657	60.309	129.700
232.000	238.764	65.397	145.962	58.066	81.044	.891	60.293	129.657	168.294	156.382	60.701	156.757	81.044	.891	60.293	129.657
232.500	238.860	65.398	145.958	58.072	81.014	.934	60.249	129.550	167.239	155.234	59.219	155.234	81.014	.934	60.249	129.550
233.000	238.955	65.399	145.955	58.076	80.950	.943	60.205	129.446	166.201	154.106	58.120	154.106	80.950	.943	60.205	129.446
233.500	239.047	65.400	145.951	58.084	80.884	.938	60.160	129.427	166.120	154.011	58.030	149.995	80.884	.938	60.160	129.427
234.000	239.136	65.401	145.947	58.090	80.874	.977	60.200	129.331	165.149	152.957	54.011	149.897	80.874	.977	60.200	129.331
234.500	239.224	65.402	145.944	58.096	80.813	1.063	60.160	129.331	165.149	152.957	54.011	149.897	80.813	1.063	60.160	129.331
235.000	239.309	65.403	145.940	58.102	80.810	1.084	60.159	129.323	165.195	153.000	57.046	149.857	80.810	1.084	60.159	129.323
235.500	239.392	65.404	145.936	58.108	80.820	1.054	60.166	129.333	165.438	153.255	53.255	149.116	80.820	1.054	60.166	129.333
236.000	239.473	65.405	145.933	58.114	80.811	1.078	60.161	129.316	165.368	153.173	57.219	152.331	80.811	1.078	60.161	129.316
236.500	239.551	65.406	145.929	58.119	80.812	1.106	60.163	129.313	165.460	153.266	53.173	149.030	80.812	1.106	60.163	129.313
237.000	239.627	65.407	145.925	58.125	80.772	1.124	60.137	129.249	164.838	152.590	56.653	149.124	80.772	1.124	60.137	129.249
237.500	239.701	65.408	145.922	58.131	80.758	1.092	60.129	129.224	164.675	152.408	58.408	148.242	80.758	1.092	60.129	129.224
238.000	239.773	65.409	145.918	58.137	80.759	1.053	60.131	129.222	164.771	152.506	56.575	148.340	80.759	1.053	60.131	129.222
238.500	239.842	65.410	145.915	58.143	80.714	1.006	60.101	129.150	164.044	151.717	55.806	147.531	80.714	1.006	60.101	129.150
239.000	239.909	65.411	145.911	58.149	80.653	1.015	60.061	129.056	163.055	150.646	54.761	146.434	80.653	1.015	60.061	129.056
239.500	239.974	65.412	145.907	58.155	80.666	.976	60.071	129.071	163.342	150.950	55.060	146.744	80.666	.976	60.071	129.071
240.000	240.036	65.413	145.904	58.161	80.668	.905	60.013	129.069	163.433	151.043	55.050	146.837	80.668	.905	60.013	129.069
240.500	240.096	65.413	145.900	58.167	80.644	.875	60.058	129.030	163.078	150.656	54.775	146.439	80.644	.875	60.058	129.030
241.000	240.154	65.414	145.896	58.173	80.641	.823	60.057	129.022	163.085	150.659	54.780	146.441	80.641	.823	60.057	129.022
241.500	240.210	65.415	145.893	58.178	80.639	.766	60.056	129.014	163.091	150.662	54.784	146.443	80.639	.766	60.056	129.014
242.000	240.263	65.416	145.889	58.185	80.615	.723	60.041	128.974	162.725	150.263	54.396	146.034	80.615	.723	60.041	128.974
242.500	240.314	65.417	145.885	58.190	80.592	.704	60.026	128.935	162.872	154.015	49.872	145.633	80.592	.704	60.026	128.935
243.000	240.363	65.418	145.882	58.196	80.605	.646	60.036	128.951	162.653	150.315	51.178	145.944	80.605	.646	60.036	128.951
243.500	240.410	65.419	145.900	58.202	80.629	.622	60.053	128.982	163.116	150.672	54.799	146.449	80.629	.622	60.053	128.982
244.000	240.454	65.420	145.875	58.208	80.600	.671	60.035	128.936	162.660	150.178	54.317	145.942	80.600	.671	60.035	128.936
244.500	240.496	65.421	145.871	58.214	80.612	.694	60.043	128.949	162.902	150.435	54.570	146.205	80.612	.694	60.043	128.949
245.000	240.536	65.422	145.867	58.220	80.664	.593	60.080	129.023	163.866	151.471	55.582	147.263	80.664	.593	60.080	129.023
245.500	240.573	65.423	145.864	58.226	80.642	.511	60.065	128.985	163.504	151.077	55.198	146.860	80.642	.511	60.065	128.985
246.000	240.608	65.424	145.860	58.232	80.645	.479	60.088	128.986	163.600	151.178	54.298	146.962	80.645	.479	60.088	128.986
246.500	240.641	65.425	145.856	58.238	80.675	.492	60.089	129.022	164.155	151.773	55.880	147.570	80.675	.492	60.089	129.022
247.000	240.672	65.426	145.853	58.243	80.632	.517	60.061	128.958	163.424	150.983	55.109	146.761	80.632	.517	60.061	128.958
247.500	240.700	65.427	145.849	58.249	80.672	.449	60.089	129.014	164.162	155.776	54.884	147.572	80.672	.449	60.089	129.014
248.000	240.726	65.428	145.845	58.256	80.639	.402	60.068	128.961	163.610	151.180	55.302	146.961	80.639	.402	60.068	128.961
248.500	240.750	65.428	145.842	58.261	80.633	.363	60.065	128.948	163.526	151.088	55.213	146.866	80.633	.363	60.065	128.948
249.000	240.772	65.429	145.838	58.267	80.674	.321	60.093	129.004	164.267	151.884	55.991	147.884	80.674	.321	60.093	129.004
249.500	240.791	65.430	145.834	58.273	80.631	.368	60.065	128.986	163.530	151.089	55.215	146.866	80.631	.368	60.065	128.986
250.000	240.808	65.431	145.831	58.279	80.672	.287	60.093	128.993	164.263	151.877	55.985	147.672	80.672	.287	60.093	128.993
250.500	240.822	65.432	145.827	58.285	80.655	.243	60.083	128.965	163.994	151.586	55.701	147.374	80.655	.243	60.083	128.965
251.000	240.835	65.433	145.824	58.291	80.671	.239	60.095	128.983	164.275	151.888	55.996	147.683	80.671	.239	60.095	128.983
251.500	240.845	65.434	145.820	58.297	80.707	.239	60.120	129.033	164.917	152.579	55.178	148.389	80.707	.239	60.120	129.033
252.000	240.853	65.435	145.816	58.303	80.733	.186	60.138	129.088	165.378	153.074	55.156	148.896	80.733	.186	60.138	129.088
252.500	240.858	65.436	145.813	58.309	80.753	.167	60.152	129.094	165.733	153.457	55.215	149.288	80.753	.167	60.152	129.094
253.000	240.862	65.437	145.809	58.315	80.742	.167	60.146	129.073	165.543	153.252	55.173	149.078	80.742	.167	60.146	129.073
253.500	240.863	65.438	145.805	58.321	80.716	.148	60.129	129.050	165.093	152.766	55.855	148.581	80.716	.148	60.129	129.050
254.000	240.861	65.439	145.802	58.327	80.732	.123	60.141	129.050	165.370	153.066	55.147	149.887	80.732	.123	60.141	129.050
254.500	240.858	65.440	145.798	58.348	80.713	.109	60.152	129.069	165.638	153.355	54.429	153.355	80.713	.109	60.152	129.069
255.000	240.852	65.441	145.794	58.339	80.739	.099	60.130	129.013	165.022	152.691	55.782	148.504	80.739	.099	60.130	129.013

TIME	PAYLOAD COORDINATES			POINTING			TANG. POINT COORD.		
	ALT.	LAT.	LONG.	HEADING	GP	QROT	LAT.	LONG.	TANHT-1
255.500	240.844	65.442	145.791	58.345	80.733	.033	60.144	129.039	165.368
256.000	240.834	65.443	145.787	58.350	80.743	.018	60.152	129.050	165.539
256.500	240.821	65.443	145.783	58.356	80.713	.014	60.133	129.001	164.996
257.000	240.806	65.444	145.780	58.362	80.735	.033	60.148	129.030	165.372
257.500	240.789	65.445	145.776	58.368	80.777	.033	60.177	129.089	166.086
258.000	240.769	65.446	145.772	58.374	80.736	.014	60.151	129.024	165.358
258.500	240.747	65.447	145.769	58.380	80.675	.033	60.111	128.928	164.264
259.000	240.723	65.448	145.765	58.386	80.739	.032	60.154	129.019	165.352
259.500	240.697	65.449	145.761	58.392	80.797	-.044	60.195	129.103	166.345
260.000	240.668	65.450	145.758	58.398	80.804	-.058	60.200	129.108	166.431
260.500	240.637	65.451	145.754	58.404	80.800	-.025	60.198	129.099	166.337
261.000	240.604	65.452	145.750	58.410	80.797	-.026	60.197	129.090	166.246
261.500	240.569	65.453	145.747	58.416	80.609	-.068	60.206	129.103	166.417
262.000	240.531	65.454	145.743	58.422	80.816	-.097	60.211	129.110	166.502
262.500	240.491	65.455	145.740	58.428	80.813	-.101	60.210	129.101	166.407
263.000	240.449	65.456	145.736	58.434	80.810	-.121	60.209	129.092	166.311
263.500	240.404	65.457	145.732	58.440	80.812	-.140	60.211	129.091	166.300
264.000	240.357	65.457	145.729	58.446	80.799	-.135	60.203	129.067	166.027
264.500	240.308	65.458	145.725	58.452	80.801	-.135	60.206	129.067	166.025
265.000	240.256	65.459	145.721	58.458	80.830	-.120	60.226	129.105	166.464
265.500	240.203	65.460	145.718	58.464	80.832	-.103	60.228	129.105	166.452
266.000	240.147	65.461	145.714	58.470	80.820	-.140	60.221	128.082	166.183
266.500	240.088	65.462	145.710	58.476	80.854	-.159	60.244	129.129	166.710
267.000	240.028	65.463	145.707	58.482	80.841	-.159	60.237	129.106	166.432
267.500	239.965	65.464	145.703	58.488	80.845	-.159	60.240	129.107	166.436
268.000	239.900	65.465	145.699	58.494	80.805	-.102	60.215	129.044	165.691
268.500	239.832	65.466	145.696	58.500	80.783	-.121	60.201	129.006	165.233
269.000	239.763	65.467	145.692	58.506	80.844	-.154	60.242	129.093	166.219
269.500	239.691	65.468	145.688	58.512	80.878	-.178	60.266	129.141	166.738
270.000	239.616	65.469	145.695	58.518	80.793	-.121	60.211	129.009	165.204
270.500	239.540	65.470	145.681	58.524	80.981	-.178	60.270	129.136	166.436
271.000	239.461	65.471	145.677	58.530	80.911	-.159	60.291	129.177	167.065
271.500	239.380	65.471	145.674	58.536	80.849	-.123	60.251	129.081	165.935
272.000	239.296	65.472	145.670	58.543	80.878	-.178	60.270	129.120	166.341
272.500	239.211	65.473	145.666	58.549	80.952	-.181	60.321	129.227	167.518
273.000	239.123	65.474	145.662	58.554	80.984	-.173	60.241	129.009	165.985
273.500	239.032	65.475	145.659	58.561	90.927	-.140	60.306	129.181	166.913
274.000	238.940	65.476	145.655	58.567	80.871	-.099	60.270	129.093	165.877
274.500	238.845	65.477	145.651	58.573	80.842	-.092	60.251	129.045	165.279
275.000	238.748	65.478	145.648	58.579	80.920	-.139	60.304	129.158	166.516
275.500	238.648	65.479	145.644	58.585	80.935	-.101	60.315	129.177	166.683
276.000	238.547	65.480	145.640	58.591	80.957	-.135	60.330	129.205	166.942
276.500	238.443	65.481	145.637	58.597	80.987	-.140	60.358	129.263	167.532
277.000	238.336	65.482	145.633	58.604	80.992	-.163	60.355	129.250	167.765
277.500	238.228	65.483	145.629	58.610	80.966	-.135	60.339	129.207	166.785
278.000	238.117	65.484	145.626	58.616	80.936	-.130	60.320	129.158	166.172
278.500	238.004	65.485	145.622	58.622	80.962	-.097	60.338	129.193	166.505
279.000	237.888	65.485	145.618	58.628	80.983	-.101	60.353	129.221	166.742
279.500	237.770	65.486	145.615	58.634	80.978	-.095	60.360	129.209	166.537
280.000	237.650	65.487	145.611	58.640	80.974	-.030	60.349	129.199	166.353

PAYLOAD COORDINATES				POINTING				TANG. POINT COORD.			
TIME	ALT.	LAT.	LONG.	GP	QROT	LAT.	LONG.	GP	QROT	LAT.	LONG.
280.500	237.528	65.488	145.607	58.647	81.001	-0.045	60.368	129.235	166.687	154.754	158.716
281.000	237.403	65.489	145.604	58.653	81.002	-0.064	60.369	129.232	166.580	154.648	158.610
281.500	237.277	65.490	145.600	58.659	80.977	-0.024	60.353	129.190	166.032	154.067	154.648
282.000	237.147	65.491	145.596	58.665	80.999	0.008	60.369	129.220	166.277	154.342	154.309
282.500	237.016	65.492	145.592	58.672	81.022	0.009	60.385	129.250	166.526	154.622	158.574
283.000	236.882	65.493	145.589	58.678	81.028	0.013	60.390	129.255	166.500	154.605	158.554
283.500	236.746	65.494	145.585	58.684	80.956	0.051	60.343	129.143	165.158	153.166	153.166
284.000	236.608	65.495	145.581	58.690	80.943	0.052	60.335	129.119	164.799	152.789	156.776
284.500	236.467	65.496	145.578	58.697	81.054	0.038	60.410	129.282	166.564	158.602	158.664
285.000	236.324	65.497	145.574	58.703	81.061	0.033	60.415	129.288	166.501	154.651	158.586
285.500	236.179	65.498	145.570	58.709	81.057	0.009	60.414	129.278	166.294	154.439	158.375
286.000	236.031	65.499	145.567	58.715	80.997	0.034	60.375	128.183	165.136	153.199	157.162
286.500	235.882	65.499	145.563	58.722	80.999	0.086	60.377	129.183	165.030	153.098	153.098
287.000	235.730	65.500	145.559	58.728	81.013	0.129	60.387	129.199	165.111	153.198	153.198
287.500	235.575	65.501	145.556	58.734	81.036	0.134	60.403	129.229	165.336	157.398	153.453
288.000	235.418	65.502	145.552	58.741	81.043	0.167	60.409	129.237	165.312	153.440	157.382
288.500	235.259	65.503	145.548	58.747	81.035	0.177	60.405	129.221	165.020	153.137	157.082
289.000	235.098	65.504	145.544	58.753	81.038	0.186	60.408	129.221	164.913	153.035	156.979
289.500	234.935	65.505	145.541	58.759	81.052	0.206	60.417	129.237	164.976	157.054	153.116
290.000	234.769	65.506	145.537	58.766	81.060	0.244	60.424	129.246	164.950	153.102	157.036
290.500	234.601	65.507	145.533	58.772	81.004	0.264	60.441	129.278	165.186	153.371	157.295
291.000	234.430	65.508	145.530	58.774	81.043	0.264	60.449	129.237	165.312	153.440	149.402
291.500	234.258	65.509	145.526	58.785	81.060	0.177	60.405	129.221	165.020	153.137	149.095
292.000	234.082	65.510	145.522	58.792	81.047	0.302	60.408	129.221	164.913	153.035	148.995
292.500	233.905	65.511	145.518	58.798	81.021	0.359	60.402	129.237	164.976	157.054	149.082
293.000	233.726	65.512	145.515	58.804	81.015	0.362	60.399	129.152	163.154	151.541	149.072
293.500	233.544	65.512	145.511	58.811	80.944	0.429	60.353	129.099	162.152	151.246	155.200
294.000	233.359	65.513	145.507	58.817	81.072	0.301	60.433	129.255	164.811	152.980	156.908
294.500	233.173	65.514	145.504	58.824	81.060	0.315	60.426	129.232	164.436	152.522	152.588
295.000	232.984	65.515	145.500	58.830	80.966	0.494	60.370	129.209	164.054	152.190	156.129
295.500	232.793	65.516	145.496	58.837	81.003	0.512	60.395	129.113	162.029	150.106	154.064
296.000	232.600	65.517	145.493	58.843	80.997	0.546	60.392	129.099	163.737	149.807	149.768
296.500	232.404	65.518	145.489	58.850	81.022	0.555	60.410	129.134	161.973	150.078	154.027
297.000	232.206	65.519	145.485	58.856	81.011	0.569	60.404	129.113	161.593	149.941	152.888
297.500	232.006	65.520	145.481	58.863	80.938	0.609	60.356	128.998	160.154	148.144	147.328
298.000	231.803	65.521	145.478	58.869	81.026	0.589	60.415	129.127	161.438	149.548	149.548
298.500	231.598	65.522	145.474	58.876	80.969	0.628	60.378	129.036	160.276	148.309	148.309
299.000	231.391	65.523	145.470	58.883	80.996	0.698	60.397	129.073	160.528	148.598	148.598
299.500	231.182	65.524	145.466	58.889	81.026	0.724	60.418	129.115	160.829	148.941	148.897
300.000	230.970	65.525	145.463	58.896	80.990	0.747	60.395	129.055	160.008	148.071	148.034
300.500	230.756	65.526	145.459	58.902	80.964	0.742	60.379	129.013	159.367	147.396	147.396
301.000	230.540	65.527	145.455	58.909	80.975	0.781	60.387	129.025	159.333	147.376	147.376
301.500	230.321	65.527	145.452	58.916	80.939	0.819	60.364	128.967	158.513	146.509	146.509
302.000	230.100	65.528	145.448	58.923	80.956	0.853	60.376	128.987	158.573	146.591	146.591
302.500	229.877	65.529	145.444	58.929	80.946	0.896	60.370	128.969	158.190	146.196	146.196
303.000	229.651	65.530	145.440	58.936	80.925	0.929	60.367	128.932	157.603	145.581	145.581
303.500	229.424	65.531	145.437	58.943	80.886	0.972	60.332	128.869	156.711	144.635	144.635
304.000	229.193	65.532	145.433	58.949	80.876	1.010	60.327	128.851	156.326	144.238	144.238
304.500	228.961	65.533	145.429	58.956	80.888	1.016	60.335	128.865	156.297	144.227	144.227
305.000	228.726	65.534	145.425	58.963	80.900	1.088	60.344	128.878	156.269	144.215	144.215

PAYLOAD COORDINATES		POINTING		TANG. POINT COORD.		TANHT-1		TANHT-2		TANHT-3		TANHT-4		TANHT-5		
TIME	ALT.	LAT.	LNG.	HEADING	GP	QROT	LAT.	LONG.	HEADING	GP	QROT	LAT.	LONG.	HEADING	GP	
305.500	228.439	65.535	145.418	58.970	80.902	60.346	28.877	155.855	145.004	148.010	144.010	139.914	143.806	139.914	139.914	
306.000	228.250	65.536	145.418	58.976	80.903	60.335	28.875	155.855	143.806	147.805	143.806	139.911	143.806	139.911	139.911	
306.500	228.008	65.537	145.414	58.983	80.884	60.336	28.842	155.291	143.217	147.224	143.217	139.114	143.013	139.114	139.114	
307.000	227.764	65.538	145.411	58.990	80.886	60.339	28.841	155.084	143.013	147.019	143.013	138.911	143.013	138.911	138.911	
307.500	227.518	65.539	145.407	58.997	80.914	60.334	28.878	155.305	143.272	147.272	143.272	139.82	143.272	139.82	139.82	
308.000	227.270	65.539	145.403	59.004	80.843	60.311	28.767	153.849	141.719	145.744	141.719	137.598	141.719	137.598	137.598	
308.500	227.019	65.540	145.399	59.011	80.778	60.318	28.666	152.468	140.272	144.325	140.272	136.123	140.272	136.123	136.123	
309.000	226.766	65.541	145.396	59.017	80.774	60.317	28.667	128.655	152.165	139.944	143.999	135.944	135.944	135.944	135.944	
309.500	226.510	65.542	145.392	59.024	80.846	60.316	28.759	153.47	141.023	145.046	141.023	136.904	141.023	136.904	136.904	
310.000	226.253	65.543	145.388	59.031	80.823	60.302	28.720	152.496	140.342	144.375	140.342	136.212	140.342	136.212	136.212	
310.500	225.993	65.544	145.384	59.038	80.825	60.304	28.719	152.283	140.133	144.164	140.133	136.005	140.133	136.005	136.005	
311.000	225.730	65.545	145.381	59.045	80.782	60.276	28.650	151.271	139.062	143.112	139.062	134.914	143.112	134.914	134.914	
311.500	225.466	65.546	145.377	59.052	80.806	60.293	28.681	151.424	139.247	143.288	139.247	135.111	143.288	135.111	135.111	
312.000	225.199	65.547	145.373	59.059	80.829	60.310	28.713	151.570	139.426	143.426	139.426	135.301	143.426	135.301	135.301	
312.500	224.930	65.548	145.369	59.066	80.801	60.292	28.667	150.823	138.642	142.683	138.642	134.504	142.683	134.504	134.504	
313.000	224.658	65.549	145.366	59.073	80.795	60.288	28.653	150.440	138.251	142.295	138.251	134.110	142.295	134.110	134.110	
313.500	224.384	65.550	145.362	59.080	80.782	60.705	28.781	128.629	149.951	137.745	141.795	133.599	137.745	133.599	133.599	
314.000	224.108	65.551	145.358	59.087	80.719	60.759	28.739	128.530	148.577	136.286	140.363	136.286	132.112	140.363	132.112	132.112
314.500	223.830	65.552	145.354	59.095	80.699	60.835	28.727	128.496	147.952	135.634	139.720	135.634	131.452	139.720	131.452	131.452
315.000	223.549	65.553	145.351	59.102	80.742	60.854	28.557	128.557	148.435	136.176	140.243	136.176	132.013	140.243	132.013	132.013
315.500	223.266	65.554	145.347	59.109	80.757	60.267	28.574	148.403	136.164	140.244	136.164	132.008	140.244	132.008	132.008	
316.000	222.981	65.554	145.343	59.116	80.730	60.811	28.529	147.651	135.377	139.449	135.377	131.209	139.449	131.209	131.209	
316.500	222.693	65.555	145.339	59.123	80.729	60.815	28.521	128.524	147.359	135.084	139.156	135.084	130.916	139.156	130.916	130.916
317.000	222.403	65.556	145.336	59.130	80.744	60.717	28.521	128.543	147.333	135.079	139.144	135.079	130.918	139.144	130.918	130.918
317.500	222.111	65.557	145.332	59.138	80.717	60.777	28.524	128.499	146.581	134.291	138.368	134.291	130.119	138.368	130.119	130.119
318.000	221.816	65.558	145.328	59.145	80.634	60.820	28.570	128.370	144.838	132.437	136.550	132.437	128.226	136.550	128.226	128.226
318.500	221.519	65.559	145.324	59.153	80.581	60.155	28.286	143.602	131.129	135.265	131.129	126.897	135.265	126.897	126.897	
319.000	221.220	65.560	145.321	59.167	80.666	60.739	28.408	144.795	132.438	136.348	136.348	128.243	136.348	128.243	128.243	
319.500	220.919	65.561	145.317	59.167	80.617	60.733	28.408	128.408	144.795	132.438	136.342	136.342	127.006	136.342	127.006	127.006
320.000	220.615	65.562	145.313	59.174	80.644	60.719	28.408	128.368	143.819	131.433	135.541	131.433	127.30	135.541	127.30	127.30
320.500	220.309	65.563	145.309	59.182	80.701	60.662	28.322	141.469	132.198	138.281	132.198	128.019	132.198	128.019	128.019	
321.000	220.001	65.564	145.306	59.189	80.617	60.739	28.318	142.732	130.310	134.430	130.310	126.095	134.430	126.095	126.095	
321.500	219.690	65.565	145.302	59.197	80.676	60.681	28.403	143.462	131.121	135.214	135.214	126.932	135.214	126.932	126.932	
322.000	219.377	65.565	145.298	59.204	80.649	60.667	28.307	128.359	142.688	130.311	134.416	130.311	126.110	134.416	126.110	126.110
322.500	219.062	65.566	145.294	59.212	80.593	60.716	28.306	143.645	131.322	135.342	131.322	127.006	135.342	127.006	127.006	
323.000	218.744	65.567	145.290	59.219	80.641	60.643	28.303	128.338	141.916	131.433	135.541	131.433	127.30	135.541	127.30	127.30
323.500	218.424	65.568	145.287	59.226	80.633	60.646	28.309	128.322	141.469	129.072	133.184	129.072	124.865	133.184	124.865	124.865
324.000	218.102	65.569	145.283	59.234	80.591	60.700	28.255	140.403	130.121	135.205	130.121	127.950	135.205	127.950	127.950	
324.500	217.778	65.570	145.279	59.279	80.630	60.642	28.308	140.763	128.363	132.476	132.476	128.363	132.476	128.363	128.363	
325.000	217.451	65.571	145.275	59.249	80.594	60.585	28.251	128.251	139.816	127.369	131.497	127.369	123.145	131.497	123.145	123.145
325.500	217.122	65.572	145.272	59.257	80.657	60.581	28.251	128.194	138.053	126.374	130.517	126.374	122.135	130.517	122.135	122.135
326.000	216.790	65.573	145.268	59.265	80.636	60.584	28.238	128.138	140.127	125.602	129.755	125.602	121.353	129.755	121.353	121.353
326.500	216.457	65.574	145.264	59.272	80.575	60.547	28.209	128.09	138.486	126.014	130.150	126.014	121.782	130.150	121.782	121.782
327.000	216.121	65.575	145.260	59.281	80.630	60.514	28.171	128.214	138.269	125.807	129.939	125.807	121.578	129.939	121.578	121.578
327.500	215.792	65.576	145.257	59.288	80.599	60.552	28.176	128.222	139.073	125.621	129.750	125.621	121.555	129.750	121.555	121.555
328.000	215.442	65.577	145.253	59.295	80.607	60.590	28.175	128.244	138.053	125.627	129.748	125.627	121.410	129.748	121.410	121.410
328.500	215.099	65.578	145.249	59.303	80.609	60.513	28.176	128.244	137.758	125.336	129.455	125.336	121.20	129.455	121.20	121.20
329.000	214.753	65.578	145.245	59.311	80.643	60.528	28.175	128.215	138.013	125.637	129.742	125.637	121.437	129.742	121.437	121.437
329.500	214.406	65.579	145.241	59.319	80.635	60.542	28.176	128.273	137.522	125.135	129.243	125.135	120.931	129.243	120.931	120.931
330.000	214.056	65.580	145.238	59.327	80.649	60.542	28.175	128.290	137.423	125.056	129.158	125.056	120.858	129.158	120.858	120.858

PAYLOAD COORDINATES	POINTING			TANG. POINT COORD.			
	TIME	ALT.	LAT.	LONG.	GP	LAT.	LONG.
TANHT-5	2013-05-30 00:00	2113.704	65.581	145.234	59.334	60.238	128.322
TANHT-4	2013-05-31 00:00	2113.349	65.582	145.230	59.342	60.241	128.322
TANHT-3	2013-05-31 00:00	2112.993	65.583	145.226	59.350	60.244	128.323
TANHT-2	2013-05-31 00:00	2112.634	65.585	145.222	59.358	60.257	128.323
TANHT-1	2013-05-31 00:00	2112.272	65.585	145.219	59.366	60.254	128.333
TANHT-0	2013-05-31 00:00	2111.909	65.586	145.215	59.374	60.268	128.358
TANHT-5	2013-05-31 00:00	2111.543	65.588	145.211	59.382	60.215	128.234
TANHT-4	2013-05-31 00:00	2111.174	65.588	145.207	59.390	60.258	128.324
TANHT-3	2013-05-31 00:00	2110.804	65.589	145.204	59.398	60.240	128.277
TANHT-2	2013-05-31 00:00	2110.431	65.590	145.200	59.407	60.248	128.288
TANHT-1	2013-05-31 00:00	2110.056	65.591	145.196	59.415	60.283	128.308
TANHT-0	2013-05-31 00:00	2109.678	65.591	145.192	59.423	60.311	128.361
TANHT-5	2013-05-31 00:00	2109.298	65.592	145.188	59.431	60.328	128.418
TANHT-4	2013-05-31 00:00	2108.916	65.593	145.185	59.440	60.309	128.393
TANHT-3	2013-05-31 00:00	2108.532	65.594	145.181	59.448	60.313	128.403
TANHT-2	2013-05-31 00:00	208.145	65.601	145.177	59.456	60.351	128.339
TANHT-1	2013-05-31 00:00	208.756	65.596	145.173	59.465	60.357	128.489
TANHT-0	2013-05-31 00:00	207.365	65.597	145.169	59.473	60.344	128.454
TANHT-5	2013-05-31 00:00	206.971	65.598	145.166	59.481	60.386	128.490
TANHT-4	2013-05-31 00:00	206.575	65.599	145.162	59.490	60.389	128.542
TANHT-3	2013-05-31 00:00	206.177	65.600	145.158	59.498	60.386	128.530
TANHT-2	2013-05-31 00:00	205.401	65.601	145.154	59.507	60.392	128.536
TANHT-1	2013-05-31 00:00	205.373	65.602	145.150	59.516	60.407	128.564
TANHT-0	2013-05-31 00:00	204.968	65.603	145.147	59.512	60.437	128.625
TANHT-5	2013-05-31 00:00	204.560	65.604	145.143	59.533	60.445	128.638
TANHT-4	2013-05-31 00:00	204.151	65.605	145.139	59.542	60.459	128.486
TANHT-3	2013-05-31 00:00	203.738	65.605	145.135	59.550	60.443	128.620
TANHT-2	2013-05-31 00:00	203.324	65.606	145.131	59.559	60.469	128.673
TANHT-1	2013-05-31 00:00	202.907	65.607	145.127	59.568	60.475	128.680
TANHT-0	2013-05-31 00:00	202.498	65.608	145.124	59.577	60.508	128.750
TANHT-5	2013-05-31 00:00	202.067	65.609	145.120	59.585	60.465	128.646
TANHT-4	2013-05-31 00:00	201.643	65.610	145.116	59.594	60.455	128.677
TANHT-3	2013-05-31 00:00	201.217	65.611	145.112	59.603	60.994	128.637
TANHT-2	2013-05-31 00:00	200.789	65.612	145.108	59.612	60.917	128.548
TANHT-1	2013-05-31 00:00	200.447	65.613	145.105	59.621	60.906	128.526
TANHT-0	2013-05-31 00:00	200.000	65.614	145.101	59.630	60.834	128.474
TANHT-5	2013-05-31 00:00	199.568	65.615	145.097	59.639	60.771	128.475
TANHT-4	2013-05-31 00:00	199.490	65.616	145.093	59.648	60.405	127.765
TANHT-3	2013-05-31 00:00	198.613	65.616	145.089	59.658	60.480	127.523
TANHT-2	2013-05-31 00:00	198.171	65.617	145.085	59.667	60.378	127.582
TANHT-1	2013-05-31 00:00	197.726	65.618	145.082	59.676	60.307	127.607
TANHT-0	2013-05-31 00:00	197.448	65.619	145.078	59.685	60.394	127.636
TANHT-5	2013-05-31 00:00	197.280	65.620	145.074	59.695	60.021	127.664
TANHT-4	2013-05-31 00:00	196.831	65.621	145.070	59.704	60.995	127.727
TANHT-3	2013-05-31 00:00	196.379	65.622	145.066	59.713	61.165	127.702
TANHT-2	2013-05-31 00:00	195.926	65.622	145.062	59.723	61.194	127.688
TANHT-1	2013-05-31 00:00	195.470	65.623	145.059	59.732	61.101	127.673
TANHT-0	2013-05-31 00:00	195.011	65.625	145.055	59.742	61.029	127.658

PROJECT SPIRIT ROCKET POSITION AND HORIZON SENSOR PARAMETERS

86/09/22. 10.47.46.

PAGE 12

PAYLOAD COORDINATES		POINTING		TANG. POINT COORD.		TANHT-1		TANHT-2		TANHT-3		TANHT-4		TANHT-5	
TIME	ALT.	LAT.	LONG.	HEADING	GP	QRROT	LONG.	LONG.	LONG.	LONG.	LONG.	LONG.	LONG.	LONG.	LONG.
355.500	193.155	65.628	145.043	59.771	75.174	-17.677	0.000	0.000	0.000	0.000	0.000	0.000	0.000	0.000	
356.000	192.685	65.628	145.039	59.780	76.740	-18.732	57.526	122.666	32.975	15.418	21.197	15.418	9.545	9.545	
356.500	192.213	65.629	145.036	59.790	78.807	-19.487	59.004	125.411	80.324	65.525	70.413	65.525	60.543	60.543	
357.000	191.739	65.630	145.032	59.000	80.514	-19.801	60.178	127.858	112.991	104.484	104.630	100.484	96.242	96.242	
357.500	191.262	65.631	145.028	59.810	81.699	-19.197	60.965	129.659	132.126	121.217	124.847	121.217	117.492	117.492	
358.000	190.783	65.632	145.024	59.820	82.609	-19.478	61.552	131.101	144.808	135.130	138.362	135.130	131.802	131.802	
358.500	190.302	65.633	145.020	59.829	83.173	-19.115	62.909	132.022	151.658	142.744	145.729	142.744	139.663	139.663	
359.000	189.818	65.634	145.016	59.839	83.451	-18.755	62.083	132.481	154.559	146.022	148.885	146.022	143.063	143.063	
359.500	189.332	65.635	145.013	59.849	83.603	-18.385	62.177	132.732	155.056	147.526	150.322	147.526	144.634	144.634	
360.000	188.844	65.636	145.009	59.859	83.593	-17.395	62.172	132.711	155.249	149.706	146.905	146.905	144.009	144.009	
360.500	188.353	65.637	145.005	59.869	83.575	-17.663	62.162	132.676	154.550	146.183	148.991	146.183	143.278	143.278	
361.000	187.860	65.638	145.001	59.880	83.440	-17.482	62.080	132.446	152.482	145.933	146.800	145.933	140.970	140.970	
361.500	187.365	65.639	144.997	59.890	83.198	-17.353	61.930	132.037	149.046	140.169	143.142	140.169	137.100	137.100	
362.000	186.868	65.640	144.993	59.900	82.873	-17.535	61.727	131.498	144.432	135.117	138.232	135.117	131.907	131.907	
362.500	186.368	65.640	144.989	59.910	82.512	-17.696	61.498	130.906	139.099	129.296	132.568	129.296	125.928	125.928	
363.000	185.866	65.641	144.986	59.921	82.156	-18.094	61.271	130.332	133.588	123.305	126.733	123.305	119.782	119.782	
363.500	185.361	65.642	144.982	59.931	81.832	-18.634	61.062	129.815	128.293	117.573	121.141	117.573	113.908	113.908	
364.000	184.854	65.643	144.978	59.942	81.409	-18.762	60.786	129.152	121.230	109.940	113.693	109.940	106.091	106.091	
364.500	184.345	65.644	144.974	59.952	81.087	-19.907	60.574	128.655	115.502	103.780	107.672	103.780	99.791	99.791	
365.000	183.834	65.645	144.970	59.962	80.712	-20.674	60.325	128.083	108.636	96.409	100.465	96.409	92.258	92.258	
365.500	183.320	65.646	144.966	59.971	80.402	-21.532	60.117	127.618	102.671	90.029	94.219	90.029	85.029	85.029	
366.000	182.804	65.647	144.962	59.981	80.098	-22.389	59.912	127.166	96.620	83.570	87.892	83.570	79.153	79.153	
366.500	182.286	65.648	144.959	59.994	79.638	-22.767	59.599	126.496	87.394	73.729	78.250	73.729	69.114	69.114	
367.000	181.766	65.649	144.955	60.005	79.333	-24.260	59.389	126.057	80.870	66.799	71.451	66.799	62.051	62.051	
367.500	181.243	65.650	144.951	60.016	78.960	-25.295	59.131	125.528	72.747	58.177	62.990	58.177	53.269	53.269	
368.000	180.718	65.651	144.947	60.027	78.522	-25.926	58.824	124.918	62.943	47.789	52.791	47.789	42.692	42.692	
368.500	180.190	65.652	144.943	60.038	78.250	-25.224	58.633	124.542	56.473	40.958	46.077	40.958	35.744	35.744	
369.000	179.660	65.652	144.942	60.049	77.941	-28.612	58.414	124.121	49.012	33.085	38.337	33.085	27.739	27.739	
369.500	179.128	65.653	144.935	60.060	77.608	-29.753	58.176	123.674	40.798	24.430	29.824	24.430	18.940	18.940	
370.000	178.594	65.654	144.932	60.071	77.295	-30.970	57.952	123.259	32.867	16.085	21.613	16.085	10.462	10.462	
370.500	178.057	65.655	144.928	60.082	76.914	-31.691	57.677	122.762	23.056	5.770	11.461	5.770	0.000	0.000	
371.000	177.518	65.656	144.924	60.093	76.703	-33.327	56.000	17.261	0.000	5.477	0.000	0.000	0.000	0.000	
371.500	176.977	65.657	144.920	60.104	76.901	-34.423	57.669	122.735	21.662	4.360	10.056	4.360	0.000	0.000	
372.000	176.433	65.658	144.916	60.115	76.590	-35.907	56.000	121.346	0.000	1.463	0.000	0.000	0.000	0.000	
372.500	175.887	65.663	144.912	60.127	76.413	-36.901	56.000	120.296	0.000	0.000	0.000	0.000	0.000	0.000	
373.000	175.339	65.660	144.908	60.138	76.152	-37.951	56.000	120.969	0.000	0.000	0.000	0.000	0.000	0.000	
373.500	174.788	65.661	144.904	60.150	75.897	-38.949	56.000	120.000	0.000	0.000	0.000	0.000	0.000	0.000	
374.000	174.236	65.662	144.901	60.161	75.733	-39.905	56.000	119.000	0.000	0.000	0.000	0.000	0.000	0.000	
374.500	173.680	65.663	144.897	60.173	75.067	-40.392	56.000	118.000	0.000	0.000	0.000	0.000	0.000	0.000	
375.000	173.123	65.664	144.893	60.184	75.554	-41.843	56.000	117.000	0.000	0.000	0.000	0.000	0.000	0.000	
375.500	172.563	65.665	144.889	60.196	75.428	-42.572	56.000	116.000	0.000	0.000	0.000	0.000	0.000	0.000	
376.000	172.001	65.665	144.885	60.208	75.228	-43.479	56.000	115.000	0.000	0.000	0.000	0.000	0.000	0.000	
376.500	171.437	65.666	144.881	60.219	74.963	-44.208	56.000	114.000	0.000	0.000	0.000	0.000	0.000	0.000	
377.000	170.870	65.667	144.877	60.231	74.853	-44.884	56.000	113.000	0.000	0.000	0.000	0.000	0.000	0.000	
377.500	170.301	65.668	144.873	60.243	74.791	-45.602	56.000	112.000	0.000	0.000	0.000	0.000	0.000	0.000	
378.000	169.730	65.669	144.869	60.255	74.629	-46.022	56.000	111.000	0.000	0.000	0.000	0.000	0.000	0.000	
378.500	169.156	65.670	144.866	60.267	6.285	-46.052	56.000	110.000	0.000	0.000	0.000	0.000	0.000	0.000	
379.000	168.580	65.671	144.862	60.279	74.799	-46.799	56.000	109.000	0.000	0.000	0.000	0.000	0.000	0.000	
379.500	168.002	65.672	144.858	60.291	74.295	-47.098	56.000	108.000	0.000	0.000	0.000	0.000	0.000	0.000	
380.000	167.422	65.673	144.854	60.304	68.017	-47.412	56.000	107.000	0.000	0.000	0.000	0.000	0.000	0.000	

PAYLOAD COORDINATES		POINTING		TANG. POINT COORD.	
TIME	ALT.	LAT.	LONG.	GP	ROT.
380.500	166.839	65.674	144.850	60.316	-47.639
381.000	166.254	65.674	144.846	60.328	0.000
381.500	165.667	65.675	144.842	60.341	-47.151
382.000	165.077	65.676	144.838	60.353	0.000
382.500	164.485	65.677	144.834	60.365	-48.009
383.000	163.891	65.678	144.831	60.378	0.000
383.500	163.294	65.679	144.827	60.391	-48.183
384.000	162.695	65.680	144.823	60.403	0.000
384.500	162.094	65.681	144.819	60.416	-48.364
385.000	161.490	65.682	144.815	60.429	0.000
385.500	160.885	65.683	144.811	60.442	-48.447
386.000	160.277	65.684	144.807	60.455	0.000
386.500	159.666	65.684	144.803	60.468	-48.545
387.000	159.054	65.685	144.799	60.481	0.000
387.500	158.439	65.686	144.795	60.494	-48.591
388.000	157.821	65.687	144.792	60.508	0.000
388.500	157.202	65.688	144.788	60.521	-49.271
389.000	156.580	65.689	144.784	60.534	0.000
389.500	155.956	65.690	144.780	60.548	-49.099
390.000	155.329	65.691	144.776	60.561	0.000
390.500	154.700	65.692	144.772	60.575	-49.501
391.000	154.069	65.693	144.768	60.589	0.000
391.500	153.436	65.694	144.764	60.602	-49.633
392.000	152.800	65.694	144.760	60.616	0.000
392.500	152.162	65.695	144.756	60.630	-49.712
393.000	151.522	65.696	144.752	60.644	0.000
393.500	150.880	65.697	144.748	60.658	-49.860
394.000	150.235	65.698	144.745	60.672	0.000
394.500	149.588	65.699	144.741	60.686	-49.679
395.000	148.938	65.700	144.737	60.701	0.000
395.500	148.287	65.701	144.733	60.715	-49.815
396.000	147.633	65.702	144.729	60.729	0.000
396.500	146.976	65.703	144.725	60.744	-49.918
397.000	146.318	65.704	144.721	60.758	0.000
397.500	145.657	65.704	144.717	60.773	-48.865
398.000	144.994	65.705	144.713	60.788	0.000
398.500	144.328	65.706	144.709	60.802	-48.956
399.000	143.660	65.707	144.705	60.817	0.000
399.500	142.990	65.708	144.701	60.832	-48.496
400.000	142.318	65.709	144.697	60.847	0.000
400.500	141.643	65.710	144.694	60.862	-46.894
401.000	140.966	65.711	144.690	60.878	0.000
401.500	140.287	65.712	144.686	60.893	-41.919
402.000	139.606	65.713	144.682	60.908	0.000
402.500	138.922	65.713	144.678	60.924	-38.397
403.000	138.236	65.714	144.674	60.939	0.000
403.500	137.547	65.715	144.670	60.955	-31.506
404.000	136.857	65.716	144.666	60.971	-28.056
404.500	136.164	65.717	144.662	60.987	-10.078
405.000	135.469	65.718	144.658	61.002	-5.297

PAYLOAD COORDINATES			POINTING			TANG. POINT COORD.		
TIME	ALT.	LAT.	LONG.	HEADING	GP	QROT	LAT.	LONG.
405.500	134.771	65.719	144.654	61.010	76.901	-4.233	0.000	0.000
406.000	134.071	65.720	144.650	61.034	78.239	-3.343	0.000	0.000
406.500	133.369	65.721	144.646	61.051	79.428	-2.618	59.522	125.844
407.000	132.665	65.722	144.642	61.067	80.027	-2.027	59.935	126.703
407.500	131.958	65.722	144.638	61.083	80.895	-1.546	60.521	127.988
408.000	131.249	65.723	144.635	61.100	81.639	-1.086	61.014	129.127
408.500	130.538	65.724	144.631	61.116	82.256	-0.578	61.416	130.998
409.000	129.825	65.725	144.627	61.133	82.874	-0.268	61.810	131.094
409.500	129.109	65.726	144.623	61.149	83.335	-0.17	62.100	131.854
410.000	128.391	65.727	144.619	61.166	83.802	-0.14	62.390	132.639
410.500	127.670	65.728	144.615	61.183	84.179	-0.13	62.620	133.283
411.000	126.948	65.729	144.611	61.200	84.400	-0.086	62.754	100.780
411.500	126.223	65.730	144.607	61.217	84.708	-0.225	63.098	97.120
412.000	125.496	65.730	144.603	61.234	84.916	-0.389	63.062	80.111
412.500	124.766	65.731	144.599	61.251	85.123	-0.900	63.184	134.562
413.000	124.035	65.732	144.595	61.269	85.269	-1.012	63.270	106.744
413.500	123.301	65.733	144.591	61.287	85.349	-1.114	63.357	100.537
414.000	122.564	65.734	144.587	61.304	85.461	-1.236	63.383	103.532
414.500	121.826	65.735	144.583	61.321	85.487	-1.338	63.399	104.517
415.000	121.085	65.736	144.579	61.339	85.521	-1.466	63.462	105.684
415.500	120.342	65.737	144.575	61.357	85.557	-1.491	63.420	105.537
416.000	119.596	65.738	144.571	61.375	85.572	-1.598	63.450	105.537
416.500	118.849	65.738	144.567	61.393	85.550	-1.742	63.439	101.219
417.000	118.099	65.739	144.563	61.411	85.502	-1.850	63.416	101.219
417.500	117.347	65.740	144.559	61.429	85.420	-1.951	63.366	101.219
418.000	116.592	65.741	144.556	61.447	85.415	-1.949	63.350	101.219
418.500	115.835	65.742	144.552	61.464	85.389	-1.994	63.300	101.219
419.000	115.076	65.743	144.548	61.484	85.354	-2.078	63.230	101.219
419.500	114.315	65.744	144.544	61.503	85.383	-2.051	63.148	101.219
420.000	113.551	65.745	144.540	61.522	85.333	-2.103	63.112	101.219
420.500	112.786	65.746	144.536	61.542	85.338	-2.122	63.024	101.219
421.000	112.017	65.747	144.532	61.559	85.283	-2.122	63.092	101.219
421.500	111.247	65.747	144.528	61.578	85.166	-2.200	63.225	101.219
422.000	110.474	65.748	144.524	61.598	85.201	-2.209	63.247	101.219
422.500	109.700	65.749	144.520	61.617	85.172	-2.258	63.231	101.219
423.000	108.922	65.750	144.516	61.636	85.135	-2.294	63.210	101.219
423.500	108.143	65.751	144.512	61.656	85.083	-2.324	63.180	101.219
424.000	107.361	65.752	144.509	61.675	85.041	-2.396	63.157	101.219
424.500	106.577	65.753	144.504	61.695	85.026	-2.479	63.149	101.219
425.000	105.791	65.753	144.500	61.715	84.993	-2.549	63.130	101.219
425.500	105.002	65.754	144.496	61.735	84.921	-2.636	63.089	101.219
426.000	104.224	65.755	144.492	61.755	84.959	-2.685	63.112	101.219
426.500	103.419	65.756	144.488	61.775	84.945	-2.756	63.105	101.219
427.000	102.623	65.757	144.484	61.795	84.962	-2.846	63.116	101.219
427.500	101.826	65.758	144.480	61.816	84.970	-2.967	63.121	101.219
428.000	101.026	65.759	144.476	61.836	84.856	-3.099	63.055	101.219
428.500	100.224	65.760	144.472	61.857	84.904	-3.122	63.084	101.219
429.000	99.420	65.761	144.468	61.878	84.942	-3.240	63.107	101.219
429.500	98.613	65.761	144.464	61.899	84.994	-3.356	63.139	101.219
430.000	97.804	65.762	144.460	61.920	85.014	-3.471	63.151	101.219

PAYLOAD COORDINATES		POINTING		TANG. POINT COORD.	
TIME	ALT.	LAT.	LONG.	HEADING	GP
430.500	96.993	65.763	144.456	61.941	84.979
431.000	96.180	65.764	144.452	61.962	84.953
431.500	95.364	65.785	144.448	61.942	84.942
432.000	94.546	65.766	144.444	62.005	84.867
432.500	93.726	65.767	144.440	62.026	84.897
433.000	92.904	65.767	144.436	62.048	84.873
433.500	92.079	65.768	144.433	62.070	85.075
434.000	91.252	65.769	144.429	62.092	85.728
434.500	90.423	65.770	144.425	62.114	86.366
435.000	89.592	65.771	144.421	62.136	86.676
435.500	88.558	65.772	144.417	62.158	86.707
436.000	87.922	65.773	144.413	62.181	86.722
436.500	87.084	65.774	144.409	62.203	86.797
437.000	86.244	65.774	144.405	62.226	86.848
437.500	85.401	65.775	144.401	62.249	87.019
438.000	84.556	65.776	144.397	62.272	87.101
438.500	83.709	65.777	144.393	62.295	87.109
439.000	82.860	65.778	144.389	62.318	87.269
439.500	82.008	65.779	144.385	62.342	87.380
440.000	81.154	65.779	144.381	62.365	87.427
440.500	80.398	65.780	144.377	62.389	87.487
441.000	79.440	65.781	144.373	62.413	87.500
441.500	78.580	65.782	144.369	62.437	87.619
442.000	77.717	65.783	144.365	62.461	87.728
442.500	76.852	65.784	144.361	62.485	87.819
443.000	75.984	65.785	144.357	62.509	87.940
443.500	75.115	65.785	144.353	62.534	87.997
444.000	74.243	65.786	144.349	62.558	88.195
444.500	73.369	65.787	144.345	62.583	88.372
445.000	72.493	65.788	144.341	62.608	88.472
445.500	71.615	65.789	144.337	62.633	88.699
446.000	70.734	65.790	144.333	62.658	88.934
446.500	69.851	65.791	144.329	62.684	89.170
447.000	68.966	65.792	144.325	62.709	89.347
447.500	68.019	65.793	144.321	62.735	89.570
448.000	67.189	65.793	144.317	62.761	90.101
448.500	66.297	65.794	144.313	62.787	90.756
449.000	65.403	65.795	144.309	62.813	91.679
449.500	64.500	65.796	144.305	62.839	93.006
450.000	63.609	65.796	144.301	62.866	94.824
450.500	62.708	65.797	144.297	62.892	97.415
451.000	61.805	65.798	144.293	62.919	100.623
451.500	60.900	65.799	144.289	62.946	104.471
452.000	59.982	65.800	144.285	62.973	104.967
452.500	58.903	65.801	144.281	63.000	105.103
453.000	58.171	65.801	144.277	63.027	118.280
453.500	57.237	65.802	144.273	63.055	122.671
454.000	56.341	65.803	144.269	63.083	125.607
454.500	55.422	65.804	144.265	63.110	126.540
455.000	54.502	65.805	144.261	63.138	124.376

PROJECT SPIRIT ROCKET POSITION AND HORIZON SENSOR PARAMETERS

86/09/22. 10.47.46.

PAGE 16

PAYLOAD COORDINATES				POINTING				TANG. POINT COORD.						
TIME	ALT.	LAT.	LONG.	HEADING	GP	QROT	LAT.	LONG.	LONG.	TANHT-1	TANHT-2	TANHT-3	TANHT-4	TANHT-5
455.500	53.579	65.806	144.257	63.167	103.989	-8.407	0.000	0.000	0.000	0.000	0.000	0.000	0.000	
456.000	52.654	65.806	144.253	63.195	95.434	-16.700	67.772	131.364	16.754	24.367	22.003	24.367	26.636	
456.500	51.727	65.807	144.249	63.224	127.068	5.340	0.000	0.000	0.000	0.000	0.000	0.000	0.000	
457.000	50.797	65.808	144.245	63.252	122.075	9.542	0.000	0.000	0.000	0.000	0.000	0.000	0.000	
457.500	49.865	65.809	144.241	63.281	106.722	9.884	0.000	0.000	0.000	0.000	0.000	0.000	0.000	
458.000	48.932	65.810	144.237	63.310	103.962	14.007	0.000	0.000	0.000	0.000	0.000	0.000	0.000	
458.500	47.995	65.811	144.233	63.339	97.854	22.739	0.000	0.000	0.000	0.000	0.000	0.000	0.000	
459.000	47.057	65.811	144.229	63.369	95.132	36.234	67.696	172.107	14.682	21.887	19.655	21.887	24.024	
459.500	46.117	65.812	144.225	63.398	94.806	47.230	67.606	132.926	17.317	24.087	21.996	24.087	26.084	
460.000	45.174	65.813	144.221	63.428	106.406	33.732	0.000	0.000	0.000	0.000	0.000	0.000	0.000	
460.500	44.229	65.814	144.217	63.458	126.929	-8.709	0.000	0.000	0.000	0.000	0.000	0.000	0.000	
461.000	43.282	65.815	144.213	63.488	128.551	-30.975	0.000	0.000	0.000	0.000	0.000	0.000	0.000	
461.500	42.333	65.815	144.209	63.518	126.789	-35.807	0.000	0.000	0.000	0.000	0.000	0.000	0.000	
462.000	41.381	65.816	144.205	63.549	127.830	-28.764	0.000	0.000	0.000	0.000	0.000	0.000	0.000	
462.500	40.427	65.817	144.201	63.579	131.628	-14.908	0.000	0.000	0.000	0.000	0.000	0.000	0.000	

Appendix C

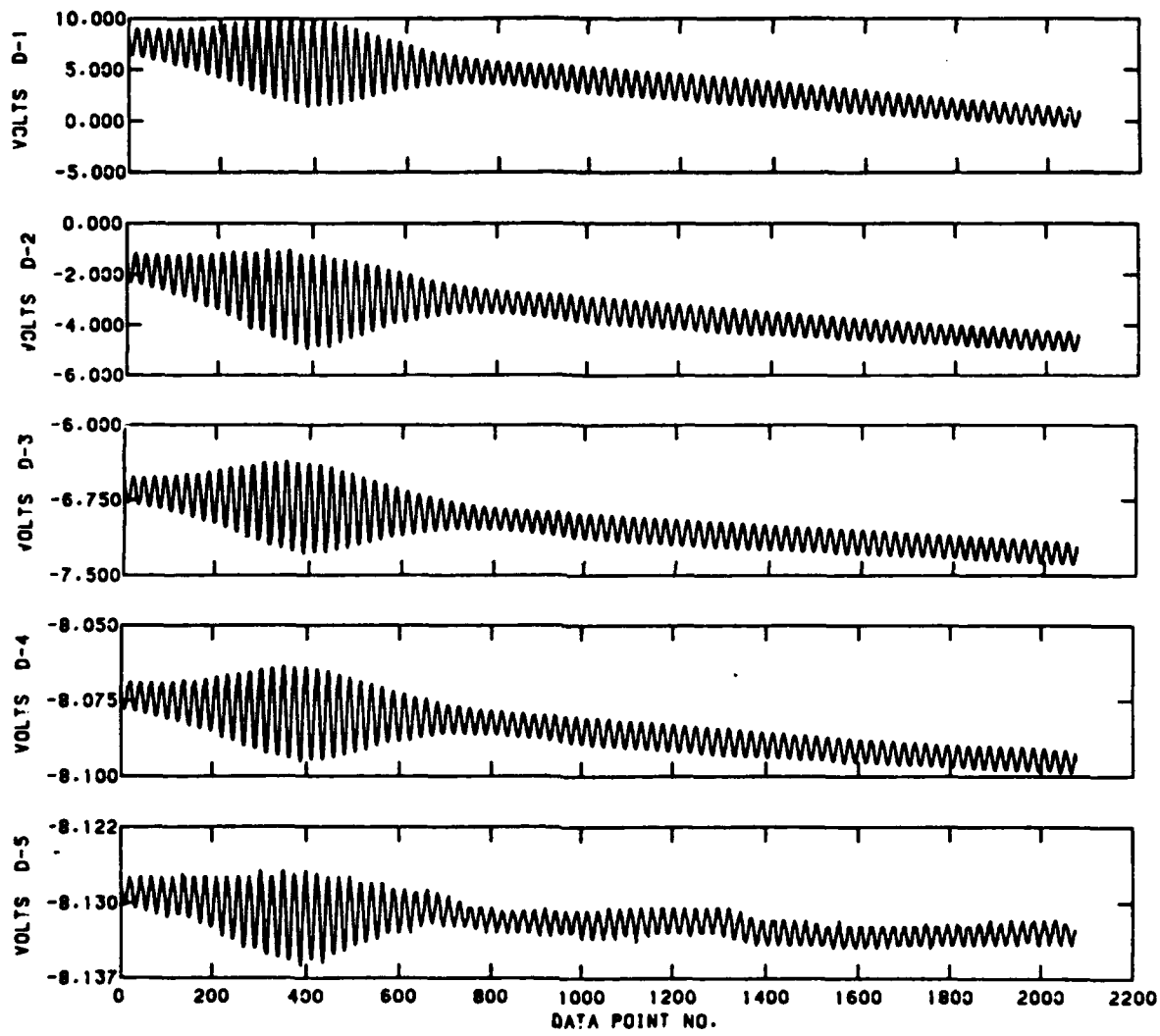
Sample of Raw Interferograms

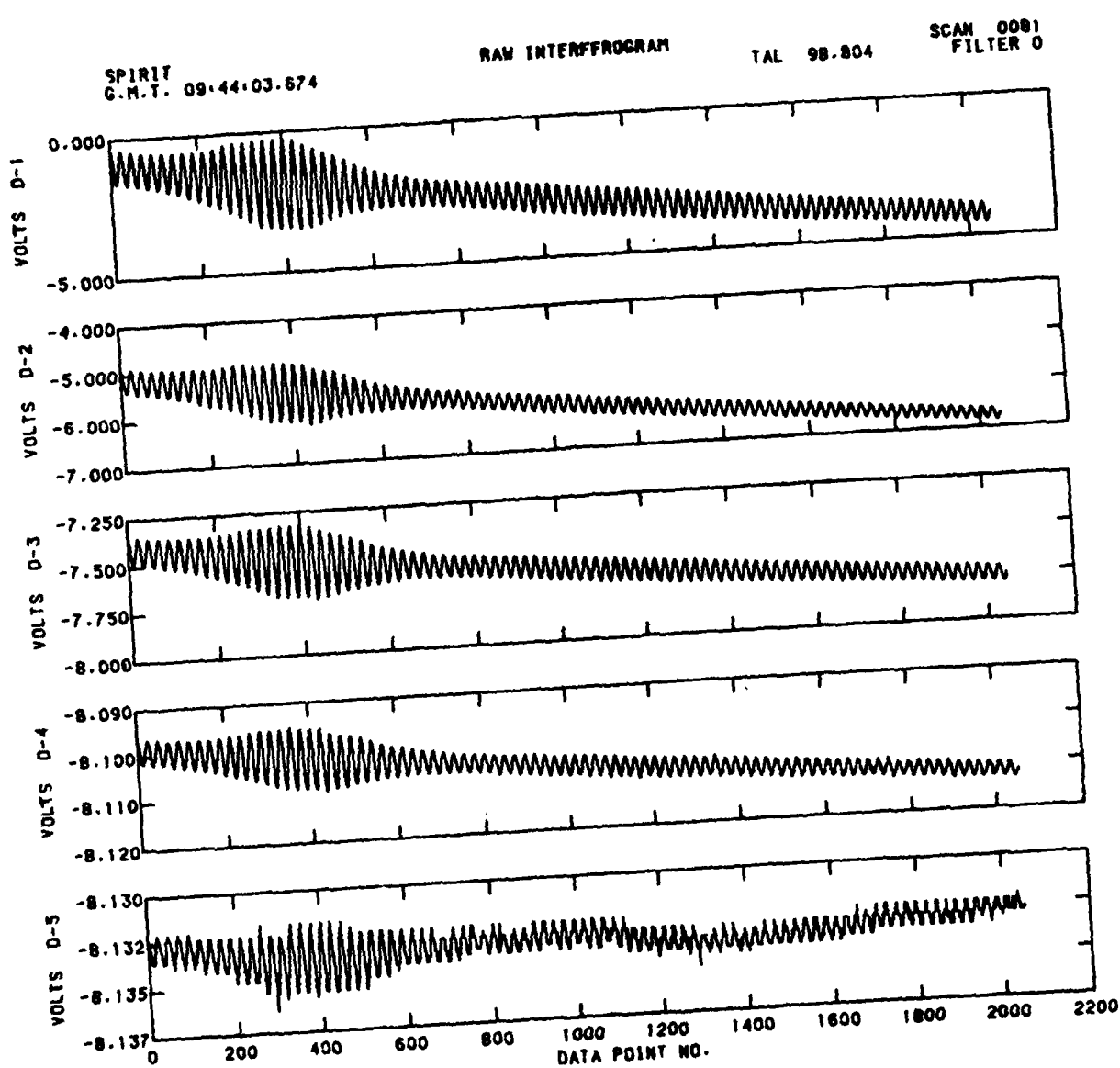
SPIRIT
C.M.T. 09:44:02.394

RAW INTERFEROGRAM

TAL 97.524

SCAN 3080
FILTER 0



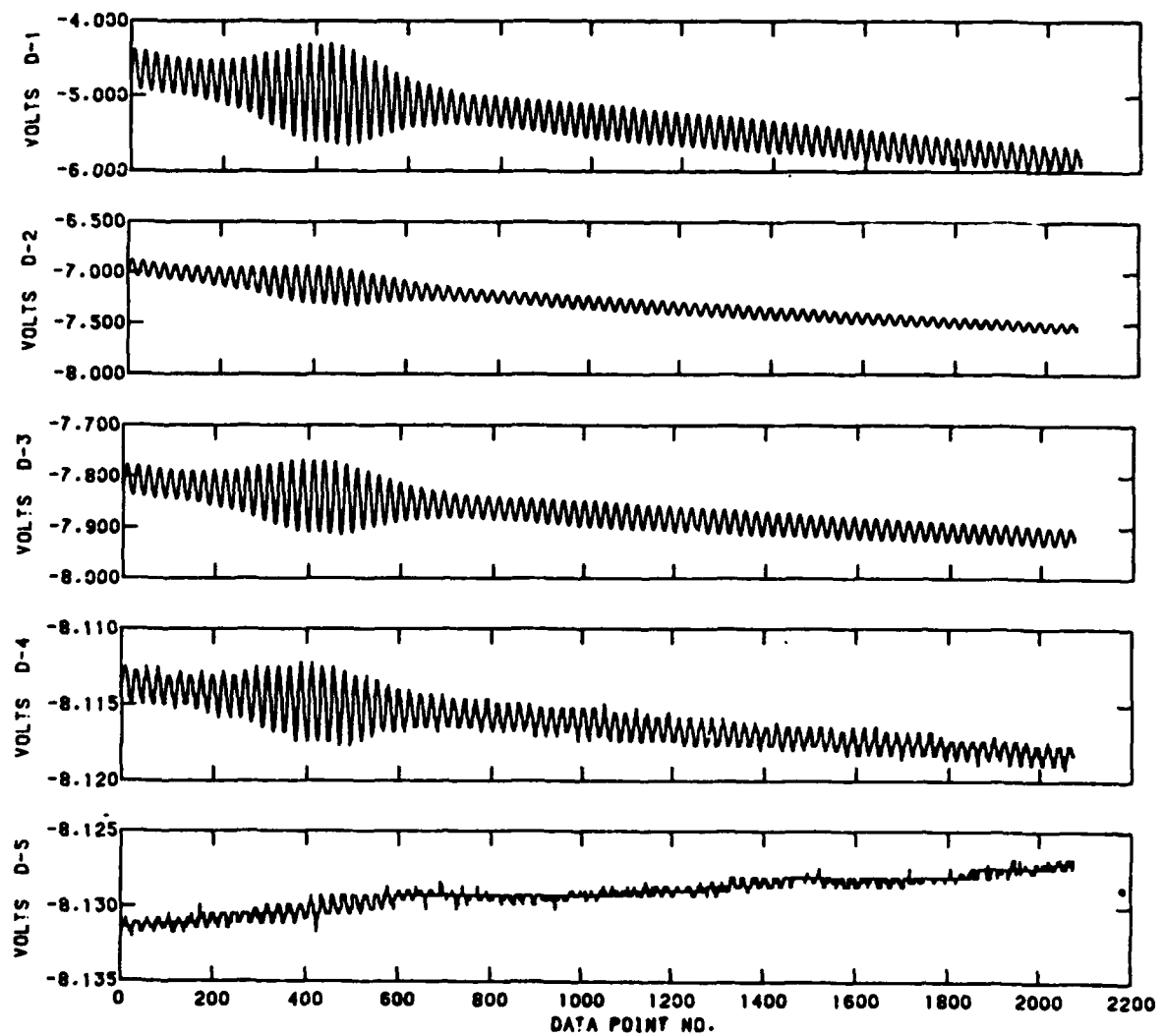


SPIRIT
G.M.T. 09:44:04.933

RAW INTERFEROGRAM

TAL 100.063

SCAN 0082
FILTER 0

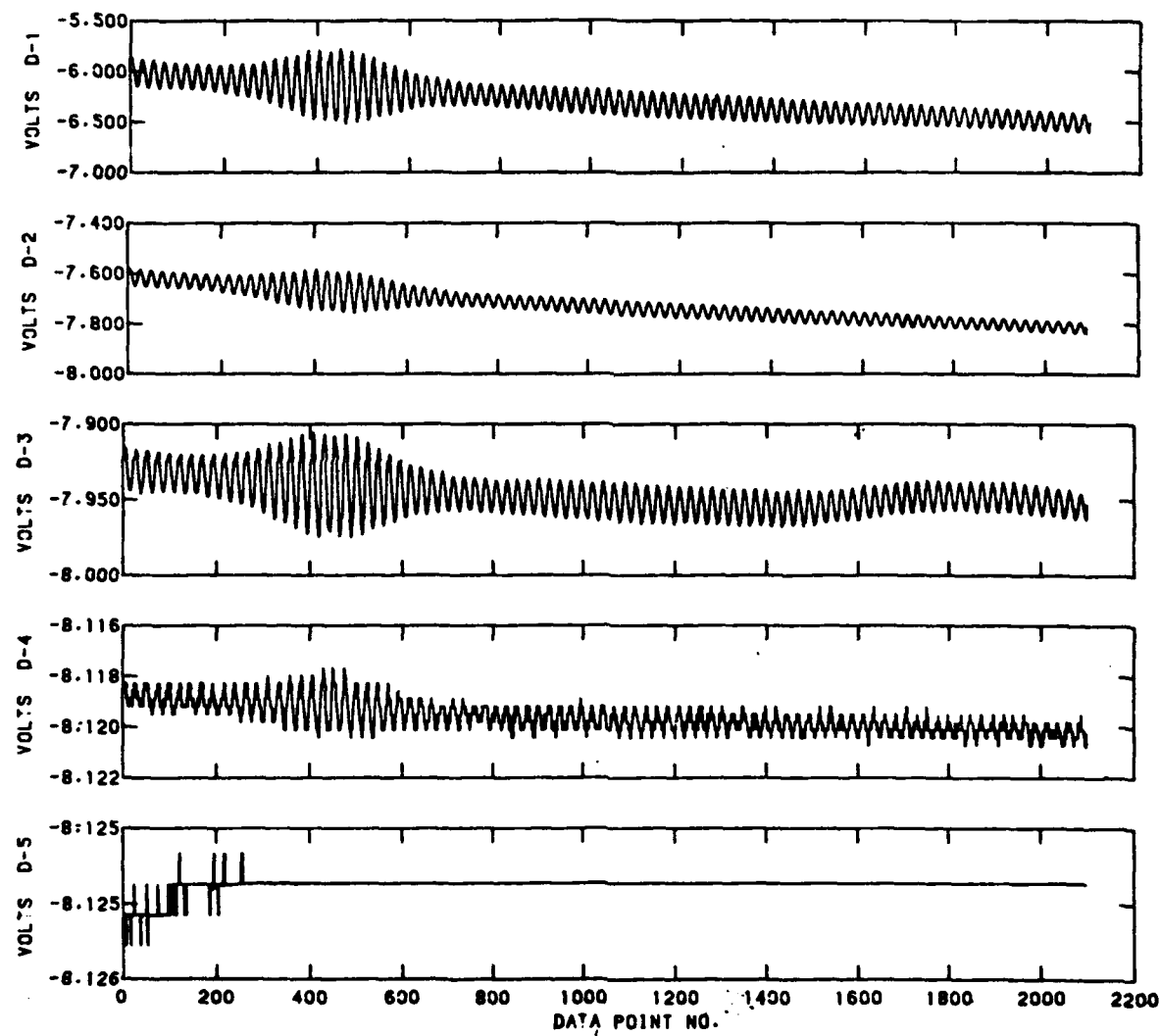


SPIRIT
G.M.T. 09:44:06.203

RAW INTERFEROGRAM

TAL 101.333

SCAN 0083
FILTER 0

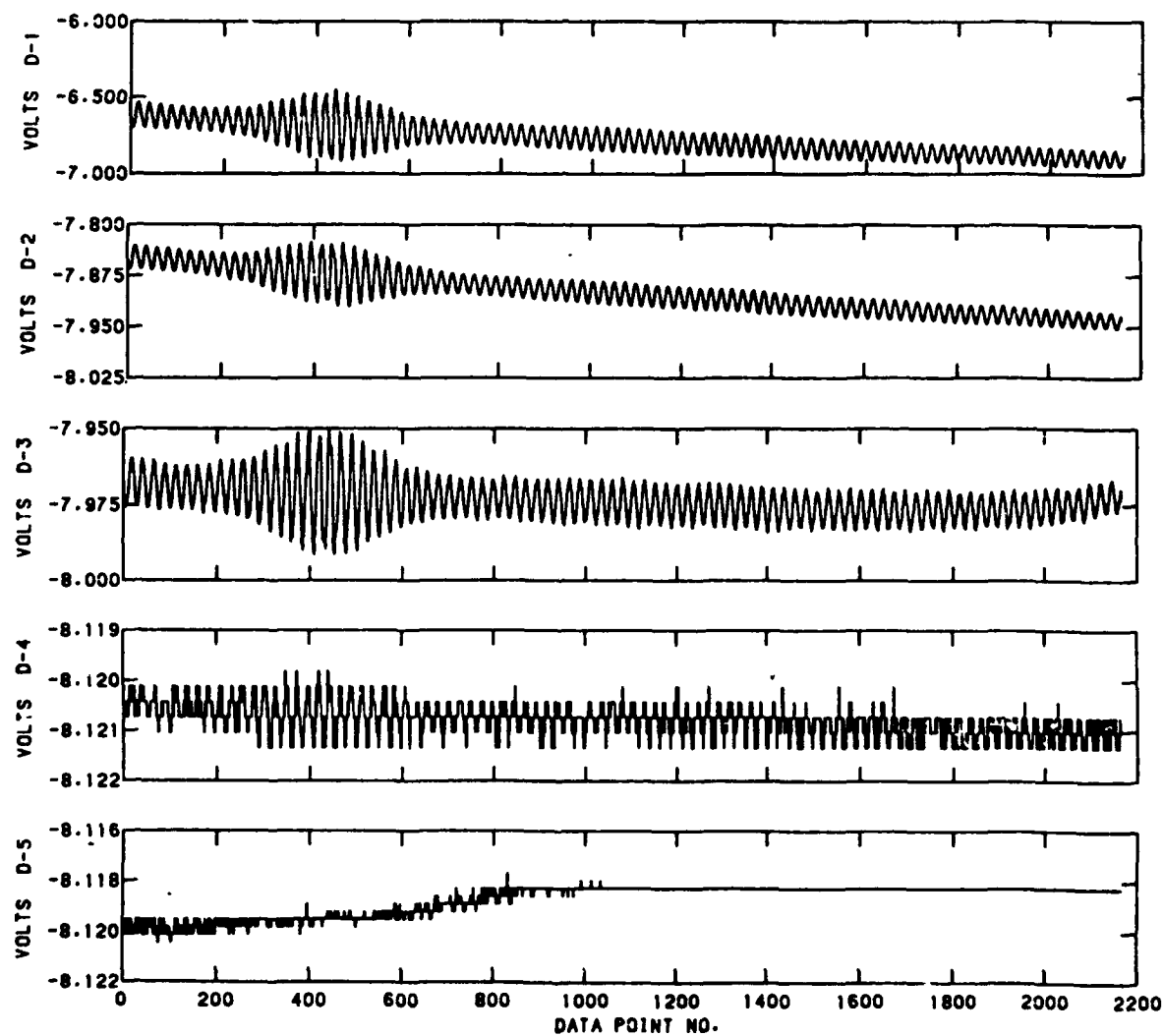


SPIRIT
G.M.T. 09:44:07.483

RAW INTERFEROGRAM

TAL 102.613

SCAN 0084
FILTER 0

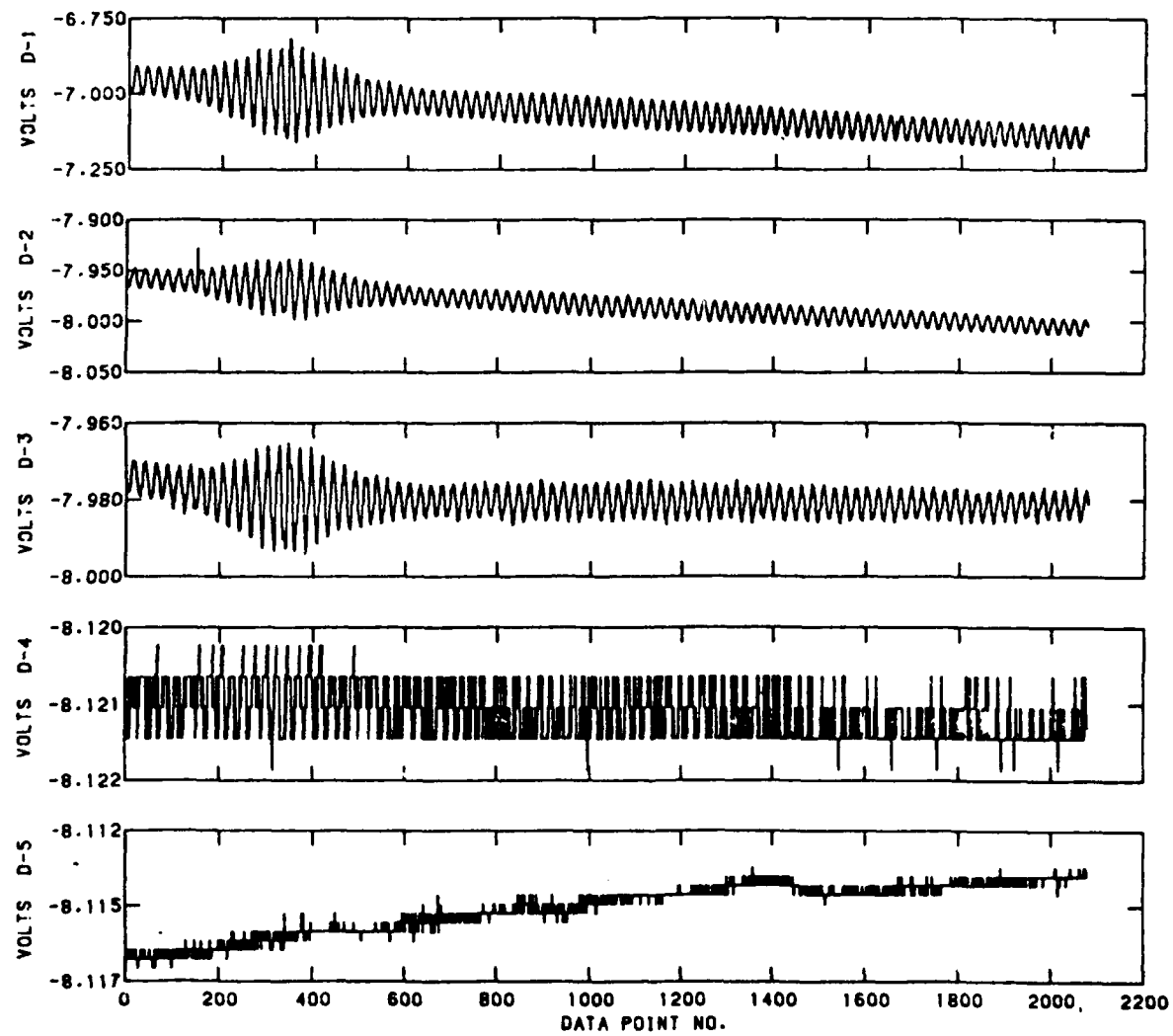


SPIRIT
G.M.T. 09:44:08.804

RAW INTERFERGRAM

TAL 103.934

SCAN 0085
FILTER 0

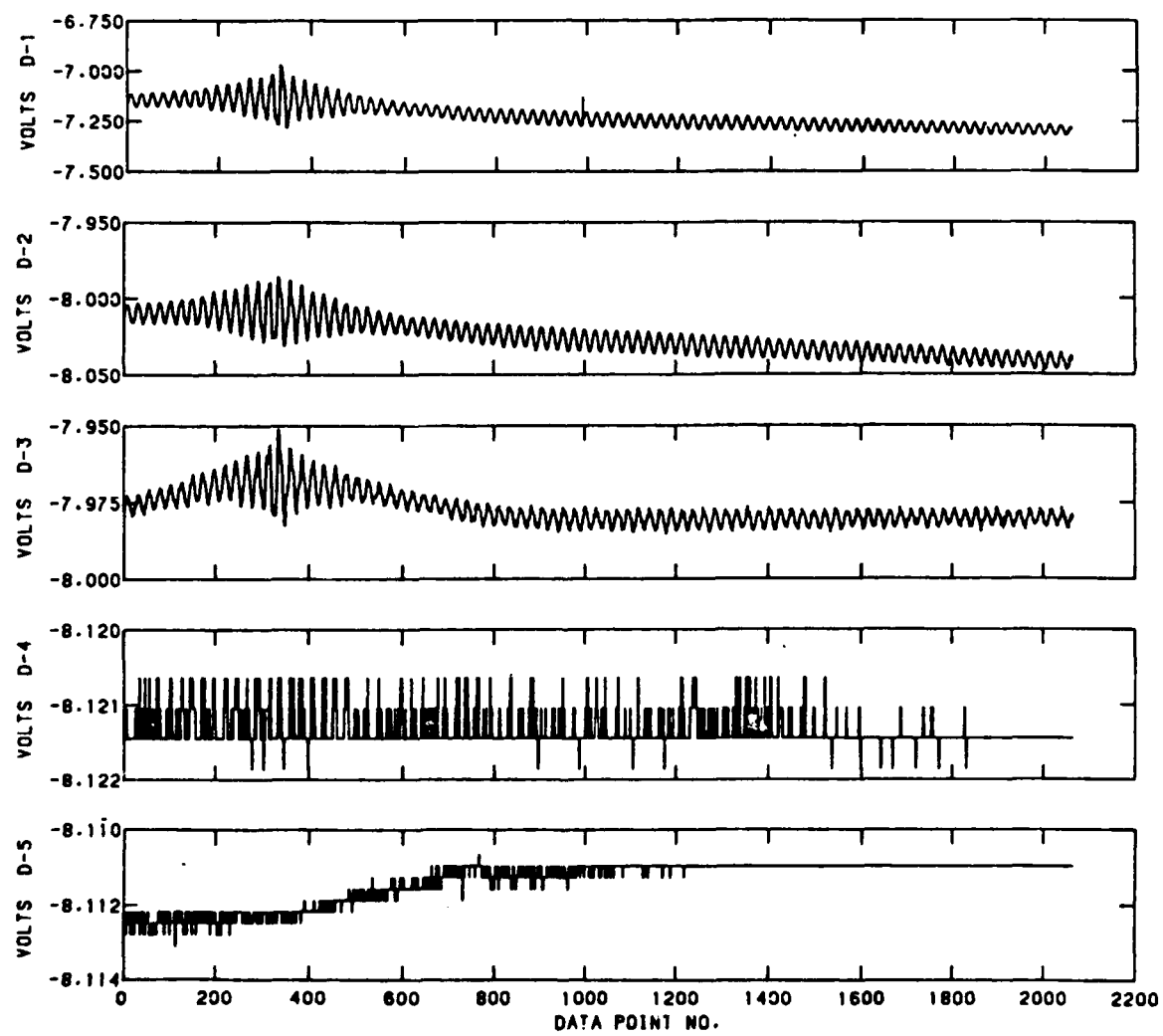


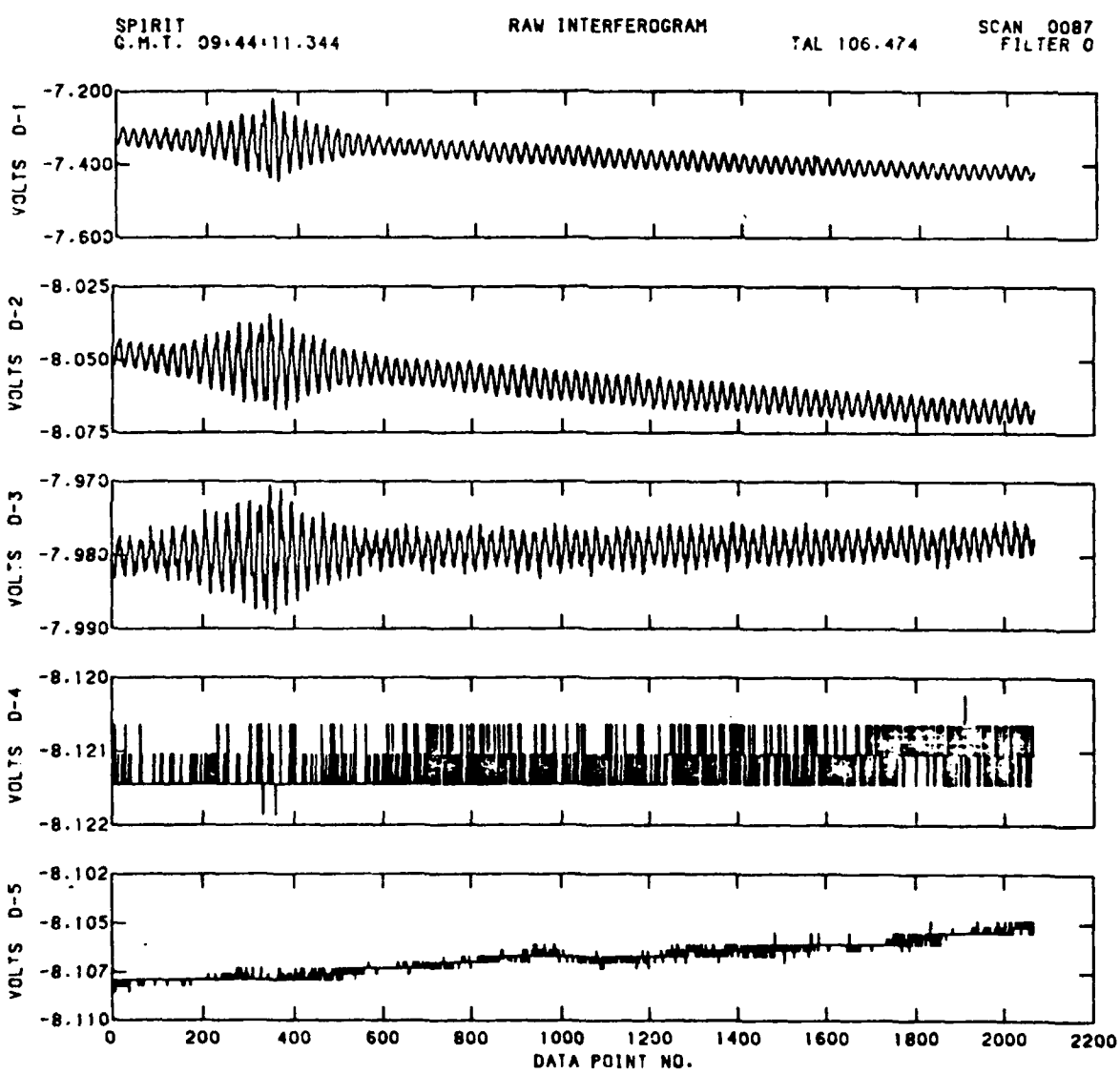
SPIRIT
G.M.T. 09:44:10.074

RAW INTERFEROGRAM

TAL 105.204

SCAN 0086
FILTER 0



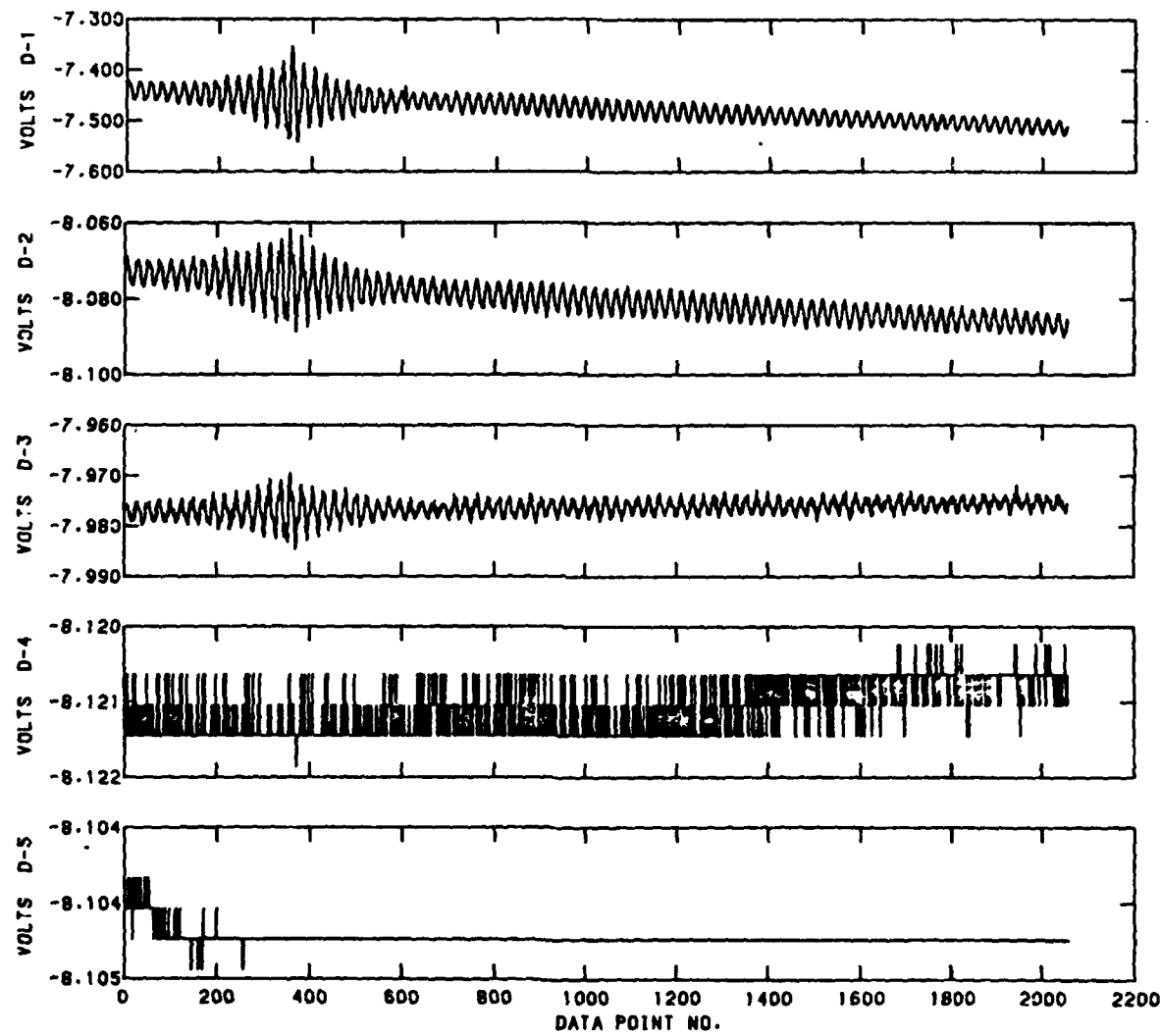


SPIRIT
C.M.T. 09:44:12.613

RAW INTERFEROMGRAM

TAL 107.743

SCAN 0088
FILTER 0

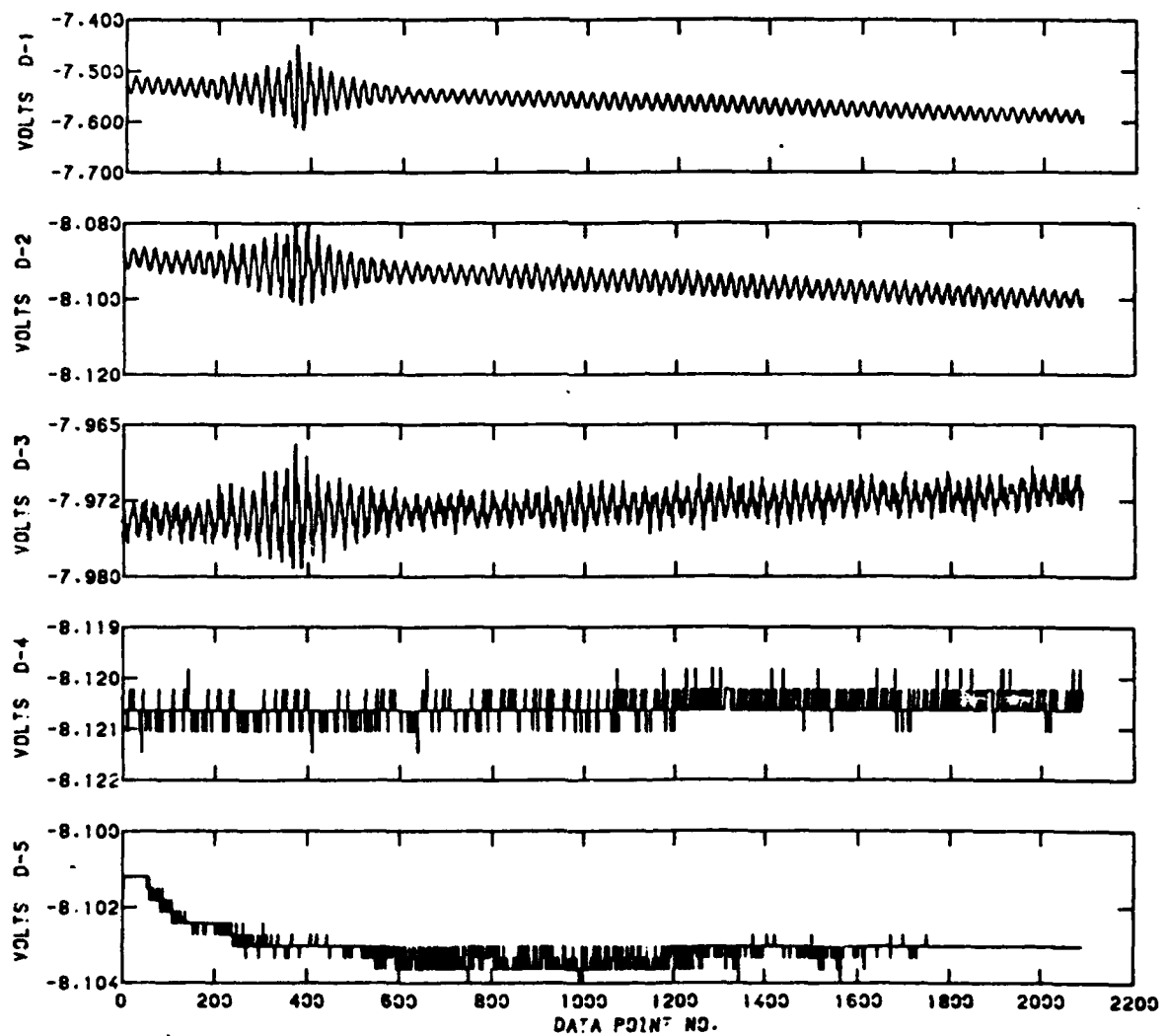


SPIRIT
G.M.T. 09:44:13.873

RAW INTERFEROGRAM

TAL 109.003

SCAN 0089
FILTER 0

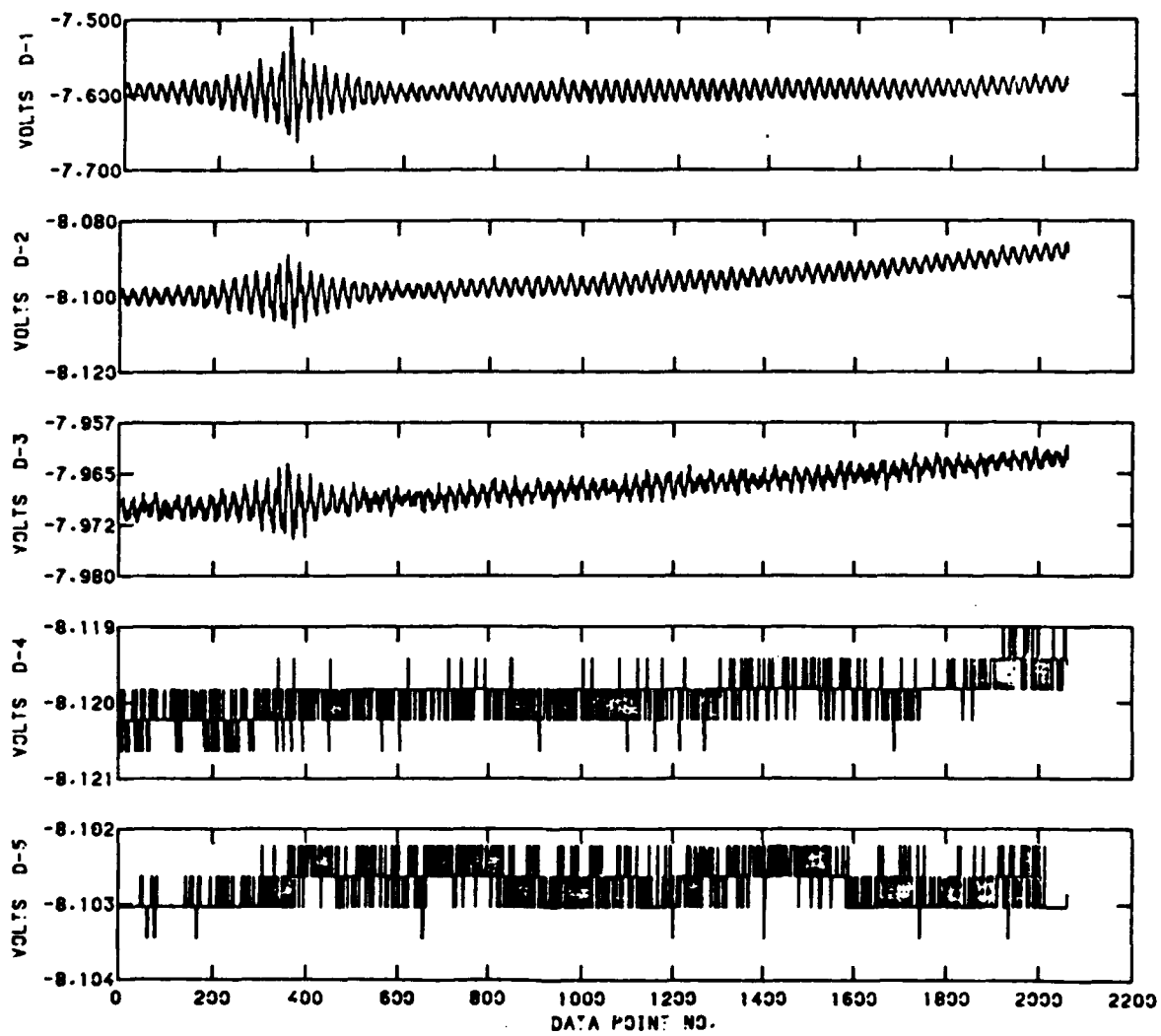


SPIRIT
G.M.T. 09:44:15.153

RAW INTERFERGRAM

TAL 110.283

SCAN 0090
FILTER 0

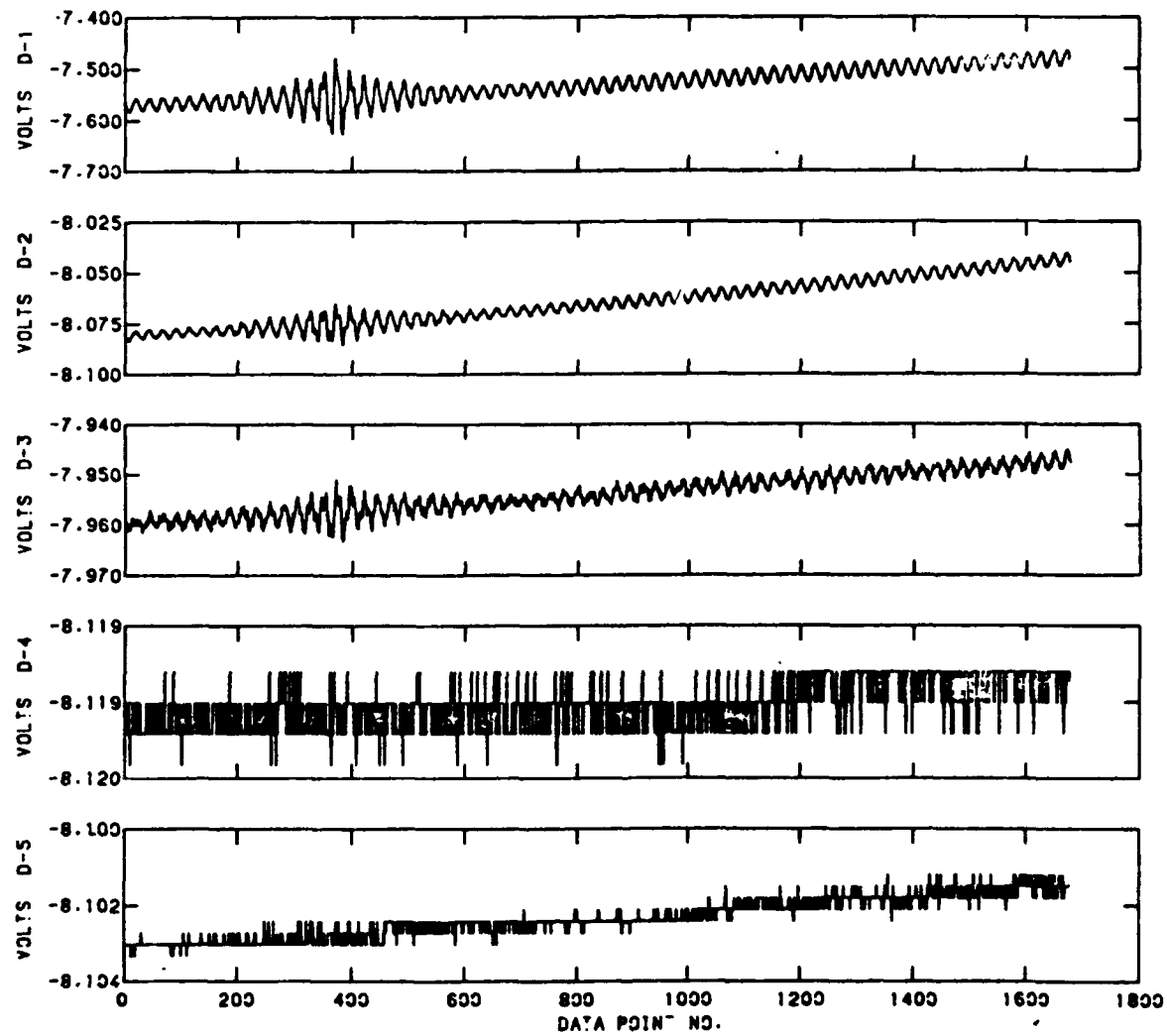


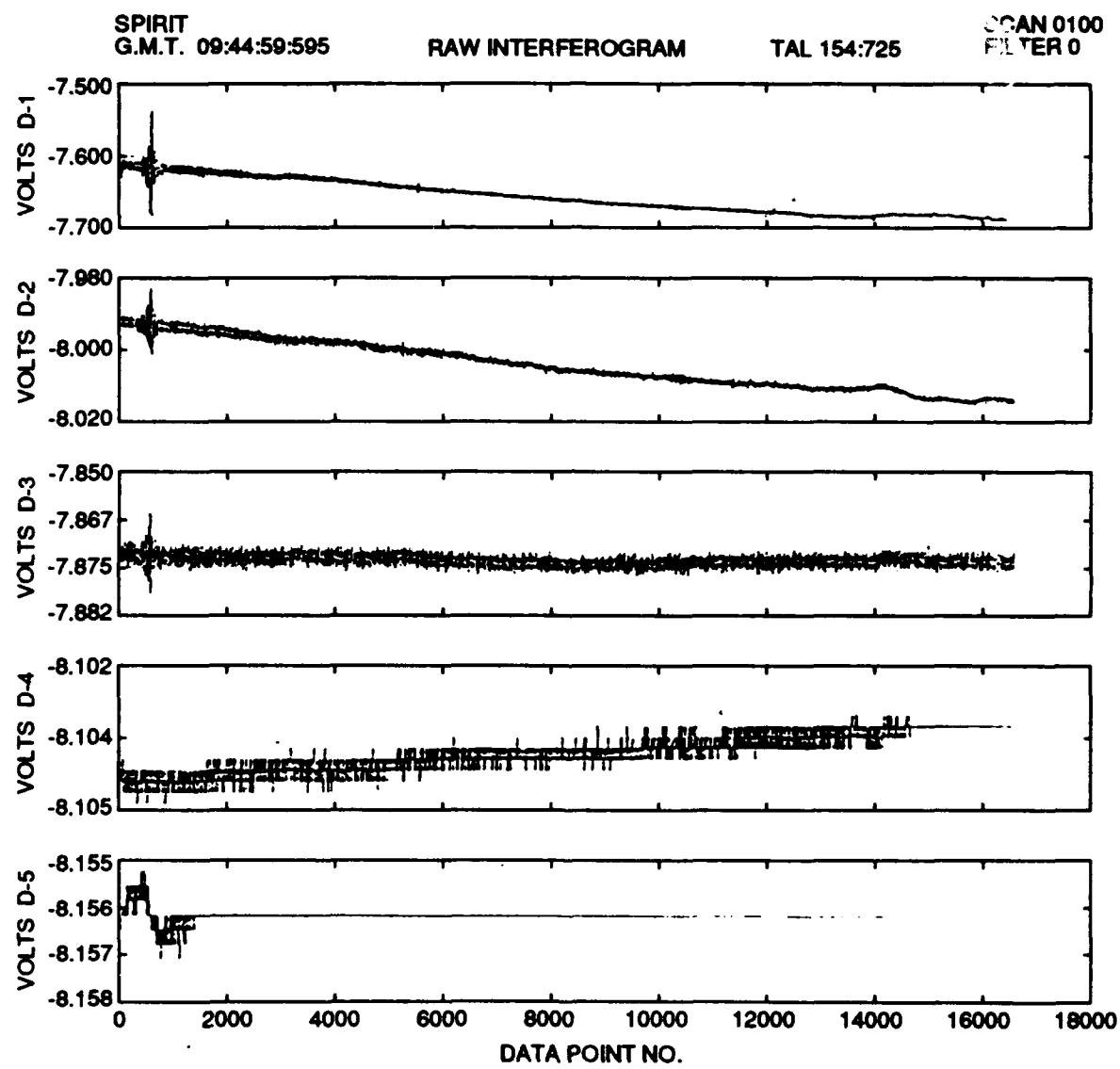
SPIRIT
G.M.T. 09:44:16.413

RAW INTERFEROGRAM

TAL 111.543

SCAN 0091
FILTER 0



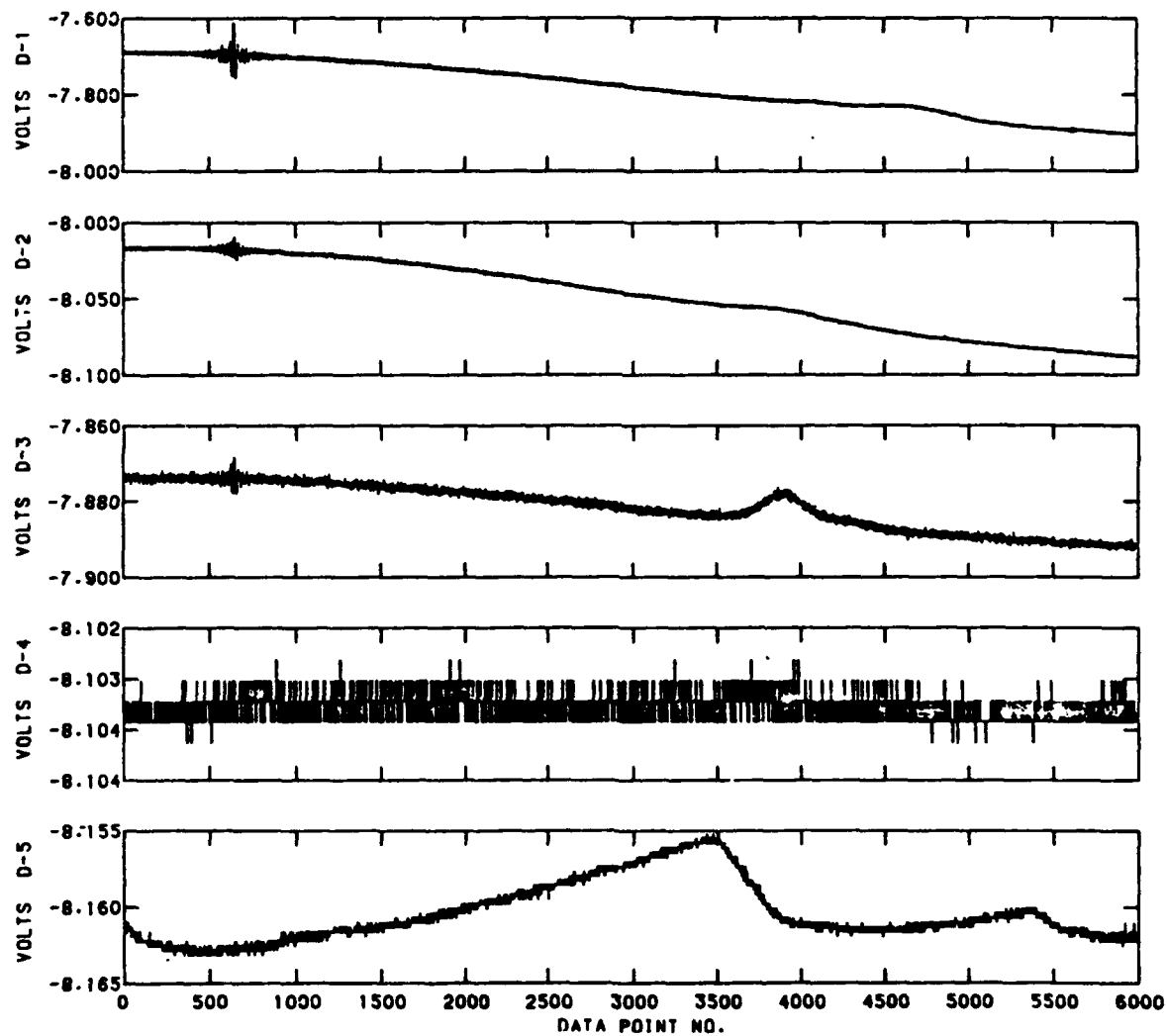


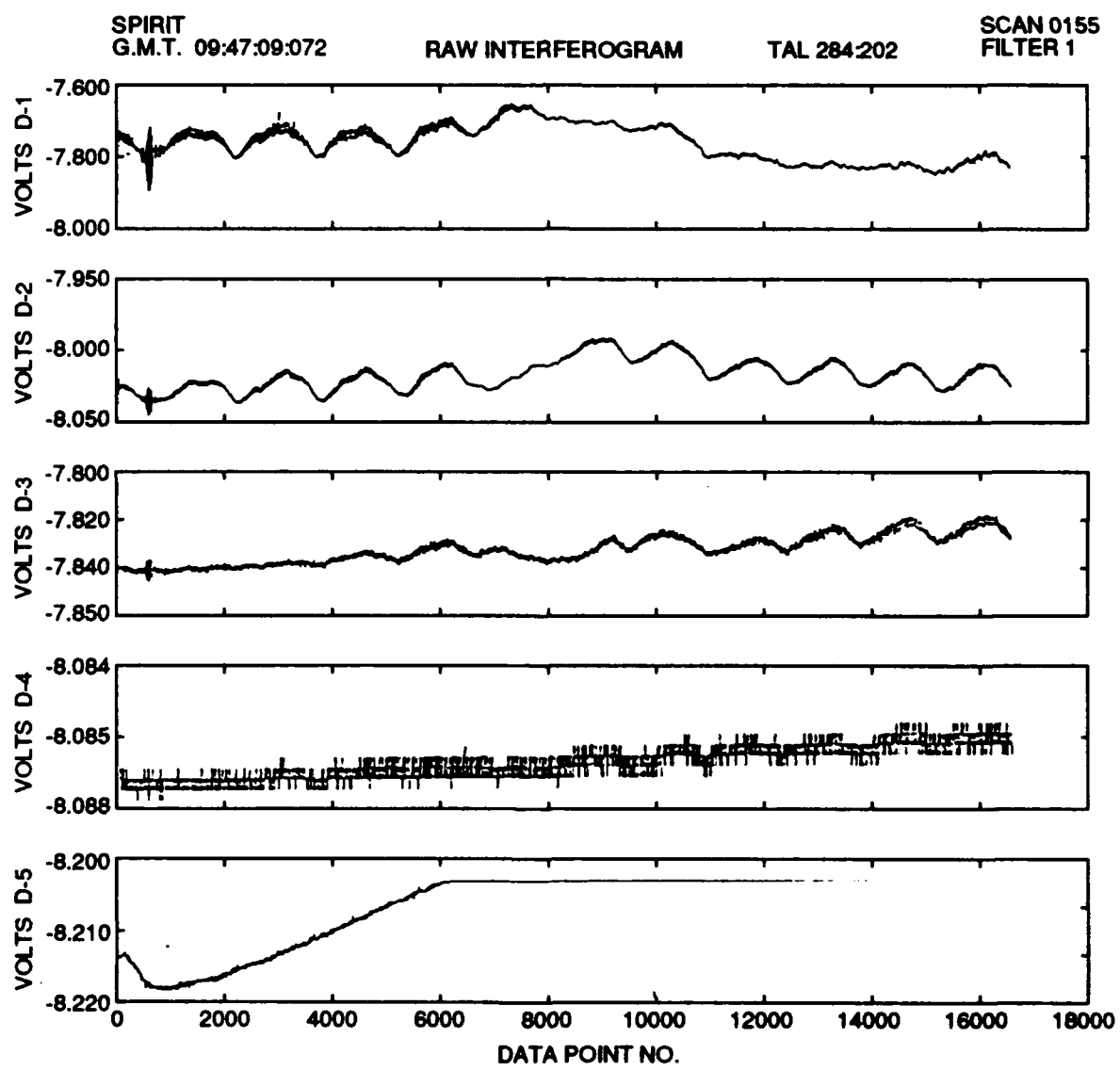
SPIRIT
G.M.T. 09:45:09.160

RAW INTERFEROGRAM

TAL 164.290

SCAN 0101
FILTER 0



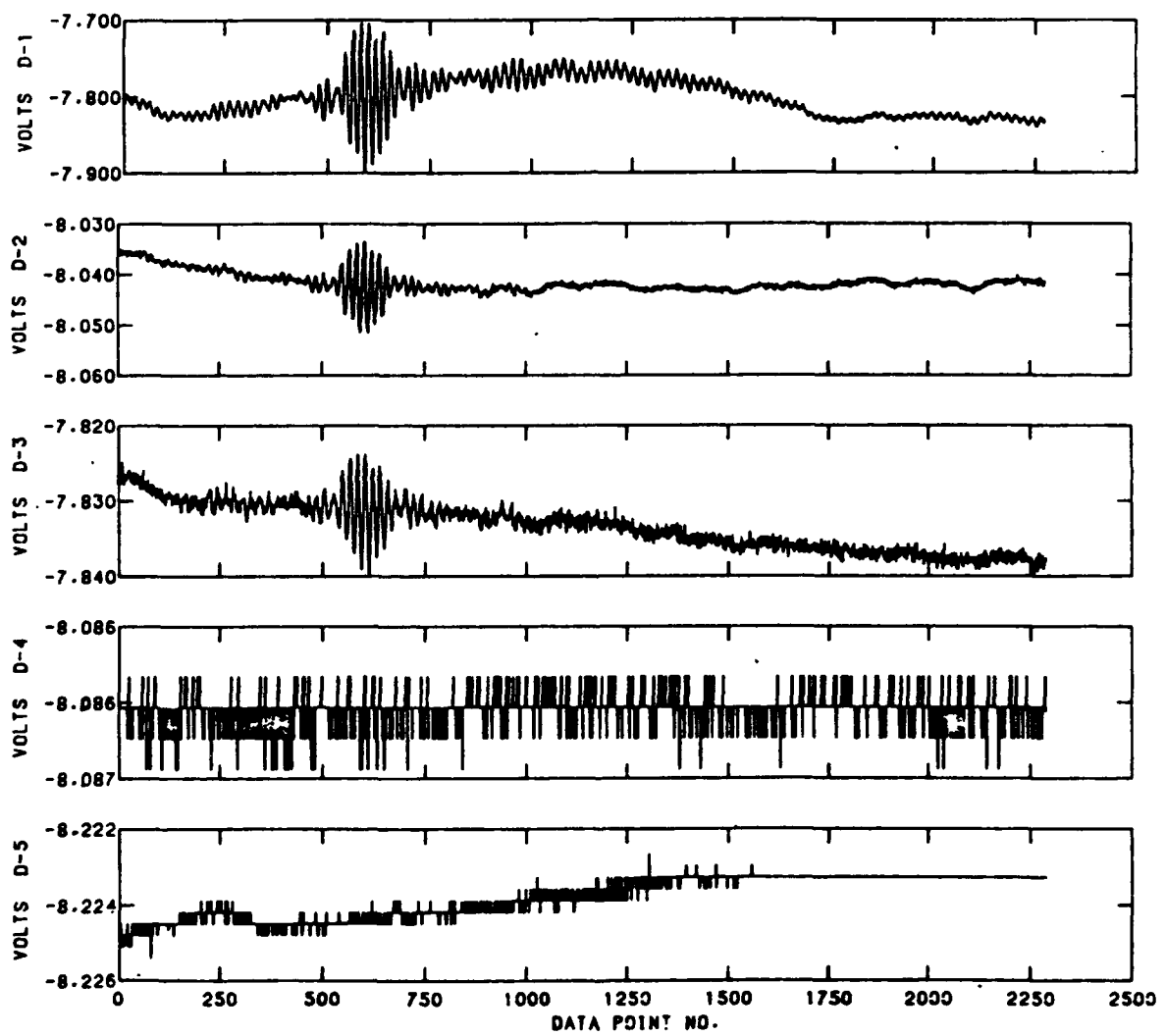


SPIRIT
G.M.T. 09:47:18.647

RAW INTERFEROMGRAM

TAL 293.777

SCAN C:56
FILTER 1

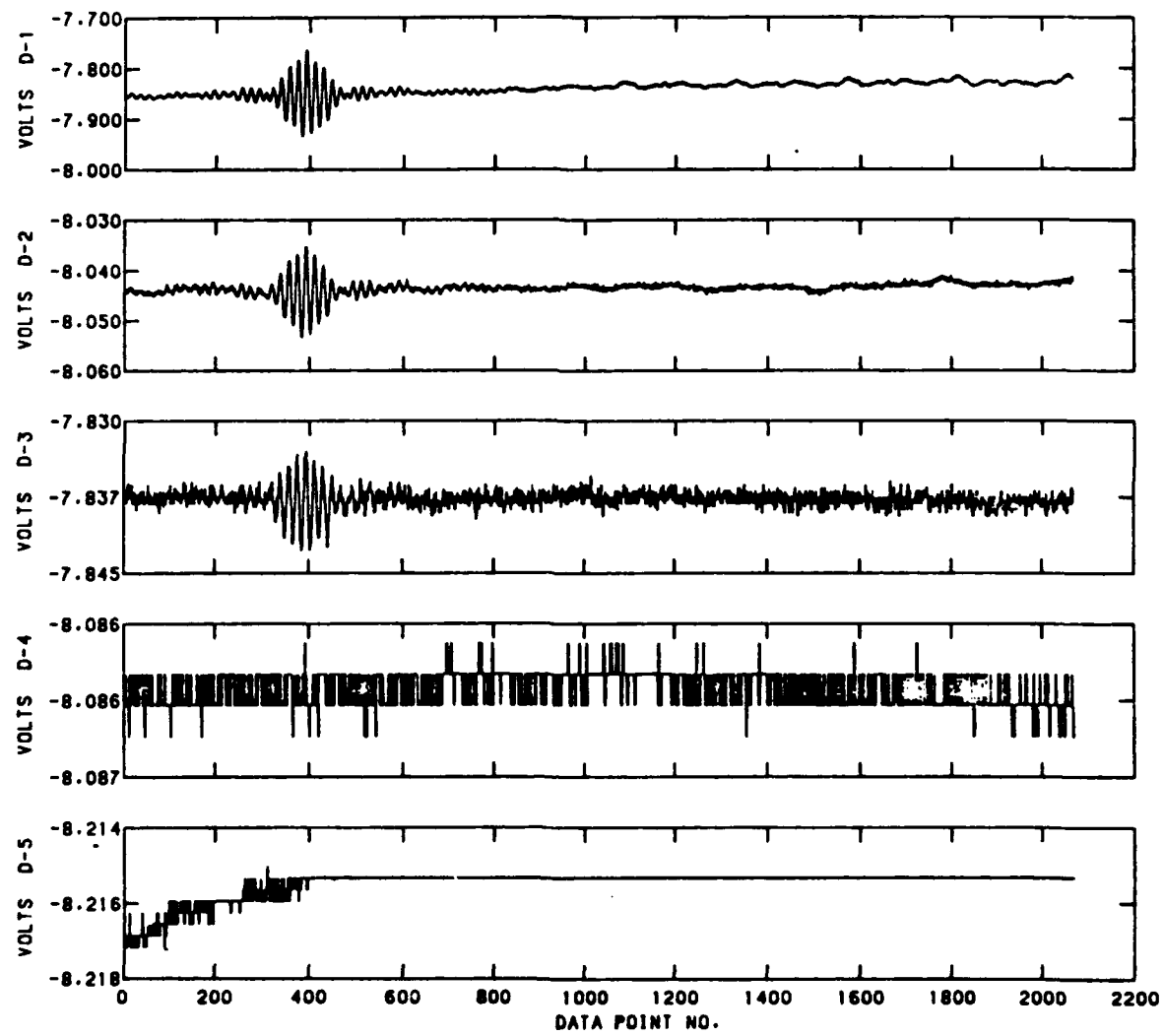


SPIRIT
G.M.T. 09:47:21.279

RAW INTERFEROMGRAM

TAL 296.409

SCAN 0158
FILTER 1

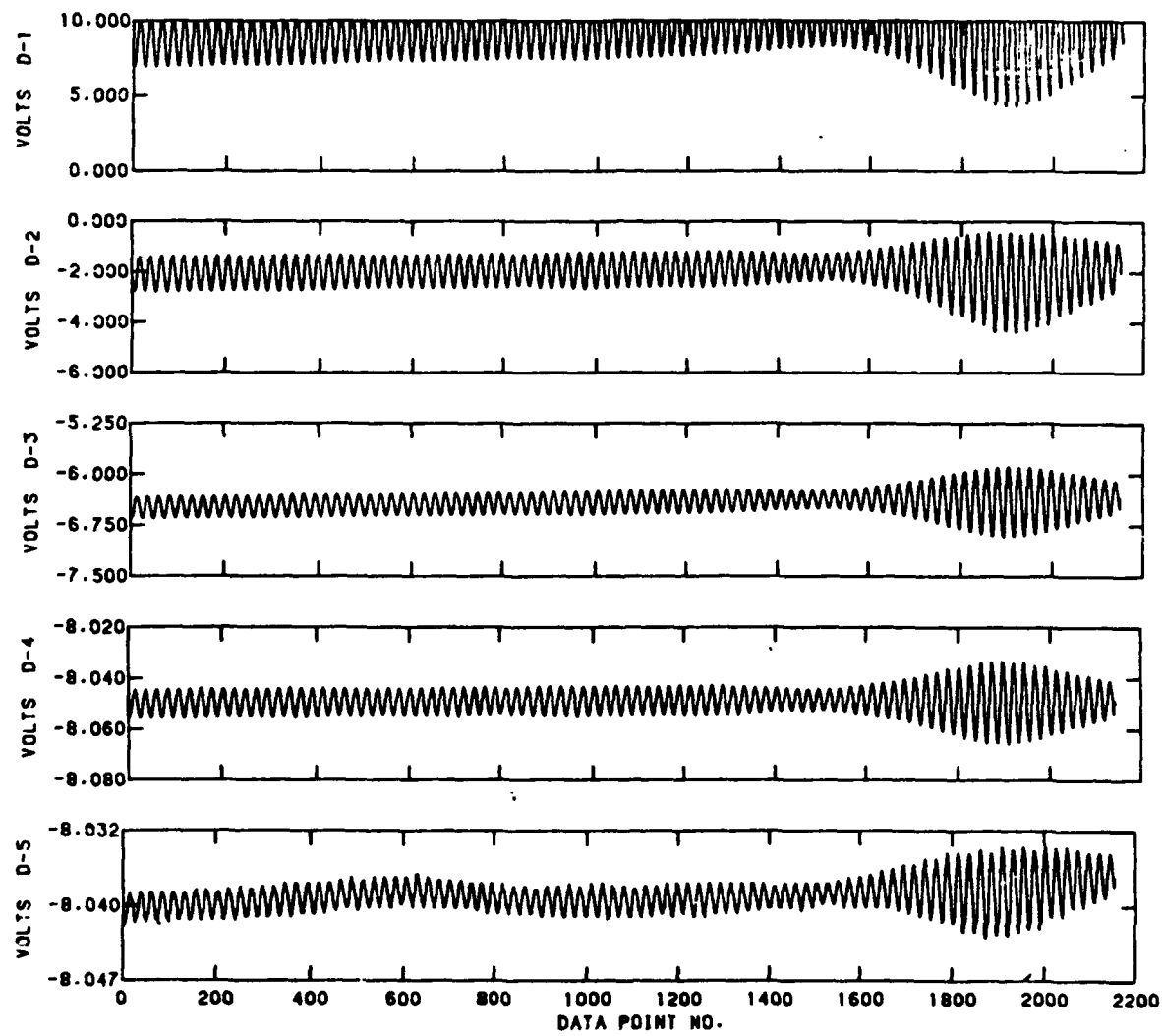


SPIRIT
G.M.T. 09:49:19.972

RAW INTERFEROGRAM

TAL 415.102

SCAN 0225
FILTER 0

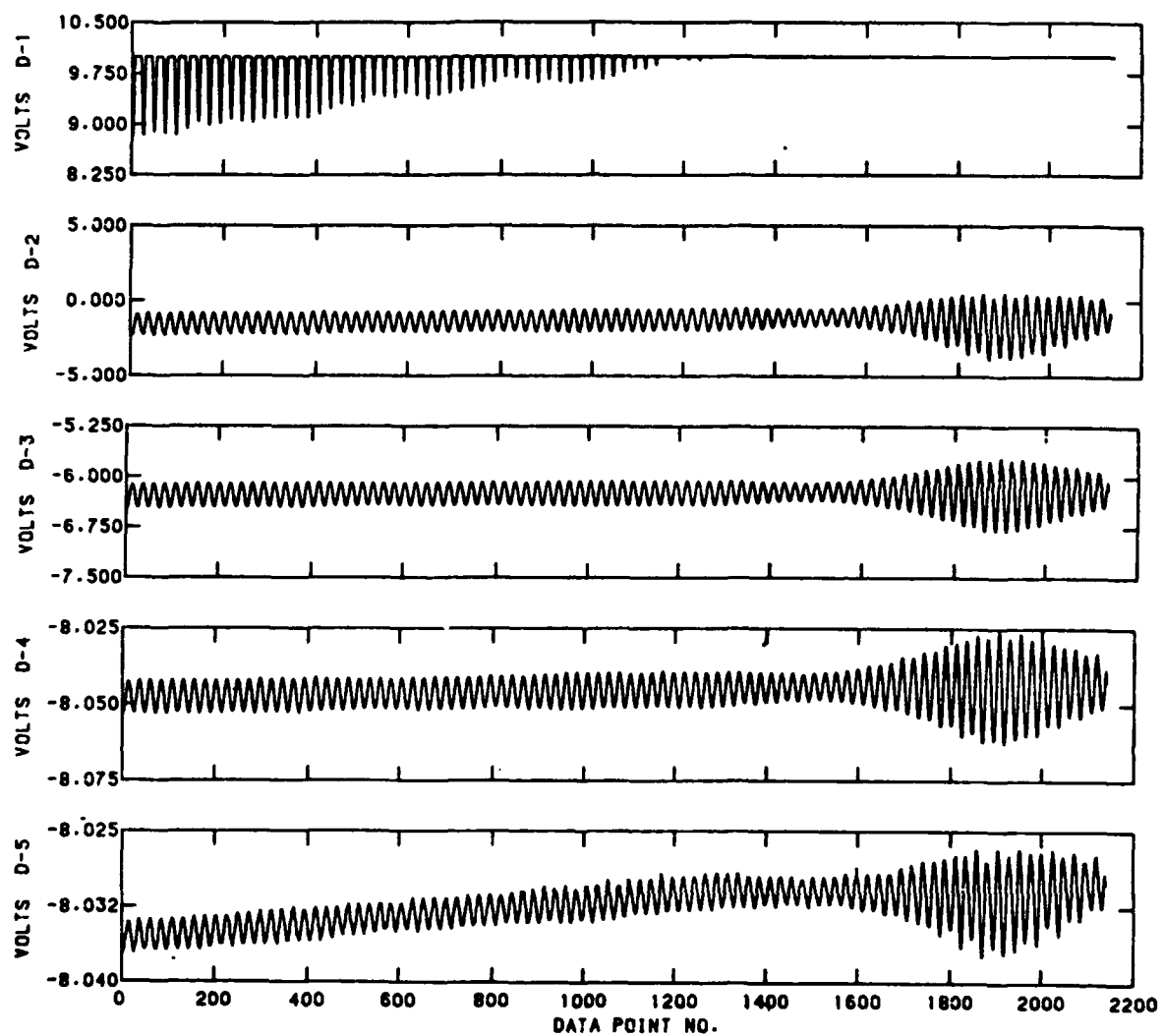


SPIRIT
G.M.T. 09:49:21.283

RAW INTERFERGRAM

TAL 416.413

SCAN 0226
FILTER 0

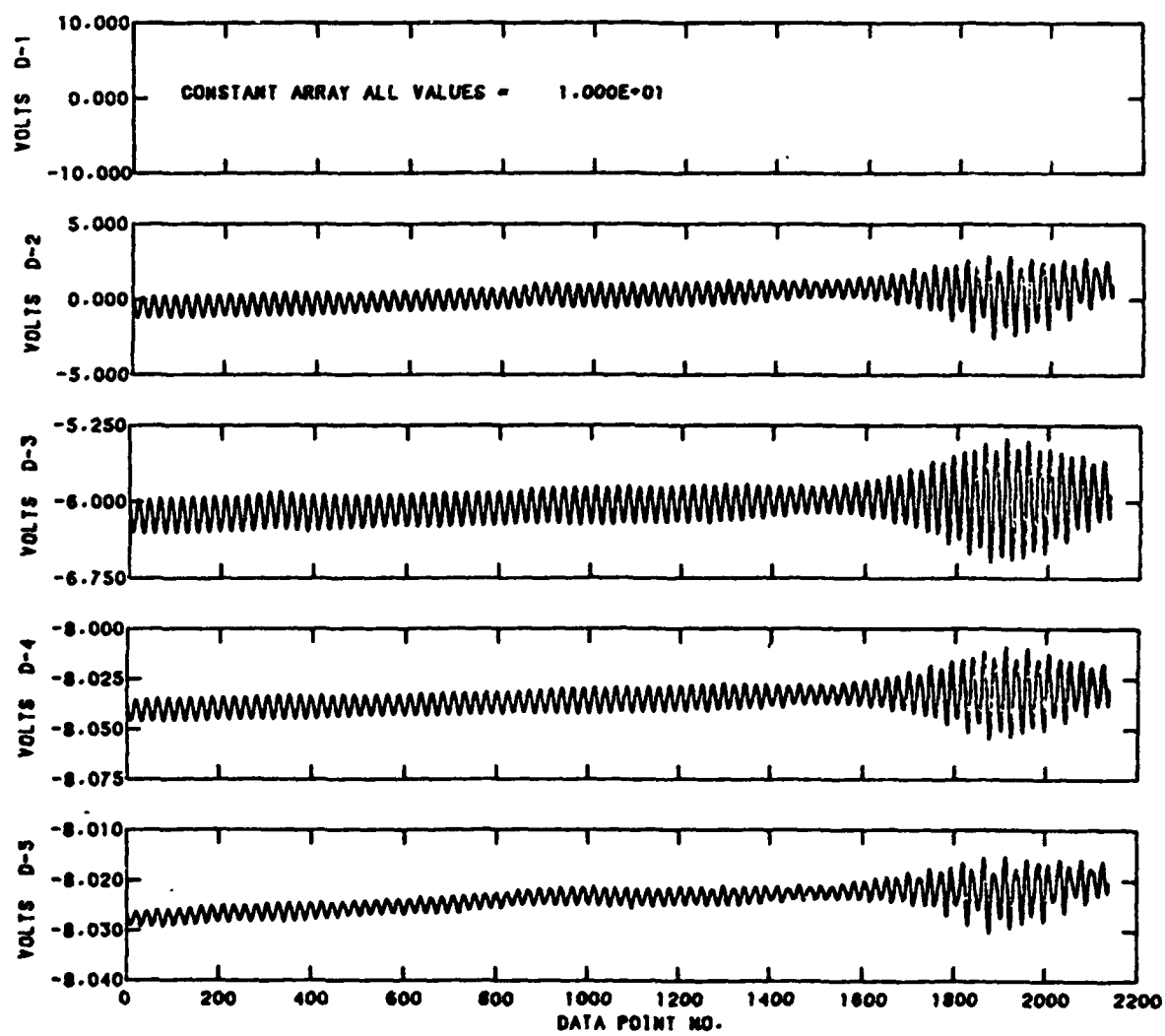


SPIRIT
G.M.T. 09:49:22.584

RAW INTERFEROMGRAM

TAL 417.714

SCAN 0227
FILTER 0

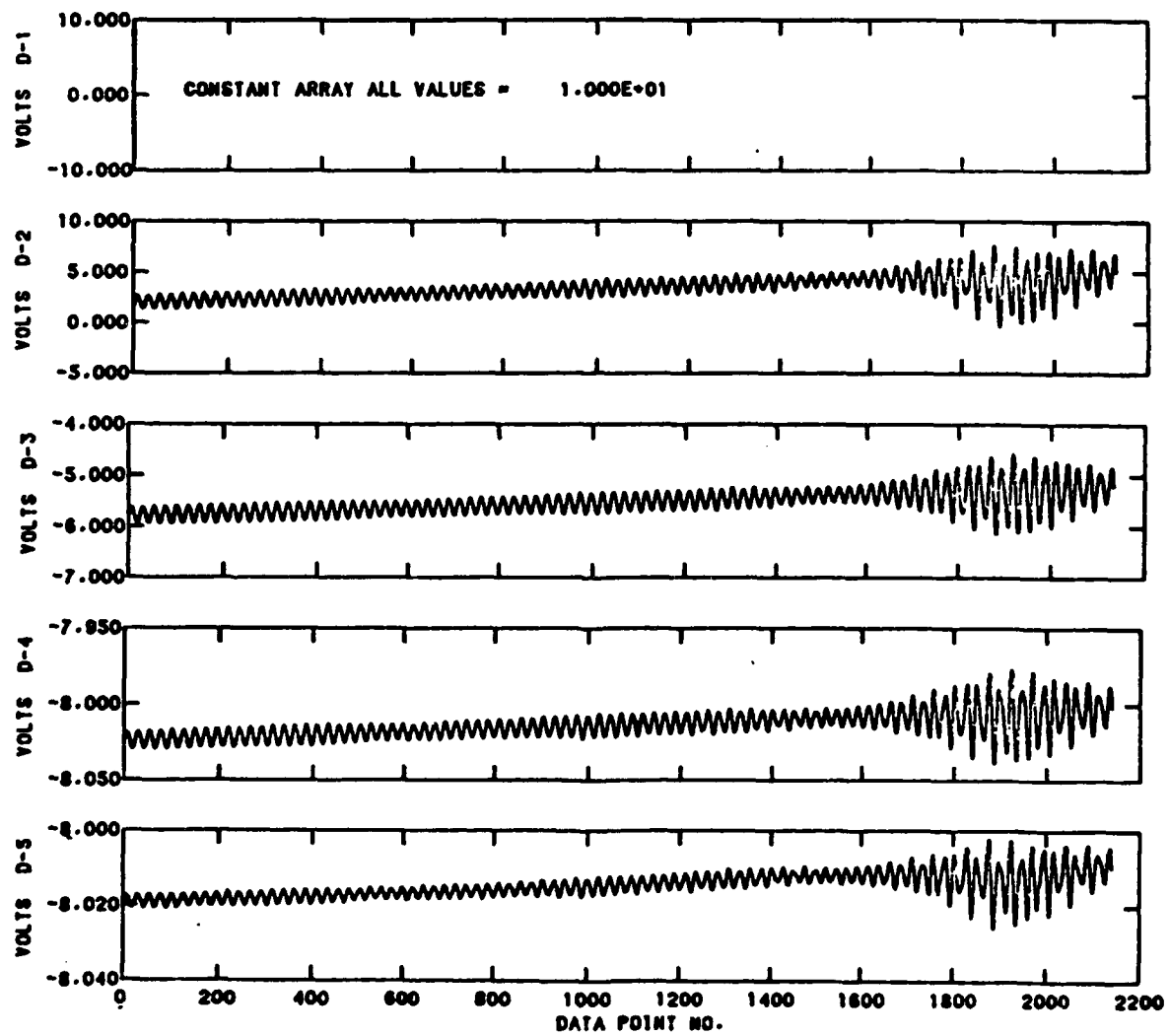


SPIRIT
G.M.T. 09:49:23.884

RAW INTERFEROMGRAM

TAL 419.014

SCAN 0228
FILTER 0

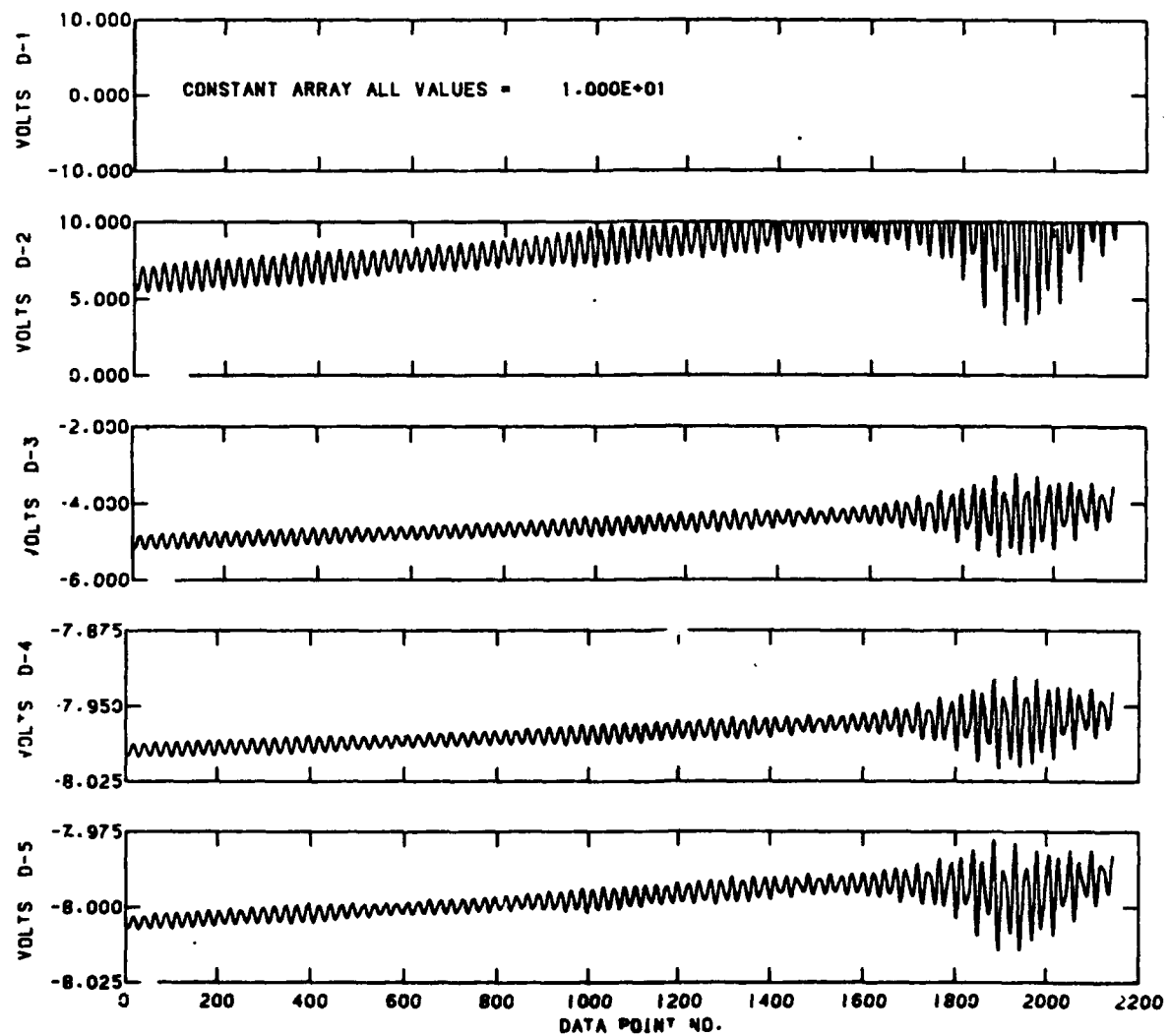


SPIRIT
G.M.T. 09:49:25.185

RAW INTERFEROGRAM

TAL 420.315

SCAN 0229
FILTER 0

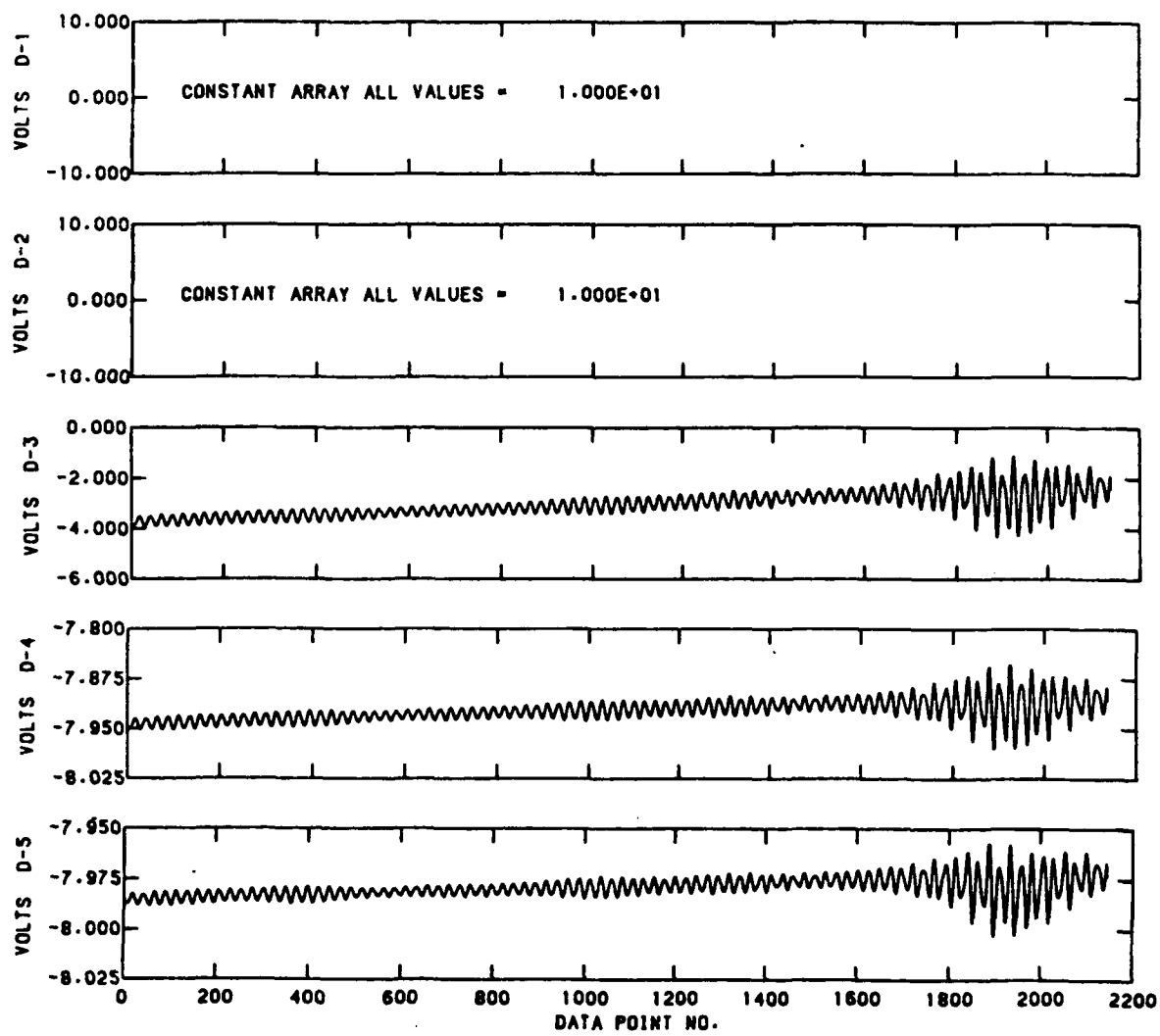


SPIRIT
G.M.T. 09:49:26.495

RAW INTERFERGRAM

TAL 421.625

SCAN 0230
FILTER 0

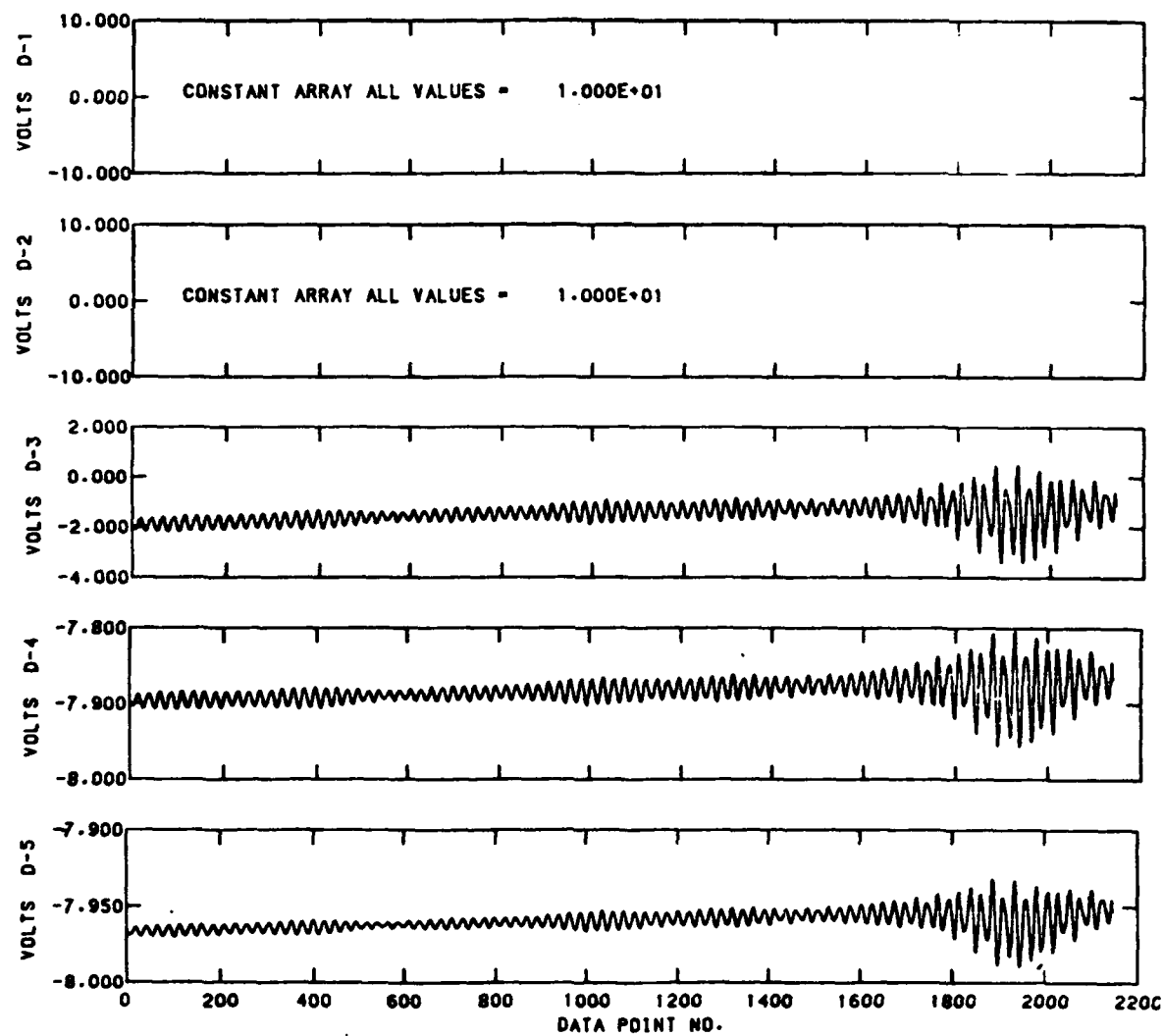


SPIRIT
G.M.T. 09:49:27.796

RAW INTERFEROGRAM

TAL 422.925

SCAN 0231
FILTER 0

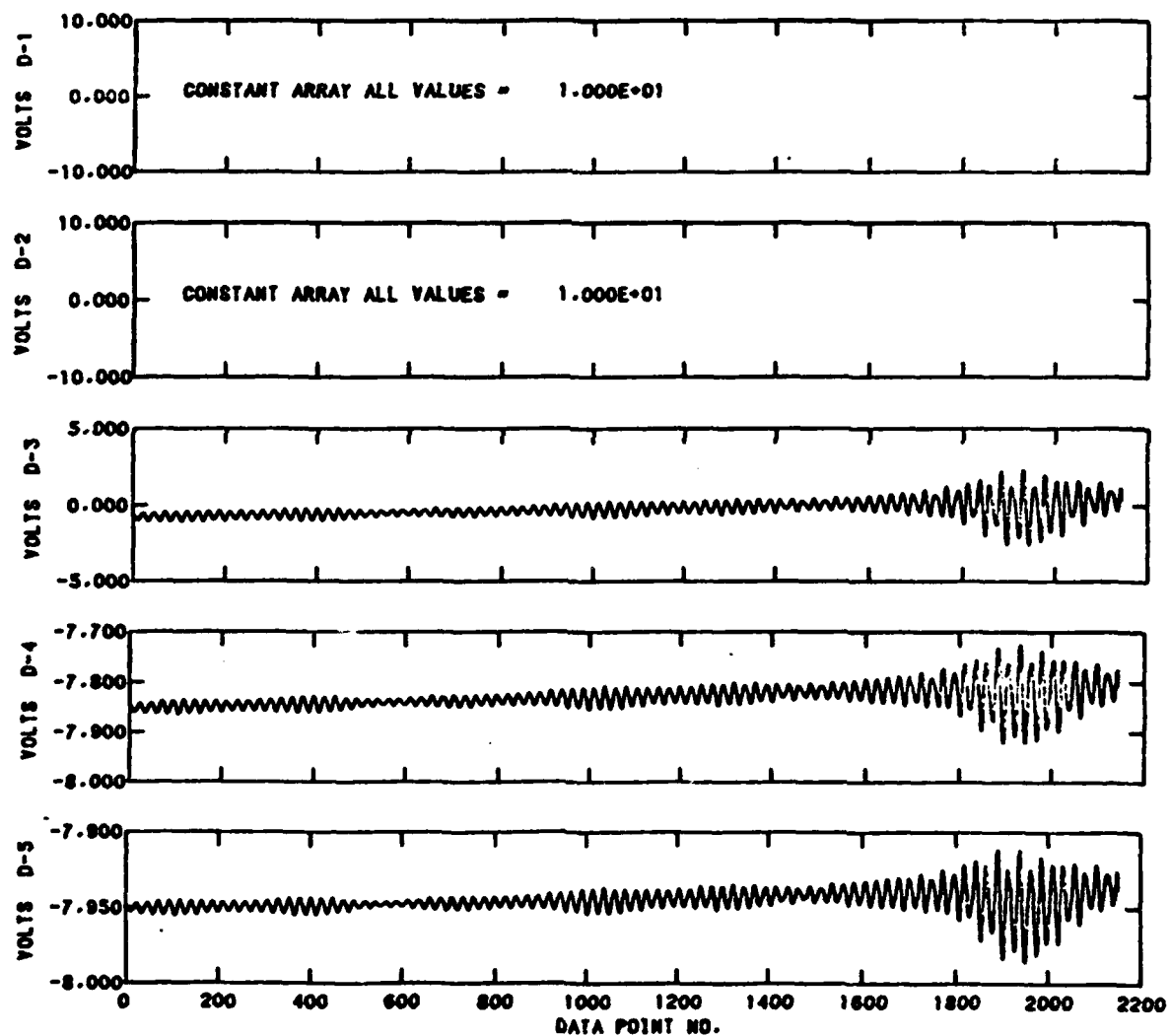


SPIRIT
G.M.T. 09:49:29.106

RAW INTERFEROGRAM

TAL 424.236

SCAN 0232
FILTER 0

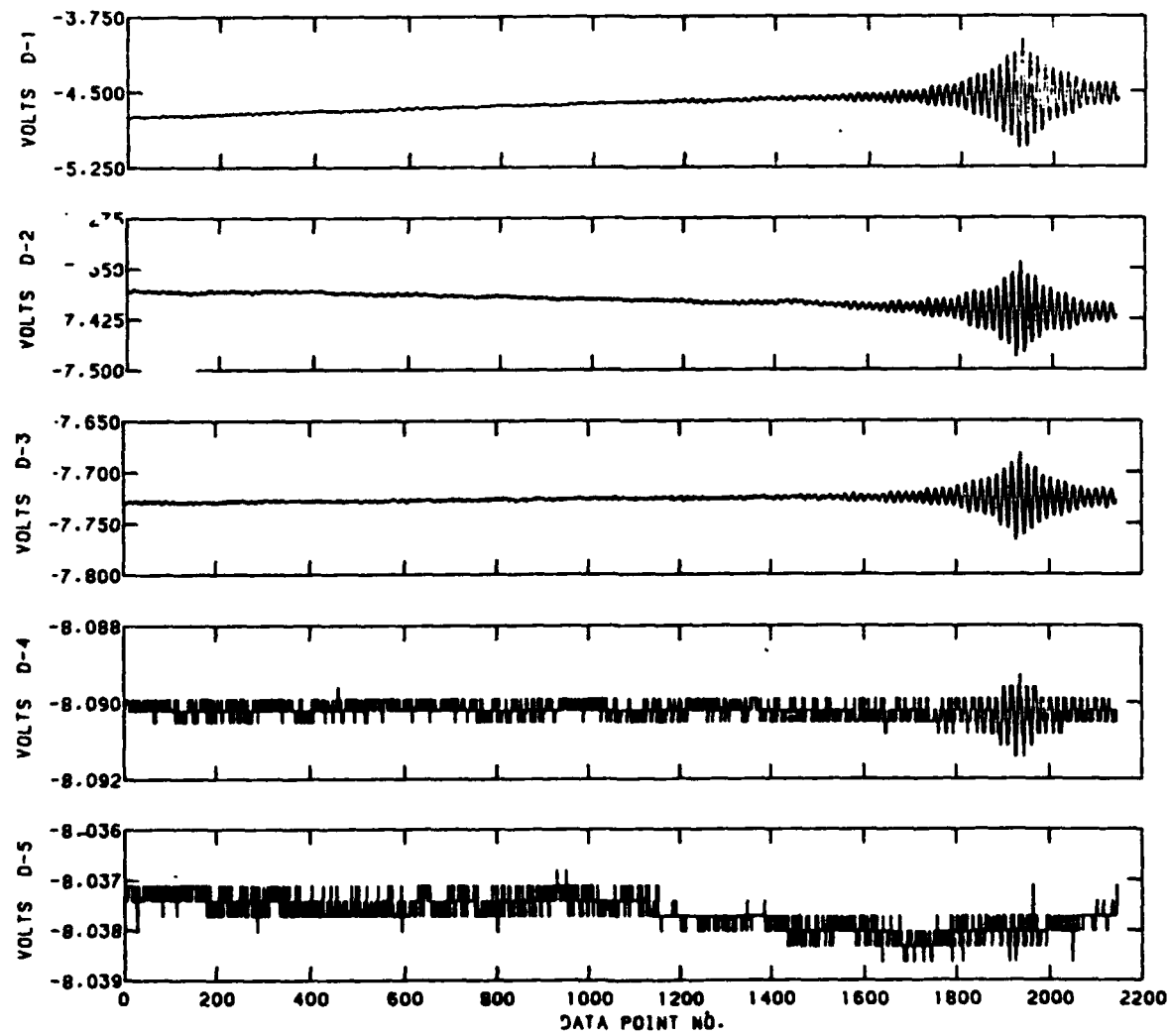


SPIRIT
G.M.T. 09:49:31.738

RAW INTERFEROMGRAM

TAL 426.868

SCAN 0234
FILTER 1

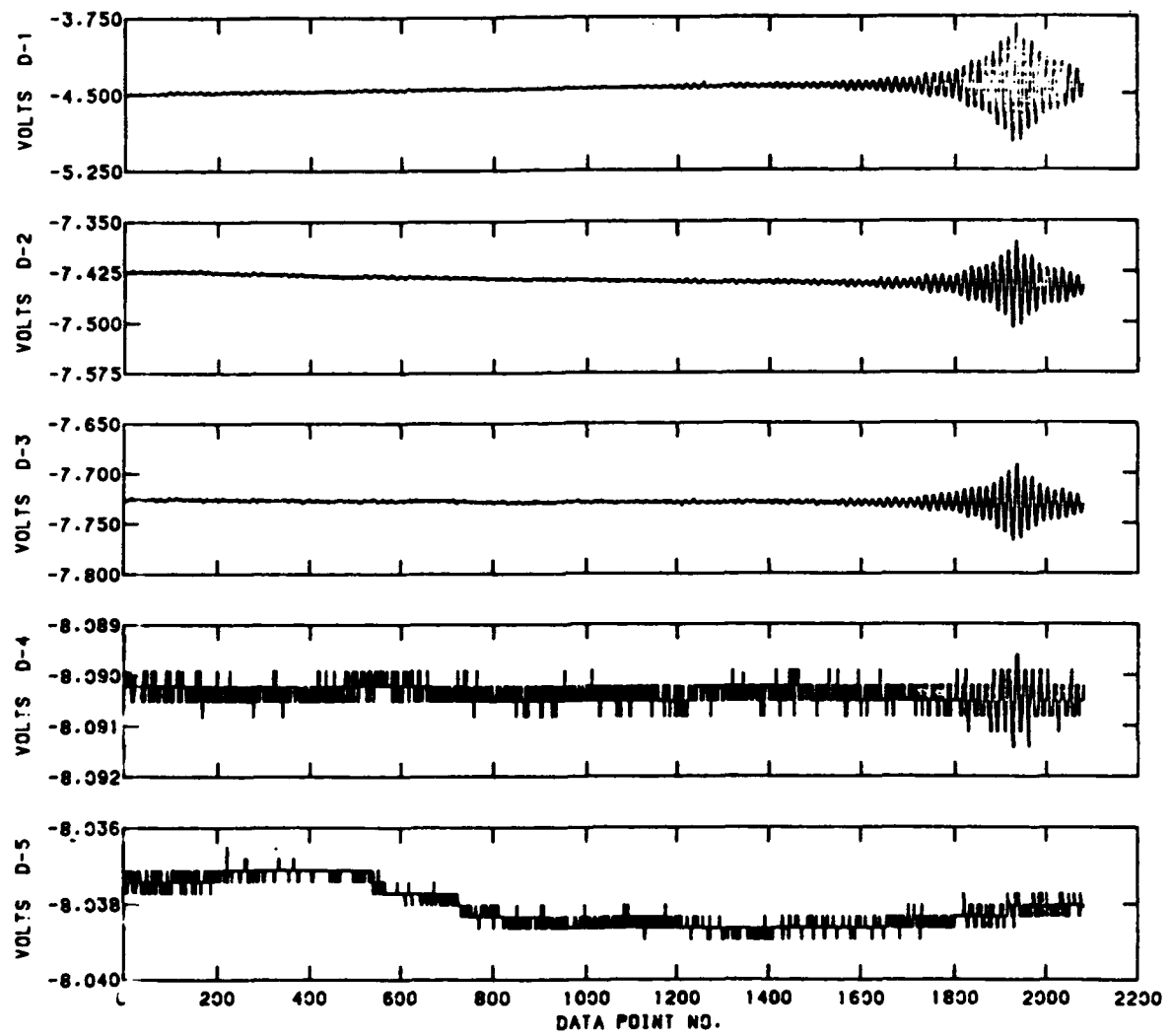


SPIRIT
G.M.T. 09:49:33.039

RAW INTERFEROMGRAM

TAL 428.169

SCAN 0235
FILTER 1

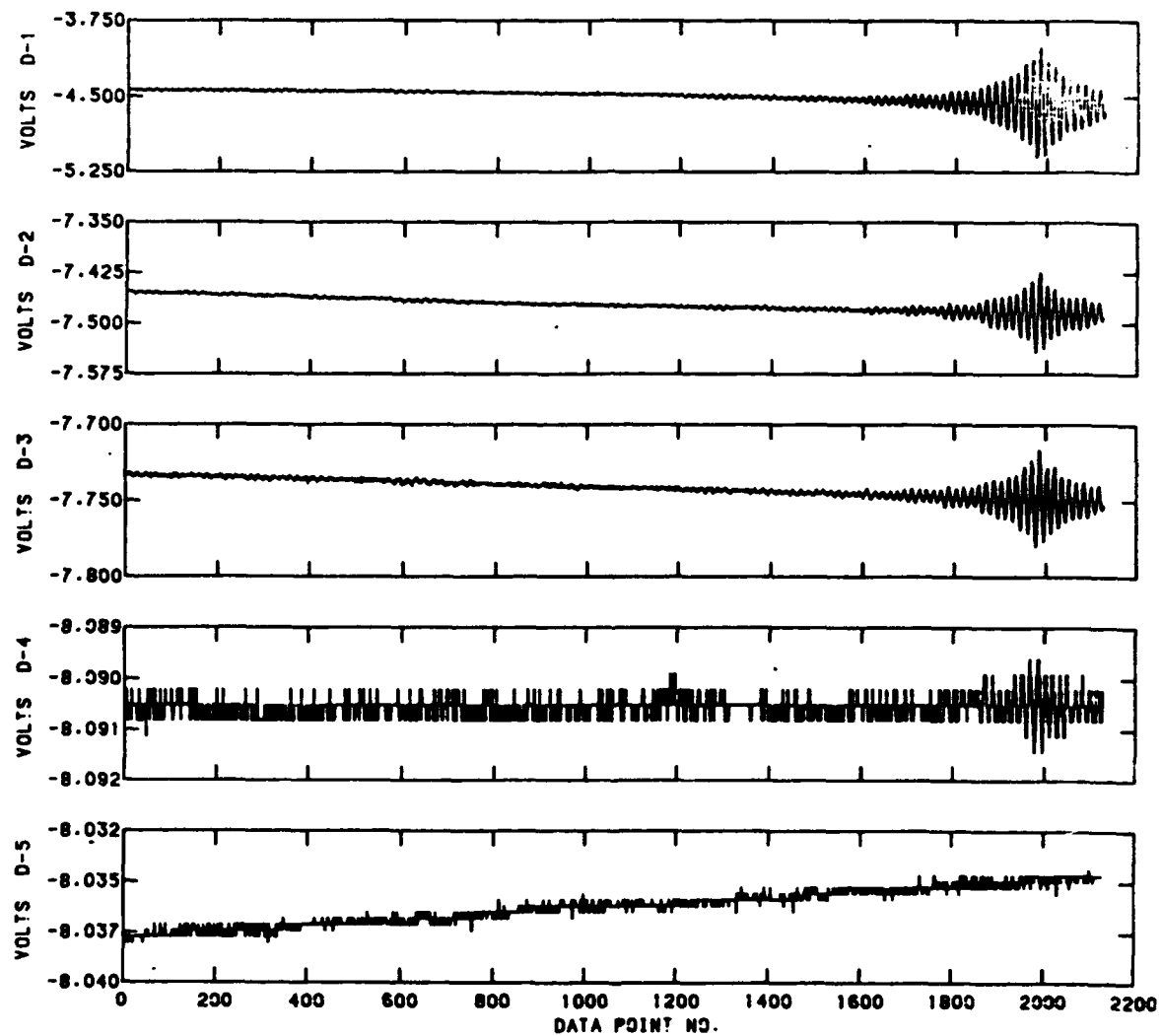


SPIRIT
G.M.T. 09:49:34.308

RAW INTERFEROMGRAM

TAL 429.438

SCAN 0236
FILTER 1

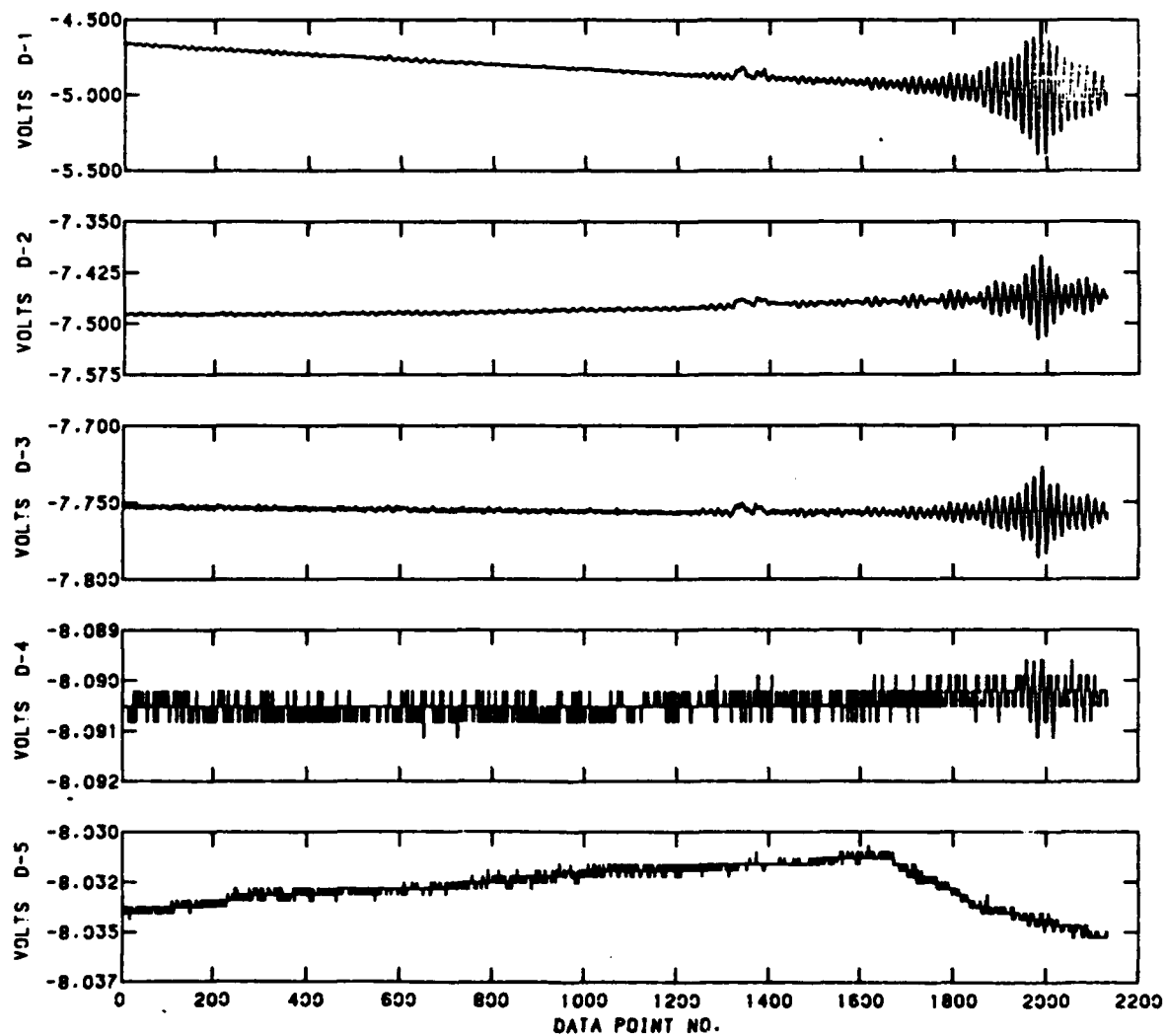


SPIRIT
C.M.T. 09:49:35.609

RAW INTERFEROMGRAM

TAL 430.739

SCAN 0237
FILTER 1

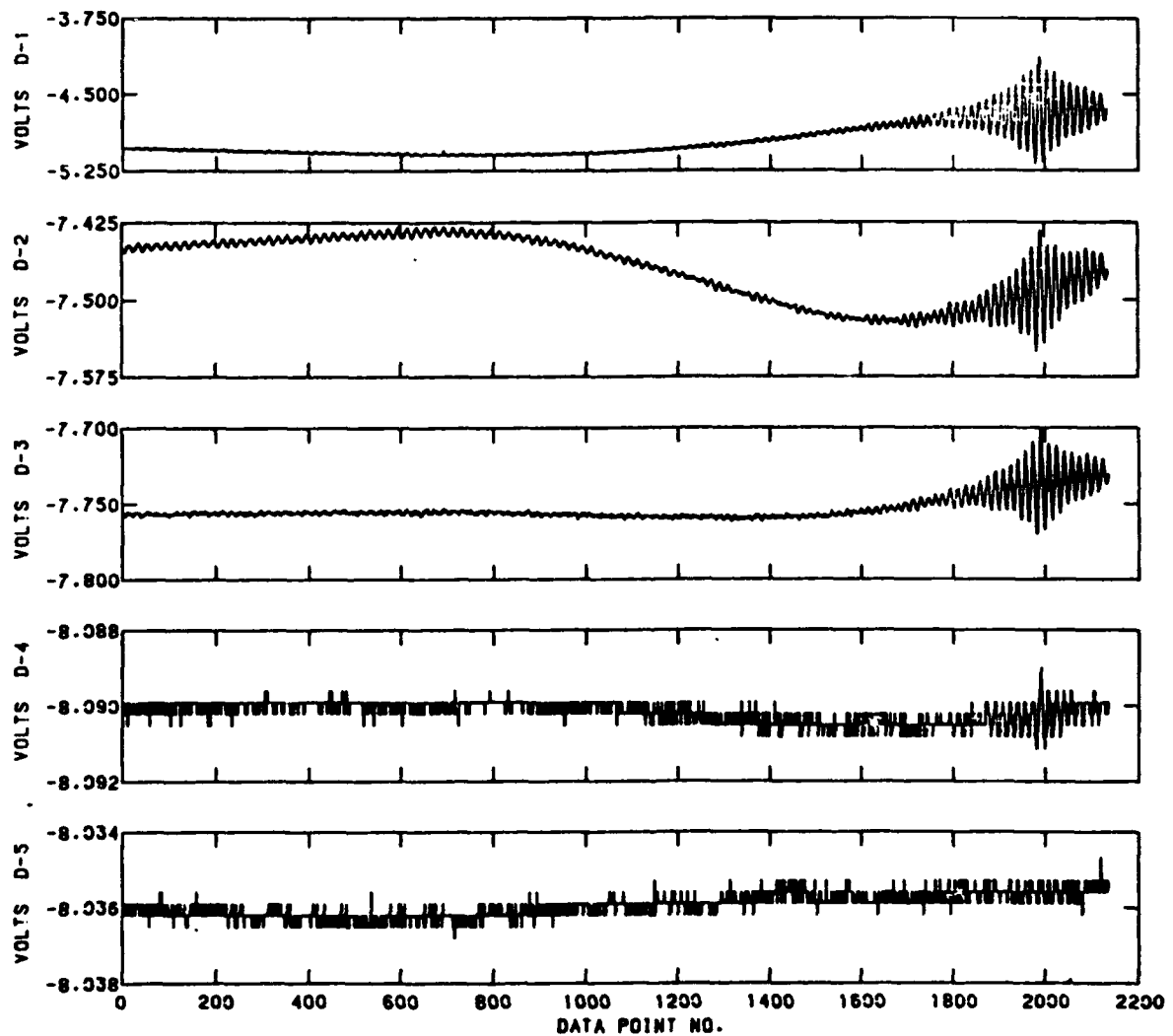


SPIRIT
G.M.T. 09:49:36.909

RAW INTERFEROMGRAM

TAL 432.039

SCAN 0238
FILTER 1

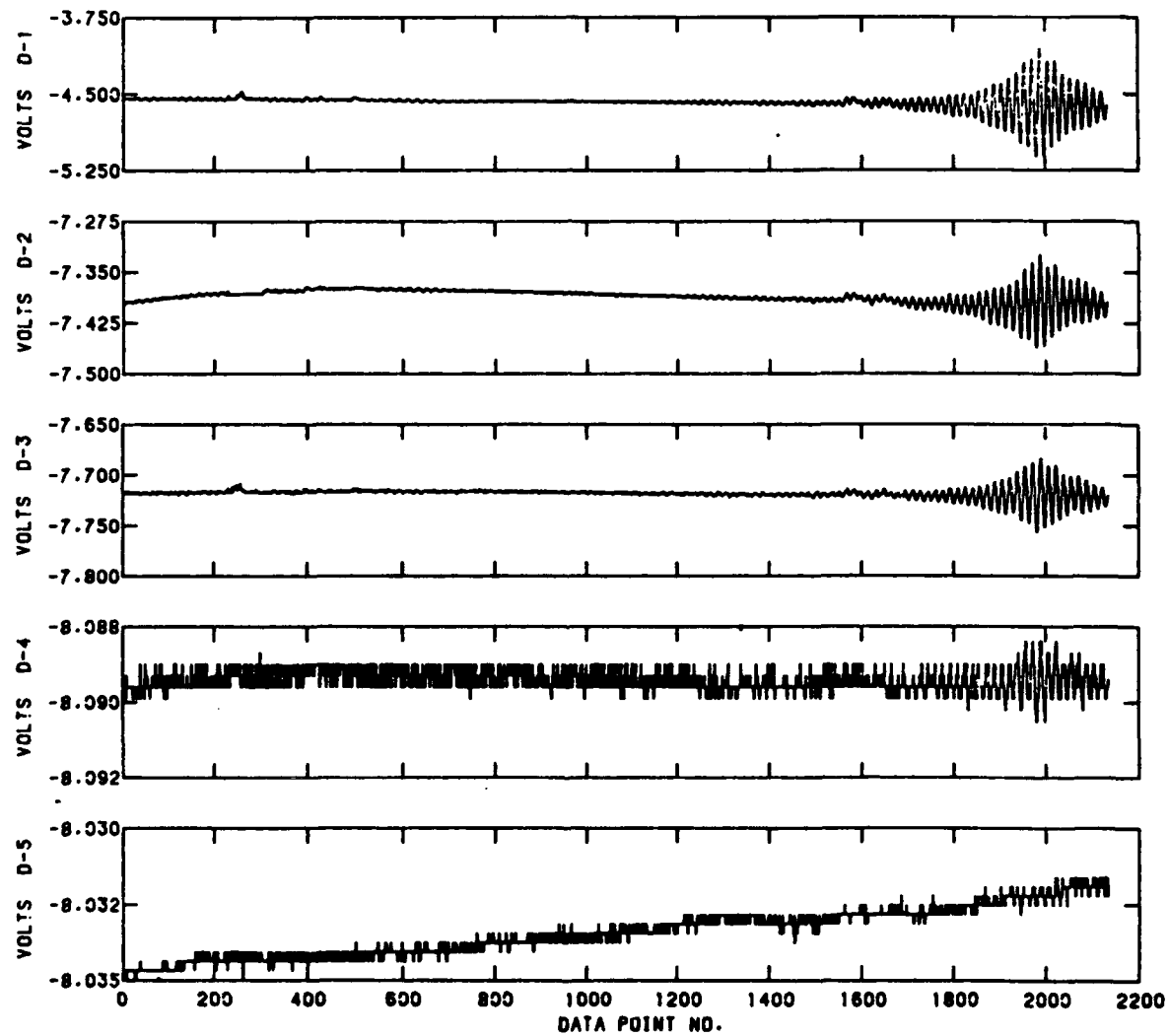


SPIRIT
G.M.T. 09:49:38.210

RAW INTERFEROMGRAM

TAL 433.340

SCAN 0239
FILTER 1

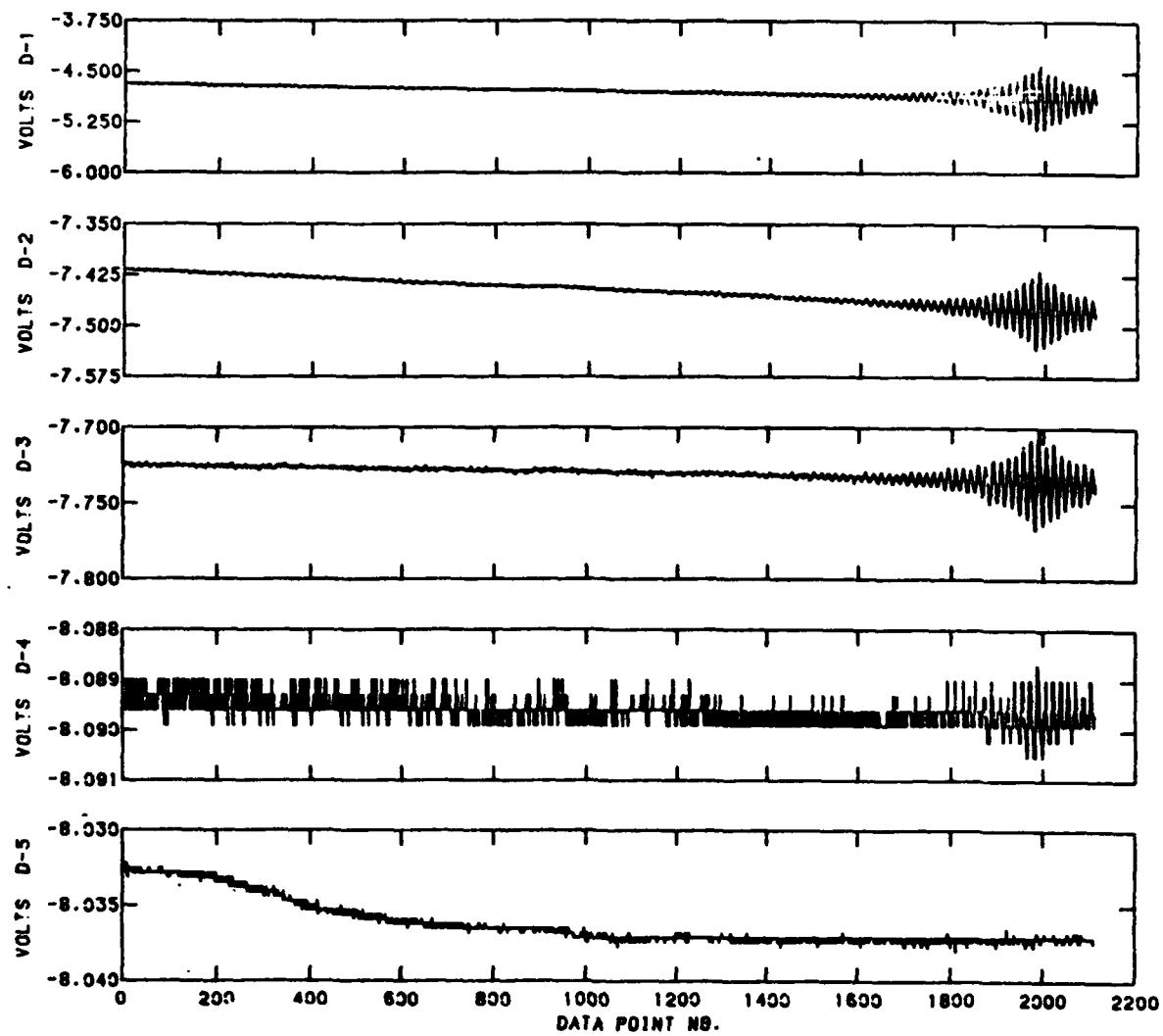


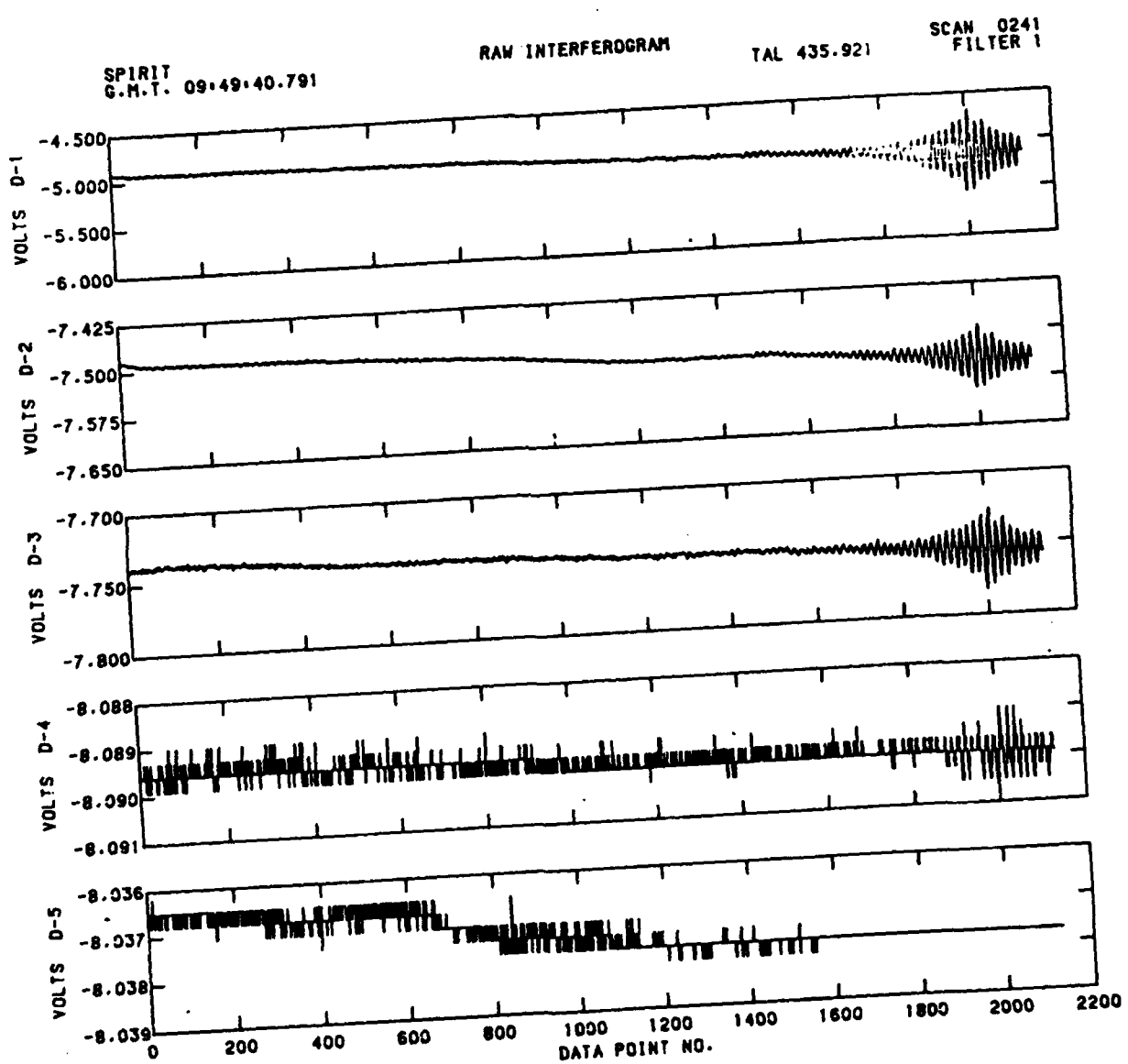
SPIRIT
G.M.T. 09:49:39.510

RAW INTERFEROMGRAM

TAL 434.640

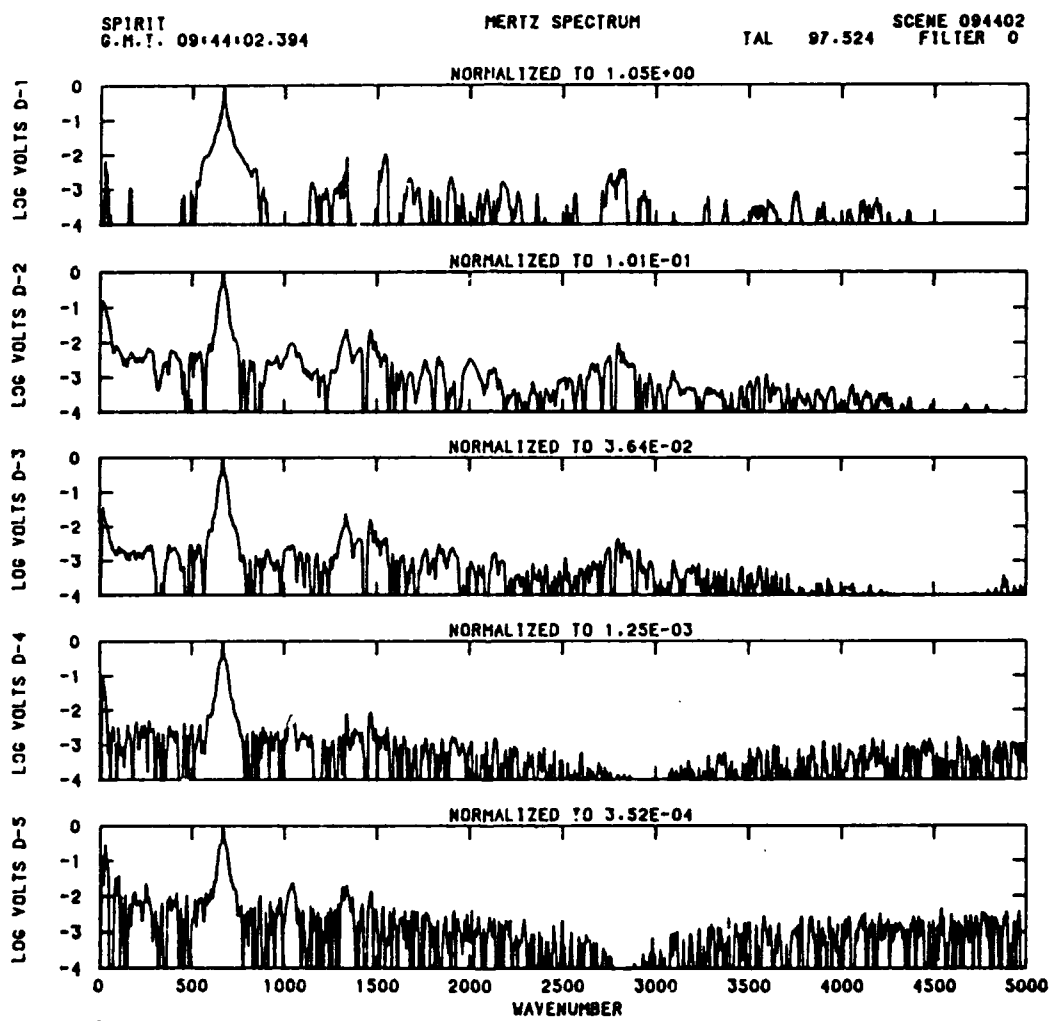
SCAN 0240
FILTER 1

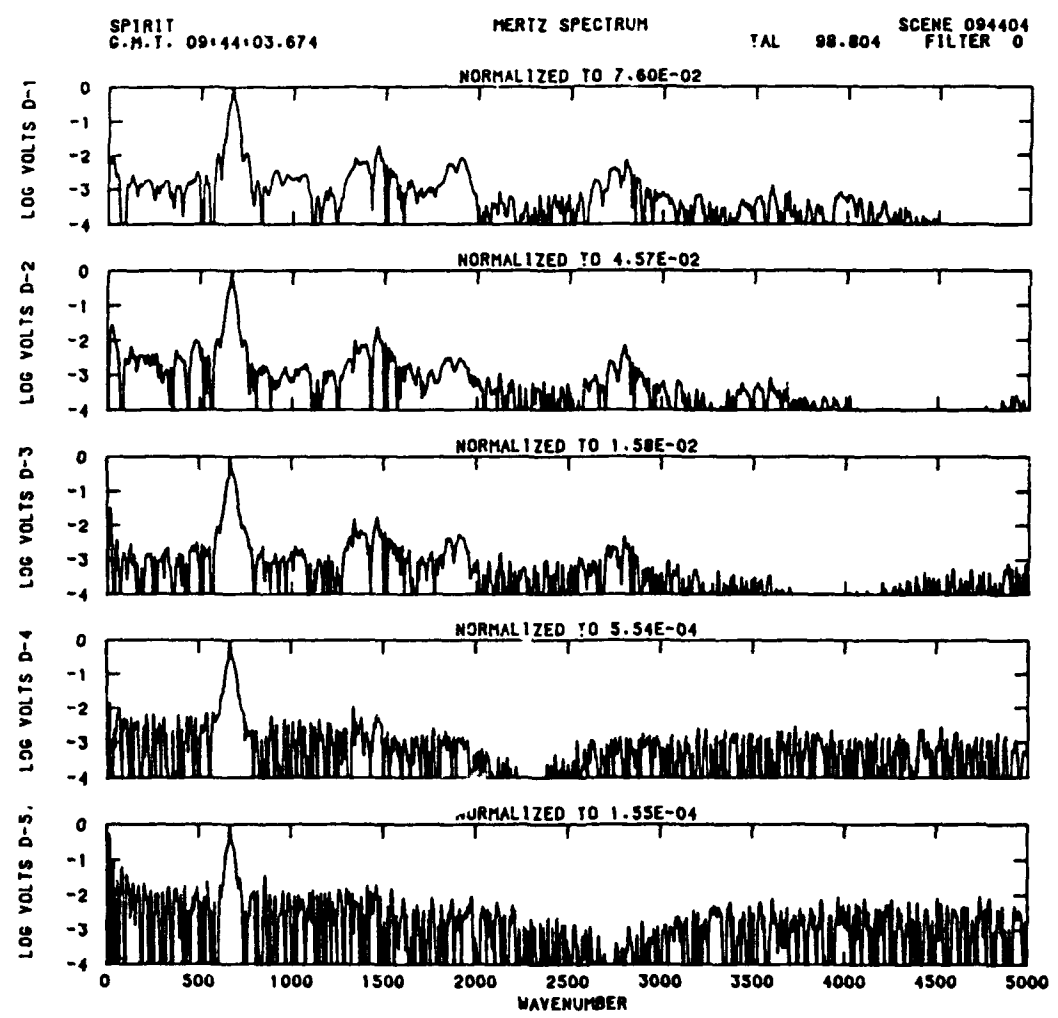


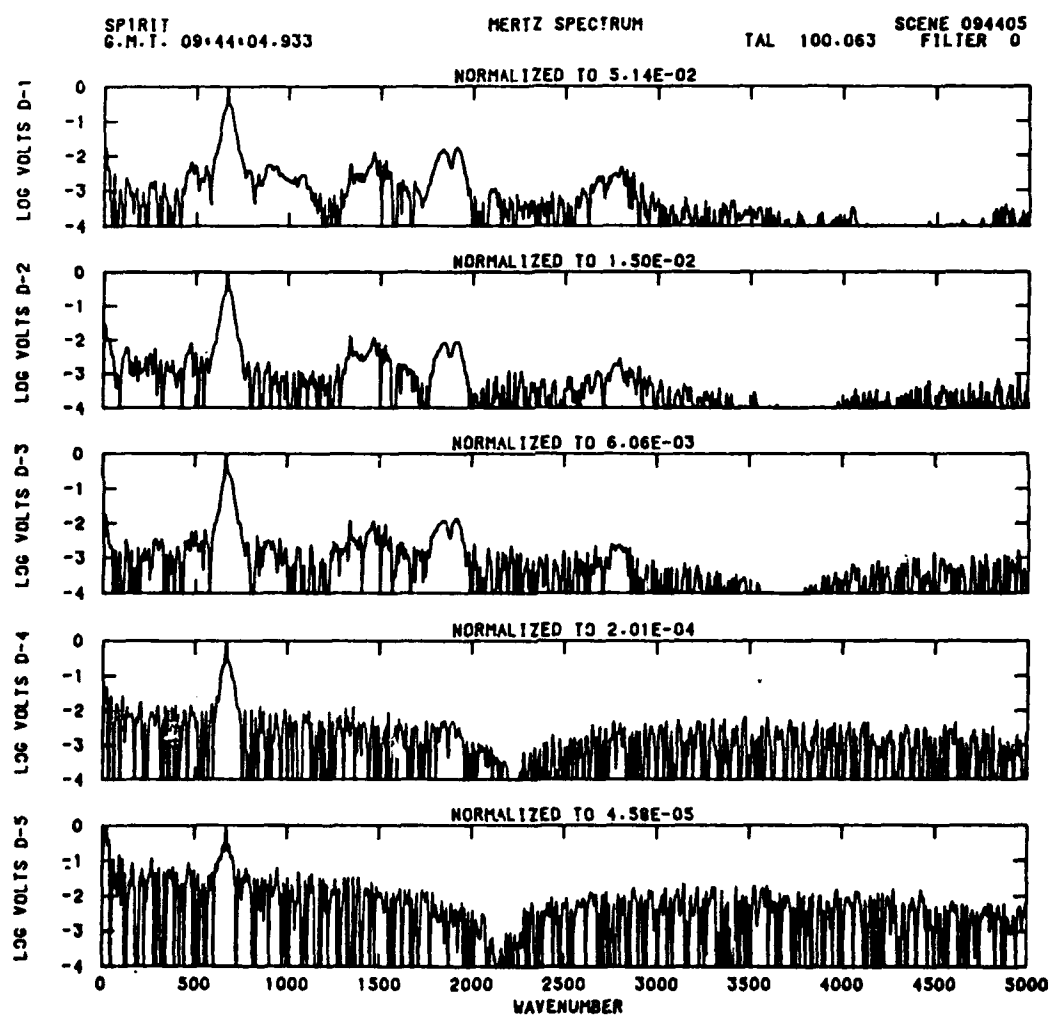


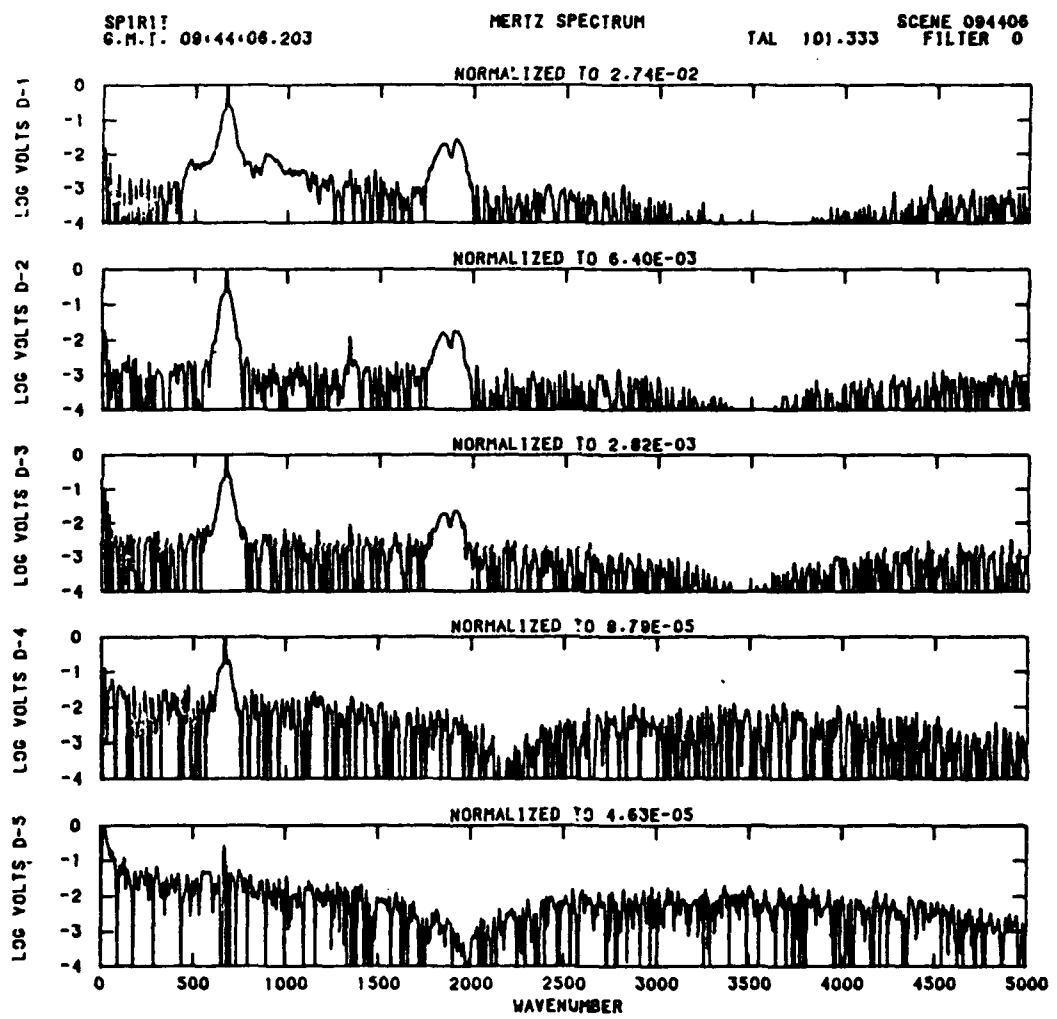
Appendix D

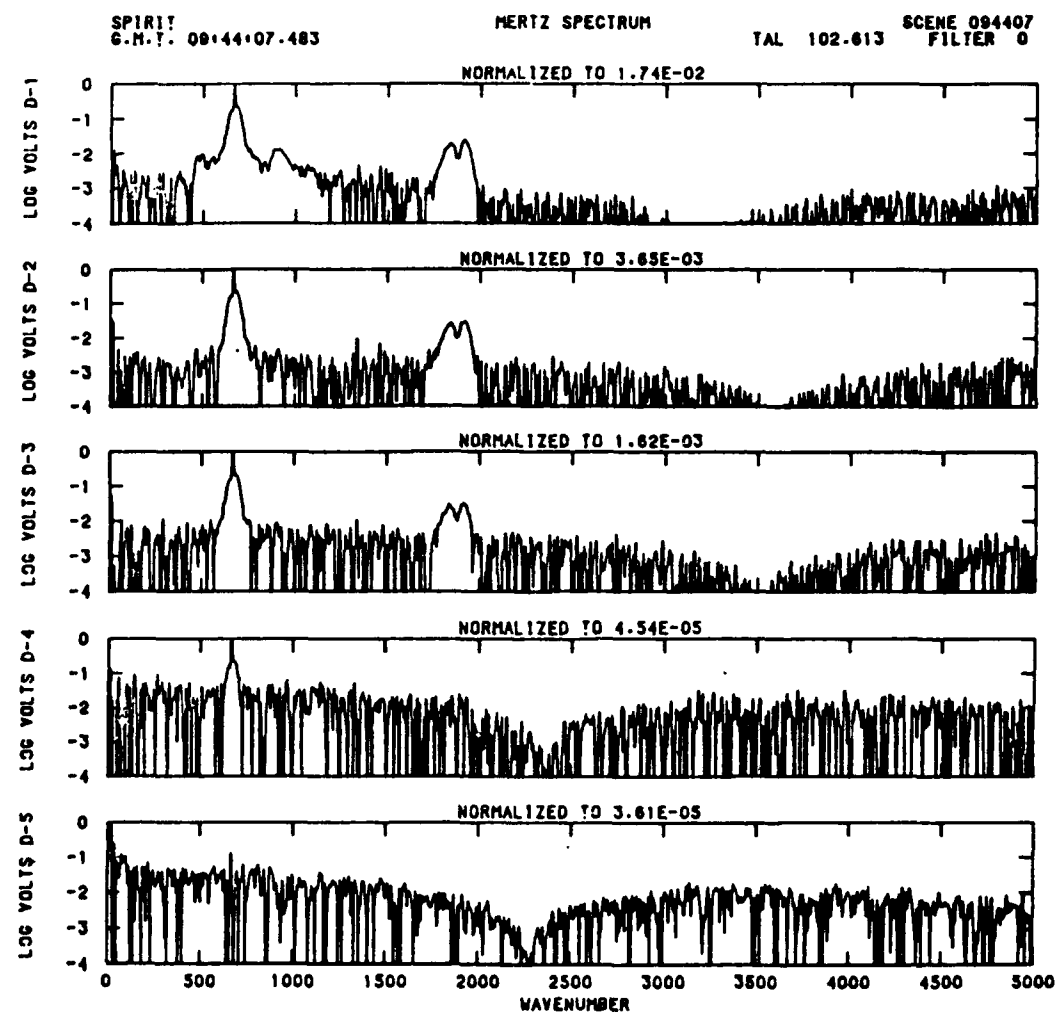
Sample of Transformed Spectra

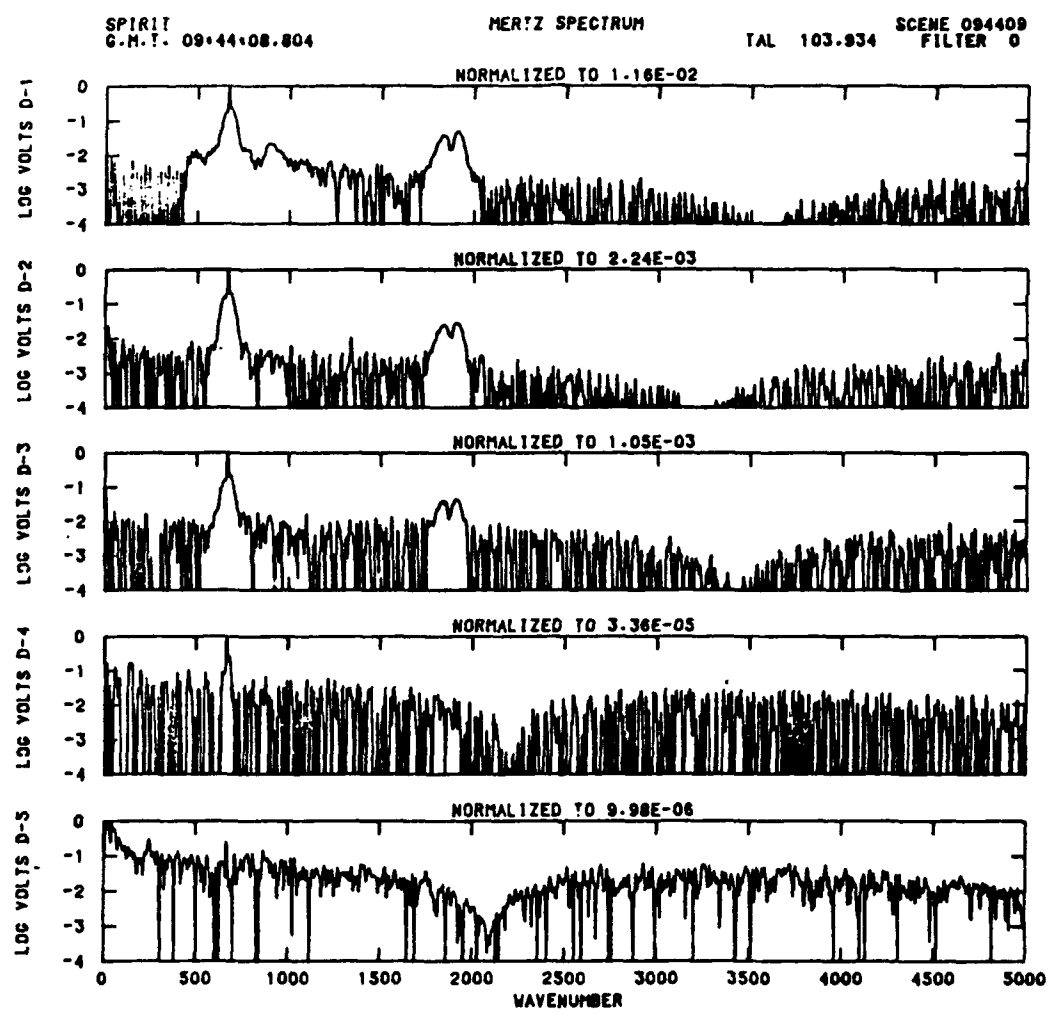


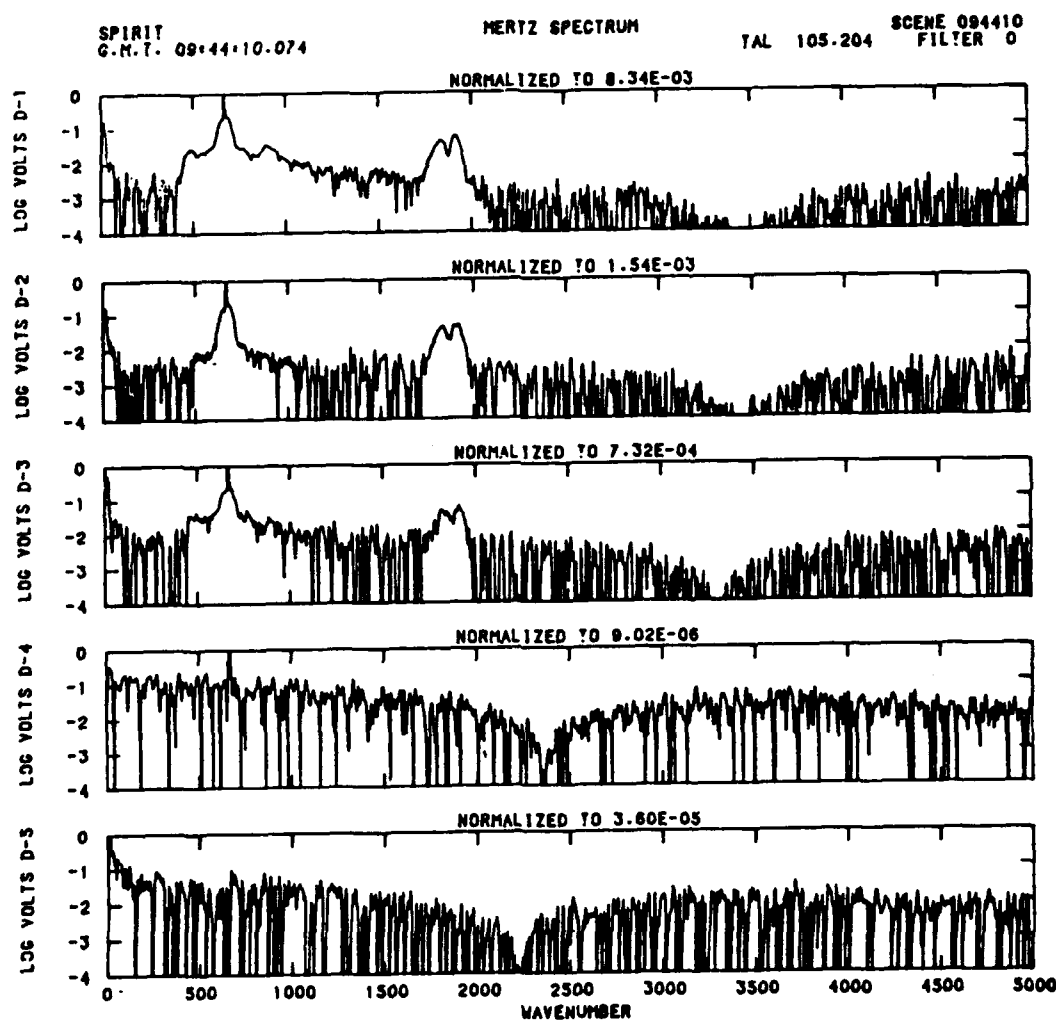


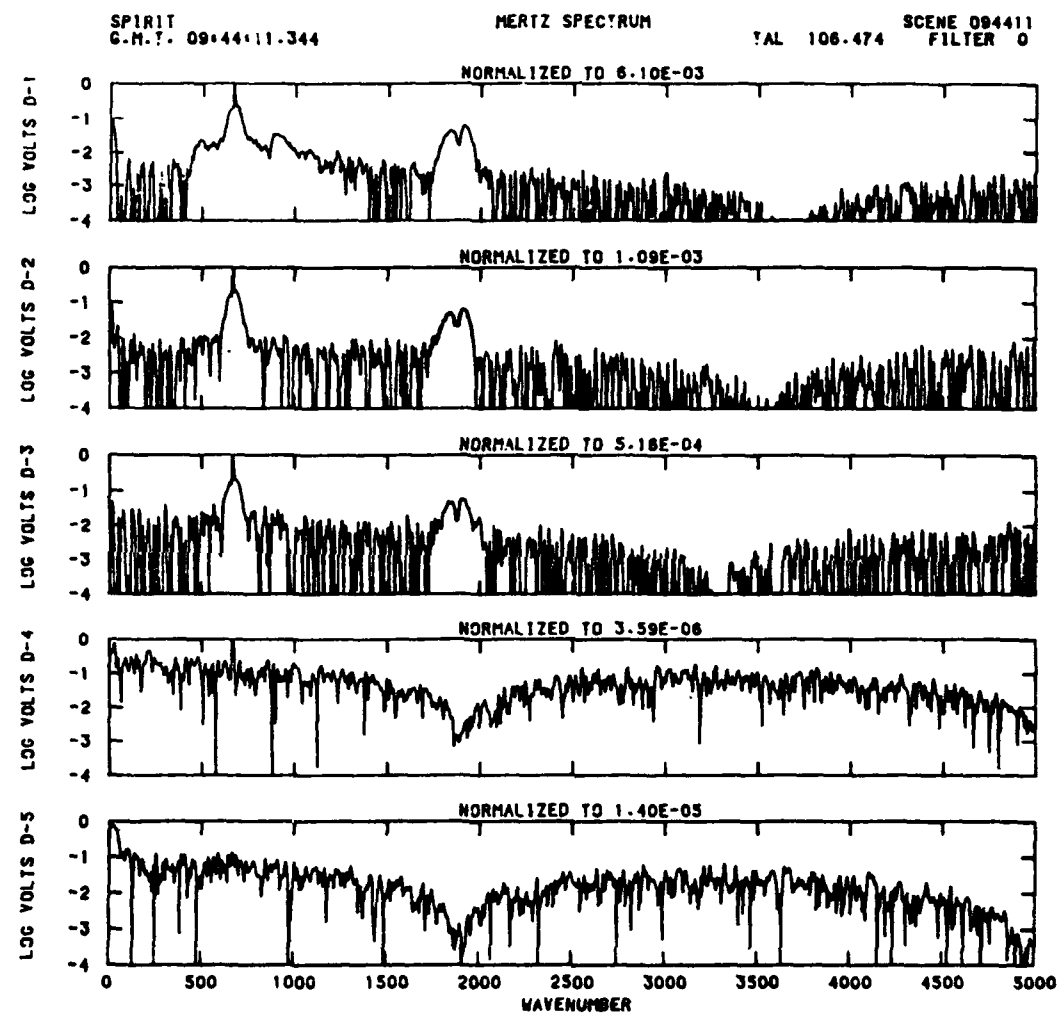


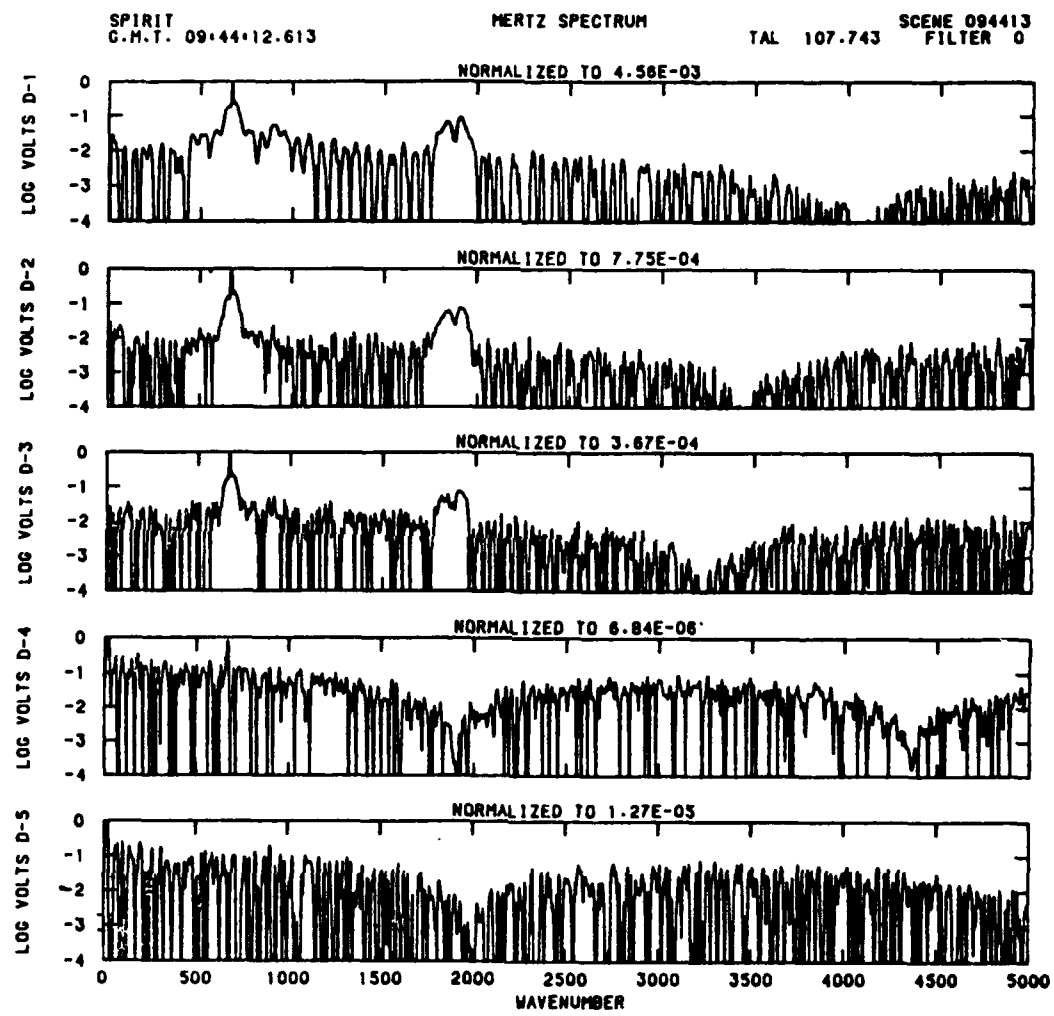


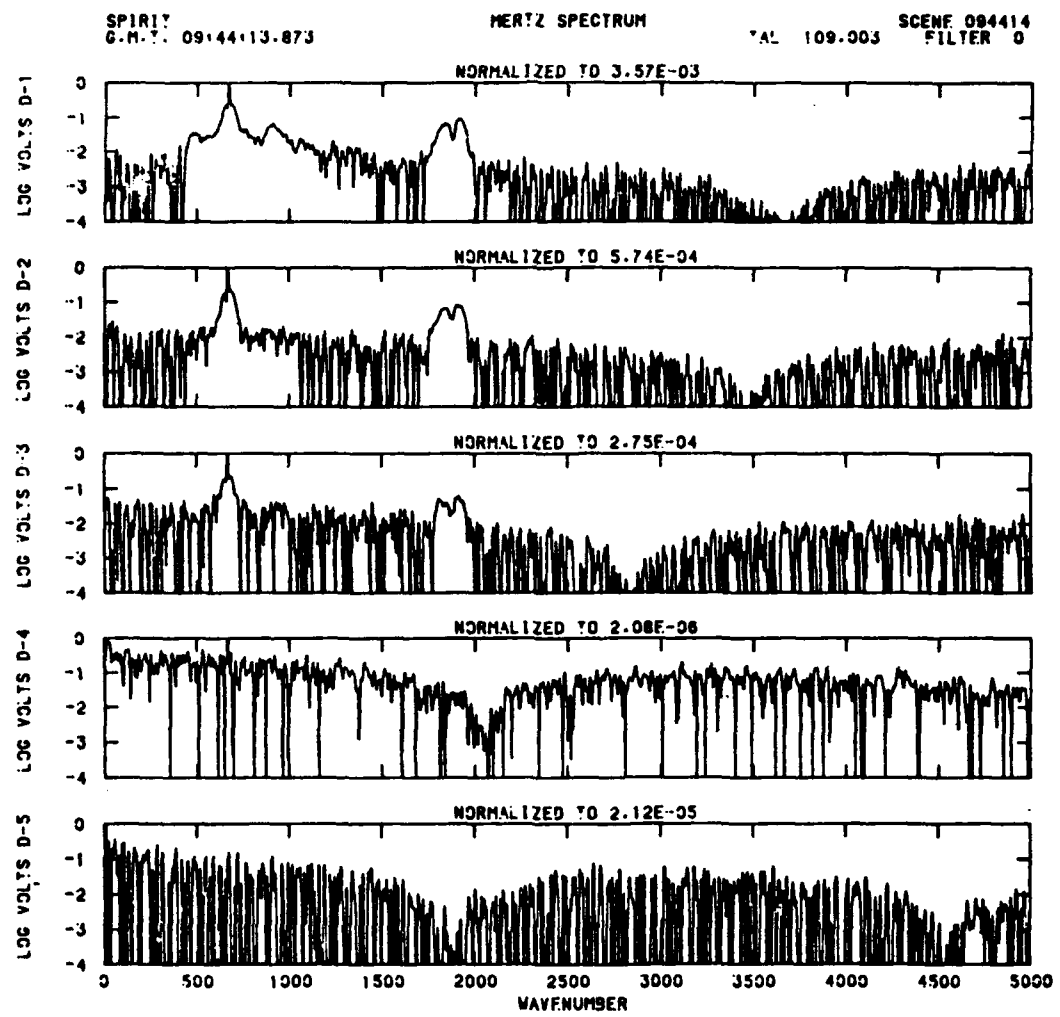


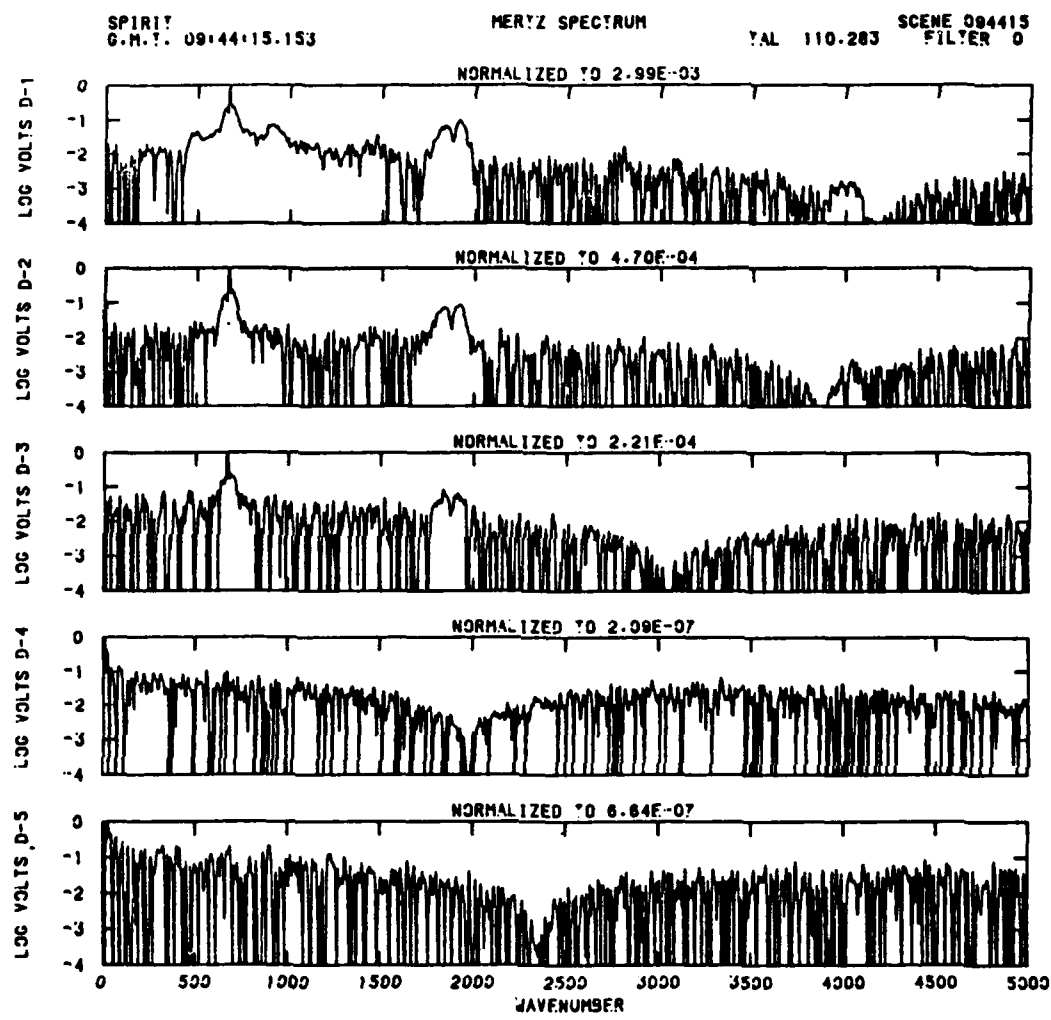


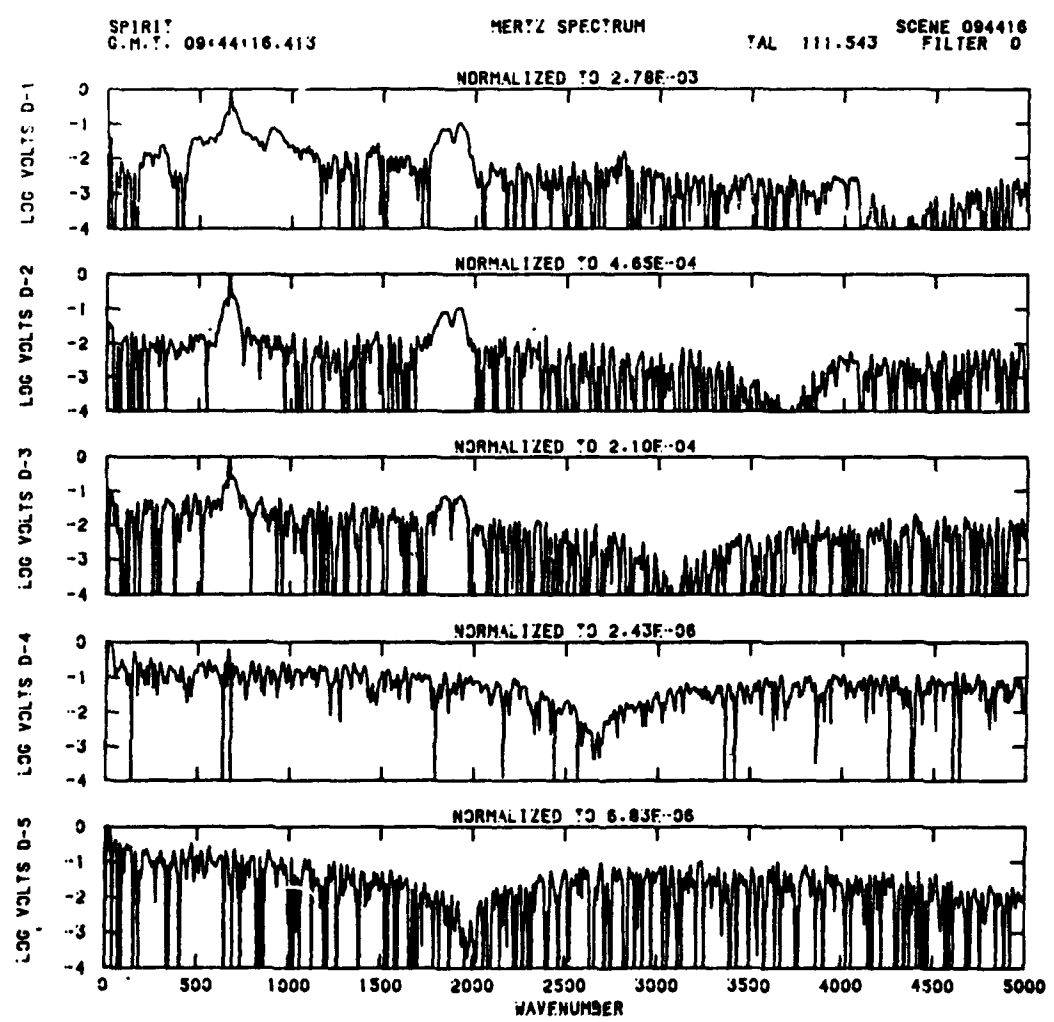


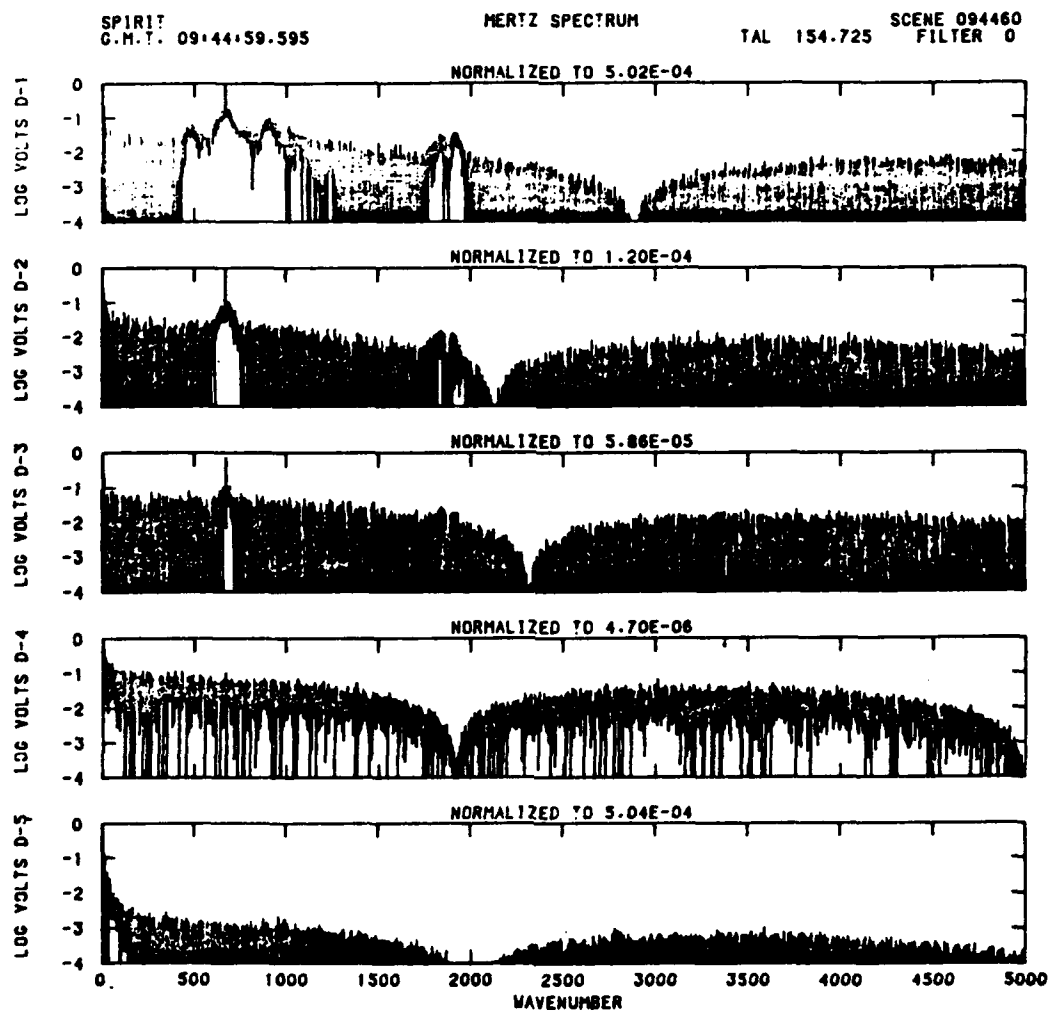


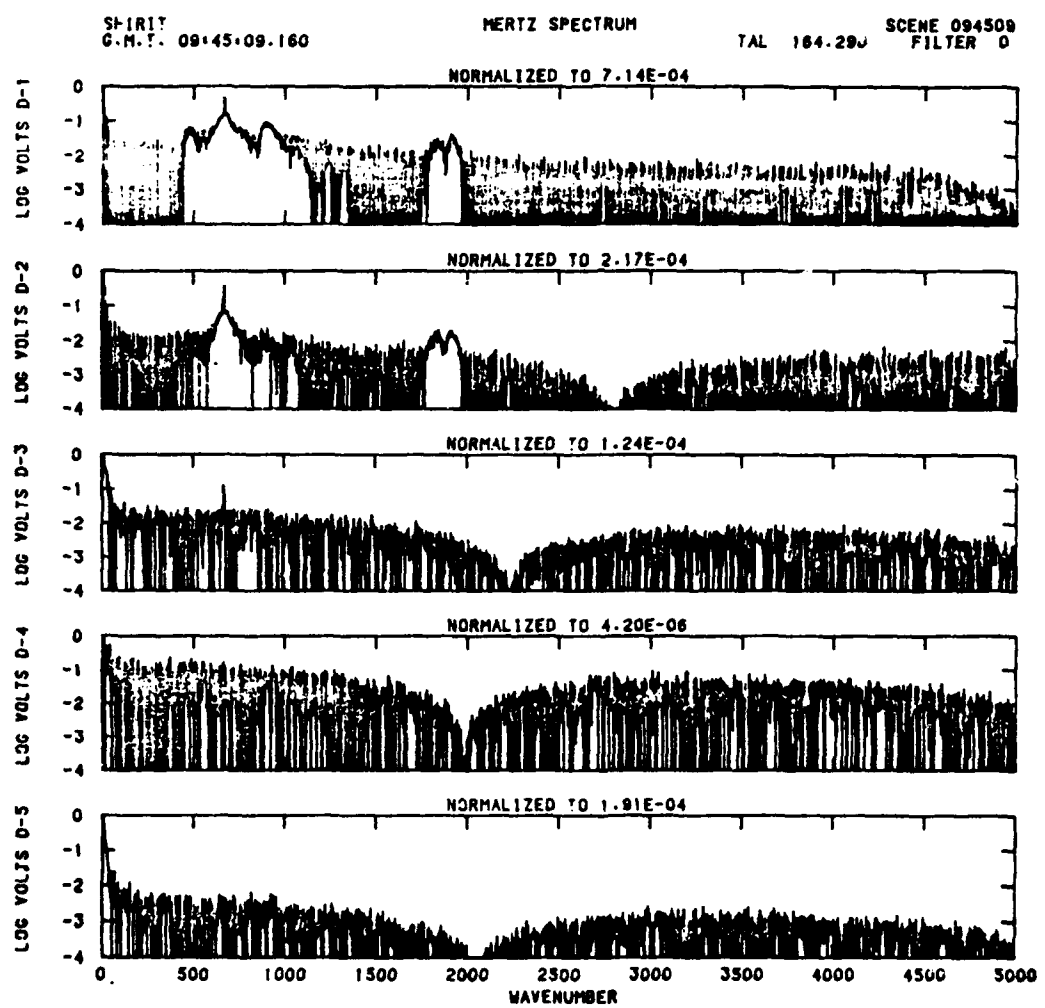


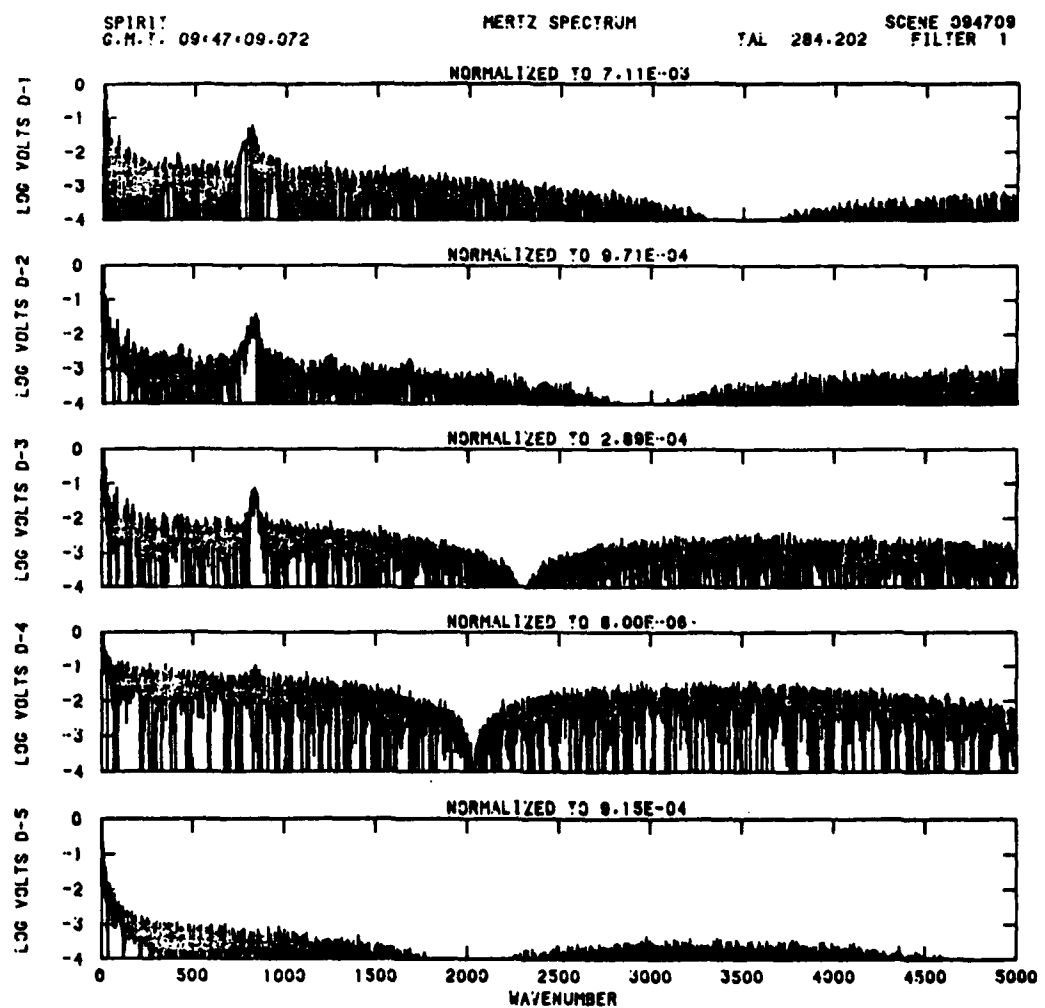


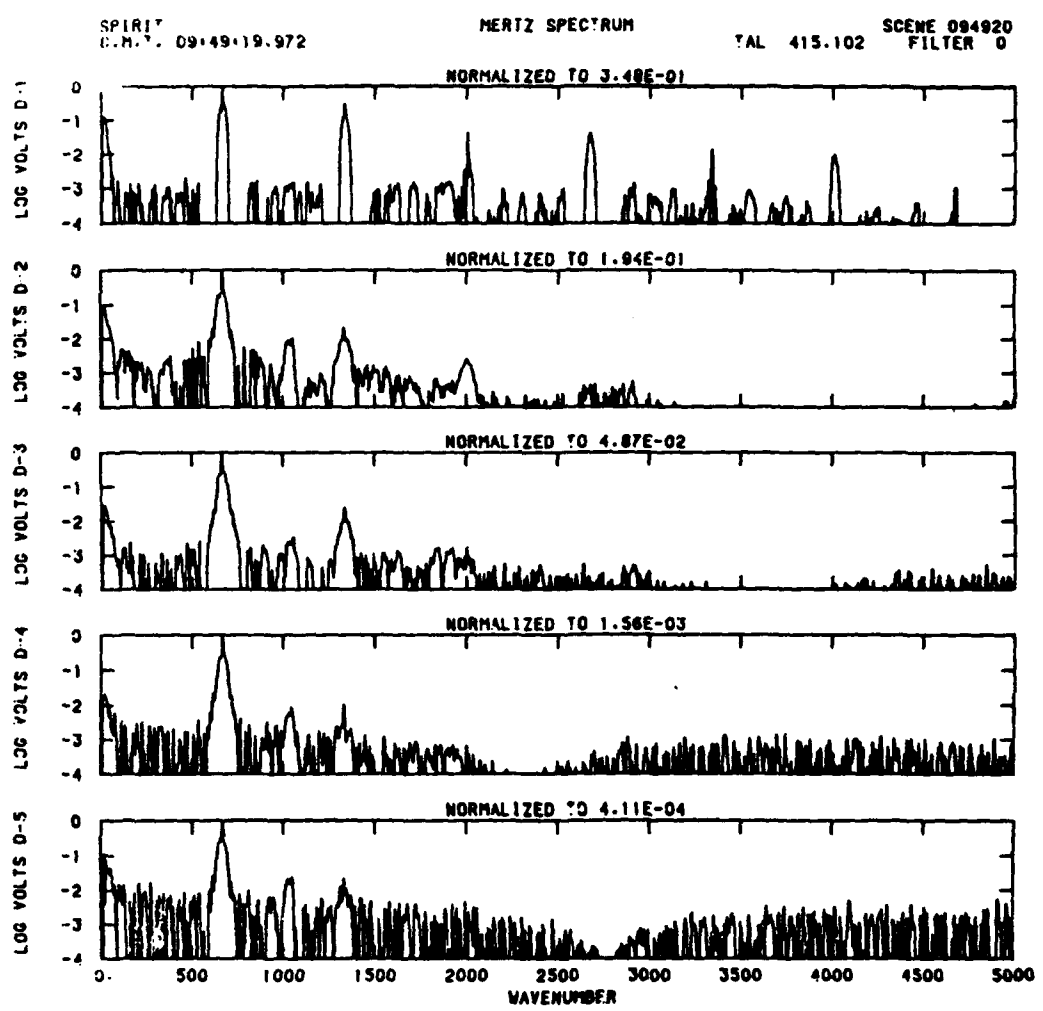


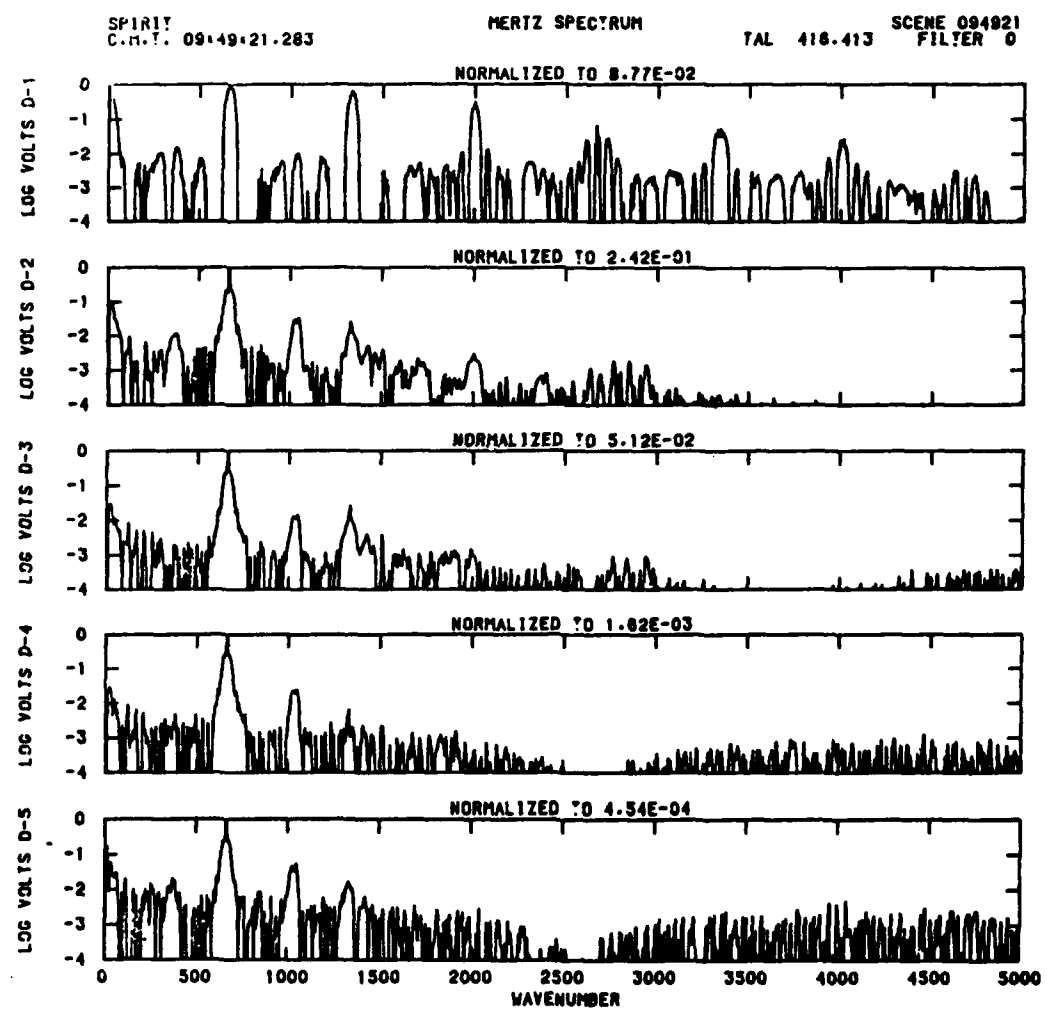


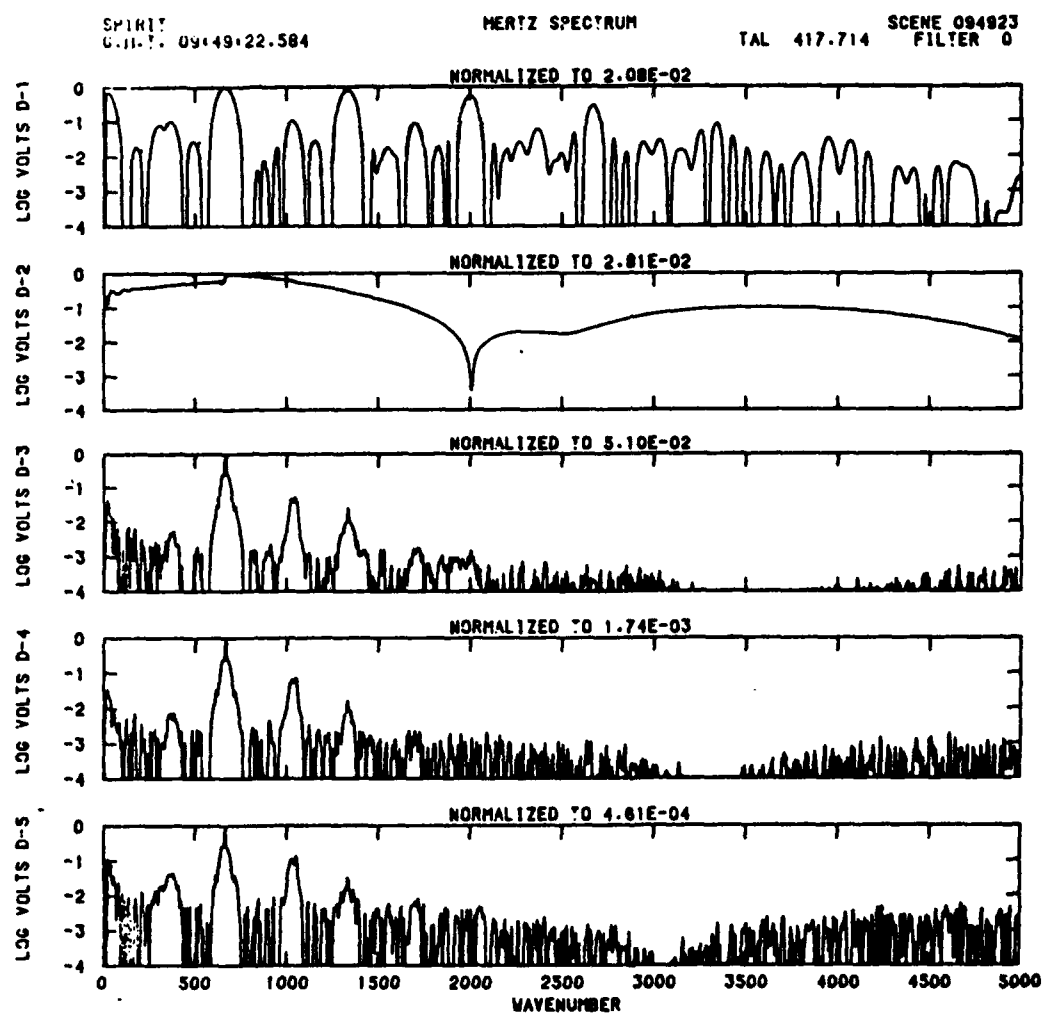


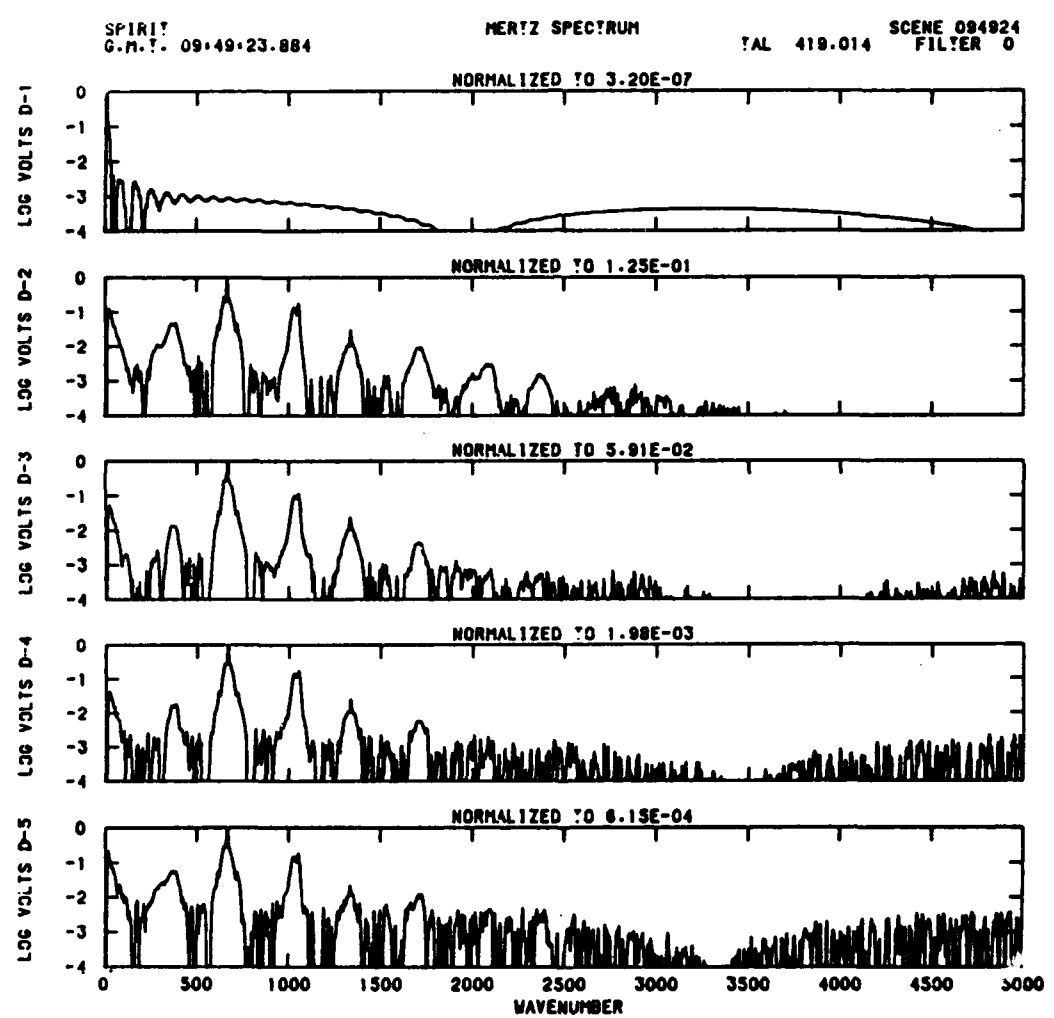








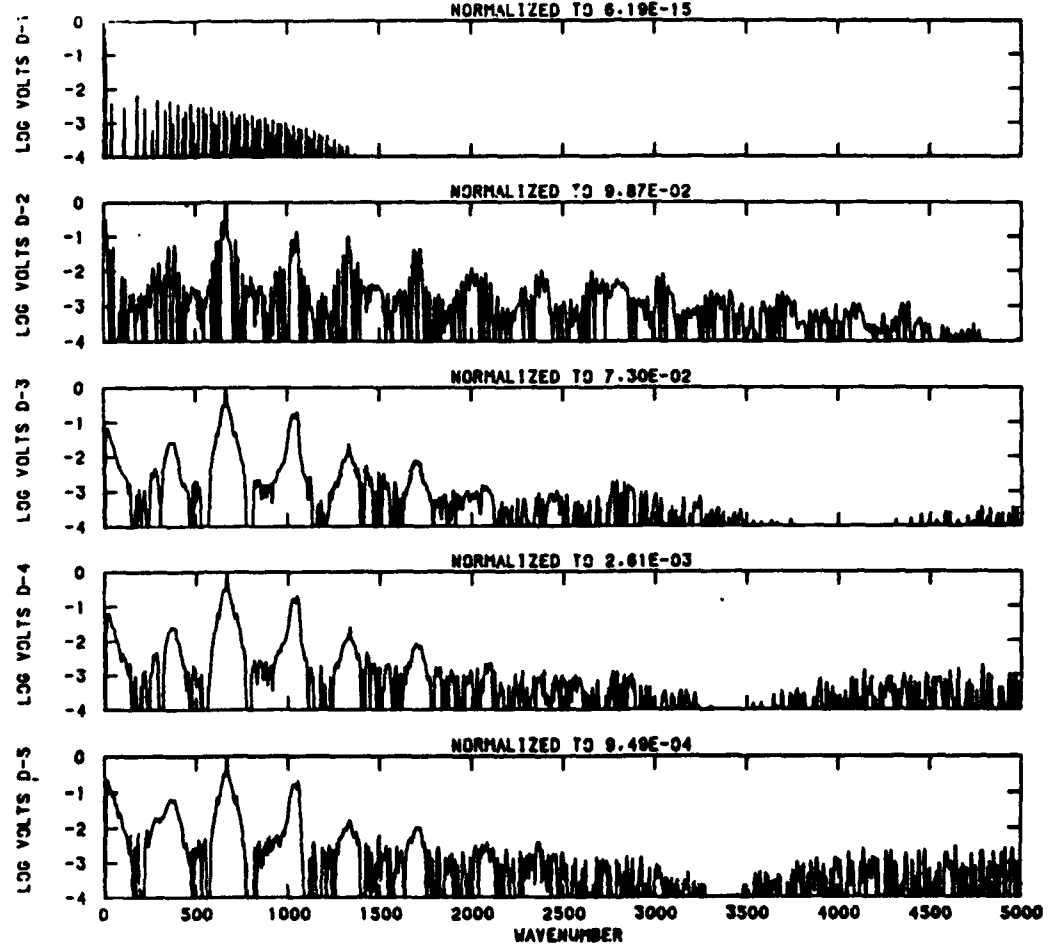


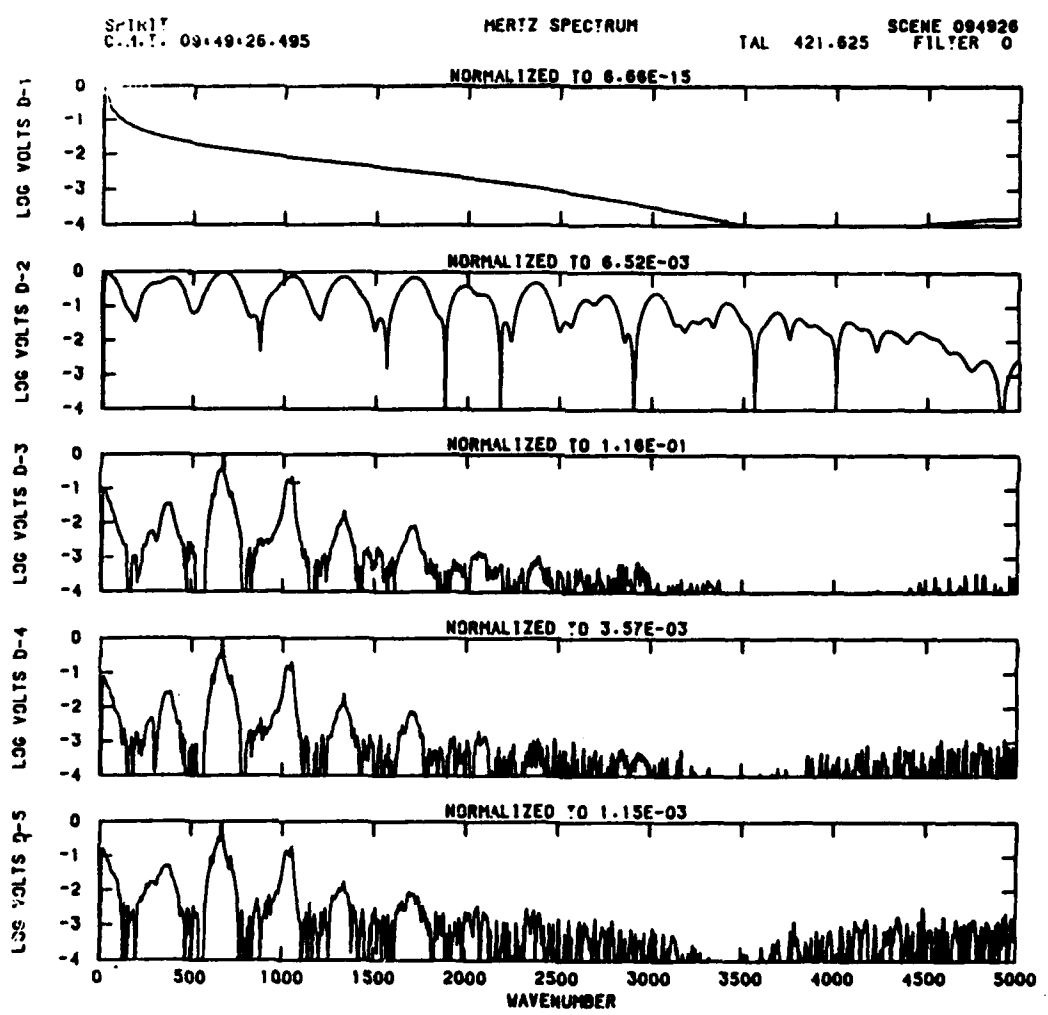


SPH17
C.M.T. 09:49:25.185

MERTZ SPECTRUM

SCENE 094925
TAL 420.315 FILTER 0

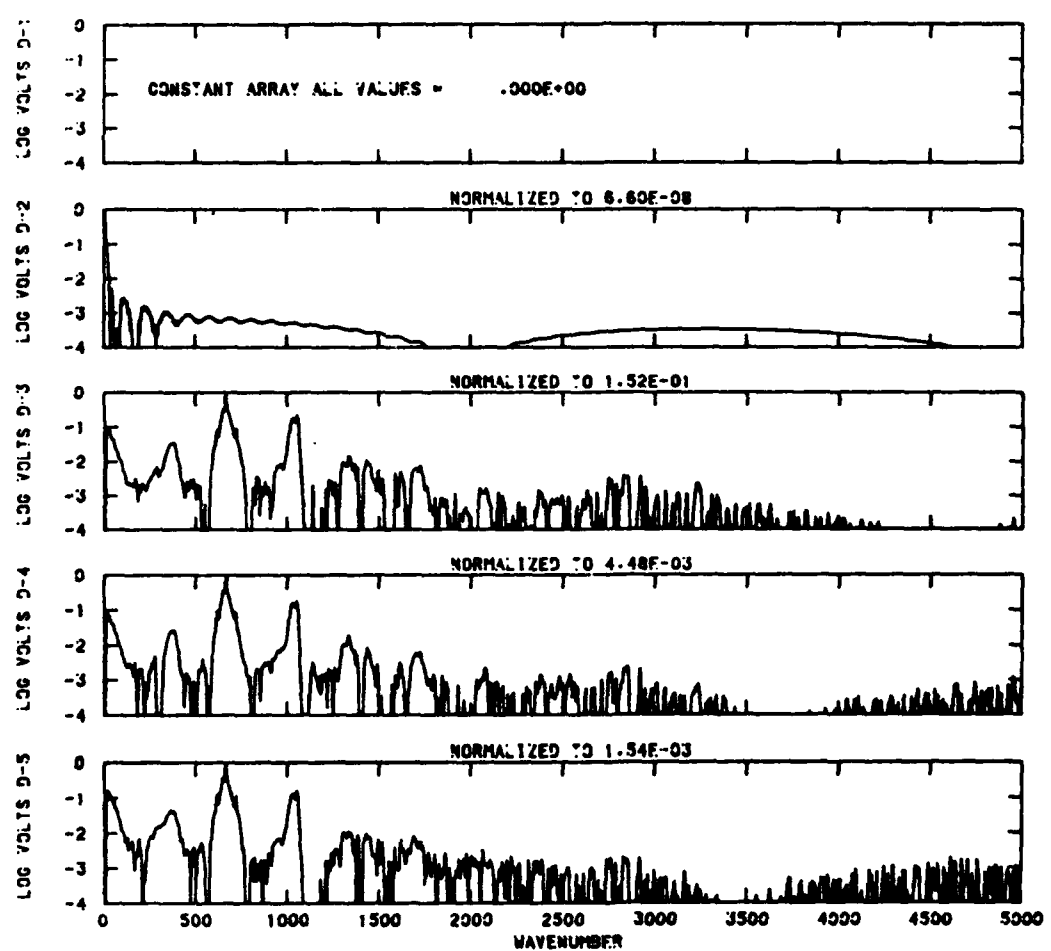


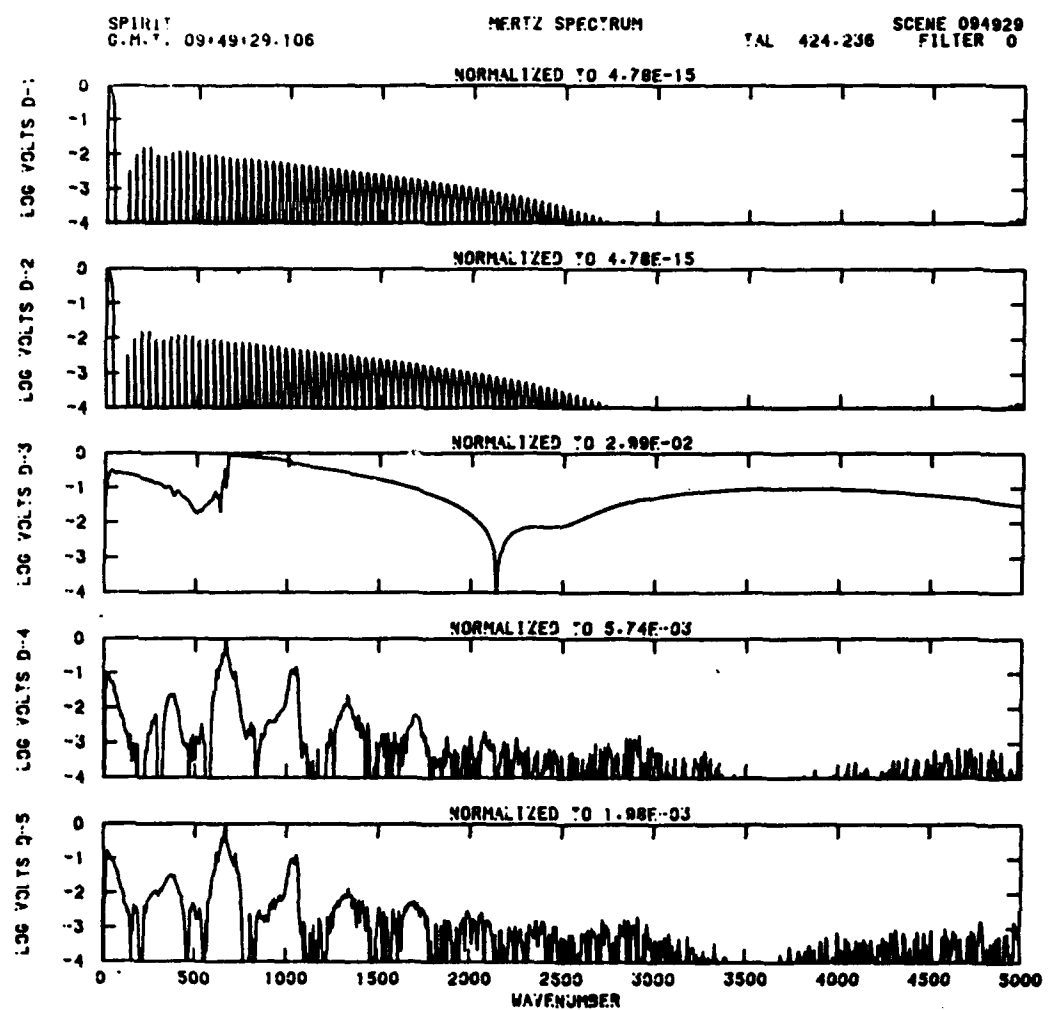


SPIRIT
C.n.t. 09-49-27-796

MERTZ SPECTRUM

TAL 422.926 SCENE 094928
FILTER 0

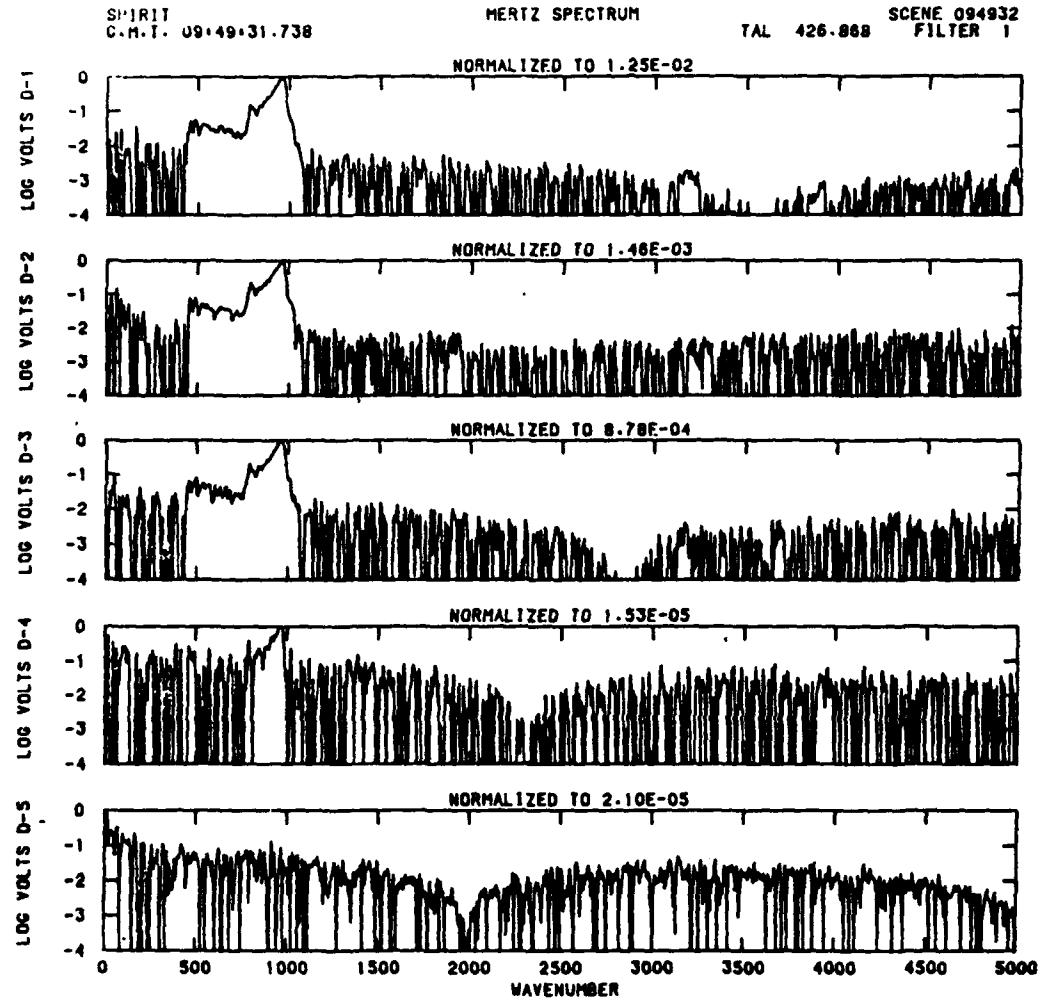


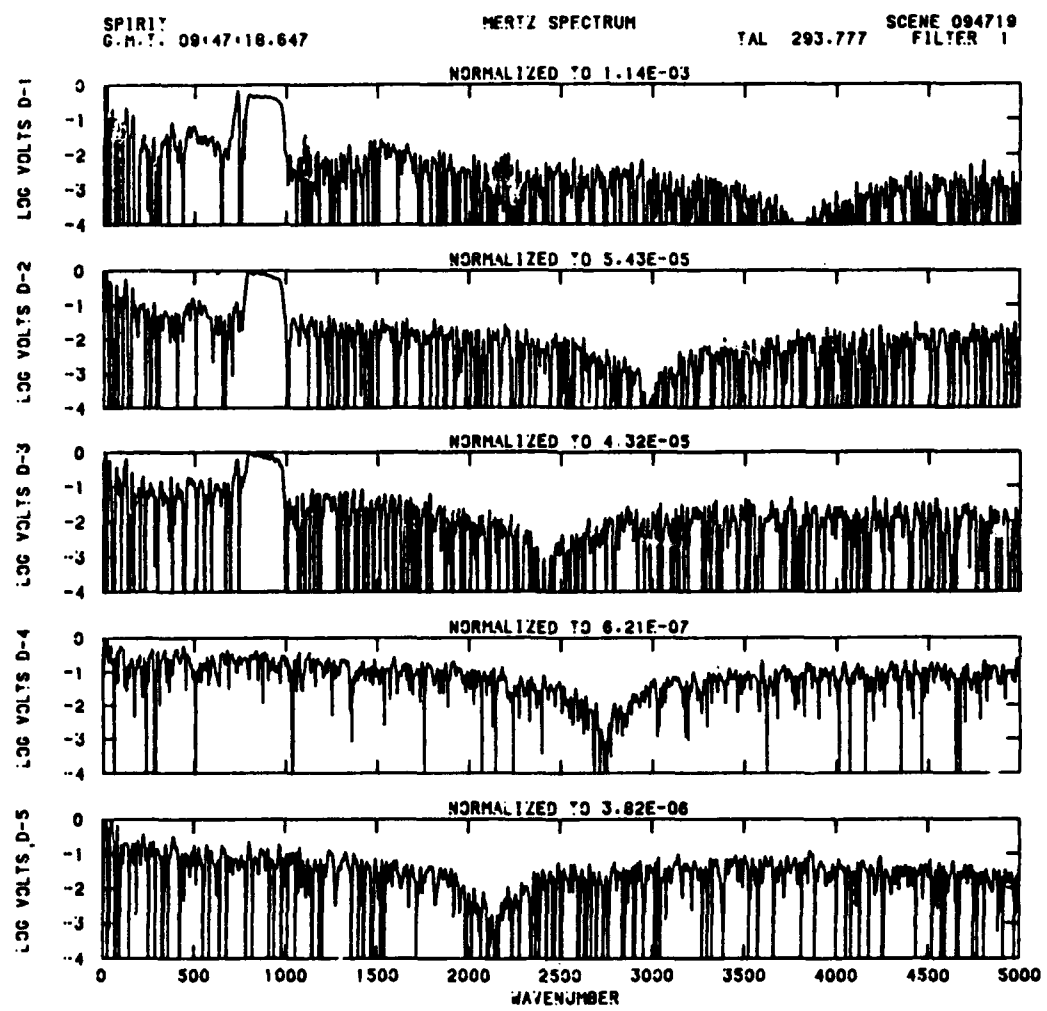


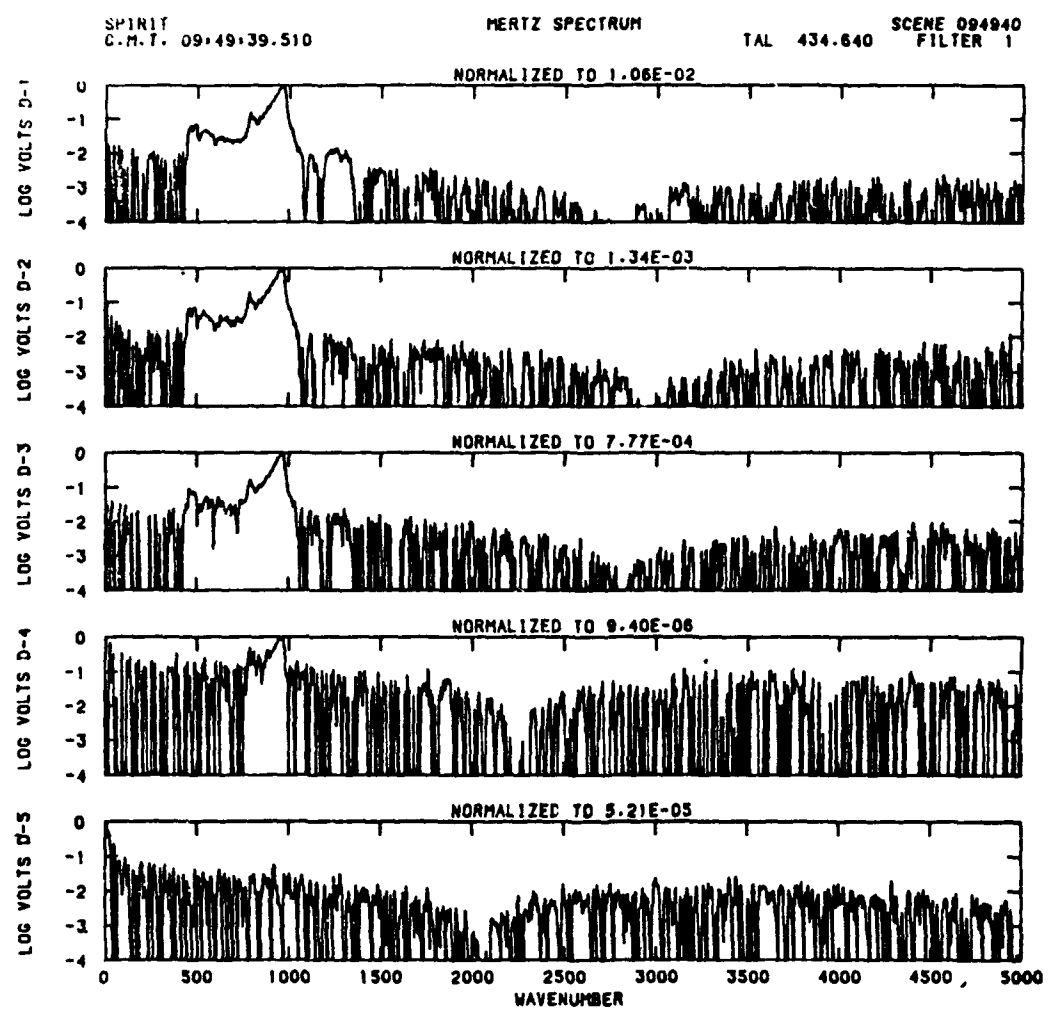
SPIRIT
C.M.T. 09:49:31.738

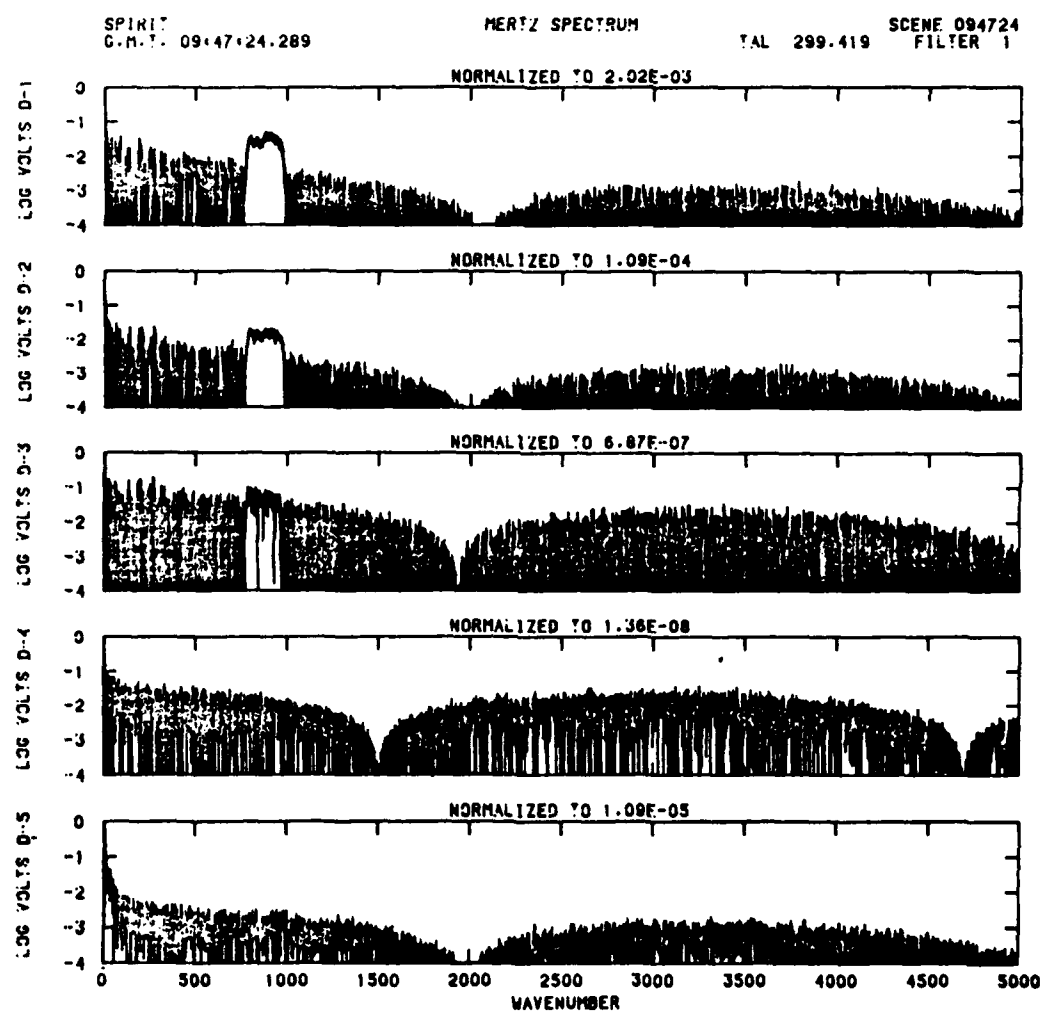
HERTZ SPECTRUM

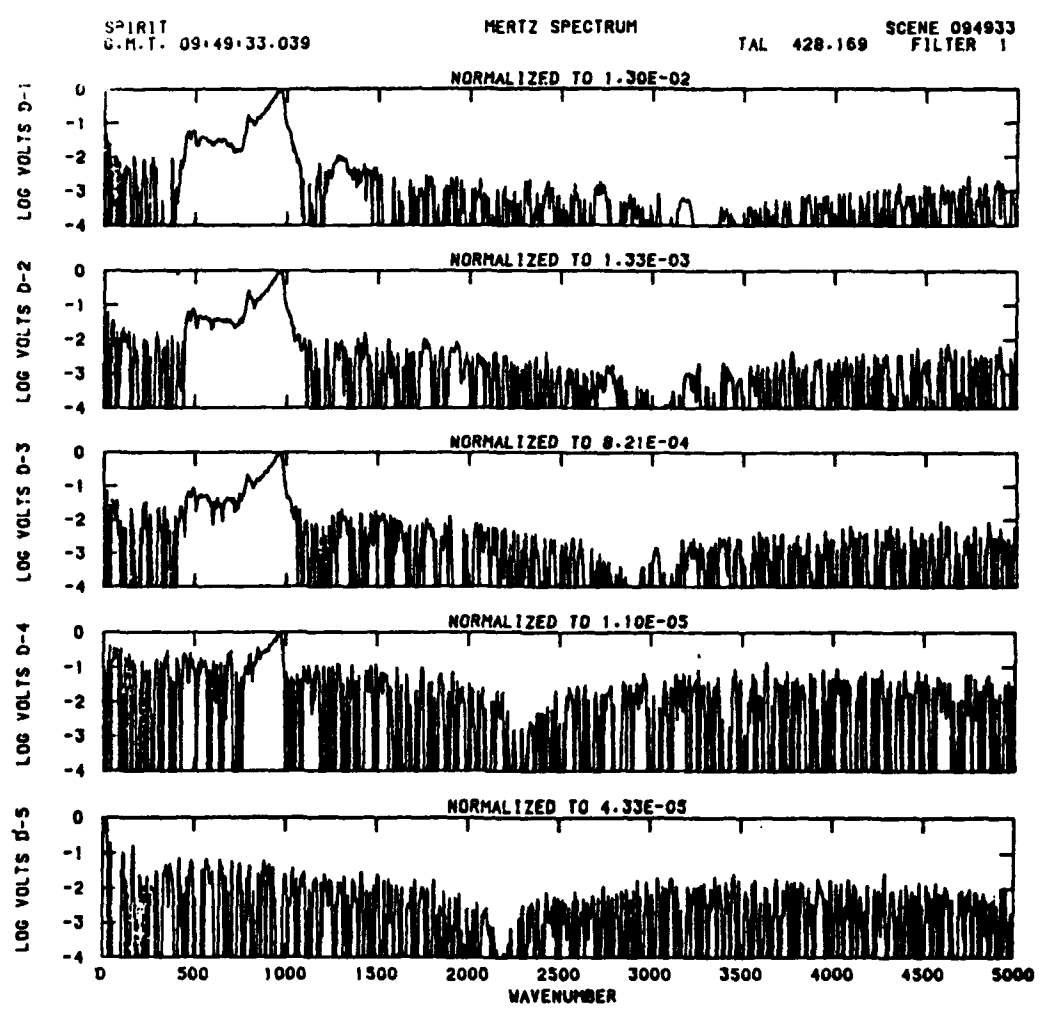
SCENE 094932
TAL 426.868 FILTER 1

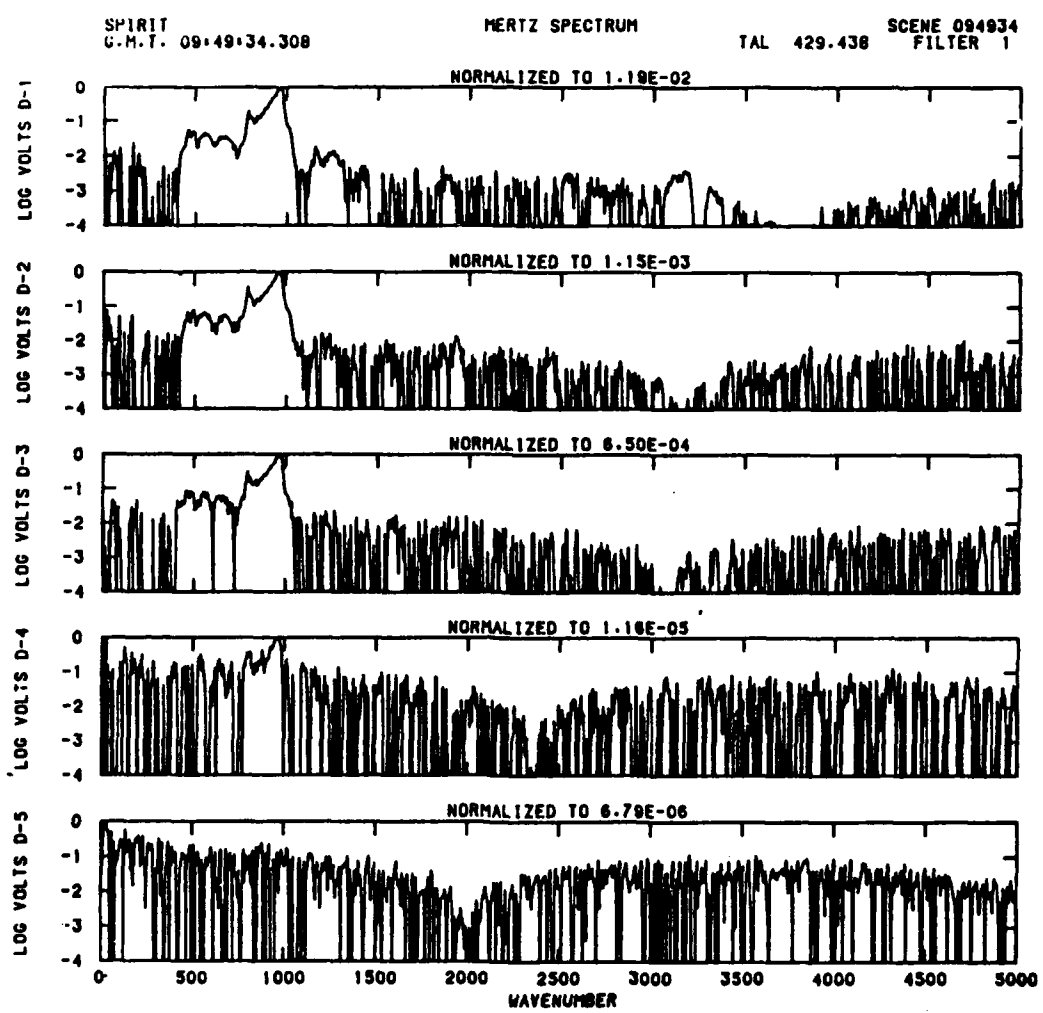


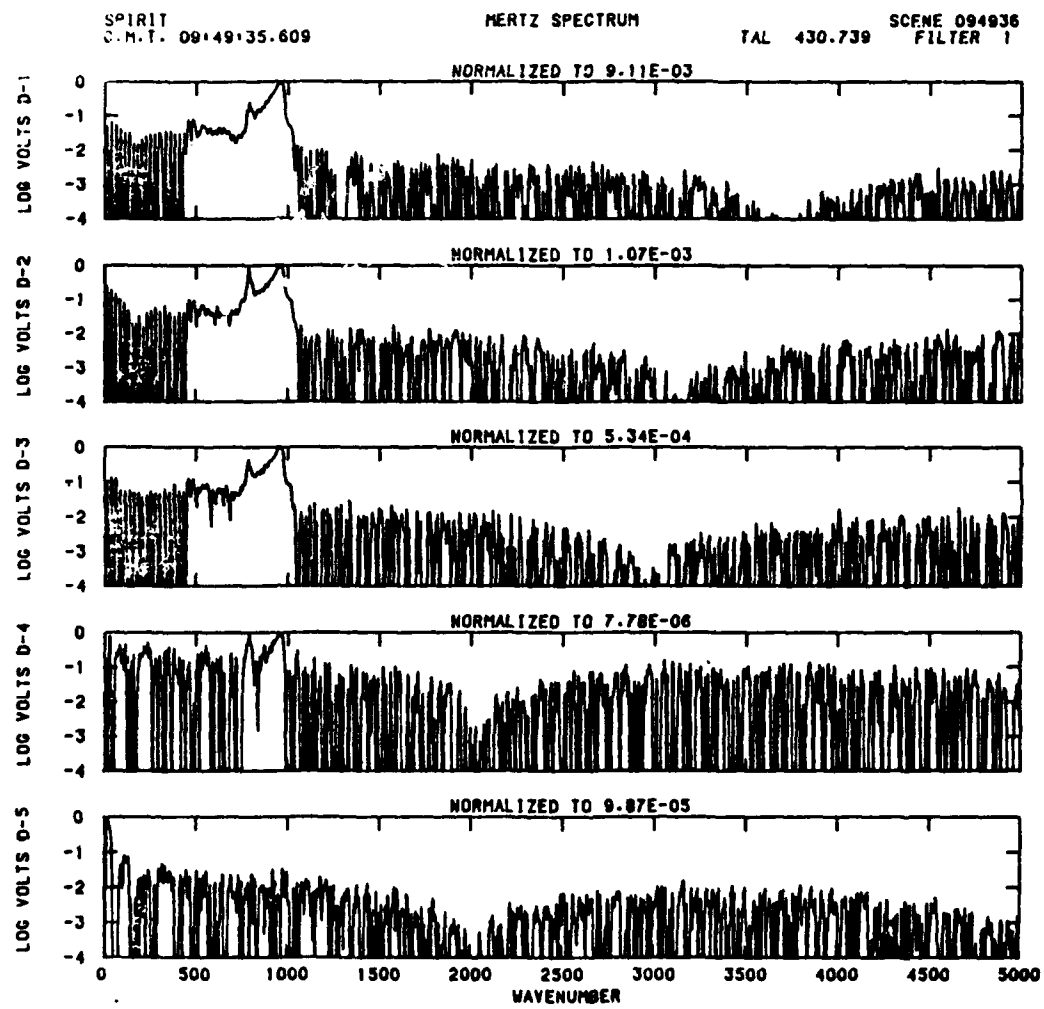


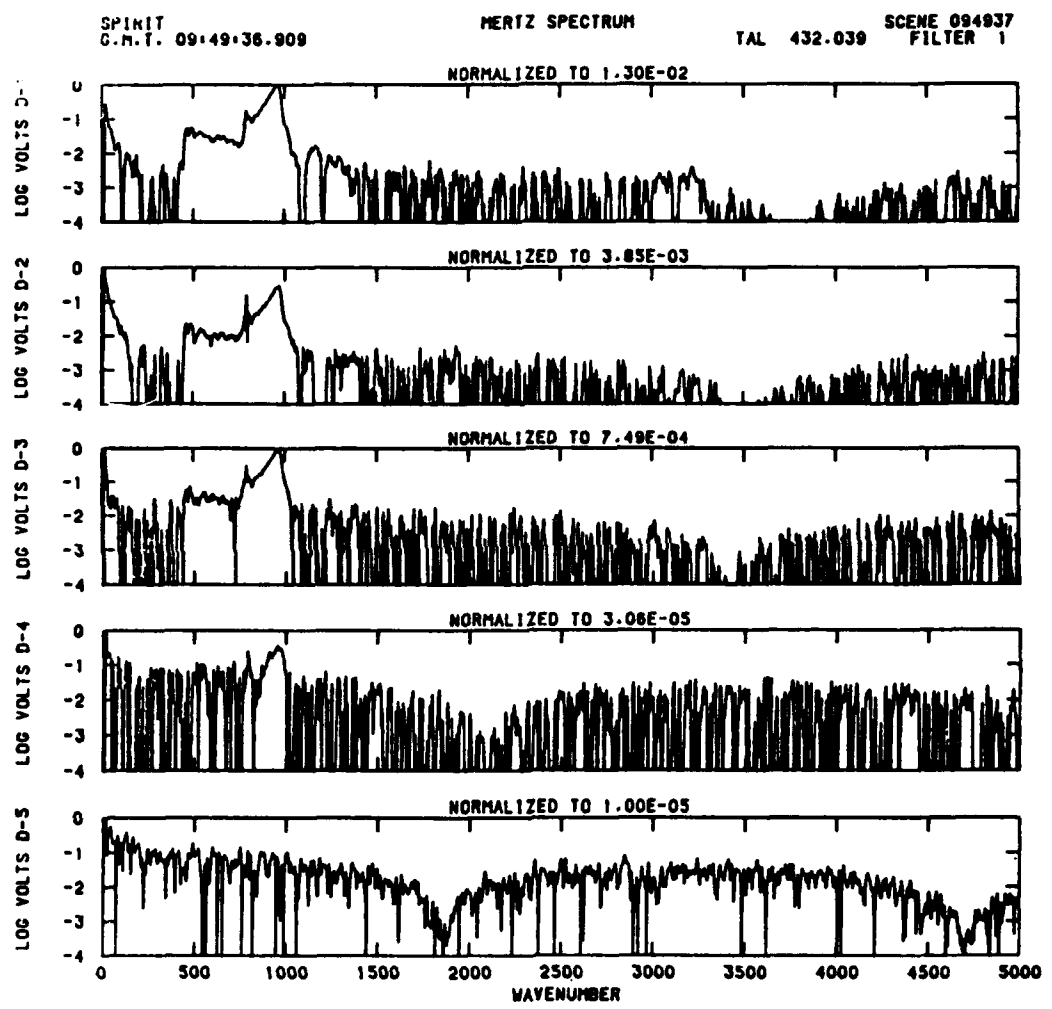


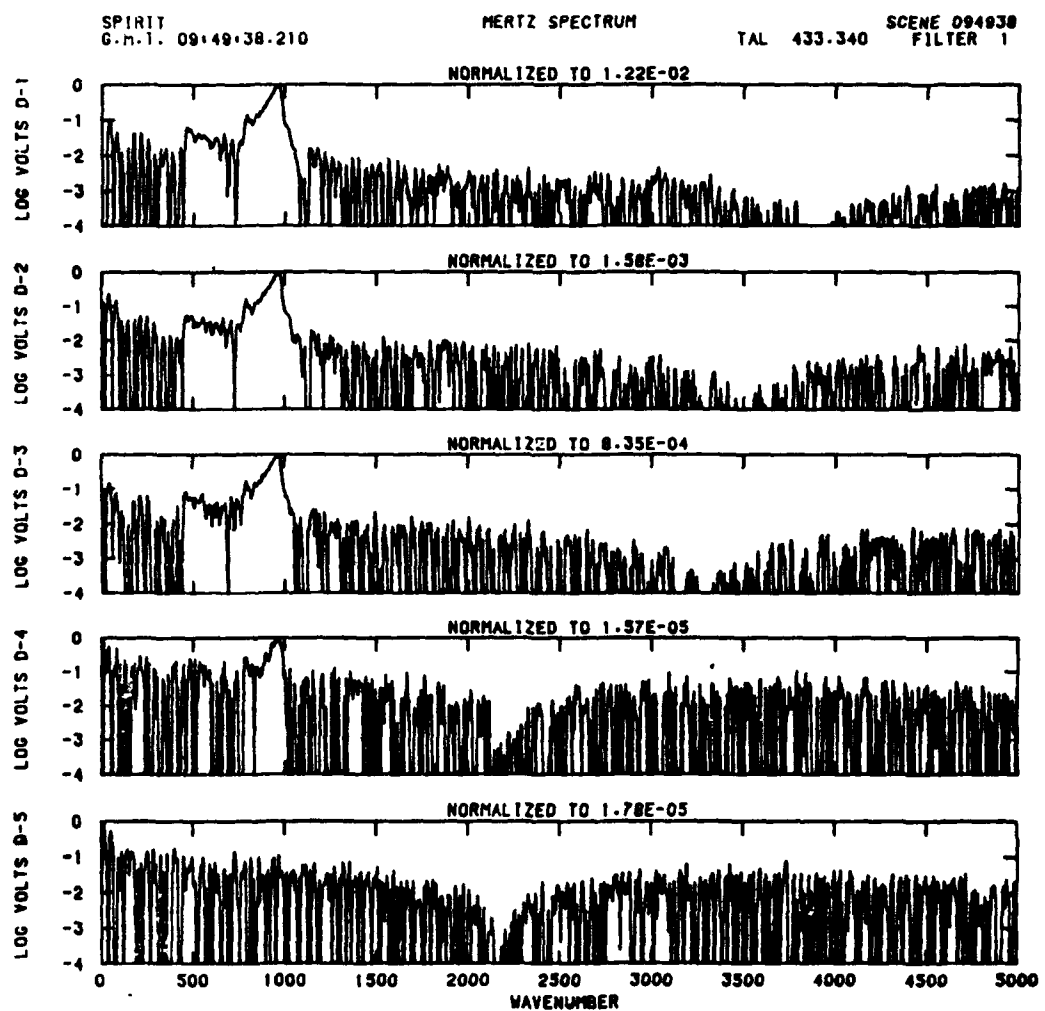


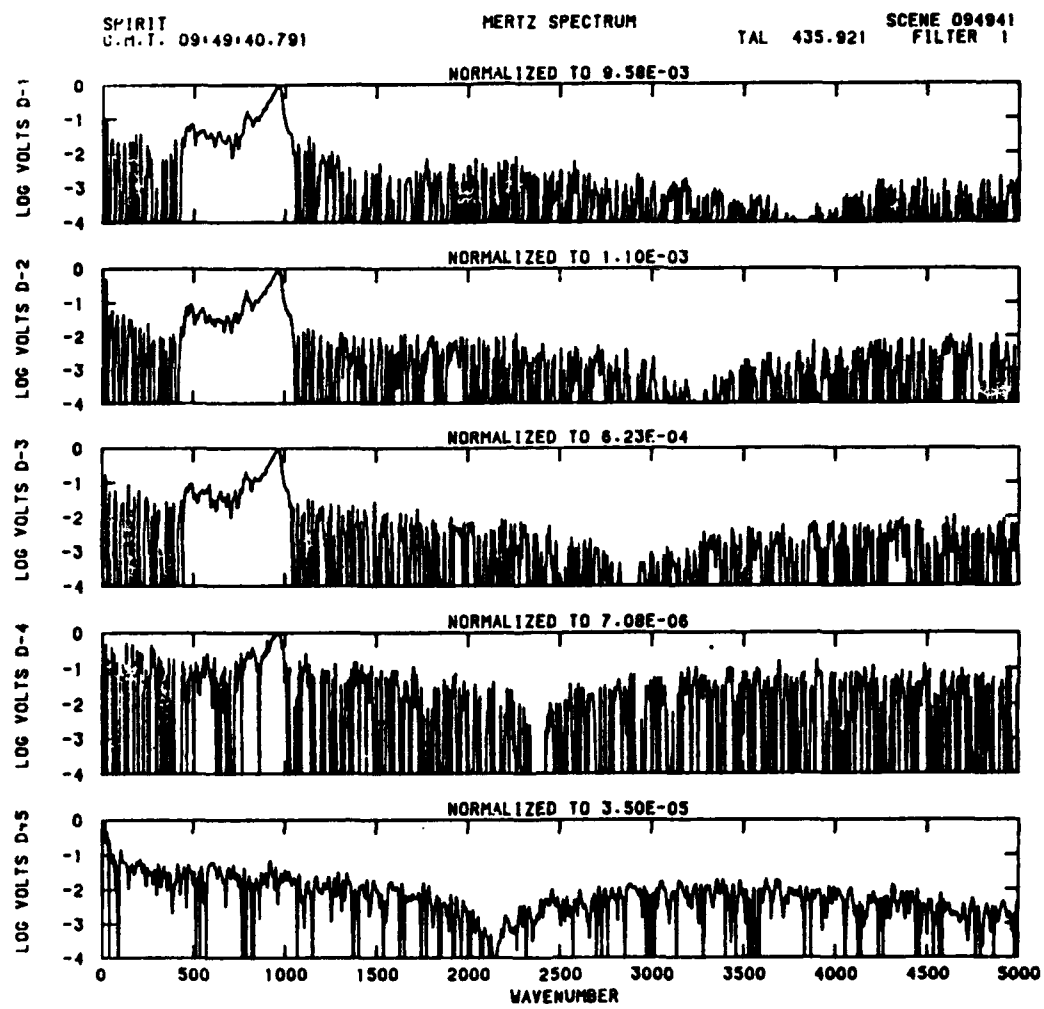












Appendix E

The 9- to 12- μ m Atmospheric Ozone Emission Observed in the SPIRIT 1 Experiment

The 9- to 12- μ m Atmospheric Ozone Emission Observed in the SPIRIT 1 Experiment

S. M. ADLER-GOLDEN AND M. W. MATTHEW

Spectral Sciences, Incorporated, Burlington, Massachusetts

D. R. SMITH AND A. J. RATKOWSKI

Geophysics Laboratory, Hanscom Air Force Base, Massachusetts

Spectra of ozone ν_3 emission in an auroral nighttime sky were obtained in the Spectral Infrared Interferometric Telescope experiment. High-quality hot band spectra reveal spectral structure not previously observable and provide a critical test of ozone radiance models. The limb radiance profile is in good agreement with previous data below ~ 95 km, but above this it falls off more rapidly.

1. INTRODUCTION

The Spectral Infrared Interferometric Telescope (SPIRIT) 1 experiment, launched on April 8, 1986, from Poker Flat Research Range, Alaska, was a rocket-borne probe designed to measure long-wavelength infrared emissions from an IBC class III aurora in the limb-viewing geometry. The primary instrument was a cryogenically cooled, five-detector Michelson interferometer mated to a high-off-axis-rejection telescope. The spectra provide a comprehensive data base on molecular emission features in the nighttime sky in the 500- to 2000- cm^{-1} (5- to 20- μm) region. An overview of the spectral data is given by Robertson *et al.* [1988], and a more complete description of the SPIRIT 1 mission is given by D. R. Smith *et al.* (SPIRIT 1 final flight report, manuscript in preparation, 1990).

This paper presents SPIRIT 1 data on the ozone ν_3 bands in the ~ 67 - to 105-km tangent height range. Of particular interest are the hot bands which appear at slightly longer wavelengths with respect to the (0 0 1) band and which constitute an important source of radiation in the 10- to 13- μm region. The SPIRIT 1 data are among the best obtained from atmospheric probes to date in this spectral region. The results presented here include limb spectra, limb radiances and volumetric emissions in various band passes, and a derived nighttime ozone profile. Comparisons are made with results from previous observations, in particular, the Spectral Infrared Rocket Experiment (SPIRE) [Stair *et al.*, 1985; Green *et al.*, 1986] flown in 1977 in a quiet atmosphere, as well as with model calculations.

2. OZONE LIMB SPECTRA

2.1. Description of Experiment

The SPIRIT 1 payload was launched on April 8, 1986, from Poker Flat Research Range in Alaska at 0942:25 UT. At that time an IBC class III aurora was observed over the SPIRIT 1 ground station at Fort Nelson, British Columbia, some 1400 km to the east. The interferometer was a Michelson flex-pivot design cooled by liquid helium. The mirror

Copyright 1990 by the American Geophysical Union.

Paper number 90JA00554.
0148-0227/90/90JA-00554\$05.00

drive length was designed to produce both high-resolution ($\sim 1 \text{ cm}^{-1}$) and medium-resolution ($8\text{--}11 \text{ cm}^{-1}$, depending on apodization) one-sided interferograms. The focal plane contained an array of five arsenic-doped silicon detectors of differing sizes and sensitivities to cover a wide dynamic range. In the "open-filter" mode the detectors were sensitive to radiation in the approximately 500- to 2000- cm^{-1} (5- to 20- μm) region. During selected portions of the flight, band-pass filters were inserted to isolate narrower spectral regions.

Tangent heights for each scan and detector were determined by analyzing data from a three-axis position gyroscope, an IR horizon sensor, and a 35-mm image-intensified celestial aspect (star-sensor) camera. The gyroscope, which provided continuous relative pointing information throughout the flight, was calibrated with data from the horizon sensor. The resulting tangent heights from the gyroscope were checked against selected celestial aspect data. Agreement was found to within ± 2 km (1σ), although occasional differences as large as 5 km were observed during the scans taken with filter 1 ($\sim 780\text{--}1000 \text{ cm}^{-1}$ band pass; see section 2.2.2). These tangent heights were used for the initial IR data analysis. Subsequently, a second, independent set of tangent heights was obtained from the horizon sensor; the gyroscope only was used to correct for time-constant effects in the horizon sensor. These new tangent heights, which are used in the current analysis, agree with the celestial aspect data to within ± 1 km (1σ).

2.2. Spectra

The majority of the spectral scans of the atmospheric limb below ~ 105 km were taken near the end of the flight and are all of medium spectral resolution. These scans are divided into two groups, open-filter scans and filter 1 scans, as discussed below.

2.2.1. *Open-filter scans (scans 225-232).* Open-filter data covered a range of tangent heights between 77 and 105 km. The best data are from detectors 2, 3, and 4, since detector 1, the most sensitive, was usually saturated and detector 5 is less sensitive than the others. To minimize leakage of strong radiation from CO_2 and O_3 into adjacent window regions, the interferograms were processed using a

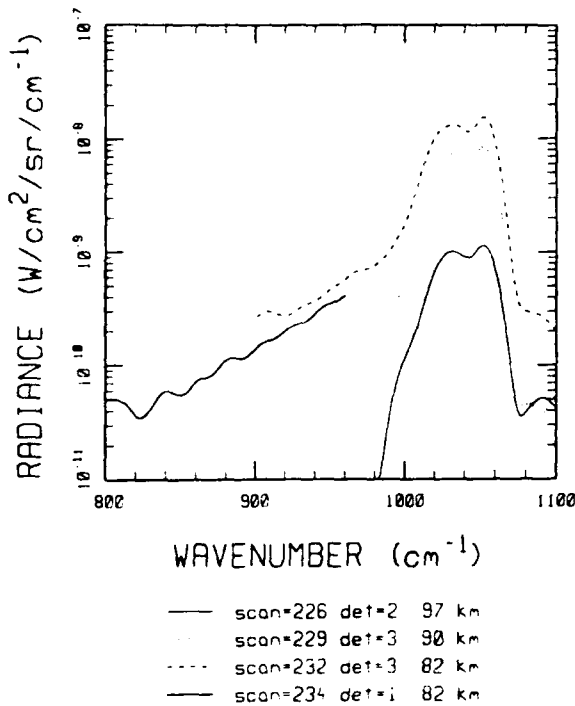


Fig. 1. Ozone limb spectra from SPIRIT 1 with Kaiser-Bessel apodization.

Kaiser-Bessel apodization window, whose response function has very small side lobes (no more than 10^{-3} of the peak). The full width at half maximum (FWHM) resolution for this function is 11 cm^{-1} .

Three examples of open-filter spectra are depicted in Figure 1 (scans 226, 229, and 232). They show the (0 0 1)-(0 0 0) O_3 band as a strong double-peaked feature centered at 1042 cm^{-1} . At higher wave numbers the weak (1 0 0)-(0 0 0) band at 1103 cm^{-1} appears as a low, noisy shoulder. The $\Delta\nu_3 = -1$ hot bands, which arise from the $\text{O} + \text{O}_2 + \text{M}$ recombination reaction, appear as a tail in all but the bottom curve (scan 226), which corresponds to a higher tangent altitude.

2.2.2. *Filter 1 scans (scans 234-247)*. A number of scans were taken with band-pass filter 1, which transmits radiation in the 10- to 13- μ m (~ 780 - to 980-cm^{-1}) region and effectively blocks strong radiation from the adjacent CO_2 bands and the O_3 (0 0 1) band. In these scans the best data are from detectors 1, 2, and 3. The interferograms were processed using both Kaiser-Bessel and triangular apodization; the latter yields improved resolution (8 cm^{-1} FWHM).

For reasons indicated below, the filter 1 scans are divided into two groups, group A and group B. Group A, consisting of scans 234-238, covers tangent heights of approximately 67-82 km. Around the end of scan 238 a rapid pointing maneuver raised the sensors' viewing angle. The subsequent scans, 239-247, form group B, which covers similar tangent heights (approximately 70-83 km) but with a different viewing geometry. For the group B scans the payload altitude had dropped to nearly the tangent height, making these scans closer to half-limb views than to the full-limb views of group A.

A representative filter 1 spectrum obtained by detector 1 is shown in Figure 1 (scan 234). Improved resolution is obtained with the triangular apodization window, as shown in the two scans in Figure 2. These scans, taken at different tangent heights, illustrate the high degree of reproducibility of the hot band spectrum as well as the greatly improved signal-to-noise ratio compared to the open filter data in the same region. This demonstrates the value of using band-pass filters in interferometers to reduce the photon noise from strong radiation outside of the spectral region of interest. Below $\sim 830\text{ cm}^{-1}$ the spectrum includes a contribution, probably from CO_2 , which is more pronounced at lower altitudes relative to the ozone hot bands.

2.3. Auroral Conditions

During the portion of the flight considered here the instrument was pointed toward the auroral arc located over Fort Nelson; the line of sight passed through the aurora at a point beyond and at least 30 km above the tangent point. Auroral intensities were measured by a 391.4-nm photometer coaligned with detector 2 and ranged from 23 to 104 kR in the open-filter scans, from 43 to 210 kR in the group A scans, and from 95 to 149 kR in the group B scans.

Since in these limb scans the bright ozone emissions from the atmospheric column below and in front of the auroral arc were in view, the only localized auroral effect which might be discernible would be some large enhancement due to an additional major ozone formation mechanism. No such enhancement is observed; the emissions are, if anything, weaker than usual, as will be discussed. It is reasonable to conclude that the ozone emission observed in SPIRIT 1 is representative of the atmosphere outside of the arc.

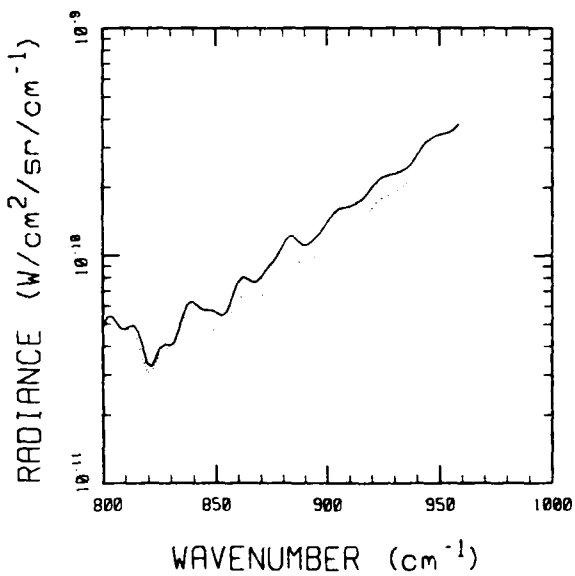


Fig. 2. Ozone hot-band spectra with triangular apodization (detector 1).

2.4. Comparison With Previous Data and Models

Figure 3 shows a complete ozone spectrum at 82 km, which was generated by splicing together open-filter and filter 1 scans. Also shown is a nighttime spectrum from the SPIRE experiment taken at a similar altitude. The SPIRE instrument utilized a circular variable filter with ~ 20 cm^{-1} resolution at these wavelengths. This lower resolution is insufficient to resolve the P and R branches of the O_3 bands. However, these spectra agree well in overall shape.

Figure 4 compares the 82-km spectrum with a full radiance model calculation using ozone kinetic and spectroscopic parameters and standard density and temperature profiles from the Air Force Geophysics Laboratory high-altitude infrared radiance model (HAIRM) code, which is described in detail by *Degges and Smith* [1977]. In the (0 0 1) band the agreement is excellent in terms of shape and within a factor of ~ 2 in intensity which, as will be discussed in section 3.1, implies a similar correspondence between the model and actual ozone column densities. The hot band spectra show only fair agreement in shape, and near 800 cm^{-1} the model spectrum is too weak by a factor of approximately 4. Refinements in the model's kinetic and spectroscopic parameters for the hot bands will considerably improve the agreement with the SPIRIT 1 data.

3. LIMB RADIANCES AND VOLUMETRIC EMISSIONS

Limb radiances were generated by integrating the spectra over a set of wavelength band passes. The (0 0 1) band pass was chosen as 9.2 – $10.0 \mu\text{m}$ (1000 – 1087 cm^{-1}); the hot bands were divided into four band passes $0.5 \mu\text{m}$ wide centered at $10.5 \mu\text{m}$ (952 cm^{-1}), $11.0 \mu\text{m}$ (909 cm^{-1}), $11.5 \mu\text{m}$ (870 cm^{-1}), and $12.0 \mu\text{m}$ (833 cm^{-1}).

For several of these band passes a linear least squares

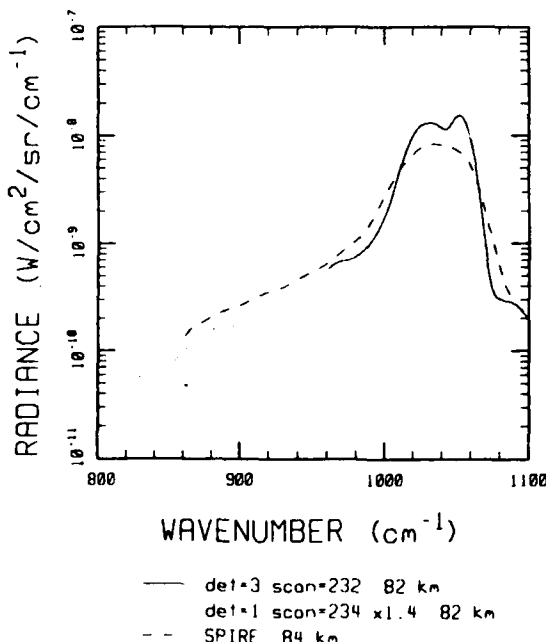


Fig. 3. Comparison of SPIRIT 1 and SPIRE ozone spectra near 82 km tangent height.

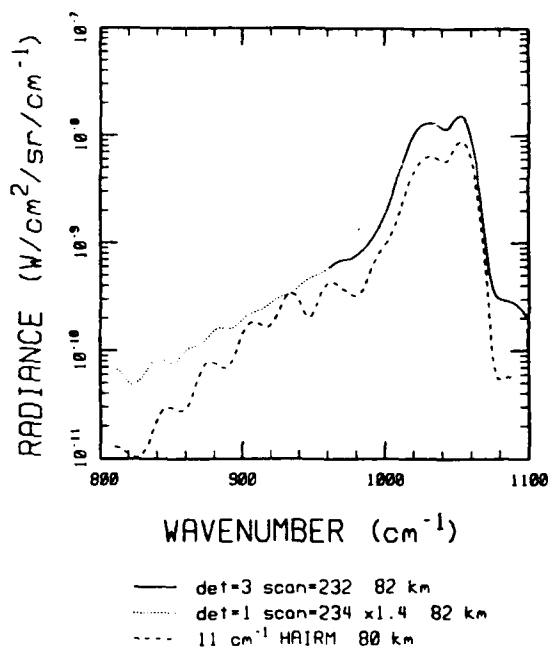


Fig. 4. Comparison of SPIRIT 1 and model (HAIRM) ozone spectra near 80 km tangent height.

fitting/inversion procedure was implemented which generated a volumetric emission function (the product of a polynomial and a Gaussian). The column integrals of this function give the best fit to the limb radiances, weighted by the reciprocal of the radiance; the σ of the fit is expressed as a radiance proportion or percentage. These calculations confirmed that except in the group B scans, virtually the full limb was viewed. The results are discussed below and compared with SPIRE data (also full-limb views) and model calculations.

3.1. (0 0 1) Band

The (0 0 1) band limb radiance data from SPIRIT 1 are shown in Figure 5, along with full-limb radiance profiles from two different least squares fits (smooth curves). The data were obtained from the open-filter scans. The volumetric emission functions associated with each of these fits is shown in Figure 6. A comparison of these functions gives a measure of the precision in the derived volumetric emission. It is seen that the volumetric emission can be derived with reasonable precision above 80 km. As will be discussed in section 4, the volumetric emission is essentially proportional to the ozone density in this altitude region.

Figure 7 compares the third-degree limb radiance fit with nighttime and terminator data from the SPIRE experiment. We have corrected the SPIRE data for off-axis radiation leakage effects by background subtraction. Below ~ 95 km the agreement is excellent, well within the calibration accuracy of the SPIRIT 1 instrument (approximately $\pm 40\%$).

At higher altitudes the ozone radiance measured in SPIRIT 1 is considerably smaller than that measured in SPIRE. The difference is roughly equivalent to a downward shift of ~ 2 km, which is within the combined tangent height

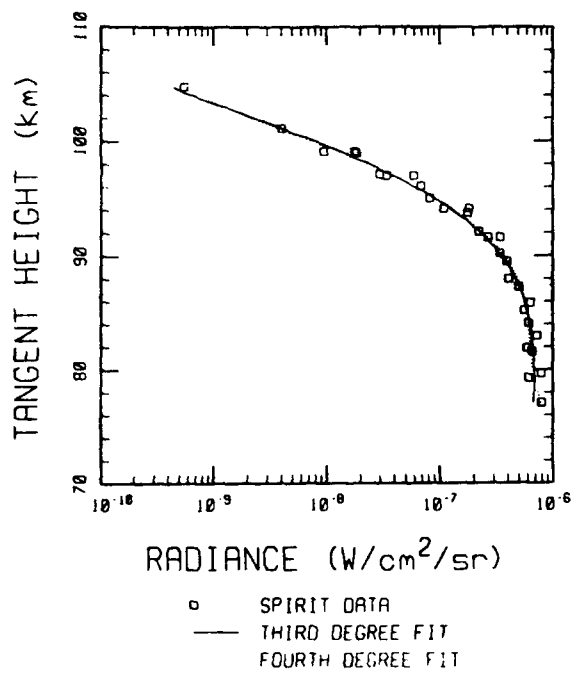


Fig. 5. Limb radiance profile of the (0 0 1)-(0 0 0) band. Data is from detectors 1-5; 1σ (scatter of fit) = 18% (third degree), 17% (fourth degree).

uncertainties in these two experiments. On the other hand, Ulwick et al. [1985] have noted similar shifts in auroral versus nonauroral ozone profiles obtained in zenith-looking experiments, where the altitude uncertainty is minimal.

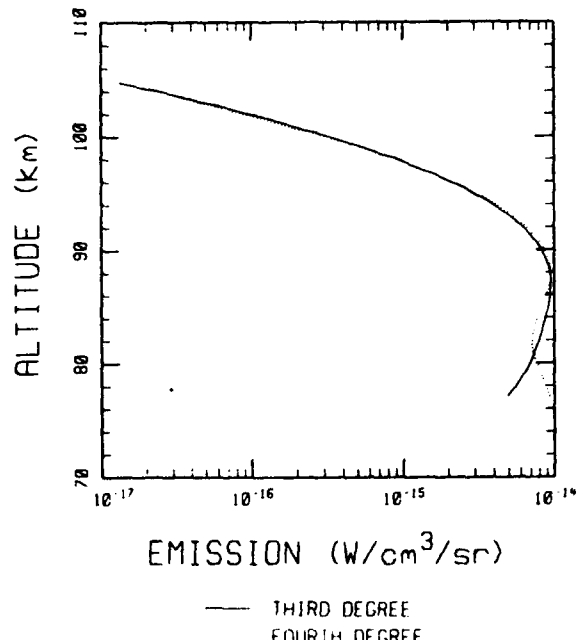


Fig. 6. (0 0 1)-(0 0 0) volumetric emission profiles corresponding to the limb radiance fits in Figure 5.

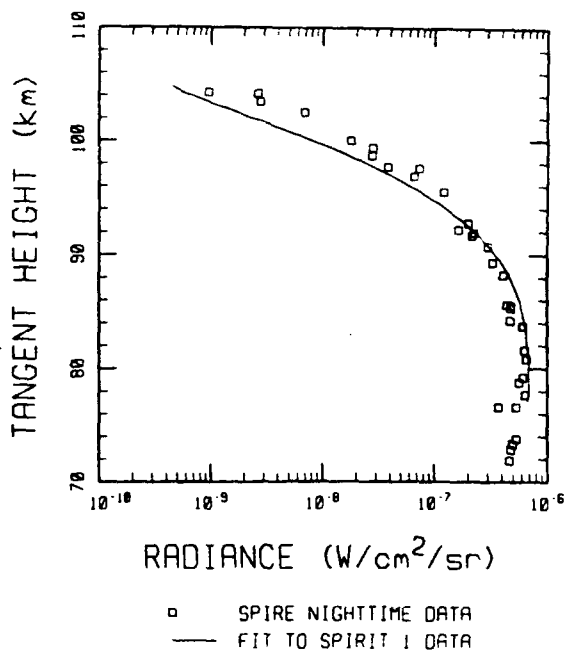


Fig. 7. Comparison of SPIRIT 1 fit (third degree) and SPIRE data on (0 0 1)-(0 0 0) limb radiance.

We have also performed a preliminary comparison of SPIRIT 1 data with results from several nighttime zenith-looking experiments, including those cited by Ulwick et al., by altitude-integrating the volumetric emission derived from SPIRIT 1. The resulting synthetic zenith profile agrees well with those from the other experiments up to around 90 km, above which point the SPIRIT 1 profile falls off much more rapidly. Part of this difference might reflect differences in the degree of background and noise contamination in these experiments, although the bulk of the difference probably reflects real ozone variability.

The large radiance differences that small vertical shifts in the ozone profile can cause emphasize the need for accurate pointing data in limb experiments as well as a thorough understanding of auroral and other sources of atmospheric variability.

3.2. Hot Bands

Limb radiances in the hot band passes are plotted in Figure 8. The data are taken from the open-filter and group A scans. The SPIRE nighttime and terminator data are typically some 2 times higher, but the shape of the profile is essentially the same. This is shown in Figure 9, which compares SPIRIT 1 and SPIRE data in the 10.25- to 10.75- μ m band pass.

The hot band emission intensity is proportional to the population of multiquantum vibrationally excited ozone, which is governed by its rates of formation and relaxation [Rawlins, 1985]. These in turn depend directly on the densities of O₂, O, and N, rather than ground state ozone. Since the O atom density is considerably more variable than the others, it is the most likely source of scan-to-scan and experiment-to-experiment differences in hot band intensity.

Variations in the O atom concentration at these altitudes can arise from Joule heating, gravity waves, and other phenomena which affect vertical transport. Variations in temperature should be too small to significantly affect the ozone formation rate, except perhaps above the thermopause where the temperature gradient increases.

Spatial variations in vibrationally excited ozone (and thus likely variations in O atom density) are evidenced by the scatter seen in the SPIRIT 1 hot band radiances when all of the data below 80 km are plotted, as is shown in Figure 10. These data have been normalized to full-limb views using the least squares/inversion procedure; otherwise, the scatter would be even larger. The group B data, which correspond to tangent points located close to the sensor, generally fall below the group A data. A possible explanation is that closer to the sensor the ozone emission profile is shifted to higher altitudes, leading to smaller fractional limb views. The scatter is reduced by half if the assumed viewing angles are uniformly shifted upward by 0.5 deg. While this apparent angular shift may suggest the presence of a pointing error, more likely it provides a measure of an altitude shift in the profile.

4. MODEL CALCULATIONS

4.1. (0 0 1) Band

As discussed by Rawlins [1985], the chief mechanism governing the nighttime (0 0 1) state population (or, alternatively, its vibrational temperature $T_v = h\nu/k \ln([0 0 0]/[0 0 1])$) at these altitudes is excitation by "earthshine" radiation originating from lower atmospheric layers followed by spontaneous emission. Other processes influencing T_v include

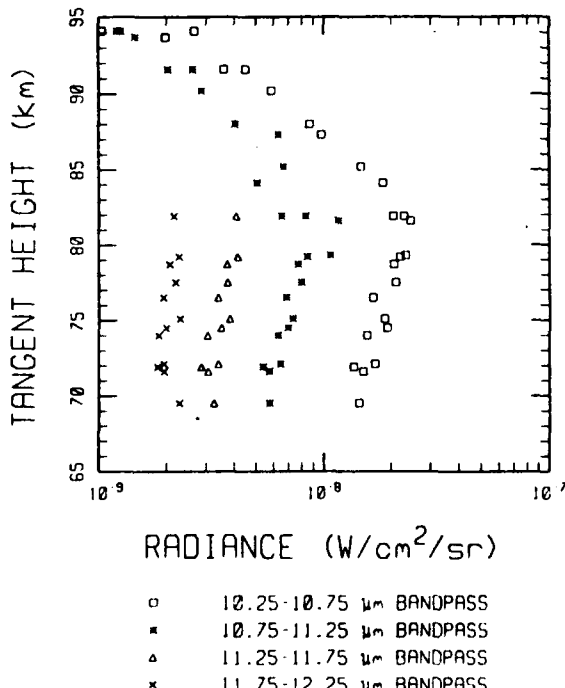


Fig. 8. Ozone hot band limb radiances in various band passes (detectors 1-4).

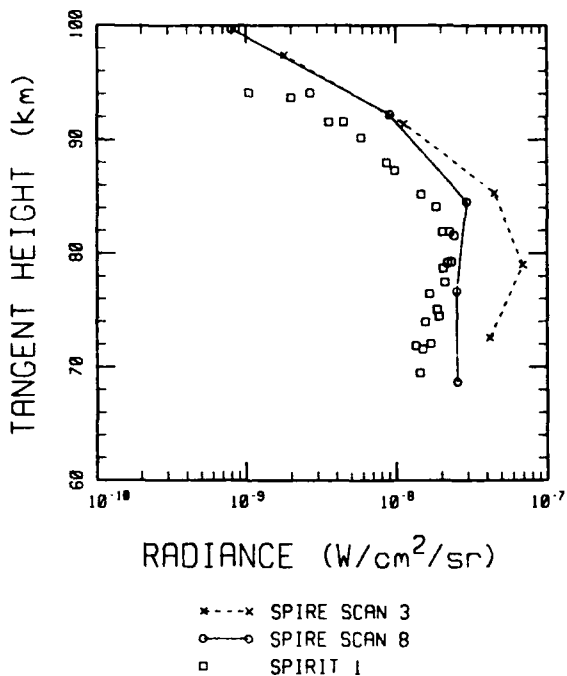


Fig. 9. SPIRIT 1 and SPIRE limb radiances in the 10.25- to 10.75- μm (930- to 976- cm^{-1}) band pass.

collisional quenching and cascade from higher vibrational levels, but their effects are modest and tend to cancel. Detailed treatments of all of these processes are incorporated in atmospheric radiance codes such as HAIRM [Degges and Smith, 1977]. However, a simple, analytical earth-shine model, described below, yields a reasonable estimate for T_v and its variability and provides considerable physical insight.

In this simple model the ozone molecule is considered to be in radiative equilibrium with a lower-lying atmospheric layer at altitude h_{ol} that has an effective blackbody temperature T_e and occupies a fractional angular subtense f (out of 4π sr). The vibrational temperature computed for this case will be denoted T_{ve} . From the facts that the [0 0 1]/[0 0 0] population ratio is proportional to f , and $T_{ve} = T_e$ when $f = 1$, the definition of vibrational temperature yields the result

$$1/T_{ve} = 1/T_e - (k/h\nu)[\ln(f)] \quad (1)$$

The effective temperature T_e for earthshine excitation of the ozone is taken as 250°K. This is the estimated atmospheric temperature at $h_{ol} = 44$ km, the approximate altitude at which mean-strength vibration-rotation lines in the band become optically thick in a zenith path. A similar effective earthshine temperature was estimated by Rawlins [1985].

Accounting for the curvature of the Earth, the angular subtense f in (1) is given by

$$2f \approx 1 - [2(h - h_{ol})/R]^{1/2} \quad (2)$$

where R is the Earth radius and h is the altitude. At the altitudes of interest here, f is close to 0.45. Neglect of the Earth curvature, as is assumed in radiance codes such as HAIRM [Degges and Smith, 1977], yields $f = 0.50$, resulting

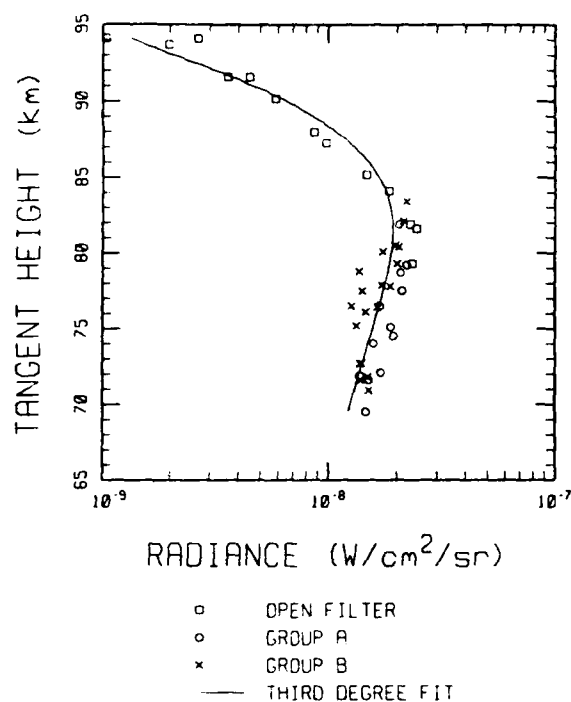


Fig. 10. Complete SPIRIT 1 data set in the 10.25- to 10.75- μm (930- to 976- cm^{-1}) band pass (detectors 1-4); 1σ (scatter of fit) = 17%.

in only a 10% error in the computed [0 0 1]/[0 0 0] population ratio. The final result for the (0 0 1) band of ozone is $T_{\nu} = \sim 220^{\circ}\text{K}$, corresponding to a [0 0 1]/[0 0 0] ratio of 0.0012.

This vibrational temperature estimate may be compared with more complete treatments. Collisional quenching and the contribution from $\text{O} + \text{O}_2 + \text{M}$ chemiluminescence were considered using a model similar to that of Rawlins [1985]. The resulting (0 0 1) vibrational temperature was found to differ from T_{ν} by no more than 6°K from 70 to 104 km. This indicates that T_{ν} is rather insensitive to the precise rates for these collisional processes. A second comparison is with the HAIRM code [Degges and Smith, 1977], which also includes these collisional processes but solves the radiation transport problem more accurately. It predicts slightly lower temperatures, averaging around 210°K at these altitudes.

A potential source of error in all of these calculations is the lack of knowledge of the true lower atmospheric temperature profile. The resulting uncertainty in T_{ν} leads to a comparable uncertainty in the vibrational temperature, as may be seen from (1). Accounting for all uncertainties, we believe that the 220°K estimate for the vibrational temperature should be accurate to within 20°K, corresponding to a factor of 2 accuracy in the [0 0 1]/[0 0 0] population ratio.

Since the (0 0 0) state accounts for nearly all of the ozone, the (0 0 1) volumetric emission can be combined with the estimated [0 0 1]/[0 0 0] ratio to yield an approximate nighttime ozone density profile. The third-degree SPIRIT 1 radiance profile in Figure 6 leads to the ozone density profile shown in Figure 11.

For comparison, a mean ozone profile developed by Degges and Smith [1977] for HAIRM is also shown. Below

100 km the agreement between these profiles is quite good, especially in view of the ozone variability and the vibrational temperature uncertainty. Above 100 km, where Degges and Smith's profile had been derived by extrapolation using a diffusive mixing model, it has a scale height several times larger than the value of ~ 2 km obtained from the SPIRIT 1 data.

We have also generated an ozone profile using the photochemical model of Allen et al. [1984], which assumes chemical destruction by atomic hydrogen. For this calculation, temperature and major species densities profiles from the 1976 U.S. Standard Atmosphere (listed by Degges and Smith [1977]) were used, along with an atomic hydrogen profile chosen to represent average nighttime conditions (assumed densities at 90, 100, and 106 km are 7.2×10^7 , 2.6×10^7 , and $1.45 \times 10^7 \text{ cm}^{-3}$, respectively). The resulting ozone profile, shown in Figure 11, differs from the "basic model" results of Allen et al., mainly owing to the differences in the assumed hydrogen profiles, but it agrees to within a factor of 2 with the SPIRIT 1 data up to around 100 km. The more rapid falloff of the SPIRIT 1 ozone profile at the highest altitudes is consistent with the unusually rapid decline in the observed radiance discussed in section 3.1.

The factor-of- ~ 2 consistency between the three ozone profiles shown in Figure 11 from 80 to 100 km should not be oversold, but it does support the claim that the essential physics and chemistry of ozone formation, destruction, and radiation at these altitudes are reasonably well understood.

4.2. Hot Bands

A calculated ozone hot band spectrum from the HAIRM code is given in Figure 4. This code uses a mechanism

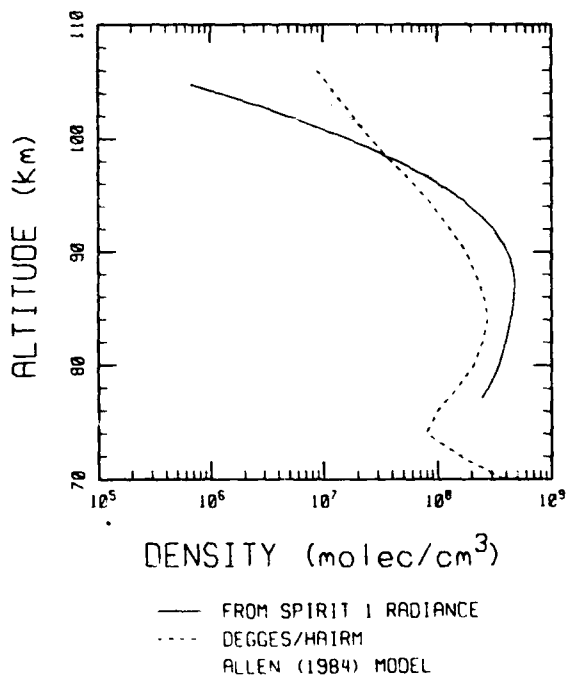


Fig. 11. Comparison of standard nighttime ozone density profiles with profile derived from SPIRIT 1 data.

similar to that proposed by Rawlins [1985] in which ozone (0 0 ν_3) vibrational levels having $\nu_3 \geq 2$ are formed from recombination according to a "quasi-nascent distribution," and relax via collisional and radiative cascades. In order to critically evaluate this mechanism we investigated ozone kinetics theoretically using a detailed state-to-state kinetic model which includes over 100 vibrational energy levels [Adler-Golden, 1987]. From these calculations we concluded that the Rawlins/HAIRM mechanism captures the essential features of the hot band spectrum but should be extended to include additional emitting bands.

The populations of the high vibrational states of ozone may in principle be derived from fitting the SPIRIT 1 hot band spectra using known or estimated band centers, Einstein coefficients, and band contours; the results may then be used to develop an upgraded ozone kinetic model. Most of the required spectroscopic information is currently available for vibrational states having up to 3-4 quanta; these include accurate vibrational energies from absorption spectra [Steinfeld et al., 1987] and theoretical Einstein coefficients [Adler-Golden et al., 1985]. For these states the band contours may be approximated using the (0 0 1) band with an appropriately shifted center [Rawlins and Armstrong, 1987; Rawlins et al., 1987].

Much less is known about the higher-lying states of ozone, whose ν_3 bands dominate the 800- to 950- cm^{-1} region covered by SPIRIT 1's filter data. Resonance Raman spectra [Imre et al., 1982; Imre, 1984] provide approximate energies (to within $\pm 10 \text{ cm}^{-1}$) for five-, six-, and seven-quantum states which are mainly unexcited in the bending mode. We have derived an energy level formula similar to that of Barbe

et al. [1974] but which agrees much better with the Raman data and with the known dissociation energy of ozone. This formula, given in the appendix, has been used to generate ν_3 band center estimates for these and other highly energetic states. A listing of potentially important ν_3 bands (Table 1) shows that the hot band emission in this spectral region arises from levels having as much as 6400-6500 cm^{-1} of energy and up to seven vibrational quanta.

In addition to uncertainties in the band centers for these highly excited states, alterations in the band contours may be significant for states having more than four asymmetric stretching quanta. If one further allows for the appearance of bands containing ν_2 excitation, many overlapping hot bands are possible, and the assignment of band centers and quantum numbers based on the spectral features in the SPIRIT 1 spectra can be hazardous. However, if one constrains the possible hot band assignments with the aid of available spectroscopic information [Steinfeld et al., 1987] and the energy level formula predictions, the SPIRIT 1 spectra can be analyzed to yield a consistent and, we believe, unique set of assignments. Details of this analysis are presented in a separate paper [Adler-Golden and Stein, 1990].

SUMMARY

High-quality ν_3 emission spectra of ozone were obtained in the SPIRIT 1 rocket experiment in an auroral nighttime sky at tangent heights of ~ 67 -105 km. An analysis of these spectra leads to the following conclusions:

1. The spectral shapes and absolute intensities are similar to previous nighttime measurements over the observed

TABLE 1. Energy Levels and Band Centers of Ozone High-Lying Vibrational States

State	Energy, cm^{-1}		ν_3 Band Center	
	Calculated	Imre [1984]	Calculated	Rawlins and Armstrong [1987] and Rawlins et al. [1987]
014	4631		935	
113	4663		920	
212	4783	4766*		
005	4910		912	916
104	4925	4921*	900	904
302	5173	5177*		
024	5254	5246†		
222	5418	5420*		
500	5441	5437*		
015	5518		888	
114	5537		874	
420	5689	5680*		
006	5767	5761*	857	
105	5774		849	
204	5961	5963†		
402	6199	6187†		
016	6342		824	
115	6351		814	
600	6496	6507*		
007	6555		787	
106	6558		783	
304	6880	6897†		
502	7202	7207†		
700	7533	7523†		

The energy values of Imre [1984] are $\pm 10 \text{ cm}^{-1}$; the ν_3 band center values of Rawlins and Armstrong [1987] and Rawlins et al. [1987] are $\pm 3 \text{ cm}^{-1}$.

*Assigned in this work.

†Assigned by Imre [1984].

wavelength range and altitudes up to ~ 95 km. However, SPIRIT 1's improved resolution reveals hot band structure that had been predicted but not previously seen.

2. An ozone density profile derived from inversion of the limb radiance agrees reasonably with available model profiles below ~ 100 km, but above it falls off more rapidly.

3. The hot band emission in the 10-12 μ m window is significantly underestimated in current limb models.

Further work on ozone emission modeling and detailed comparisons with other field data are in progress.

APPENDIX: BAND CENTERS FOR HIGH VIBRATIONAL LEVELS OF OZONE

A modification of the quadratic Darling-Dennison resonance expression of Barbe et al. [1974] for ozone vibrational energies has been developed which provides a good fit to the six- and seven-quantum resonance Raman data of Imre et al. [1982] and Imre [1984] and which also behaves realistically as the dissociation limit is approached. The new energy level expression makes use of modified anharmonic parameters X'_{11} , X'_{13} , X'_{33} , and γ' (the Darling-Dennison coupling parameter), where

$$X'_{11}/X_{11} = X'_{13}/X_{13} = X'_{33}/X_{33} = \gamma'/\gamma = \rho(v_1, v_2, v_3)$$

The unprimed parameters are the constants from Barbe et al. [1974] and

$$\rho = 1. + 0.0016x + 0.002x^2 + 0.0006x^3$$

$$x = v_1 + v_3 + 1.2v_2 - 3$$

For states having four quanta or less, ρ is close to unity, so the anharmonic parameters are in essential agreement with those of Barbe. However, above four quanta, ρ increases monotonically, resulting in increased anharmonicity and thus a lowering of the dissociation energy (the maximum in the (0 0 v_3) sequence) from around 2 eV in the original formula to 1.05 eV (8458 cm^{-1}) in the current formula at the (0 0 11) state.

Representative results are given in Table 1. The v_3 bands originating from states having $v_2 > 1$ or $v_1 > 2$ are not listed, as they are expected to be obscured by bands originating from lower-energy states.

Acknowledgments. The authors thank the many people involved in the reduction and analysis of the SPIRIT 1 data, including Ed Richards, Bill Grieder, and Brian Sullivan of Boston College, Peter Dybwad of Utah State University (Stewart Radiance Laboratory), Terry Rawlins of Physical Sciences, Incorporated, and Dave Robertson of Spectral Sciences, Incorporated. The SPIRIT 1 atmospheric measurement program was conducted by the Geophysics Laboratory with instrumentation developed and flown by Utah State University and Space Data Corporation (Chandler, Arizona.) The experiment and all subsequent postflight data analysis were supported by the Defense Nuclear Agency. The continued support and encouragement of Armen Mardigian, Ken Schwartz, and Leon Wittwer has been vital and greatly appreciated. The work at Spectral Sciences was funded under Air Force contract F19628-87-C-0130.

The Editor thanks W. T. Rawlins and T. G. Slanger for their assistance in evaluating this paper.

REFERENCES

Adler-Golden, S. M., Analysis of SPIRIT LWIR emission: An ozone v_3 model, *Rep. SSI-TR-122*, 26 pp., Spectral Sci., Inc., Burlington, Mass., 1987.

Adler-Golden, S. M., and D. R. Smith, Identification of 4- to 7-quantum v_3 bands in the atmospheric recombination spectrum of ozone, *Planet. Space Sci.*, in press, 1990.

Adler-Golden, S. M., S. R. Langhoff, C. W. Bauschlicher, Jr., and G. D. Carney, Theoretical calculation of ozone vibrational infrared intensities, *J. Chem. Phys.*, 83, 255, 1985.

Allen, M., J. I. Lunine, and Y. L. Yung, The vertical distribution of ozone in the mesosphere and lower thermosphere, *J. Geophys. Res.*, 89, 4841, 1984.

Barbe, A., C. Secriven, and P. Jouve, Infrared spectra of $^{16}\text{O}_3$ and $^{18}\text{O}_3$: Darling and Dennison resonance and anharmonic potential function of ozone, *J. Mol. Spectrosc.*, 49, 171, 1974.

Degges, T. C., and H. J. P. Smith, A High-Altitude Infrared Radiance Model (HAIRIM), *Rep. AFGL-TR-77-0271*, 300 pp., Geophys. Lab., Hanscom Air Force Base, Mass., 1977.

Green, B. D., W. T. Rawlins, and R. M. Nadile, Diurnal variability of vibrationally excited mesospheric ozone as observed during the SPIRE mission, *J. Geophys. Res.*, 91, 311, 1986.

Imre, D., Reaction dynamics studied by photoemission spectroscopy, Ph.D. thesis, Mass. Inst. of Technol., Cambridge, Mass., August 1984.

Imre, D. G., J. L. Kinsey, R. W. Field, and D. H. Katayama, Spectroscopic characterization of repulsive potential energy surfaces: Fluorescence spectrum of ozone, *J. Phys. Chem.*, 86, 2564, 1982.

Rawlins, W. T., Chemistry of vibrationally excited ozone in the upper atmosphere, *J. Geophys. Res.*, 90, 12,283, 1985.

Rawlins, W. T., and R. A. Armstrong, Dynamics of vibrationally excited ozone formed by three-body recombination, I, Spectroscopy, *J. Chem. Phys.*, 87, 5202, 1987.

Rawlins, W. T., G. E. Caledonia, and R. A. Armstrong, Dynamics of vibrationally excited ozone formed by three-body recombination, II, Kinetics and mechanism, *J. Chem. Phys.*, 87, 5209, 1987.

Robertson, D. C., L. S. Bernstein, P. K. Acharya, R. L. Sundberg, J. W. Duff, S. M. Adler-Golden, M. W. Matthew, M. R. Zakin, and P. M. Bakshi, Modeling and analysis of atmospheric radiation in the thermosphere and mesosphere, *Rep. SSI-TR-144*, 128 pp., first annual report prepared for the Geophys. Lab., Hanscom Air Force Base, Mass., contract F19628-87-C-0130, Spectral Sci., Inc., Burlington, Mass., 1988.

Stair, A. T., Jr., R. D. Sharma, R. M. Nadile, D. J. Baker, and W. F. Grieder, Observations of limb radiance with Cryogenic Spectral Infrared Rocket Experiment, *J. Geophys. Res.*, 90, 9763, 1985.

Steinfeld, J. I., S. M. Adler-Golden, and J. W. Gallagher, Critical survey of data on the spectroscopy and kinetics of ozone in the mesosphere and thermosphere, *J. Phys. Chem. Ref. Data*, 16, 911, 1987.

Ulwick, J. C., K. D. Baker, A. T. Stair, Jr., W. Frings, R. Hennig, K. U. Grossman, and E. R. Hegblom, Rocket-borne measurements of atmospheric infrared fluxes, *J. Atmos. Terr. Phys.*, 47, 123, 1985.

S. M. Adler-Golden and M. W. Matthew, Spectral Sciences, Incorporated, 99 South Bedford Street, Burlington, MA 01803.

A. J. Ratkowski and D. R. Smith, Geophysics Laboratory, Hanscom Air Force Base, MA 01731.

(Received October 27, 1989;
revised February 8, 1990;
accepted February 8, 1990.)

Appendix F

**Upper Atmospheric Infrared Radiance from CO₂ and NO
Observed During the SPIRIT 1 Rocket Experiment**

Upper Atmospheric Infrared Radiance From CO₂ and NO Observed During the SPIRIT 1 Rocket Experiment

S. M. ADLER-GOLDEN AND M. W. MATTHEW

Spectral Sciences, Incorporated, Burlington, Massachusetts

D. R. SMITH

Geophysics Laboratory, Hanscom Air Force Base, Massachusetts

Spectral limb radiance data on CO₂ ν_2 and NO 5.3- μm emissions obtained in the Spectral Infrared Interferometric Telescope rocket experiment have been analyzed. The data cover auroral intensities from several kilorayleighs to over 100 kR at 391.4 nm, and tangent heights of \sim 70–200 km at high latitudes (60°–65°N). Volumetric emission and kinetic temperature profiles have been obtained using linear least squares inversion procedures. The CO₂ ν_2 radiance profile is found to be similar to previous observations. The NO 5.3- μm emission is somewhat weaker than that typically measured; this is ascribed mainly to below-average thermospheric temperatures. Auroral enhancement of NO hot bands was not observable with the available sensitivity. An approximate thermospheric temperature profile derived from the NO band shape compares reasonably with the mass spectrometer/incoherent scatter 86 model.

1. INTRODUCTION

The Spectral Infrared Interferometric Telescope (SPIRIT) 1 experiment, launched on April 8, 1986, was a rocket-borne probe designed to measure the long-wavelength IR emission spectra from an IBC class III aurora in the limb-viewing geometry. The primary instrument, built by Utah State University/Stewart Radiance Laboratory [Dybwad *et al.*, 1987], was a cryogenically cooled, five-detector Michelson interferometer mated to a high-off-axis-rejection telescope. Approximately 140 spectral scans were recorded covering tangent heights of \sim 70–240 km at latitudes of 60°–65°N over the spectral range \sim 450–2500 cm^{-1} . Most of these scans have an apodized resolution of \sim 8 cm^{-1} ; however, 17 scans were measured at 1- cm^{-1} resolution. During most of the flight, the instrument was pointed slightly away from the bright auroral arc, while later in the flight, direct views of the arc were obtained at tangent heights below 108 km. The spectra provide a comprehensive data base on a number of molecular emission features in the nighttime sky, including CO₂ ν_2 (15 μm), O₃ ν_3 (9.6 μm), and NO $\Delta\nu = 1$ (5.3 μm). A detailed description of the SPIRIT 1 mission is presented elsewhere [Smith *et al.*, 1990].

This paper provides a summary and an analysis of the SPIRIT 1 data on NO and CO₂ emission, including volumetric emissions and kinetic temperatures derived by inversion of the limb radiances. (Data on O₃ emission have been reported separately [Adler-Golden *et al.*, 1990; Adler-Golden and Smith, 1990].) The results are compared with previous experiments, particularly the Spectral Infrared Rocket Experiment (SPIRE) [Stair *et al.*, 1985] limb-viewing mission flown in September 1977 in a quiet atmosphere from the same launch site. The CO₂ ν_2 radiance in SPIRIT 1 is found to be similar to previous observations, while the NO 5.3- μm radiance is weaker. No major auroral effects are discernible

in these bands. An approximate thermospheric temperature profile derived from the NO band shape is found to compare reasonably with the mass spectrometer/incoherent scatter 1986 (MSIS-86) model [Hedin, 1987].

2. BRIEF DESCRIPTION OF EXPERIMENT

2.1. Flight and Instrument Description

The SPIRIT 1 payload was launched on April 8, 1986, from Poker Flat Research Range, Alaska, at 0942:25 (UT). It reached an apogee of 241 km at 253 s after launch. In addition to the primary instrument, other on-board sensors included a low-light-level video camera, a 35-mm image-intensified camera for star field position data, a telescoped 391.4-nm photometer, and a scanning IR horizon sensor.

Orientation of the payload was accomplished by a microprocessor-controlled attitude control system (MACS) using gaseous nitrogen thrusters. During most of the flight the MACS was operating under a preprogrammed scan pattern, which resulted in the sensors pointing slightly above and to the south of the intense auroral arc. However, near the end of the flight (starting around 417 s after launch) the ground control system became active, enabling manual override of the preprogrammed pattern. From that point on, the instrument was pointed directly at the arc, where the 391.4-nm intensity was over 100 kR.

The interferometer is a Michelson flex-pivot design cooled by liquid helium. The interferograms on each side of the critical peak are unequal in length; the length of the long side is set for the desired spectral resolution. Typical scan times are around 1 s, except for the high-resolution scans which last around 9 s. The focal plane contains an array of five Si:As long-wave IR (LWIR) detectors designed to have a combined dynamic range of 10^8 . The detectors are numbered 1 through 5 in order of decreasing size and sensitivity. Their arrangement on the focal plane [Dybwad and Huppi, 1987] is such that detector 1 viewed the highest tangent altitude, detector 3 the next highest, and detector 5 the

Copyright 1991 by the American Geophysical Union.

Paper number 91JA00656.
0148-0227/91/91JA-0065\$05.00

lowest; detectors 2 and 4 viewed essentially the same altitude.

In "open filter" mode the detectors were sensitive to radiation in approximately the 450- to 2500-cm⁻¹ (4-22 μ m) range. During portions of the flight, band-pass filters were inserted to isolate the 11- to 13- μ m atmospheric window (filter 1) and the 5.3- μ m NO band (filter 2).

2.2. Reduction and Calibration of Spectral Data

Details of the interferogram processing are given elsewhere [Smith et al., 1990]. In brief, the processing checked for and removed data spikes and detrended the interferogram to account for radiance variations during the scan (e.g., due to variations in tangent height viewed). The resulting processed interferogram was Fourier-transformed using a Kaiser-Bessel or triangular apodization window. A Mertz phase correction [Mertz, 1967] was generated using portions of the interferogram on both sides of the critical peak and was applied to the Fourier transform. The result is a "raw" spectrum (in volts per cm⁻¹) which was further processed to correct for the detector's spectral response. Except in the long, high-resolution scans, the full width at half maximum resolution is typically 8 cm⁻¹ with triangular apodization and 11 cm⁻¹ with Kaiser-Bessel apodization. The Kaiser-Bessel apodization yields an instrument function with very low sidelobes and was used to generate the spectra shown in this paper.

Relative spectral response curves for detectors 2, 3, and 4 were obtained in a postflight calibration using variable-temperature blackbody sources [Dybawd and Huppi, 1987]. The high-wavenumber portions of the curves were estimated from filter 2 rather than "open filter" data, which exhibit nonlinear behavior. Detectors 1 and 5 failed before they could be calibrated, so their response curves were estimated using the curves from detectors 2 and 4, respectively, which are the closest in size. Both the flight and the calibration data indicate that the response curves are all very similar, except that the larger detectors have somewhat more roll-off toward high wavenumbers, owing to slight wave front curvature in the interferometer.

The relative sensitivities of the detectors were determined by using the flight data on the CO₂ ν_2 band. These were combined with calibration data for detector 2 (taken from Dybwad and Huppi [1987]) to establish absolute responsivities. It was necessary to include a flux-dependent factor in the responsivity of detector 2, to reproduce the calibration data and to achieve consistency with the data from the other detectors, which were assigned flux-independent responsivities. This difference in behavior reflects the fact that detector 2 was operated at a significantly higher bias level than were the other detectors.

2.3. Calibration Error Estimates

As will be seen in section 5, the calibrated spectra are reasonably consistent among all five detectors at all altitudes and in nearly all wavelength bands, to within the measurement scatter of 10-20%. However, in the NO band there is a factor of 1.5 spread in the radiances obtained from detectors 2, 3, and 4, with the radiances increasing in that order. This indicates that at high wavenumbers their assumed relative spectral response curves, which were obtained somewhat

indirectly, are not completely understood. Inclusion of detectors 1 and 5 (whose curves were provisionally estimated from detectors 2 and 4) further increases the spread to nearly a factor of 2, with detector 1 giving the lowest radiances. The discrepancy between detectors 1 and 5 and the others is explainable by the inverse correlation between size and high-wavenumber response. In our data analysis the detector 1 NO radiances have been corrected to match those obtained from detector 2 by multiplying by 1.2; the detector 5 data, which are very noisy, were not used.

The absolute calibration, which was derived from detector 2 postflight laboratory data near the peak of the responsivity curve, is more uncertain than the relative calibration. Calibration data from detectors 3 and 4, obtained at much higher fluxes, lead to 40% smaller radiances. Taking into account this uncertainty and the typical detector-to-detector spread in the flight data, we estimate absolute radiance error limits of -40% to +20%, for a total uncertainty spread of a factor of 2. This excludes the NO band, where the absolute radiance uncertainty includes the additional factor of 1.5 spread, for a total spread of a factor of 3.

3. DATA OVERVIEW

3.1. Atmospheric Conditions

The SPIRIT I rocket was launched when an IBC class III aurora (>100 kR at 557.7 nm) was observed over the SPIRIT I ground station at Fort Nelson, British Columbia, approximately 1400 km to the southeast of the rocket's trajectory. The geomagnetic activity indices for April 8, 1986, were $Ap = 5$, $Kp = 3$, and the solar flux index $F_{10.7}$ was 72, a value typical for a minimum in the 11-year solar cycle. With these conditions the MSIS-86 model [Hedin, 1987] predicts an exospheric temperature (T_e) of around 800 K. For comparison, this is 100-150 K lower than that calculated for the conditions of the SPIRE [Stair et al., 1985] experiment.

3.2. Chronology of Spectral Data

The spectral scans from the interferometer are summarized chronologically in Table 1. The scans began at around time after launch (TAL) = 95 s during a rapid pitch-up maneuver. Accurate tangent height assignments (see section 3.3) begin with scan 81 at 99 s, when the pitch-up slowed. This scan covers 107- to 116-km tangent heights at a moderate auroral intensity (40 kR at 391.4 nm). Subsequent scans explored tangent heights up to 236 km, until the 11- to 13- μ m band-pass filter (filter 1) was inserted at 271 s. Nearly all of the useful data above ~105 km are from this upleg series of scans, which are generally of good quality but which correspond to low-to-moderate (1-40 kR) 391.4-nm intensity.

Due to attitude control system problems (which caused the sensors to view overly high altitudes and, later, caused a brief view of the Earth) and the presence of background contamination, the next series of useful scans did not start until around TAL = 411 s in the downleg, when the tangent heights viewed were below 108 km. Between 411 s and 415 s the auroral intensity was over 100 kR in the tangent height range 97-108 km. These are the brightest auroral scans obtained with the open filter.

The data taken at the very end of the flight, after TAL = 427 s, consist of filter 1 spectra below 82 km. These spectra, discussed by Adler-Golden et al. [1990], consist primarily of

TABLE I. Chronology of SPIRIT 1 Spectral Data

Data Description	Time After Launch, s	Scan Numbers	Comments
Prelaunch calibration	-11.7 to -1.5	1-9	blackbody source
In-flight calibration (NO filter)	57.0-68.4	48-57	blackbody source
Open filter data	95.0-268.7	78-149	tangent heights to 236 km
Filter 1 data	271.5-318.6	151-163	background contaminated
NO filter data	322.5-343.5	166-170	NO 5.3- μ m band
Open filter data	344.4-347.0	171-173	background contaminated
	348.3-349.7	174-175	rapid tangent height variation
	364.1-366.7	186-188	rapid tangent height variation
	407.2-408.6	219-220	rapid tangent height variation
	412.5-424.2	223-232	tangent heights below 108 km
Filter 1 data	426.9-446.3	234-249	ozone hot bands
In-flight calibration (thin film heater)	456.9	257	blackbody source; alignment test

hot bands of ozone resulting from O + O₂ + M recombination.

3.3. Tangent Height Data

Tangent heights viewed by the central detector (detector 2) as a function of time were determined using data from three on-board instruments (a three-axis position gyroscope, the IR horizon sensor, and the celestial aspect camera), as described in the next paragraph. The orientations of the latter two sensors relative to the interferometer optical axis were determined during the preflight alignment procedure. The tangent heights for the detectors other than detector 2 were computed from the derived focal plane orientation and the known angular displacements between the detectors. Tangent heights were assigned to the interferometer scans based on the time of the critical peak.

Initial analysis of the horizon sensor data provided approximate tangent height readings which were used to calibrate the position gyroscope. The resulting tangent heights from the gyroscope were checked against results from selected celestial aspect data. Agreement was found to within ± 2 km (1σ), although occasional differences as large as 5 km were observed. Subsequently, a refined set of tangent heights was obtained by a more detailed analysis of the horizon sensor data. This analysis used the gyroscope data to correct for time-constant effects in the horizon sensor and included corrections for the Earth eccentricity. The resulting tangent heights agree with the celestial aspect data to within ± 1 km (1σ). This represents the estimated tangent height uncertainty during most of the flight. During periods of rapid payload angular motion the tangent height uncertainties are larger, of the order of 5 km. The magnitude of the variation in tangent height over the duration of the interferometer scan is typically comparable to the uncertainties quoted above.

3.4. Photometer Data at 391.4 nm

The auroral intensity at 391.4 nm observed by the SPIRIT 1 on-board photometer, which was co-aligned with detector 2, is plotted versus tangent height in Figure 1. Each point represents the start of an interferometer scan; lines connect the points in sequential order. The data are separated into those taken before TAL = 417 s, when the automatic attitude control was in operation, and those after 417 s, when manual control was achieved and the instrument was pointed

toward the arc over Fort Nelson. During the period ~ 343 -400 s, an anomaly occurred which pointed the instrument away from the aurora and down toward the Earth; data from this time interval have not been plotted.

Most of the automatic control data plotted in Figure 1 are seen to correlate systematically with tangent height. This correlation is consistent with diffuse "drizzle" as the auroral source in these data. In contrast, the manual control data are widely scattered, reflecting the strong dependence on pointing when viewing the auroral arc. Note also that the tangent altitudes of the brightest auroral data lie well below the 90- to 100-km depth to which aurorae penetrate; this is because the arc was beyond the tangent point in these views.

3.5. Telescope Leakage and Background Contamination

The background contamination mentioned in section 3.2 is not apparent in scans below ~ 100 km, where the atmospheric radiance from CO₂ and O₃ is strong. However, at

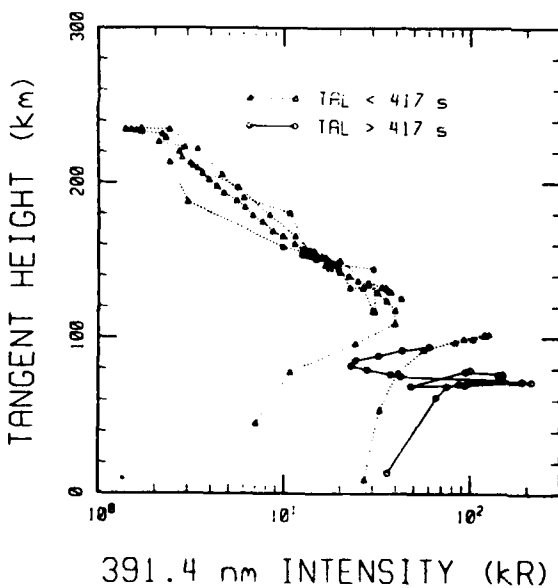


Fig. 1. Auroral intensity data from SPIRIT 1 391.4-nm photometer.

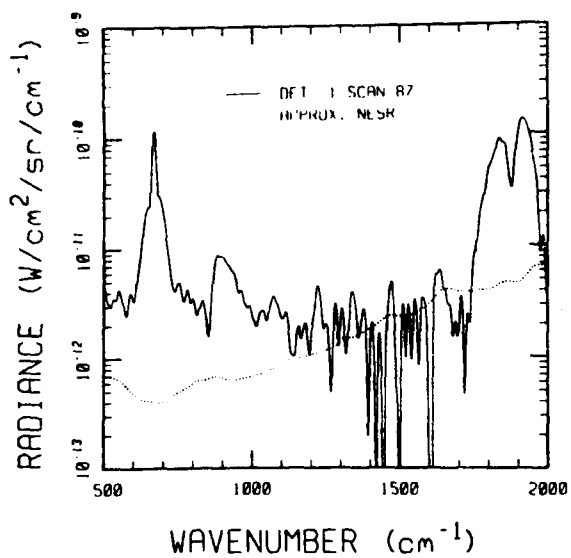


Fig. 2. Typical SPIRIT 1 spectrum at a 141-km tangent height. The three strong features are, from left to right, CO₂ ν_2 , a contamination peak around 900 cm⁻¹, and NO $\Delta\nu = 1$. The detector's approximate noise-equivalent spectral radiance (NESR) is also shown.

higher altitudes, most of the scans exhibit a low-level background spectrum, which is most easily seen in the 10- to 14- μm (700- to 1000-cm⁻¹) region. A typical high-altitude spectrum appears in Figure 2, which displays atmospheric emission from CO₂ and NO as well as a broad peak around 900 cm⁻¹, which is ascribed to a "contamination" background. The background level decreases in the order detector 1 > detector 3 > detector 2, which is the order of decreasing viewing angle above the telescope centerline. The background level also shows a weak inverse dependence on the angle between the telescope axis and the horizon. This low-level background is consistent with stray-light leakage from the Earth and/or the lower atmosphere caused by scattering from internal surfaces of the telescope or foreign material thereon. Similar problems have been encountered in other LWIR Earth limb experiments [Smith, 1988].

Occasionally during the flight, a blackbodylike background an order of magnitude or more brighter than the nominal stray-light background is observed. The intensity is approximately the same in all detectors. In many instances these bright flareups appear to be correlated with changes in payload orientation. A small number of spectra (for example, Figure 3, top) resemble the nadir view spectrum of the Earth [e.g., Wolfe and Zissis, 1978]. However, most often the spectrum has a more structured appearance, as in Figure 3, bottom. The latter spectrum appears to be identical in shape to the much weaker stray-light spectrum appearing in Figure 2.

While the precise light leakage paths associated with these background spectra are not known, the main source of leakage radiation has been determined to be the Earth-illuminated telescope baffle. The structured background spectrum has been shown to match the reflection spectrum of the black paint used on the baffle [Brown and Smith,

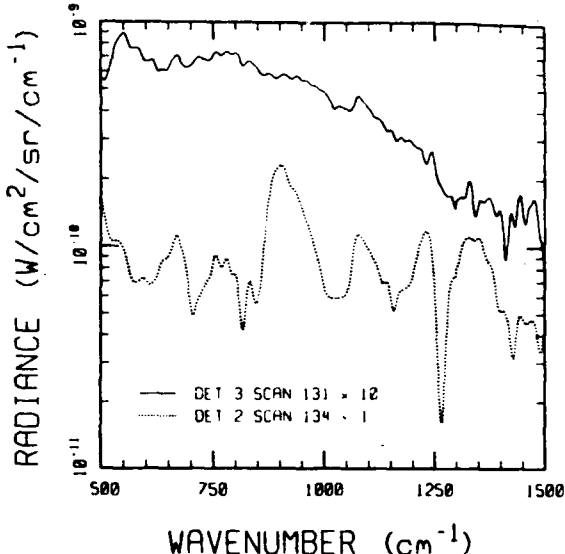


Fig. 3. Spectra showing strong background contamination. Earth-shinelike spectrum is at top, and paintlike spectrum is at bottom.

1990]. Since it is the top underside of the baffle that is illuminated, the detector viewing angles farthest above the telescope centerline are affected most. This is in agreement with the correlation of the low-level background with the detector number. The bright flare-ups suggest the further presence of frost or other particles floating in the field of view. These particles could be illuminated by either the earthlit baffle or, if they are near the telescope entrance, directly by the Earth. The latter would explain the spectrum shown in Figure 3 (top).

3.6. Data Selection and Background Correction

In the present analysis, scans and/or spectral bands which are highly background contaminated have been omitted. Also omitted are scans having uncertain or rapidly varying tangent heights, and spectral regions in which the phase angle of the interferogram is unusually large, indicating detector nonlinearity. The CO₂ radiances were corrected by subtracting a contribution ascribable to the background contamination. This background component was estimated by scaling the radiation from an adjacent "window" band pass (i.e., one that is free of atmospheric emission) using the Figure 3 contamination spectrum. This correction procedure materially affects only the highest-altitude data. No corrections were made for detector noise.

4. COLUMN INVERSION PROCEDURE

The volumetric emission profile, $I(h)$ (in units of emission per unit volume, i.e., W cm⁻³ sr⁻¹), may be determined by inversion of limb, zenith, or other column radiances, J , measured by a sensor. $I(h)$ can be used to derive quantities such as local kinetic temperature and excited state number densities. The inversion procedures used to analyze the SPIRIT 1 data, which apply to optically thin radiation (CO₂ ν_2 above ~ 120 km and the NO fundamental), are outlined

below. Applications to the ozone data from SPIRIT 1 are described by *Adler-Golden et al.* [1990].

4.1. Determination of Volumetric Emission Profile

The inversion procedure is similar to that employed by *Espy et al.* [1988], which involved a least squares fit to column radiance data. In their method, zenith column radiances were fitted to a polynomial multiplied by an exponential scale height factor; the volumetric emission function, which has the same mathematical form, was determined by differentiation of the column radiance fit. The application to limb radiance data in this work requires a generalization of this procedure, as follows. The volumetric emission function is written as

$$I(h) = \sum_i a_i f_i(h) = \sum_i a_i h^{i-1} \exp(-h/\alpha), \quad (1)$$

where h is height, α is a scale height parameter, and the a_i are coefficients to be determined. Each component term $f_i(h)$ is integrated along the line of sight applicable to each column radiance data point. The resulting column-integrated terms are used in a linear least squares fit to all of the data to determine the coefficients a_i and, hence, the volumetric emission function $I(h)$.

A problem can arise with this procedure if there is no explicit constraint to insure that the volumetric emission function remains physically reasonable (e.g., positive) above the highest altitude data point. An acceptable way to avoid this problem is to switch the $f_i(h)$ to a simple exponential,

$$f_i(h_{\max}) \exp[(h_{\max} - h)/\alpha_{\max}], \quad (2)$$

above the altitude h_{\max} of the highest data point. The volumetric emission function, being a sum of these terms will have the same exponential behavior. The value of α_{\max} should be chosen for a reasonable scale height but has little effect on the derived $I(h)$ at altitudes below h_{\max} .

Because of the wide dynamic range in the column radiances observed in SPIRIT 1, the least squares fitting was implemented using weighting that is inversely proportional to the radiance. This gave fits which had a fairly uniform percent deviation over most of the altitude range. The scale height parameter α was varied by trial and error until a stable fit was obtained for a given number of terms, n , in the fit. The limb radiance fits were generally found to be stable to within a few percent against variations in the input parameters, including n , as long as n is small enough to smooth out noise in the data. The volumetric emission $I(h)$ was generally equally stable, except in certain fits to the NO data, where the volumetric emission below the maximum at 130 km was found to be somewhat sensitive to n .

4.2. Determination of Kinetic Temperature Profile

It is well known that atmospheric temperature profiles may in principle be derived from observed vibrational band shapes. The typical procedure is to invert the limb spectral radiance at different wavelengths and fit the resulting volumetric emission spectra to synthetic spectra [Caledonia et al., 1985; Zachor et al., 1985]. Since the inversion procedure amplifies noise in the spectra, the results need to be considerably averaged or smoothed in the altitude and/or wavelength domains.

For the current SPIRIT 1 data analysis we have developed an alternative method, described below, in which the inverted quantities are spectral moments rather than spectral radiances. Since the moments are wavelength-averaged quantities, the method is numerically stable, and it is much more efficient computationally since no spectral fitting and only two limb inversions are required.

The kinetic temperature influences vibrational band shapes mainly through the rotational state distribution, which controls the width of the spectrum. A quantitative measure of the spectral width is the variance σ^2 , which is the ratio of the second moment around the mean wavenumber to the integrated intensity. Thus a kinetic temperature profile $T(h)$ can be computed from the volumetric emission function $\sigma^2(h)$, given by

$$\sigma^2(h) = I_2(h)/I(h) \quad (3)$$

where $I_2(h)$ is the second moment of the volumetric emission $I(h)$. $I(h)$ and $I_2(h)$ are, in turn, derived by inversion of the column radiances J and second moments J_2 . In computing J_2 , the vibrational band center may be used instead of the mean wavenumber.

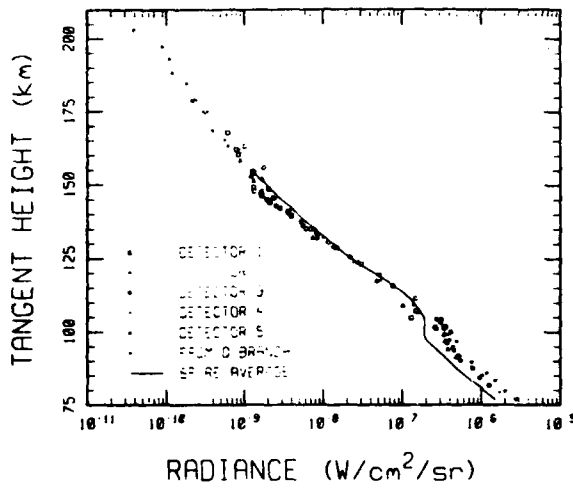
$T(h)$ is determined from $\sigma^2(h)$ by establishing the functional relationship between the kinetic temperature and the variance using synthetic emission spectra. The synthetic spectrum generation is the only significant computational effort in the $T(h)$ determination and was performed using the HITRAN line atlas [Rothman et al., 1987]. The calculations accounted for SPIRIT 1 instrumental resolution (typically 8–11 cm⁻¹), which has a small (few percent) effect on σ^2 for CO₂ ν_2 and a negligible effect for NO $\Delta\nu = 1$. The function $T(\sigma^2)$ was accurately represented via a low-order polynomial fit to 5–10 spectra over the 200–1000 K range. Since in this range, σ^2 and T are roughly proportional, fractional errors in the determined temperature are comparable to the fractional errors in σ^2 .

In addition to the rotational state distribution, the intensities of hot bands located in the band pass under consideration can also affect the spectral moments. In the local thermodynamic equilibrium (LTE) approximation the hot bands are linked to the kinetic temperature. However, for best accuracy, non-LTE effects should be incorporated in the model spectra by using independent vibrational temperatures T_v , which may differ from the kinetic temperature T that characterizes the rotational and translational modes. Depending on the relative values of T_v and T , the ratio of hot band to cold band emission may be enhanced or suppressed compared to LTE ($T_v = T$).

It turns out that the NO 5.3-μm spectral shapes are quite insensitive to the T_v value, since the high vibrational frequency leads to very small Boltzmann factors for hot bands over a wide range of T_v . For simplicity, we have assumed $T_v = T$ in the NO computations. The CO₂ ν_2 spectra are more sensitive to T_v , however. To test the effect of T_v on the kinetic temperature determination, the CO₂ computations were performed for two limiting cases, $T_v = T$ and $T_v = 0$, as discussed in section 5.3.

4.3. Column Kinetic Temperatures

Analogous to the local variance $\sigma^2(h)$ and the local kinetic temperature $T(h) = T[\sigma^2(h)]$ are the column variances $\sigma_{\text{column}}^2 = J_2/J$ and the corresponding column kinetic tem-

Fig. 4. CO₂ ν₂ limb radiance profile and average of SPIRE data.

peratures, which for limb views are denoted T_{limb} . It is possible to derive the local variance by directly inverting the column variances, as opposed to inverting the J and J_2 separately. Alternatively, the limb kinetic temperatures may be used to estimate the local kinetic temperature profile without performing an inversion, using the approximation

$$T(h) \approx T_{\text{limb}}(h - \alpha/2), \quad (4)$$

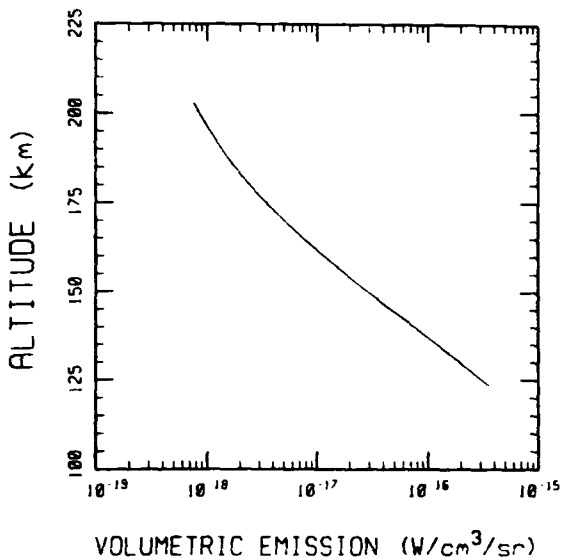
where α is the emission scale height. According to (4), the local kinetic temperature may be approximated from the limb emission band shape at a tangent height one half of a scale height below. In model calculations this approximation is found to be quite accurate. Equation (4) also implies that the altitude range over which $T(h)$ is valid is somewhat higher than the tangent height range spanned by the limb radiance data.

5. RESULTS AND DISCUSSION

5.1. CO₂ 15 μm (ν₂)

5.1.1. *Results.* CO₂ ν₂ limb radiance data from all five detectors in SPIRIT I are shown in Figure 4. Most of the data were derived by integrating the spectra over 614–725 cm^{-1} (14–16 μm). These data are accurate up to ~ 165 km, where the background due to telescope leakage becomes dominant. To extend the data to higher altitudes, additional points were obtained from detector 1 and detector 2 spectra, using the intensity of the narrow Q branch peak at 667 cm^{-1} , which is less influenced by the leakage background than is the band-pass-integrated intensity. The peak intensities were converted to band radiances by matching to band-pass-integrated data at lower altitudes. This procedure is valid since the $\sim 8\text{-cm}^{-1}$ resolution of the scans used exceeds the width of the Q branch, insuring a constant proportion between the peak intensity and the band radiance. The results provide additional CO₂ ν₂ radiances up to approximately 200 km.

With the exception of data from tangent heights of 140–150 km, the instrument was sufficiently above the tangent point that it viewed essentially the full limb. The smooth curve

Fig. 5. CO₂ ν₂ volumetric emission profile, from fit to detector 1 and 2 data.

shown in the figure is derived from an average of full-limb data taken in the SPIRE experiment [Stair et al., 1985]. The results from the two experiments are virtually identical above 105 km; below that, the SPIRIT 1 radiances are higher by up to a factor of 2. Given the calibration uncertainties in both experiments, which may include flux-dependent effects as well as uncertainties in absolute scale factors, the differences below 105 km may not be entirely real.

For the limb inversion, data from detectors 1 and 2 were selected above 120 km where the emission is essentially optically thin. The volumetric emission function obtained from a second-degree fit to these data is shown in Figure 5. The column radiance evaluated over the full limb is shown in Figure 6; the points are the data after correction to full-limb views, while the curve is from the volumetric emission function in Figure 5. The good agreement between the curve and the data points illustrates the success of the limb inversion/least squares fitting method as well as the high quality of the data.

A representative sampling of CO₂ ν₂ spectra is given in Figure 7a. Two high-resolution (1 cm^{-1}) spectra are shown in Figure 7b. In the wings, where the Q branches of hot bands may be seen, the spectra are sensitive to the relative populations (or temperatures) of the various vibrational levels. The high-resolution spectra reveal the hot bands more clearly, but the apparent rotational structure is largely spurious due to interference from a "channel spectrum," or etalon, in the instrument which has around a 3-cm^{-1} spacing. However, the channel spectrum does not affect the lower-resolution spectra or the radiances or temperatures determined therefrom. Detailed analysis of these spectra and comparisons with atmospheric radiation code simulations are in progress.

5.1.2. *Discussion.* In addition to SPIRIT I and SPIRE, other experiments which have observed CO₂ ν₂ radiation include the ICECAP 1973 and 1974 missions [Rodgers et al., 1977] and rocket probes launched in Salvo B of the Energy

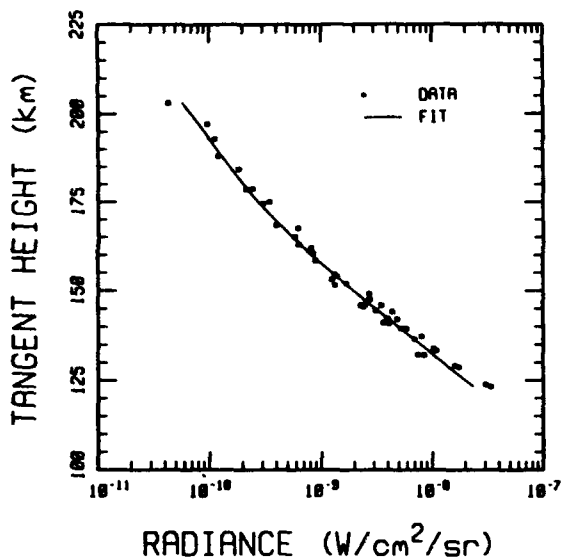


Fig. 6. CO₂ ν_2 limb radiance profile from fit and original data corrected to full-limb view.

Budget Campaign in 1980; these have been compared and discussed by Ulwick *et al.* [1985]. Factor-of-2 differences in CO₂ radiance were observed among these experiments and were ascribed to spatial variations as well as auroral excitation (in ICECAP 1973). The auroral excitation effect was postulated to be caused by local Joule heating associated with high geomagnetic activity.

The magnitude and variability of CO₂ ν_2 radiation may be understood from the main excitation mechanisms, which are pumping of the $1\nu_2$ level (denoted (01101) in HITRAN notation [Rothman *et al.*, 1987]) by collisions and by earth-shine. The earthshine excitation rate is sensitive to the kinetic temperature of the atmosphere at lower altitudes where CO₂ ν_2 is optically thick. Below 100 km the collisional excitation rate constant, given by

$$k_{\text{coll}} = k_q \exp(-h\nu/kT), \quad (5)$$

where k_q is the rate constant for ν_2 deactivation, is fairly sensitive to T . Above 110 km, where the kinetic temperature is higher, the collisional excitation rate is much less sensitive to it. An important factor above ~ 90 km is the density of atomic oxygen, which is the most efficient collision partner. Excitation by O atoms is the chief cause of the inflection in observed CO₂ ν_2 limb radiance curves near 100 km [Sharma and Wintersteiner, 1990].

The overall factor-of-2 range in CO₂ radiance among the experiments to date seems reasonable, given calibration uncertainties as well as expected variations in kinetic temperature and O atom and CO₂ densities associated with different degrees of geomagnetic and solar activity and the presence of aurorae.

The possibility of excitation of CO₂ ν_2 via electrons or other energetic species in an aurora was proposed as an explanation for seemingly large radiances and high vibrational temperatures observed in the HIRIS experiment [Stair *et al.*, 1983], which flew close to an IBC III+ aurora (up to 300–500 kR at 391.4 nm). However, in that experiment the

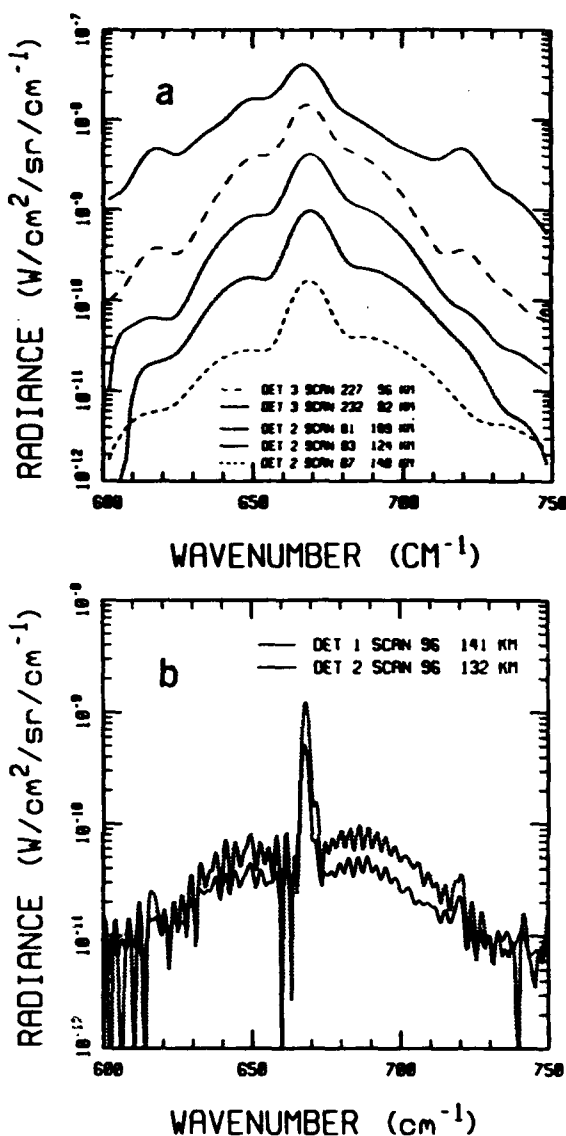


Fig. 7. Typical CO₂ ν_2 spectra at different tangent heights: (a) 11-cm⁻¹ resolution and (b) 1-cm⁻¹ resolution.

pointing of the sensor was highly uncertain due to rapid payload tumbling. A recent reanalysis (D. R. Smith, unpublished data, 1990) of the HIRIS pointing and spectral data has resulted in considerably lower pointing angles and vibrational temperatures than previously proposed. This suggests that any auroral excitation effects that may exist would be too small to be discernable in the SPIRIT I spectra.

5.2. NO 5.3 μ m

5.2.1. *Results.* Below around 120 km the high-wavenumber region of the spectra is very noisy, and the NO data are of poor quality. However, the higher-altitude NO spectra are acceptable and were used to derive integrated band radiances. A second-degree fit is shown in Figure 8, along with the radiance data after correction to full-limb

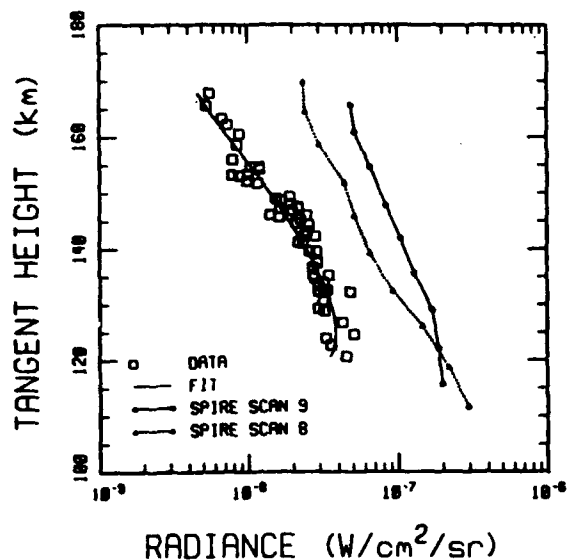


Fig. 8. NO $\Delta v = 1$ (5.3 μm) limb radiance profile, showing second-degree fit and full-limb-corrected data. SPIRE full-limb data are also plotted.

views. The radiances are approximately a factor of 4 lower than in SPIRE [Stair *et al.*, 1985; Zachor *et al.*, 1985], although the profile shapes are quite similar. The scatter in the NO radiances is greater than in the CO₂ radiances and appears to be larger than expected from noise in the spectra.

The corresponding volumetric emission function from the second-degree fit is shown in Figure 9, along with a typical volumetric emission profile obtained from SPIRE [Zachor *et al.*, 1985]. As with the limb radiance profile, the volumetric emission profile from SPIRIT 1 has a similar shape but lower overall intensity.

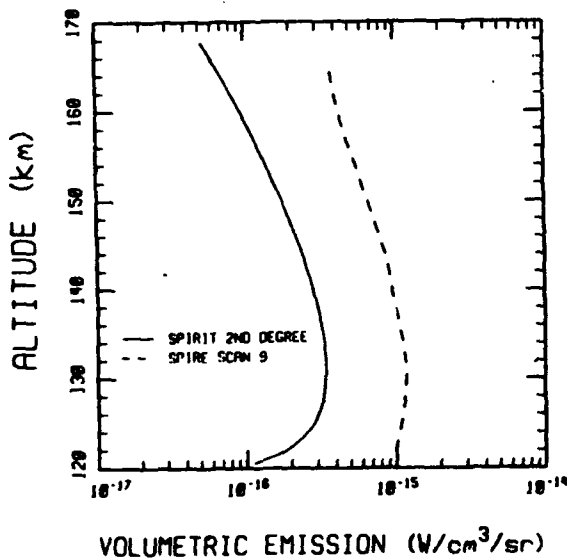


Fig. 9. NO $\Delta v = 1$ volumetric emission profiles, from SPIRIT 1 and from SPIRE scan 9 [Zachor *et al.*, 1985].

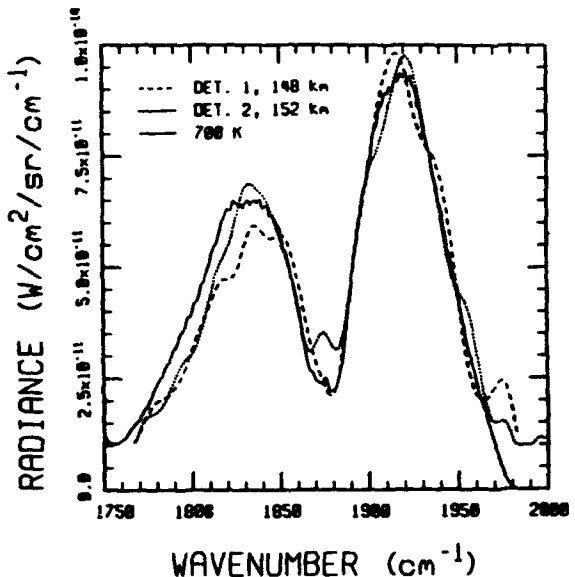


Fig. 10. Comparison of SPIRIT 1 NO $\Delta v = 1$ spectra and a synthetic 700 K spectrum.

Figure 10 displays NO spectra taken with detectors 1 and 2 at similar tangent heights. The synthetic spectrum was computed for a kinetic temperature close to T_{limb} , the "effective" temperature of the observed spectrum. Given the noise level of $(5-10) \times 10^{-12} \text{ W cm}^{-2} \text{ sr}^{-1} \text{ cm}$, the three spectra are in reasonable agreement. This argues against a major contribution from hot bands associated with high vibrational levels, which have been observed in two other experiments which probed aurorae (see section 5.2.2). Significant hot band contributions would increase the relative intensity in the region of the *P* branch, causing the band to be skewed to low wavenumbers. However, in the Figure 10 spectra the *P* branch is, if anything, slightly weaker than in the synthetic spectrum, which has only a 2% hot band component.

Quantitative estimates of possible hot band contributions were attempted using the ratio of intensities of the *P* and *R* branches as well as the mean frequency of the band at various tangent heights, but no significant contribution was found. The same conclusion was reached in an independent analysis (W. T. Rawlins, personal communication, 1989) which used least squares spectral fitting. These results suggest an upper limit to the hot band intensity of around 10% of the total, based on the approximate contribution from noise and other sources of scan-to-scan and detector-to-detector spectral variation. The spectral variations may reflect detector noise, as well as possible systematic problems related to detector nonlinearity (see section 5.3) and calibration uncertainties.

5.2.2. *Discussion.* The absence of observable NO hot bands produced by the auroral $\text{N}^2\text{D} + \text{O}_2 \rightarrow \text{NO}(\nu) + \text{O}$ mechanism is consistent with the modest auroral intensities in these scans (<40 kR at 391.4 nm) combined with obscuration by the cold band radiation (which is especially strong in limb views) and instrumental noise. Using results from HIRIS [Rawlins *et al.*, 1981] and the Field-Widened Inter-

ferometer experiment [Espy *et al.*, 1988], the NO hot band radiance anticipated for this auroral intensity would be around $2 \times 10^{-9} \text{ W cm}^{-2} \text{ sr}^{-1}$. This is half of the maximum possible hot band radiance in SPIRIT 1 estimated in the previous section.

Also found in the Field-Widened Interferometer spectra are weak band heads resulting from highly excited rotational states. The signal-to-noise level in the current SPIRIT 1 spectra is too poor to reveal these features. However, it may be possible to improve the signal-to-noise level somewhat by averaging and/or more sophisticated processing of the interferograms.

A large data base from previous experiments is available on spectrally unresolved $\Delta\nu = 1$ radiance in the thermosphere. Reidy *et al.* [1982] and Ulwick *et al.* [1985] have discussed the results from several high-latitude rocket flights in 1973–1974 as well as from the 1980 Energy Budget Andoya rocket probe. They concluded that in weak aurorae the N(²D) mechanism makes a small contribution compared to collisional excitation of ground-state NO by atomic oxygen. This conclusion is also consistent with the results from SPIRIT 1 and the Field-Widened Interferometer experiment [Espy *et al.*, 1988].

NO emission intensities observed in previous experiments have been quite variable but typically are larger than those found in SPIRIT 1. The variations can be caused by differences in O atom density, NO density, kinetic temperature, or some combination of the three. To assess these possible effects, a model calculation was performed using the O atom excitation mechanism employed by previous investigators [Zachor *et al.*, 1985; Caledonia and Kennealy, 1982]. The calculation employed the vibrational deactivation rate constant k_q from Zachor *et al.* [1985], which agrees with the measurements by Fernando and Smith [1979], together with kinetic temperature and atomic oxygen profiles from the MSIS-86 model [Hedin, 1987]. The atomic oxygen profile from MSIS-86 is very similar to that assumed by Zachor for SPIRE. However, the assumed temperature profile is significantly cooler in SPIRIT 1 in accord with the lower T_e (see section 3.1), and results in a reduced rate of collisional excitation.

The resulting NO density profile is shown in Figure 11. Due to the relatively cool temperatures the calculated NO density is only a factor of 2 below Caledonia and Kennealy's "median" profile [Caledonia and Kennealy, 1982] that fits the SPIRE data. This factor-of-2 difference may not be significant due to uncertainties in the actual atomic oxygen and temperature profiles and in the SPIRIT 1 absolute calibration. In any case, it is clear that Caledonia and Kennealy's "auroral" profile, which is an order of magnitude larger still, is highly inappropriate for the SPIRIT 1 conditions.

The inferred NO density in SPIRIT 1 is qualitatively consistent with correlations between NO production and solar and geomagnetic activity [Iwagami and Ogawa, 1987]. The SPIRIT 1 experiment was flown during a period of relatively low solar activity, and the geomagnetic activity indices were moderate despite the presence of the aurora. A full understanding of thermospheric NO density and radiance variations will require a comprehensive survey of observations combined with model calculations of NO production and transport.

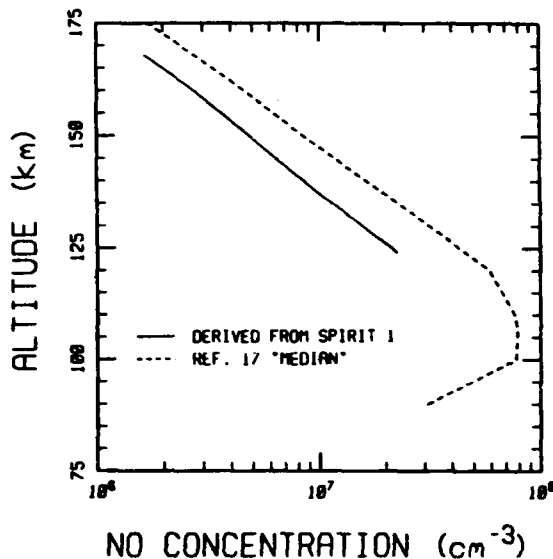


Fig. 11. NO density profile calculated from SPIRIT 1 volumetric emission, and "Median" profile from Caledonia and Kennealy [1982].

5.3. Kinetic Temperature Profile

Kinetic temperature profiles extracted from CO₂ ν_2 and NO 5.3- μm spectra are shown in Figures 12 and 13, respectively. The two CO₂ calculations correspond to $T_v = T$ (LTE conditions, hot bands included) and $T_v = 0$ (hot bands excluded). Also shown in these figures is the MSIS-86 model [Hedin, 1987] profile calculated for the conditions of the SPIRIT 1 flight. The data points are the limb temperatures extracted from individual scans. By comparing the data points with the smooth limb temperature curve, the uncertainty in the limb temperature profile can be estimated. Essentially the same uncertainty applies to the local temperature profile. This uncertainty is indicated in the figures by the error bars centered around the local temperature curve. In all cases the local temperature curve resembles the limb temperature curve except for being displaced upward by ~ 7 km, which is approximately half the typical NO and CO₂ emission scale heights. This is in accord with (4).

Below 125 km the inferred kinetic temperatures from both CO₂ calculations are well above the MSIS-86 model, but this is expected since the inversion method assumes optically thin conditions, which do not apply in limb views at these altitudes. Above 127 km the $T_v = 0$ (Figure 12a) and $T_v = T$ (Figure 12b) profiles generally bracket MSIS up to 160 km, where the data are noisy and the background level is comparable in size to the CO₂ signal. The $T_v = 0$ temperatures are higher than the $T_v = T$ temperatures since the omission of the hot bands makes the spectra narrower, requiring a higher kinetic temperature to account for the observed width.

With currently accepted mechanisms for CO₂ hot band excitation, atmospheric radiance codes [Degges and Smith, 1977; Sharma *et al.*, 1989] predict vibrational temperatures for most CO₂ vibrational states to be of the order of 200 K. This would lead to extracted kinetic temperatures better represented by the $T_v = 0$ curve than by the $T_v = T$ curve.

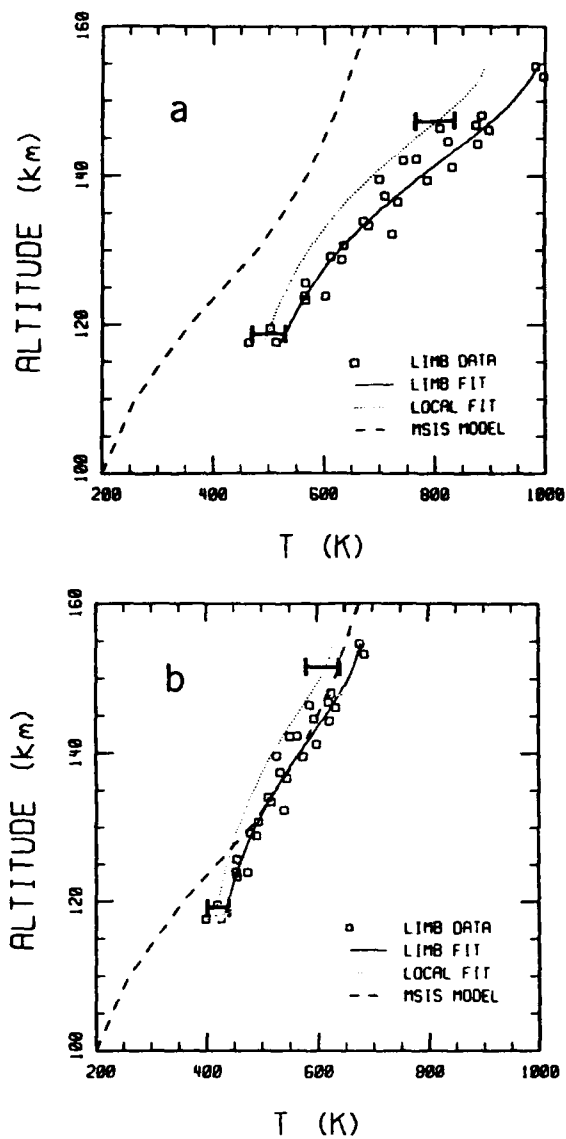


Fig. 12. Limb and local kinetic temperature profiles from SPIRIT 1 CO₂ ν_2 data. Error bars show approximate uncertainty in local temperature. Vibrational temperatures used for band shape calculations were (a) $T_v = 0$ and (b) $T_v = T$.

However, this behavior is the reverse of what is found when comparing the SPIRIT 1 and MSIS profiles in Figures 12a and 12b. Even at around 130 km, where optical thickness effects are absent and the signal-to-noise ratio is still good, the MSIS curve is slightly closer to the $T_v = T$ result.

The high apparent temperature profile could be caused by a systematic error, such as in the wavelength response or incomplete background subtraction (leading to excessive values of σ^2), or, alternatively, somewhat stronger hot bands than are predicted by current models. Comparisons of atmospheric radiance code simulations with available spectra, particularly the high-resolution spectra from SPIRIT 1, are under way to address this question. If elevated hot band intensities are confirmed, the possibility of a contribution

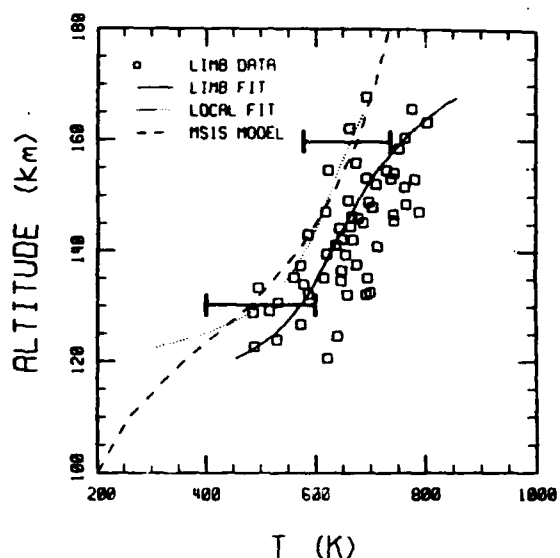


Fig. 13. Limb and local kinetic temperature profiles from SPIRIT 1 NO $\Delta v = 1$ data. Error bars show approximate uncertainty in local temperature.

from an auroral excitation source, mentioned in section 5.1.2, must be considered.

At sufficiently low atmospheric densities, rotation-translation equilibrium may break down, in which case the band shape would not accurately reflect the kinetic temperature profile. Below 150 km the gas kinetic collision rate exceeds the Einstein coefficient for CO₂ ν_2 emission by at least an order of magnitude. Thus unless rotational equilibration in CO₂ were slower than 0.1 of the gas kinetic rate, which seems unlikely, rotation-translation disequilibrium would occur only at higher altitudes.

The NO data do not suffer from problems of optical thickness or sensitivity to hot band vibrational temperatures and yield a local temperature profile quite close to MSIS; however, the error bars are very large. The scatter cannot merely be due to radiance fluctuations, which cancel out when the variance is taken, or detector noise, which is small in the lower-altitude scans. The best explanation for the scatter involves interference from the strong CO₂ ν_2 emission, which may have contributed photon statistical noise and, in the presence of detector nonlinearity, caused phase and amplitude distortion in the interferograms. Indeed, anomalies can be seen in the phase spectra, particularly at tangent heights below 120–130 km.

Previous attempts to extract thermospheric temperature profiles from CO₂ ν_2 and NO 5.3- μm bands have been made using SPIRE data [Zachor et al., 1985; Caledonia et al., 1985] and encountered similar scatter and background problems. While the concept of using IR spectral shapes to extract T and T_v profiles remains promising, better quality spectra are required for the accuracy needed to critically test current models.

6. SUMMARY

Spectral limb radiance data for CO₂ ν_2 and NO 5.3- μm emissions obtained in the SPIRIT 1 rocket experiment have

been analyzed. The data cover auroral intensities from several kilorayleighs to over 100 kR at 391.4 nm, and tangent heights above ~70 km at high latitudes (60°–65°N). Volumetric emission and kinetic temperature profiles were obtained using linear least squares inversion procedures. The main conclusions are as follows:

1. The CO₂ ν_2 emission intensity agrees well with previous observations in quiet as well as auroral atmospheres.
2. The NO emission intensity is smaller than that typically observed at high latitudes, due mainly to a low thermospheric temperature. A model calculation leads to a profile of NO density around half of the "median" profile of Caledonia and Kennealy [1982], subject to the considerable uncertainties in the atomic oxygen profile and the absolute calibration.
3. A smooth kinetic temperature profile derived from the NO band shape agrees closely with the MSIS-86 model, being well within the $\sim \pm 100$ K scatter of individual data points. The results from the CO₂ band are more difficult to interpret but may suggest higher-than-predicted vibrational or kinetic temperatures.
4. NO hot bands associated with the auroral N(²D) + O₂ mechanism are not visible, leading to a hot band radiance upper limit of 4×10^{-9} W/sr at 391.4-nm intensities below 40 kR. This is compatible with previous observations.

Further analysis of these and other emission features observed in the SPIRIT I experiment is in progress.

Acknowledgments. The authors are grateful to Tony Ratkowski of the Geophysics Laboratory (GL), who acted as field director for the SPIRIT I program, as well as the many people involved in the data reduction, calibration, and analysis, including Ed Richards, Bill Grieder, and Brian Sullivan of Boston College, Peter Dybwad of Utah State University (Stewart Radiance Laboratory), W. T. Rawlins of Physical Sciences, Inc., and David Robertson of Spectral Sciences, Inc. The SPIRIT I atmospheric measurement program was conducted by GL with instrumentation developed and flown by Utah State University and Space Data Corp. The experiment and all subsequent postflight data analysis were supported by the Defense Nuclear Agency. The continued support and encouragement of Arman Mardigian, Ken Schwartz, and Leon Wittwer have been vital and greatly appreciated. The work at Spectral Sciences was funded under Air Force contract F19628-87-C-0130.

The Editor thanks G. E. Caledonia and another referee for their assistance in evaluating this paper.

REFERENCES

Adler-Golden, S. M., and D. R. Smith, Identification of 4- to 7-quantum ν_3 bands in the atmospheric recombination spectrum of ozone, *Planet. Space Sci.*, 38, 1121, 1990.

Adler-Golden, S. M., M. W. Matthew, D. R. Smith, and A. J. Ratkowski, The 9- to 12- μm atmospheric ozone emission observed in the SPIRIT I experiment, *J. Geophys. Res.*, 95, 15,243, 1990.

Brown, C. W., and D. R. Smith, High-resolution spectral reflectance measurements on selected optical black baffle coatings in the 5- to 20- μm region, *Proc. Int. Soc. Opt. Eng.*, 1331, 210, 1990.

Caledonia, G. E., and J. P. Kennealy, NO infrared radiation in the upper atmosphere, *Planet. Space Sci.*, 30, 1043, 1982.

Caledonia, G. E., B. D. Green, and R. M. Nadile, The analysis of SPIRE measurements of atmospheric limb CO₂ (ν_2) fluorescence, *J. Geophys. Res.*, 90, 9783, 1985.

Degges, T. C., and H. J. P. Smith, A high altitude infrared radiance model, *Rep. AFGL-TR-77-0271*, Geophys. Lab., Hanscom AFB, Mass., 1977. (Available as NTIS ADA059242 from Natl. Tech. Inf. Serv., Springfield, Va.)

Dybawd, J. P., and R. J. Huppi, SPIRIT I post-flight calibration, *Rep. SRL-87-2*, Utah State University/Stewart Radiance Lab., Bedford, Mass., 1987.

Dybawd, J. P., R. J. Huppi, R. E. McKenna, D. P. Saletnik, B. J. Thomas, and V. Griffiths, Report on a rocket-borne, telescopized Fourier transform spectrometer operating at 10°K, *Proc. SPIE Int. Soc. Opt. Eng.*, 787, 114, 1987.

Espy, P. J., C. R. Harris, A. J. Steed, J. C. Ulwick, and R. Haycock, Rocketborne interferometer measurement of infrared auroral spectra, *Planet. Space Sci.*, 36, 36, 543, 1988.

Fernando, R. P., and I. W. Smith, Vibrational relaxation of NO by atomic oxygen, *Chem. Phys. Lett.*, 66, 218, 1979.

Hedin, A. E., MSIS-86 thermospheric model, *J. Geophys. Res.*, 92, 4649, 1987.

Iwagami, N., and T. Ogawa, Thermospheric NO profiles observed at the diminishing phase of solar cycle 21, *Planet. Space Sci.*, 35, 191, 1987.

Mertz, L., Auxiliary computation for Fourier spectrometry, *Infra-red Phys.*, 7, 17, 1967.

Rawlins, W. T., G. E. Caledonia, J. J. Gibson, and A. T. Stair, Jr., Infrared emission from NO ($\Delta v = 1$) in an aurora: Spectral analysis and kinetic interpretation of HIRIS measurements, *J. Geophys. Res.*, 86, 1313, 1981.

Reidy, W. P., T. C. Degges, A. G. Hurd, A. T. Stair, Jr., and J. C. Ulwick, Auroral nitric oxide concentration and infrared emission, *J. Geophys. Res.*, 87, 3591, 1982.

Rodgers, J. W., A. T. Stair, Jr., N. B. Wheeler, C. L. Wyatt, and D. J. Baker, LWIR (7–24 μm) measurements from the launch of a rocketborne spectrometer into a quiet atmosphere (1974), *Rep. AFGL-TR-0113*, *Environ. Res. Pap.* 597, Geophys. Lab., Hanscom AFB, Mass., 1977.

Rothman, L. S., et al., The HITRAN database: 1986 edition, *Appl. Opt.*, 26, 4058, 1987.

Sharma, R., and P. P. Wintersteiner, Role of carbon dioxide in cooling planetary thermospheres, *Geophys. Res. Lett.*, 17, 2201, 1990.

Sharma, R., A. J. Ratkowski, R. L. Sundberg, J. W. Duff, L. S. Bernstein, P. K. Acharya, J. H. Gruninger, and D. C. Robertson, The strategic high-altitude atmospheric radiation code (SHARC) user instructions, *Rep. AFGL-TR-89-0062*, Geophys. Lab., Hanscom AFB, Mass., 1989.

Smith, D. R., Evidence of off-axis leakage radiance in high-altitude IR rocketborne measurements, *Proc. SPIE Int. Soc. Opt. Eng.*, 967, 30, 1988.

Smith, D. R., A. J. Ratkowski, S. M. Adler-Golden, M. W. Matthew, W. F. Grieder, and E. Richards, SPIRIT I final flight report, *Rep. AFGL-TR-88-0125*, Geophys. Lab., Hanscom AFB, Mass., in press, 1990.

Stair, A. T., Jr., J. Pritchard, I. Coleman, C. Bohne, W. Williamson, J. Rogers, and W. T. Rawlins, Rocketborne cryogenic (10 K) high-resolution interferometer spectrometer flight HIRIS: Auroral and atmospheric emission spectra, *Appl. Opt.*, 22, 1056, 1983.

Stair, A. T., Jr., R. D. Sharma, R. M. Nadile, D. J. Baker, and W. F. Grieder, Observations of limb radiance with cryogenic spectral infrared rocket experiment, *J. Geophys. Res.*, 90, 9763, 1985.

Ulwick, J. C., K. D. Baker, A. T. Stair, Jr., W. Frings, R. Hennig, K. U. Grossman, and E. R. Hegblom, Rocket-borne measurements of atmospheric infrared fluxes, *J. Atmos. Terr. Phys.*, 47, 123, 1985.

Wolfe, W. L., and G. J. Zissis (Eds.), *The Infrared Handbook*, Office of Naval Research, Department of the Navy, Washington, D. C., 1978.

Zachor, A. S., R. D. Sharma, R. M. Nadile, and A. T. Stair, Jr., Inversion of a spectrally resolved limb radiance profile for the NO fundamental band, *J. Geophys. Res.*, 90, 9776, 1985.

S. M. Adler-Golden and M. W. Matthew, Spectral Sciences, Inc., 99 South Bedford Street, #7, Burlington, MA 01803.
D. R. Smith, Geophysics Laboratory, Hanscom AFB, Bedford, MA 01731.

(Received August 27, 1990;
revised November 29, 1990;
accepted January 15, 1991.)

Appendix G

**Identification of 4- to 7-Quantum v_3 Bands in the
Atmospheric Recombination Spectrum of Ozone**

IDENTIFICATION OF 4- TO 7-QUANTUM v_3 BANDS IN THE ATMOSPHERIC RECOMBINATION SPECTRUM OF OZONE

S. M. ADLER-GOLDEN

Spectral Sciences, Inc., 99 South Bedford Street, Burlington, MA 01803-5169, U.S.A.

and

D. R. SMITH

Geophysics Laboratory, Hanscom AFB, MA 01731, U.S.A.

(Received 10 April 1990)

Abstract—Spectra of ozone hot band chemiluminescence obtained in the *SPIRIT 1* rocket experiment have been analyzed with the aid of laboratory data and vibrational energy and band contour predictions. Band centers and energies for previously unreported vibrational states of ozone having up to seven quanta have been derived. The assignments are supported by the predictions of an improved Darling-Dennison-type energy level formula which behaves realistically towards dissociation. Bands associated with bending as well as stretching excitation appear due to an accidental vibrational resonance and a non-mode-specific population distribution.

1. INTRODUCTION

Emission from high-lying vibrational levels of ozone in the v_3 band is an important source of i.r. radiation in the upper atmosphere in the 10–12.5 μm (800–1000 cm^{-1}) region (Stair *et al.*, 1985). These levels are in a steady-state population distribution resulting from $\text{O} + \text{O}_2 + \text{M}$ recombination, forming ozone at energies near the dissociation limit, followed by collisional and radiative cascade to lower levels. A thorough understanding of this hot band chemiluminescence is required for accurate atmospheric background radiance modeling.

Spectroscopic information on high-lying ozone vibrational states has previously been obtained from laboratory studies of i.r. absorption (Barbe *et al.*, 1974; Steinfeld *et al.*, 1987), i.r. emission (Rawlins and Armstrong, 1987; Rawlins *et al.*, 1987) and u.v. resonance Raman scattering (Imre *et al.*, 1982; Imre, 1984). These data have led to band center estimates for up to five-quantum states with an accuracy of several cm^{-1} , as well as rough (10–20 cm^{-1} accuracy) energy estimates for up to seven-quantum states observed in the Raman spectrum.

Atmospheric emission spectra of ozone v_3 hot bands have heretofore provided very limited information due to resolution, signal-to-noise, or other problems. Recently, atmospheric limb spectra with improved resolution ($\sim 4 \text{ cm}^{-1}$) have been obtained from a rocketborne interferometer probe, *SPIRIT 1*, which reveal new spectral features in the hot bands

(Adler-Golden *et al.*, 1990). An analysis of these and other data on ozone is presented here which has resulted in energies and assignments for ozone vibrational states not previously observed with up to seven vibrational quanta and energies as high as $\sim 6350 \text{ cm}^{-1}$. Support for the analysis is provided by the very good agreement with predictions of an improved Darling-Dennison-type energy level formula (Adler-Golden *et al.*, 1990) derived from i.r. absorption and Raman spectra.

With reasonably precise ($\pm 2\text{--}4 \text{ cm}^{-1}$) hot band centers and assignments in hand, and using estimated band emission intensities, relative vibrational state populations may be derived from spectral simulations. From these populations, insight into the kinetics of vibrationally excited ozone may be obtained. Some general conclusions regarding the vibrational relaxation mechanism are drawn; a detailed model will await further investigation.

2. DATA

2.1. SPIRIT 1 spectra

The atmospheric emission spectra of ozone obtained in the *SPIRIT 1* rocket experiment are described elsewhere (Adler-Golden *et al.*, 1990). In brief, the spectra were taken with a telescoped, cryogenically cooled Michelson interferometer viewing tangent heights of 70–80 km. The hot band spectra analyzed here were taken through a bandpass filter

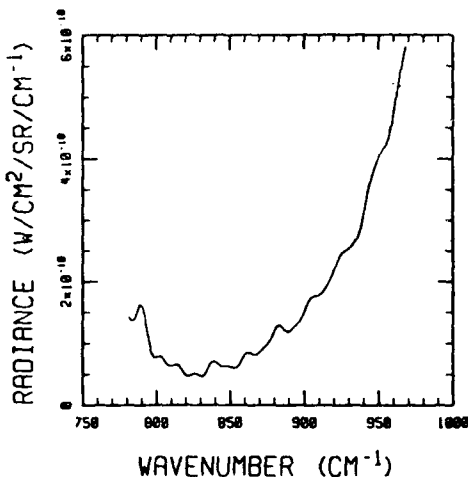


FIG. 1. *SPIRIT 1* SPECTRUM OF THE OZONE v_3 HOT BAND REGION, WITH TRIANGULAR APODIZATION (SCAN 236, DETECTOR 1); TANGENT HEIGHT = 79 km.

which transmitted the 780–980 cm^{-1} region; the unapodized resolution is 4 cm^{-1} . The interferograms were processed to remove stray points and de-trended using the dc level to compensate for radiance variations during the scan (Grieder *et al.*, 1987), which would otherwise lead to self-apodization. The de-trending method was largely successful, although some shortcomings are indicated by occasional scan-to-scan variations in the apparent resolution. Better consistency, but of course lower resolution, was obtained when an apodization window was applied.

Typical spectra are shown in Figs 1 and 2. Figure

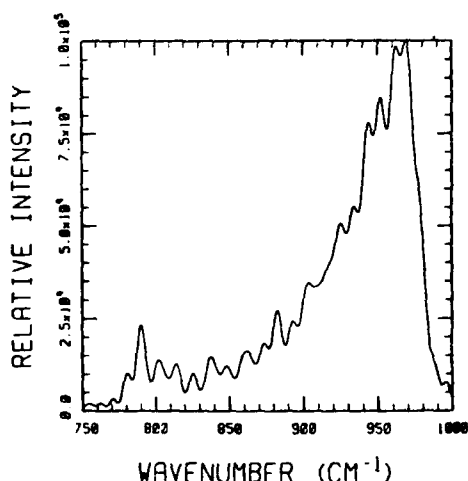


FIG. 2. UNAPODIZED, UNCALIBRATED SPECTRUM FROM THE SAME SCAN AS SHOWN IN FIG. 1.

1 is a triangularly apodized spectrum corrected for the instrument and bandpass filter response. Figure 2 is the unapodized, uncalibrated spectrum, and shows the rolloffs in the filter transmission below $\sim 800 \text{ cm}^{-1}$ and above $\sim 970 \text{ cm}^{-1}$. Between these points, the system response curve is flat to within $\pm 10\%$. Except for faint 8 cm^{-1} oscillations in the wings of the unapodized spectrum, which arise from the sidelobes of the $\sin(x)/x$ function, the spectral structure is all real, as has been verified using apodized spectra further processed with resolution-enhancement techniques (Howard, 1983; Zachor *et al.*, 1987).

Below around 820 cm^{-1} , where the emission begins to rise, CO_2 bands may contribute. The peak near 791 cm^{-1} is the Q branch of the CO_2 (11101)–(10002) band [in HITRAN notation (Rothman *et al.*, 1987)] at 791.5 cm^{-1} , and provides a wavelength calibration point. Above 810–820 cm^{-1} , the spectrum scales uniformly with tangent height (Adler-Golden *et al.*, 1990), and is assigned entirely to ozone.

2.2. Other ozone spectra

To better understand the data from *SPIRIT 1*, we also examined a long-path ($\sim 60 \text{ atm-cm}$) absorption spectrum of ozone taken by Damon *et al.* (1981). A portion of their spectrum is reproduced in Fig. 3, which shows the 4900–4930 cm^{-1} region at a resolution of 0.04 cm^{-1} . (The y axis has been truncated, so the bottom of each trace corresponds to 60% rather than 0% transmission.) Partially resolved rotational structure from weak high-overtone or combination bands of ozone not previously reported may be seen. Much stronger ozone bands are observed at lower frequencies.

An approximate analysis of portions of the Damon *et al.* spectrum was performed using synthetic band contours generated as described in Section 3.3. As noted by Barbe *et al.* (1974), the high-overtone and combination bands have a low, elongated P branch and a sharp, compressed R branch with an abrupt cutoff. The R branch peaks are predicted to occur typically 10 cm^{-1} beyond the band center, with the cutoffs occurring typically 3 cm^{-1} beyond the peak. Inspection of Fig. 3 reveals an R branch in each of the top and bottom traces. The band centers are estimated as 4895 ± 1 and $4918 \pm 1 \text{ cm}^{-1}$, and are assigned respectively to the (311) and (005) bands. Band centers were similarly derived for the much stronger (103) and (113) combination bands which appear at lower frequencies (see Table 1).

The resonance Raman spectra obtained by Imre and co-workers also deserve a mention. Approximate energies obtained from their low-resolution spectrum (8 Å FWHM) appear in Imre *et al.* (1982). Sub-

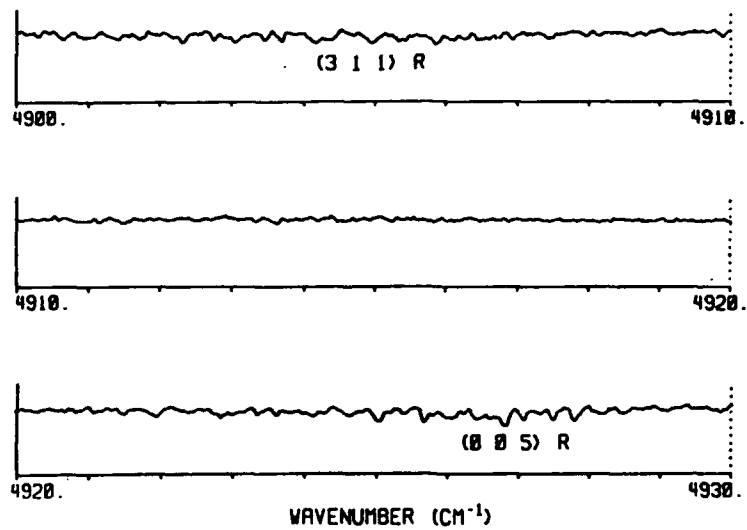


FIG. 3. THE ABSORPTION SPECTRUM OF OZONE FROM 4900 TO 4930 cm^{-1} , REPRODUCED FROM DAMON *et al.* (1981), SHOWN WITH CURRENT R-BRANCH ASSIGNMENTS.
Bottom of the y axis is 60% transmission.

TABLE I. ENERGIES AND BAND CENTERS FOR OZONE VIBRATIONAL STATES

State	Calc.	Energy (cm^{-1})		Band center (cm^{-1})		
		Obs.	Current	Calc.	Obs.	Current
003	3045	$3046 \pm 1^*$	3046	987	$987 \pm 3\ddagger$	988
004	3999		4000	954	$952 \pm 3\ddagger$	954\ddagger
005	4910\\$			911\\$		
	4918\\$\dagger	$4918 \pm 1\ \dagger$	4919	919\\$\dagger	$916 \pm 3\ddagger$	919
311	4902\\$					
	4894\\$\dagger	$4895 \pm 1\ \dagger$	4894	895**\\$\dagger		894**
006	5767	$5761 \pm 10\ddagger\ddagger$	5771	841\\$		
				849\\$\dagger		852
				873**\\$\dagger		877**
102	3085	$3084 \pm 1^*$	3083	975	$971 \pm 3\ddagger$	972
103	4025	$4019 \pm 1\ \dagger$	4020	940	$939 \pm 3\ddagger$	937\ddagger
104	4925		4926	900	$904 \pm 3\ddagger$	906\ddagger
105	5774		5778	849		852\ddagger
013	3695	$3697 \pm 1^*$	3697	970		971
014	4631		4633	936		936
015	5519		5517	888		884\ddagger
016	6342		6345	823		828\ddagger
112	3743		3743	958		958
113	4663	$4659 \pm 1\ \dagger$	4660	920		917
114	5537		5536	874		876\ddagger
115	6351		6353	814		817\ddagger

* Barbe *et al.* (1974); absorption.

\† Rawlins and Armstrong (1987); emission.

\‡ Q branch identified in SPIRIT 1 spectrum.

\\$ Excludes (311)-(005) resonance.

*\dagger Includes (311)-(005) resonance.

\|\ Contour analysis of Damon *et al.* (1981) absorption spectrum.

**\dagger Crossover band.

\ddagger Imre (1984); Raman spectrum.

sequently, a higher-resolution spectrum (1 Å FWHM) was taken which showed that many of the features found in the low-resolution spectrum consist of clumps of several vibrational bands. The energies of the individual bands in the 1 Å spectrum are reported in Imre (1984), and were used in deriving the improved energy level formula (see Section 3.2).

3. ANALYSIS AND RESULTS

3.1. Analysis overview

As found previously in the COCHISE laboratory spectra (Rawlins and Armstrong, 1987; Rawlins *et al.*, 1987), below six quanta the v_3 hot bands are dominated by transitions from the dyads of near-resonant states $(00v)$ and $(10v-1)$. These states correlate with the symmetric and antisymmetric combinations of pure local modes containing all of the vibrational energy in one bond, and approach degeneracy in the high v_3 limit. Given their closeness in energy, the states within each dyad are collisionally equilibrated to the kinetic temperature. The prominence of these essentially pure v_3 states in the spectrum seems to be due to a combination of a "colder" v_2 mode, the $\sim v_3$ -scaling of the Einstein coefficients for emission, and the large v_3 anharmonicity, which enhances the visibility of these bands by spacing them widely along the wavelength axis.

Trial values for up to five-quantum band centers were based on the COCHISE (Rawlins and Armstrong, 1987) results and on our analysis of the Damon *et al.* (1981) absorption spectrum described in Section 2. In addition to establishing the locations of the (005) , (311) , and (113) states, the Damon *et al.* spectrum led us to revise the location of the (103) state from $4026 \pm 1 \text{ cm}^{-1}$ reported by Barbe *et al.* (1974) to $4020 \pm 1 \text{ cm}^{-1}$, which in turn affected our estimate for the $(104)-(103)$ band center. Final values for the band centers were determined by locating their Q branches in unapodized *SPIRIT* 1 spectra where possible, and confirming the Q branch assignment with a spectral simulation. The simulations, described below, verified that these as well as most of the other peaks in the *SPIRIT* 1 spectrum are due to Q branch rather than P or R branch maxima. However, the latter tend to dominate at lower resolution.

In assigning the hot bands for six or more quanta, we initially considered only the dyads mentioned in the first paragraph. However, since there are more features in the observed spectrum than can be accounted for by these states alone, we expanded the list of candidate states to include the bending-excited states $(01v)$ and $(11v-1)$. Trial values for the band

centers were obtained from the six- and seven-quantum energies given by the formula (Adler-Golden *et al.*, 1990). This and related vibrational energy formulas are discussed in Section 3.2 below. As in the case of the lower-energy bands, final values for the centers were determined by tentatively locating the Q branches and confirming these assignments with a spectral simulation.

The band centers and vibrational energies derived from this analysis are summarized in Table 1. Eight bands whose isolated Q branches were observed in the *SPIRIT* 1 spectrum appear in the "Current" column of the table with the symbol \ddagger ; their centers are accurate to within $\sim 2 \text{ cm}^{-1}$ or better.

In addition to these observed bands, the "Current" column contains our best estimates for 10 other bands in this spectral region associated with states having $v_1 = 0$ or 1 and $v_2 = 0$ or 1. These bands either do not have a clearly distinguishable Q branch [e.g. bands associated with the (005) and (311) states] or else are obscured by another band. In most cases other data on the band center or the upper state energy are available (see the "Obs." columns). For three states, (006) , (014) and (112) , no reliable information is available, and their energies have been estimated using formula predictions and the energy of their dyad counterpart as guides. The estimated uncertainty for these band centers is $3-4 \text{ cm}^{-1}$.

The spectral simulations were generated on a 1 cm^{-1} grid from a set of assumed band centers and band contours. Due to the modest resolution of the *SPIRIT* 1 spectra (4 cm^{-1} unapodized) and the lack of data on rotational constants for the high-lying vibrational states of ozone, it was deemed neither necessary nor feasible to generate highly accurate vibration-rotation lines for each band. Instead, the band contours were derived using approximate vibration-rotation lines from a symmetric-top model, described in Section 3.3.

3.2. Energy level formulas

The standard formula for ozone vibrational energies is a quadratic expression containing Darling-Dennison coupling. Using parameter values obtained by Barbe *et al.* (1974), up to four-quantum states are fit to within several cm^{-1} . However, many of the approximately one dozen five- to seven-quantum states cited by Adler-Golden *et al.* (1990) which appear in the Raman spectrum (Imre, 1984) are overpredicted by tens of cm^{-1} .

Recent variants of the quadratic Darling-Dennison formula have incorporated a slightly different form for the Darling-Dennison coupling term (Benjamin *et al.*, 1983), as well as modified parameter values

chosen to fit the Raman data (Lehmann, 1984; Kellman, 1985). The newer formulas provide better overall fits, but still tend to overpredict the energies of the high v_3 states, which correlate with large-amplitude local-mode stretches. This indicates a flattening of the ozone potential surface along the bond coordinates when compared with a Morse oscillator description, to which these quadratic formulas best correspond.

The breakdown in the quadratic formulas for ozone vibrational energy is not at all surprising when one considers the magnitude of the dissociation energy, D_e , which may be identified with the maximum energy in the (00 v) and (10 v) sequences. The Barbe *et al.* formulas predicted that D_e is roughly twice the experimental (Stull *et al.*, 1971) D_e of 1.05 ± 0.02 eV (8500 cm^{-1}), and the newer formulas perform only slightly better.

An improved vibrational energy formula for ozone based on a higher-order expansion is called for. This approach potentially introduces a large number of empirical spectroscopic constants (i.e. fitting parameters) and, depending on the particular set selected, can lead to non-unique predictions. To minimize these difficulties, we used a combination of theoretical arguments, detailed below, and trial and error to develop an improved formula containing the fewest additional parameters while still giving a good fit to available vibrational energy data as well as the correct D_e . This formula is generated by multiplying four of the Barbe *et al.* anharmonic constants by a third-degree polynomial in the v_i , resulting in an overall degree of five. The polynomial, ρ , is given by

$$\rho = c_0 + c_1 x + c_2 x^2 + c_3 x^3, \quad x = v_1 + v_3 + c_4 v_2 - 3 \quad (1)$$

and multiplies the constants X_{11} , X_{13} , X_{33} , and γ (the Darling-Dennison coupling constant) which characterize the anharmonicity in the stretching coordinates. The number of new fitting parameters involving the stretching quanta v_1 and v_3 is only four since the quanta are summed. An extra parameter c_4 is included to improve the fit of high vibrational levels containing bending quanta; c_4 essentially scales v_2 to an equivalent number of stretching quanta in computing the variable x in ρ . The constant “-3” in x was included for convenience to make the value of c_0 close to unity.

The improved formula, while largely empirical, was constructed with theoretical considerations in mind. Lehmann (1983) and Kellman (1985) have shown that a coupled Morse-oscillator Hamiltonian for a triatomic molecule can be algebraically transformed to the normal-mode, quadratic Darling-Dennison form. In particular, Lehmann showed that transformation of the Child and Lawton (1981) model Hamiltonian

TABLE 2. ENERGY LEVEL FITTING PARAMETERS FOR EQUATION (1)

Parameter	Fit I*	Fit II†	Fit III‡
c_0	1.0	1.0015	1.0 (fixed)
c_1	0.0016	0.0060	0.00289
c_2	0.0020	0.0026	0.00118
c_3	0.0006	0 (fixed)	0.00033
c_4	1.2	2.21	1.91
D_e (eV)	1.05	1.22	1.13

* From Adler-Golden *et al.* (1990), fit to i.r. and Raman data, constrained D_e ; ω_i , X_{ij} , γ from Barbe *et al.* (1974).

† Least-squares fit to i.r. and Raman data, unconstrained D_e ; ω_i , X_{ij} , γ from Barbe *et al.* (1974).

‡ Least-squares fit to i.r. and Raman data including SPIRIT 1 bands, unconstrained D_e ; $\omega_1 = 1135.8$, $\omega_2 = 714.6$, $\omega_3 = 1088.9$, $X_{11} = -5.28$, $X_{22} = -0.7$, $X_{33} = -10.5$, $X_{13} = -35.2$, $X_{23} = -16.3$, $X_{12} = -8.75$, $\gamma = -27.37$, in cm^{-1} .

results in fixed ratios among the anharmonic constants X_{11} , X_{13} , X_{33} and γ , and that their absolute values scale with the Morse parameter $\omega_e x_e$. The predicted anharmonic constant ratios are in approximate agreement with those computed from the Barbe *et al.* constants for ozone. In this context, the use of the factor ρ in the current energy formula for ozone may be thought of as generating a new set of anharmonic “constants” which are maintained in these same ratios, but which increase steadily with increasing vibrational energy to represent a flatter Morse potential with a larger $\omega_e x_e$ and thus a reduced D_e .

Initial values for c_0 through c_4 were derived by manual trial-and-error fits to the available Raman and i.r. absorption data, while constraining D_e to within 100 cm^{-1} of the measured value. The resulting energies (Table 1) and fitting parameters (Table 2, Fit I) have been reported previously (Adler-Golden *et al.*, 1990).

Later, when the SPIRIT 1 bands had been tentatively assigned, two more fits were developed, this time using a weighted, non-linear least-squares fitting routine with no D_e constraint. The weights were assigned to yield an accurate fit (to within tenths of cm^{-1}) to the low-energy states and a less precise fit (within the 10 cm^{-1} experimental uncertainty) to the Raman data. In the first fit (Fit II) up to five quantum states from i.r. measurements (absorption and SPIRIT 1) as well as the six- and seven-quantum Raman states were included; c_4 , which was poorly determined, was set to zero. The D_e of the resulting fit turned out to be 1.22 eV, somewhat above the measured value. In the second fit (Fit III) the new six- and seven-quantum energies derived from SPIRIT 1 observations (reported in the “Current” column of Table 1) were included, and all spectroscopic con-

stants except for c_0 , which in this case is redundant, were allowed to vary. The D_e of the resulting fit, 1.13 eV, is closer to the measured value.

The three energy level fits will be compared in Section 4; their important characteristics may be summarized briefly. All of the fits are essentially equivalent to the quadratic Barbe *et al.* formula below five quanta. This is because c_0 is unity or close to unity, and the sum of the remaining terms in ρ is small at low numbers of stretching quanta, so ρ is close to unity. In Fit III the spectroscopic constants were allowed to vary, but they nonetheless turned out to be very similar to the Barbe *et al.* constants used in Fits I and II. The predictions of all three fits for up to six-quantum states agree to within typically several cm^{-1} . The seven-quantum predictions show a wider spread, however, correlating with the differences in dissociation energies.

3.3. Band contour model

In a non-rigid symmetric top approximation, the vibration-rotation energies are given by

$$E_R = \bar{B}J(J+1) + (A - \bar{B})K^2 - \Delta_K K^4 - \Delta_{JK} J(J+1)K^2 - \Delta_J J^2(J+1)^2 \quad (2)$$

with $\bar{B} = (B+C)/2$. The line intensities are derived from the Hoenl-London factors for A -type bands combined with v^4 scaling, which is appropriate for an emission spectrum in units of watts per cm^{-1} . In this approximation all off-diagonal matrix elements, including Coriolis coupling elements, of the rotational Hamiltonian in the symmetric-top, uncoupled anharmonic oscillator basis set are neglected. The

rotational constants A , B , and C are given to first order in vibration-rotation coupling by

$$A = A_0 + \alpha_1' v_1 + \alpha_2' v_2 + \alpha_3' v_3, \quad (3)$$

with similar equations for B and C . Here the v_i are the quantum numbers of the uncoupled vibrational states. A_0 , B_0 , C_0 refer to the ground state and their values are listed (Steinfeld *et al.*, 1987); the α s are taken from Barbe *et al.* (1974). The centrifugal distortion terms Δ in equation (2) are taken to be vibration-independent, and are fixed to the ground state values (Pickett *et al.*, 1985).

The band contours were generated by calculating the vibration-rotation transitions and intensities, binning to the nearest wavenumber, and smoothing slightly. In generating synthetic spectra to be compared with *SPIRIT* I data, the instrument function [e.g. $\sin(x)/x$ for unapodized interferograms] was convolved with the band contours.

Results for the (001) band are shown in Fig. 4, along with an "exact" spectrum generated from line positions and intensities in the HITRAN line atlas (Rothman *et al.*, 1987). The excellent agreement validates the accuracy of the symmetric-top contour approximation, at least for low vibrational levels.

Above one stretching quantum, the pure vibrational part of the Hamiltonian contains Darling-Dennison off-diagonal elements. Diagonalization of the vibrational Hamiltonian leads to vibrational eigenstates with rotational constants

$$A = A_0 + \alpha_1' \langle v_1 \rangle + \alpha_2' \langle v_2 \rangle + \alpha_3' \langle v_3 \rangle, \quad (4)$$

etc. where " $\langle \rangle$ " denotes expectation value. In the

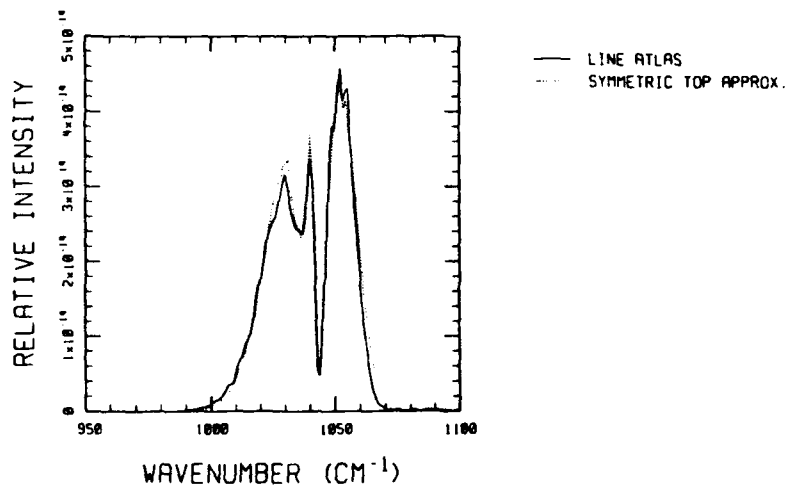


FIG. 4. SYNTHETIC OZONE (001) EMISSION SPECTRUM AT 180 K, 2 cm^{-1} RESOLUTION.

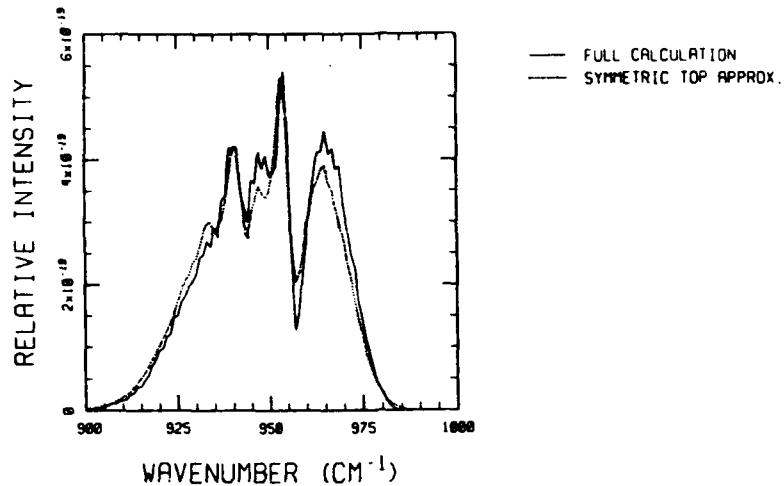


FIG. 5. SYNTHETIC EMISSION SPECTRUM FOR OZONE $v_2 = 0, v_1 + v_3 = 4$ TO $v_1 + v_3 = 3$ TRANSITIONS AT 180 K.
 2 cm^{-1} RESOLUTION.

The main contributions are from the (004)-(003) and (103)-(102) bands. The vibrational Hamiltonian is from Barbe *et al.* (1974).

current work we have also included an off-diagonal matrix element of 11 cm^{-1} which couples the (005) and (311) eigenstates in a subsequent diagonalization (see Section 4).

Equation (4) derives from equation (3) assuming neglect of Darling-Dennison coupling terms involving rotational operators. This assumption is reasonable according to the analysis by Flaud *et al.* (1980) of the (200), (101), and (002) states. Flaud *et al.* were able to discern only one non-zero coupling term of this type multiplying the J^2 operator, with a very small coefficient (much smaller than the α s). This coupling term and others may therefore be neglected, at least for moderate vibrational excitation.

A potential limitation of equation (2) at high vibrational energies arises from the neglect of Coriolis interactions, especially between the (0 v_2, v) and (1 $v_2, v-1$) states which lie very close in energy. To more critically assess the validity of this approximation, a "full" vibration-rotation calculation was run on the ($v_1 + v_3 = 4$) \rightarrow ($v_1 + v_3 = 3$) transitions with $v_2 = 0$ using the asymmetric rotor program developed by Pickett *et al.* (1985). In this calculation all nine Coriolis- and Darling-Dennison-interacting vibrational states were included, with appropriate coupling elements as well as high-order centrifugal distortion terms. The resulting emission spectrum is shown in Fig. 5, along with a calculation using the symmetric-top approximation and the same uncoupled band centers and Darling-Dennison elements. The two spectra are in reasonable agreement.

At higher energies, the (00 v) and (10 $v-1$) states lie even closer together. However, this is compensated by a decrease in the Coriolis coupling operator brought on by the Darling-Dennison resonance, which is associated with increasing local-mode behavior of the vibrational wavefunctions. Thus, we believe that the current band contour approach will remain reasonable even for high levels of vibrational excitation.

3.4. Spectral simulations

3.4.1. *Intensity constraints.* If each of the 17 vibrational states listed in Table I were assigned an independent population, there would be equally many independent band intensities required for a synthetic spectrum. It is much more sensible to reduce this number using fixed population and band strength ratios between the (0 v_2, v) and (1 $v_2, v-1$) dyad member states. That is, the bands of a given dyad are treated as single, independent spectral components. The (311) state is grouped with the (005) and (104) states since it is assumed to be in resonance with (005) (see Section 4). This results in a total of eight components, which are listed in Table 3. In accordance with the discussion in Section 3.1, the population ratios within each component are given by the Boltzmann ratio at a mesospheric temperature taken as 180 K.

For completeness, two additional bands not appearing in Table I have been included; these are (311)-(310) and the corresponding crossover band (005)-(310). The (310) energy is taken as 3963 cm^{-1} . As is typical for bands associated with large v_1 ,

TABLE 3. COMPONENT POPULATIONS AND TRANSITION DIPOLES USED IN SYNTHETIC SPECTRUM

No.	Component states	Relative population*	Band	$\langle \mu \rangle^2 / \langle \mu \rangle_{001}^2 \dagger$
1	(003)+(102)	1.5	(003)-(002) (102)-(101)	2.5 1.7
2	(004)+(103)	0.75	(004)-(003) (103)-(102)	3.0 2.2
3	(005)+(311)+(104)	0.89	(005)-(004) (005)-(310) (311)-(004) (311)-(310) (104)-(103)	2.2 0.2 1.1 0.4 2.7
4	(006)+(105)	0.25	(006)-(005) (006)-(311) (105)-(104)	2.2 1.1 3.1
5	(013)+(112)	0.94	(013)-(012) (112)-(111)	2.5 1.7
6	(014)+(113)	0.21	(014)-(013) (113)-(112)	3.0 2.3
7	(015)+(114)	0.21	(015)-(014) (114)-(113)	3.3 2.7
8	(016)+(115)	0.20	(016)-(015) (115)-(114)	3.4 3.1

* Total component population, from least-squares fit.

† Squared transition dipole relative to (001) band, from equation (5).

or v_2 , they are overlapped by other, much stronger bands, and thus have little impact on the spectrum.

The band intensities within each component are scaled using calculated transition dipole moments based on a fit to an *ab initio* calculation (Adler-Golden *et al.*, 1985) which probed up to four-quantum states. The fit, expressed in the uncoupled vibrational basis, is given by

$$\langle v_1 v_2 v \rangle \mu[v_1 v_2 v - 1] / \text{a.u.} = \sqrt{v(0.06932 - 0.003v_1 - 0.006v_2 - 0.0012v)} \quad (5)$$

with all other dipole matrix elements set to zero. Equation (5) was used to generate relative transition dipole moments, which are given in Table 3.

3.4.2. *Procedure and results.* Relative populations for the eight independent components were initially selected to give qualitative agreement with results from previous data (Rawlins and Armstrong, 1987; Rawlins *et al.*, 1987) and models. The populations and band centers were then refined by trial and error within fairly narrow limits in order to improve the agreement with the *SPIRIT* 1 spectrum. When the band centers were finalized, a new set of populations was derived from a least-squares fit to the unapodized *SPIRIT* 1 spectrum in the 820–960 cm⁻¹ range. The results are shown in Fig. 6, where the synthetic and observed spectra are compared. Figure 7 shows the individual components which make up the synthetic spectrum. The relative state populations from the

least-squares fit are given in Table 3.

The overall agreement between the calculated and observed spectrum is encouraging, and supports the band assignments in Table 1. At low wavenumbers, the *Q* branches in the synthetic spectrum are somewhat less pronounced and the *P* and *R* branches are more pronounced compared with the observed spectrum. These differences may partly reflect self-apodization, etalon fringes or other instrumental effects, but more likely involve shortcomings in the synthetic contours for the six- and seven-quantum bands. Given the lack of perfect agreement, the derived populations in Table 3 are approximate. Precise error bars are difficult to assign since some of the components (e.g. components 1 and 5) are similar in shape and therefore strongly correlated. Also, we suspect that the (015) and (114) populations have been underestimated since the (114) *Q* branch peak at ~875 cm⁻¹ is missing in the synthetic spectrum. At lower resolution, the agreement between the synthetic and observed spectra improves.

4. DISCUSSION

4.1. *Ozone vibrational energies and band assignments*

The analysis of atmospheric spectra taken in the *SPIRIT* 1 rocket experiment, together with previous laboratory spectra, has led to a consistent set of vibrational energies and v_1 band centers for up to

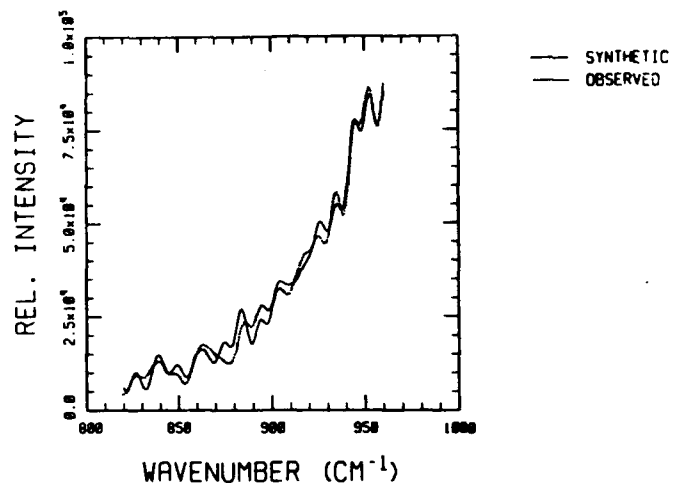


FIG. 6. COMPARISON OF OBSERVED AND SYNTHETIC UNAPODIZED OZONE SPECTRA.

seven-quantum vibrational states of ozone with accuracies of $2\text{--}4\text{ cm}^{-1}$. The agreement with the predictions of the Adler-Golden *et al.* (1990) energy level formula is only slightly worse than this for all states except (005) and (311) (see below). The six- and seven-quantum energies are predicted to within 4 cm^{-1} , and the splittings between the ($0\nu_2\nu$) and ($1\nu_2\nu-1$) dyad members are predicted even more accurately. The (103) state energy is 5 cm^{-1} off, but this is partly because the formula parameters had been derived from a fit containing the energy value reported by Barbe *et al.* (1974), which we now believe is around 6 cm^{-1} too high.

The energies of the (005) and (311) states, whose transitions to the ground state are found side-by-side in the Damon *et al.* (1981) absorption spectrum (see Fig. 3), differ from the formula predictions by unusually large amounts. The actual energy separation between these states is $\sim 24\text{ cm}^{-1}$, compared with the much smaller separations of $3\text{--}10\text{ cm}^{-1}$ predicted by formula Fits I-III. This observation, and the surprising strength of the (311) combination band, leads us to infer a resonance between these near-coincident states. Using the Adler-Golden *et al.* (1990) formula (Fit I) for the uncoupled energies, the effective coupling matrix element is found to be $\sim 11\text{ cm}^{-1}$. This

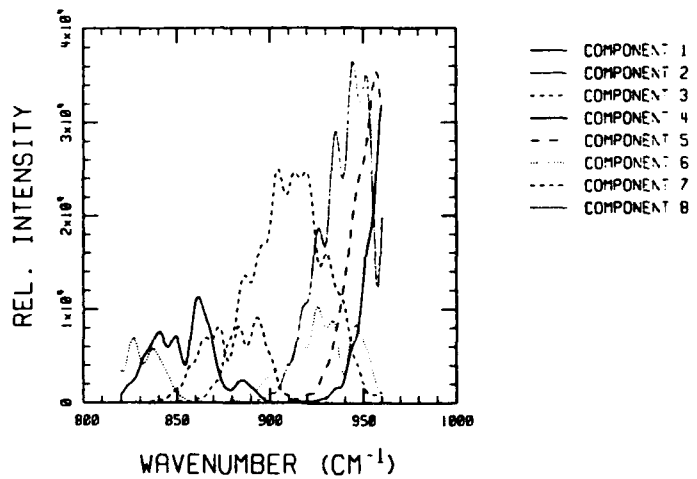


FIG. 7. INDIVIDUAL COMPONENT CONTRIBUTIONS TO THE FIG. 6 SYNTHETIC SPECTRUM.

leads to mixing coefficients in a 2:1 ratio, which is indeed consistent with the estimated relative band strengths in Fig. 3.

While a coupling matrix element of $\sim 11 \text{ cm}^{-1}$ seems large for two states which formally differ by eight vibrational quanta, it is not unreasonable when one considers the strong interaction between the stretching modes. For example, the Darling-Dennison resonance mixes the zeroth-order (311) and (113) states, and the zeroth-order (005) and (203) states. The (113) and (203) states differ by only two quanta, and can be coupled in second order via cubic terms in the normal mode potential expansion. Other possibly observable states besides (005) and (311) could also have chance energy coincidences. However, they would typically differ by many bending quanta and therefore couple much more weakly.

The coupling between the (005) and (311) states weakens the "normal" (006)-(005) and (005)-(004) bands and introduces "crossover" bands (311)-(004) and (006)-(311) which have been included in Tables 1 and 3 and in the synthetic spectrum. Both the normal and crossover bands are predicted to have atypical contours with degraded Q branches. The crossover bands cannot be unambiguously identified in the spectrum, but their impact is significant since they contribute intensity which otherwise would have to be accommodated by the (114), (015), and (104) v_3 bands.

While it is difficult to prove conclusively that all of the current band assignments in the *SPIRIT* 1 spectrum are correct, their agreement with the formula band center predictions is a strong argument in their favor. Table 4 compares the predictions of Fits I-III with the *SPIRIT* 1 assignments for bands with observable Q branches. For up to six-quantum states the total spread in predicted band centers is at most 6 cm^{-1} among all three fits, and we have obtained similar levels of consistency using other types of energy level formulas. This maximum spread is smaller than the $\sim 10 \text{ cm}^{-1}$ spacing of recognizable peaks in the spectrum, which are mainly Q branches, so most of them can be confidently identified. The seven-quantum band center predictions vary over a wider range, and one might argue that the current assignments, which invoke v_2 (bending) excitation, may not be the only ones possible. On the other hand, the $v_2 = 0$ bands (007) and (106) are predicted to occur at much lower frequencies regardless of the fit (see Table 4), and are unlikely alternative candidates.

Additional considerations further reduce the ambiguity in the band assignments, such as the occurrence of the bands in pairs corresponding to the $v_1 = 0$ and $v_1 = 1$ dyad members [for example (016) and (115)].

TABLE 4. COMPARISON OF PREDICTED BAND CENTERS (cm^{-1}) FROM TABLE 2 FITS

Band	Fit I	Fit II	Fit III	<i>SPIRIT</i> 1 observed
(004)-(003)	954	952	953	954
(103)-(102)	940	938	939	937
(104)-(103)	900	897	900	906
(105)-(104)	849	851	855	852
(015)-(014)	888	893	887	884
(114)-(113)	874	879	874	876
(016)-(015)	823	841	827	828
(115)-(114)	814	831	818	817
(007)-(006)	787	801	803	—
(106)-(105)	783	797	799	—

Except for bands affected by the (005)-(311) resonance, the bands in the pair have nearly equal intensities. Also, the spacing between them should agree well with formula predictions, which depend only on the dyad splittings and are extremely insensitive to the parameters employed.

4.2. Ozone vibrational state populations and kinetics

An important conclusion from the analysis of the *SPIRIT* 1 atmospheric hot band spectrum is the significant population of bending-excited states in ozone recombination. At four to five quanta their presence is not obvious in the spectrum due to overlapping $v_2 = 0$ bands, but at six and seven quanta the $v_2 = 1$ states are clearly visible and their populations are comparable to the (006) and (105) states (see Table 3).

Earlier studies (Rawlins and Armstrong, 1987; Rawlins *et al.*, 1987) examined the recombination spectrum obtained in the cryogenic COCHISE facility using microwave-discharged oxygen/argon mixtures. Their analyses revealed up to five-quantum vibrational states, but found no evidence of bending-excited states. Our own preliminary simulations of the COCHISE spectra suggest that significant $v_2 = 1$ band contributions can be incorporated, especially at the higher energies; however, the (011) band is virtually absent. Additional simulations and the examination of unfiltered *SPIRIT* 1 spectra (see Adler-Golden *et al.*, 1990), which cover higher frequencies, would help characterize more accurately the vibrational populations in COCHISE and atmospheric spectra, and the effects, if any, caused by the different experimental conditions.

The presence of high-energy bending-excited states of ozone in the recombination spectrum is expected from considerations of vibrational relaxation kinetics. It is generally believed that the increased density of states at high energies, even in small molecules, causes vibrational state distributions to lose most mode-

TABLE 5. COMPARISON OF OBSERVED AND MODEL VIBRATIONAL STATE POPULATIONS

Component	V	Relative population	
		Obs.*	Equation (6)
1	3	1.5	1.5
2	4	0.75	0.75
3	5	0.89	0.64
4	6	0.25	0.27
5	4	0.94	0.75
6	5	0.21	0.43
7	6	0.21	0.27
8	7	0.20	0.18

* Least-squares fit to spectrum, from Table 3.

specificity, so that all vibrational states at a given energy are comparably populated. In ozone the decreasing energy gaps between the (v_1, v_2, v_3) and (v_1, v_2+1, v_3-1) states with increasing energy may speed the conversion of stretching quanta into bending quanta, which is a key vibrational relaxation mechanism at low energies (Steinfeld *et al.*, 1987).

In line with these expectations, the relative state populations derived from the *SPIRIT* 1 spectrum (see Table 3) are found to correlate approximately with the vibrational energy. The correlation is even better with the total number of vibrational quanta, denoted V , since the bending mode, which has the lowest frequency, does appear slightly colder than the others. This behavior suggests a simple, phenomenological model in which the ozone molecules, formed by recombination in states near the dissociation limit, relax stepwise from states V to $V-1$ with a characteristic first order rate constant k_V . The steady-state population of any state $[V]$ is then given by

$$[V] = \frac{R/k_V}{1 + 1.5V + 0.5V^2}, \quad (6)$$

where the denominator represents the number of states containing V quanta, and R is the rate of recombination. Allowing for the uncertainties in the Table 3 populations, reasonable agreement is obtained if one assumes a linear relaxation rate, $k_V \sim V$ (see Table 5). Linear V -dependence is consistent with radiative relaxation as well as collisional deactivation with harmonic-oscillator probability scaling.

5. SUMMARY

Analysis of the atmospheric emission spectrum of ozone v , hot bands, utilizing previous spectroscopic data and formulas and band contour simulations, has resulted in approximate energies and band centers for vibrational states having up to seven quanta. $v_2 = 1$

as well as $v_2 = 0$ bands have been found, and the existence of an accidental resonance between the (005) and (311) states is inferred with the aid of a long-path absorption spectrum (Damon *et al.*, 1981). These results should be of considerable value for upper atmospheric radiance modeling and for improving our understanding of ozone's vibrational relaxation kinetics.

Acknowledgements—We greatly thank Dr Herb Pickett (Jet Propulsion Laboratory) for informative discussions and the use of his asymmetric rotor program, and Dr John Gruninger (Spectral Sciences Inc.) for assistance with the non-linear energy level fitting. The *SPIRIT* 1 atmospheric measurement program was conducted by the Geophysics Laboratory with instrumentation developed and flown by Utah State University and Space Data Corp. (Tempe, Arizona). The experiment and all subsequent post-flight data analysis were supported by the Defense Nuclear Agency. The continued support and encouragement of Maj. Arman Mardigian, Dr Ken Schwartz, and Dr Leon Wittner has been vital and greatly appreciated. The work at Spectral Sciences was funded under Air Force contract F19628-87-C-0130.

REFERENCES

- Adler-Golden, S. M., Langhoff, S. R., Bauschlicher, C. W., Jr. and Carney, G. D. (1985) Theoretical calculation of ozone vibrational infrared intensities. *J. chem. Phys.* **83**, 255.
- Adler-Golden, S. M., Matthew, M. W., Smith, D. R. and Ratkowski, A. J. (1990) 9–12 μm atmospheric ozone emission observed in the *SPIRIT* 1 experiment. *J. geophys. Res.* (in press).
- Barbe, A., Scroun, C. and Jouve, P. (1974) Infrared spectra of $^{16}\text{O}_3$ and $^{18}\text{O}_3$: Darling and Dennison resonance and anharmonic potential function of ozone. *J. molec. Spectrosc.* **49**, 171.
- Benjamin, I., Levine, R. D. and Kinsey, J. L. (1983) High-lying levels of ozone via an algebraic approach. *J. phys. Chem.* **87**, 727.
- Child, M. S. and Lawton, R. T. (1981) *Faraday Discuss.* **71**, 273.
- Damon, E., Hawkins, R. L. and Shaw, J. H. (1981) A spectrum of ozone from 760 to 5800 cm^{-1} . Report RF Project 761420/711626, Interim Technical Report, The Ohio State University Research Foundation, Columbus, OH, Grant No. NSG-4749.
- Flaud, J.-M., Camy-Peyret, C., Barbe, A., Scroun, C. and Jouve, P. (1980) Line positions and intensities for the $2v_3$, $v_1 + v_3$, and $2v_1$ bands of ozone. *J. molec. Spectrosc.* **80**, 185.
- Grieder, W. F., Richards, E. N., Delay, S. H. and Foley, C. I. (1987) *SPIRIT* 1 interferometer data base. Final Report, Utah State University Subcontract 85-062, Contract F19628-83-C-0056, Space Data Analysis Laboratory, Boston College, Newton, MA.
- Howard, S. J. (1983) Improved resolution of spectral lines using minimum negativity and other constraints, in *Spectrometric Techniques* (Edited by Vanasse, G. A.), Vol. III. Academic, New York.
- Imre, D. (1984) Reaction dynamics studied by photo-emission spectroscopy. Ph.D. thesis, Massachusetts Institute of Technology.

Imre, D. G., Kinsey, J. L., Field, R. W. and Katayama, D. H. (1982) Spectroscopic characterization of repulsive potential energy surfaces: fluorescence spectrum of ozone. *J. phys. Chem.* **86**, 2564.

Kellman, M. E. (1985) Algebraic resonance dynamics of the normal/local transition from experimental spectra of ABA triatomics. *J. chem. Phys.* **83**, 3843.

Lehmann, K. K. (1983) On the relation of Child and Lawton's harmonically coupled anharmonic-oscillator model and Darling-Dennison coupling. *J. chem. Phys.* **79**, 1098.

Lehmann, K. K. (1984) Comment on "High-lying levels of ozone via an algebraic approach." *J. phys. Chem.* **88**, 1047.

Pickett, H. M., Cohen, E. A. and Margolis, J. S. (1985) The infrared and microwave spectra of ozone for the (0, 0, 0), (1, 0, 0), and (0, 0, 1) states. *J. molec. Spectrosc.* **110**, 186.

Rawlins, W. T. and Armstrong, R. A. (1987) Dynamics of vibrationally excited ozone formed by three-body recombination. I. Spectroscopy. *J. chem. Phys.* **87**, 5202 (1987).

Rawlins, W. T., Caledonia, G. E. and Armstrong, R. A. (1987) Dynamics of vibrationally excited ozone formed by three-body recombination. II. Kinetics and mechanism. *J. chem. Phys.* **87**, 5209.

Rothman, L. S., Gamache, R. R., Goldman, A., Brown, L. R., Toth, R. A., Pickett, H. M., Poynter, R. L., Flaud, J.-M., Camy-Peyret, C., Barbe, A., Husson, N., Rinsland, C. P. and Smith, M. A. H. (1987) The HITRAN database: 1986 Edition. *Appl. Optics* **26**, 4058.

Stair, A. T., Jr., Sharma, R. D., Nadile, R. M., Baker, D. J. and Grieder, W. F. (1985) Observations of limb radiance with cryogenic spectral infrared rocket experiment. *J. geophys. Res.* **90**, 9763.

Steinfeld, J. I., Adler-Golden, S. M. and Gallagher, J. W. (1987) Critical survey of data on the spectroscopy and kinetics of ozone in the mesosphere and thermosphere. *J. phys. Chem. Ref. Data* **16**, 911.

Stull, D. R. and Prophet, H. (1971) *JANAF Thermochemical Tables*, second edition. NBS 37, Office of Standard Reference Data, National Bureau of Standards, Washington, D.C., Contract No. F04611-67C-0009.

Zachor, A. S., Sharma, R. D., Winick, J. R. and Picard, R. H. (1987) Resolution enhancement of atmospheric emission spectra. Final Report, Utah State University Subcontract 86-502, Contract F19628-83-C-0056, Atmospheric Radiation Consultants, Acton, MA.

Appendix H

Program Participants

Program Participants

Government Agencies

Strategic Defense Initiative (SDI)
Defense Nuclear Agency (DNA)
Phillips Laboratory, Geophysics Directorate

Responsibilities

Program Sponsor
Program Sponsor, Experiment Requirements
Program Management, Scientific Direction,
Data Management & Analysis

Supporting Contractors

Utah State University (USU)

Responsibilities

Cryo, Interferometer, TV, Photom,
Celestial Aspect Sensor, Fort Nelson,
and Peace River Support

Space Data Corporation (SDC)

Launch Vehicle, ACS, TM Integration

Epsilon Laboratories

Hasselblad 70 mm Film
Camera, Alignment

Ithaco Corporation

Horizon Sensor

Space Vector Corp (SVC)

Recovery System

University of Alaska (PFRR)

Launch SPT, Wind Weighting, Recovery

NASA-Wallops

Telemetry and Tracking - PFRR

Northeastern University

Telemetry Support - PFRR

Oklahoma State University (OSU)

Telemetry Support - Ft. Yukon

Tech International Corp (TIC)

Watson Lake Support

Boston College

Mission Planning, Data Reduction &
Analysis